

# **Electrochemical synthesis of metal complexes in batch and flow**

Hamish Robert Stephen

Submitted in accordance with the requirements for the degree of  
Doctor of Philosophy

The University of Leeds  
School of Chemistry

June 2022

The candidate confirms that the work submitted is his own and that appropriate credit has been given where reference has been made to the work of others.

This copy has been supplied on the understanding that it is copyright material and that no quotation from the thesis may be published without proper acknowledgement.

The right of Hamish Robert Stephen to be identified as Author of this work has been asserted by him in accordance with the Copyright, Designs and Patents Act 1988.

© 2022 The University of Leeds and Hamish Robert Stephen

The candidate confirms that the work submitted is his own, except where work which has formed part of jointly authored publications has been included. The contribution of the candidate and the other authors to this work has been explicitly indicated below. The candidate confirms that appropriate credit has been given within the thesis where reference has been made to the work of others.

References for jointly authored publications:

1. Hamish R. Stephen, Christiane Schotten, Thomas P. Nicholls, Madeleine Woodward, Richard A. Bourne, Nikil Kapur and Charlotte E. Willans, "A versatile electrochemical batch reactor for synthetic organic and inorganic transformation and analytical electrochemistry", *Org. Process. Res. Dev.*, **2020**, 24, 6, 1084-1089.

The work reported in this publication is presented in Chapter 2 of this thesis. Reactor design was performed by Dr Charlotte Willans, Prof. Nikil Kapur and the candidate. The gold reactions were performed by Madeleine Woodward. Some of the sulphonamide synthesis was performed by Dr Christiane Schotten. All other work was performed by the candidate.

2. Hamish R. Stephen, Sarah Boyall, Christiane Schotten, Richard A. Bourne, Nikil Kapur and Charlotte E. Willans, "Steps, hops and turns: examining the effects of channel shapes on mass transfer in continuous electrochemical reactors", *React. Chem. Eng.*, **2022**, 7, 264-268.

The work reported in this publication is presented in Chapter 3 of this thesis. Design of the third generation reactor was performed by Dr Charlotte Willans, Prof. Nikil Kapur and the candidate. The effects of alternating polarity was investigated by Dr Christiane Schotten. The systematic studies were conducted with Sarah Boyall. All other work was performed by the candidate.

## Acknowledgements

Firstly, I would like to thank my primary supervisor Dr Charlotte Willans for all of the guidance over the past few years and for finding the funding in the first place. It has been a pleasure to be part of your research group and work on such an interdisciplinary project. Thank for giving me the opportunities to try out some of my own ideas and being there to remind me what the important results are.

I would also like to thank my other supervisors, Prof. Richard Bourne and Prof. Nikil Kapur. Richard, you came up with loads of great ideas, particularly when it came to troubleshooting our flow set ups, it was a shame we never quite got round to automating our reaction. Special thanks should go to Nik and his unwavering patience, I think me and Chrissi found a way to break every reactor you made for us! Thank you for teaching me how to conduct CFD myself, if nothing else it kept me occupied during lockdown.

Thank you to my industrial sponsors for helping to fund this project and providing such wonderful expertise in the forms of Dr Martin Jones and Dr Rachel Munday from AstraZeneca, Dr Peter Ellis and Dr Crina Corbos from Johnson Matthey and Dr Stanley Lai from Syngenta. The advice from all of you has been invaluable.

Thank you to Dr Chris Pask for your help with X-ray crystallography over the years and managing to keep the department going almost single handed. A huge thank you to Dr Mark Howard for keeping the NMR spectrometers going despite all of my paramagnetic samples and all the times you joined us for coffee in our office. Thank you to Dr Alexander Kulak for his help with the SEM and EDX. Thank you to Dr Marc Ried, from the University of Strathclyde, for his help with the colour analysis experiments and interesting discussions despite the best attempts of the fire alarm to disrupt them. I would also like to thank the iPRD, and in particular the Bourne group, for entertaining my vague questions about DoE and servicing pumps.

A special thanks to everyone who has been a part of the 1.25 and 1.33 offices, this thesis would not have been possible without you all. Frances, thank you for looking after me during my MChem, showing me the dark arts of air sensitive chemistry and always being willing to talk about climbing. Ed, thank you for instigating the office bake off and setting the standard so high, I don't think any subsequent bakes have lived up to your infamous meringue. Thank you to Chrissi for introducing me to flow chemistry and for smuggling back a great assortment of cakes and biscuits from Germany. Tazzi Tom, thank you for looking after the group whilst Charlotte was away and for your sage advice which included such gems as 'never start a column on an empty stomach' and 'just whack it on the kuggi'. Thank you to Maddie, Sarah and Helen, you were all wonderful master and summer students. This thesis would have been significantly shorter without your inputs.



Tom, your infallible optimism will always amaze me, as will your impressive procrastination skills. The lab is much more organised thanks to your tidying sprees, even if I can no longer find anything. Matt, the honorary member of the Willans group, I don't know how I'll complete a crossword without your encyclopaedic geography knowledge. Thank you for your calming influence on the office. Ellis, you've managed to hold the fort in 1.25 on your own and make a great banana bread. I've no doubt that it will be chaos in your lab when you leave. James, I have never known anyone so enthusiastic and yet so cynical, woe betide any reaction that doesn't do what it's supposed to. Thank you for keeping me company in our corner of the lab. Megan, your no nonsense approach to chemistry and life has been quite impressive, as has your choice of satnav voice. Thank you for sharing my nickel frustrations, I know the project is in good hands. Abi, we started at the same time and it's been a pleasure to work with you. Thank you for somehow managing to keep the peace in the office and helping me to figure out my chemistry. I can only apologise for saddling you with the electrochemistry.

Thank you to all of my climbing friends, you've really made Leeds feel like home. You have all kept me going, despite the best attempts of my chemistry and ensured that weekends remained a work free zone. It was great to have people outside of chemistry to talk to and I'm looking forward to many more climbing trips, if only for the pastries.

Lastly, thank you to my family and family friends for our many adventures and instilling the importance of a healthy work-life balance. Even though I don't venture south very often, it's always nice to see you all. In particular thank you to my grandpa for fostering a sense of curiosity and inquisitiveness. Thank you to my parents for supporting me throughout and providing me with all of the opportunities and none of the pressure.

## Abstract

First-row transition metal complexes have received considerable interest as catalysts, yet despite this they remain underutilised. This could be partially attributed to the challenges in synthesising these, often air sensitive, complexes. Electrochemistry offers an attractive alternative to traditional methodologies, being very atom efficient and providing easy access to low oxidation state metal complexes. This thesis explores some of the challenges associated with electrochemical synthesis and aims to increase the accessibility of this methodology.

A new flexible and standardised electrochemical batch reactor enabling both organic and inorganic transformations and analytical electrochemistry was designed, developed and tested. This enabled the synthesis of an assortment of organometallic species, some of which were exceedingly air sensitive. In addition, the batch reactor was used to perform organic reactions in parallel, allowing the quick optimisation of a literature procedure. The design of this reactor is freely available, inexpensive and versatile. Furthermore, it will be commercialised in collaboration with Asynt, increasing the accessibility of electrochemistry to the synthetic chemistry community.

This project has also combined organometallic synthesis, electrochemical analysis and computational approaches to investigate how changing the shape of flow channels within an electrochemical flow reactor affects mass transfer and ultimately reaction outcome. Through these experiments it was demonstrated that by increasing the number of times that a flow channel passes through an electrode, in a 'hop', you can significantly increase the effective mass transfer coefficient. This phenomenon was exploited through the design of a new flow channel with numerous 'hops' which increased the efficiency of the reactor.

The Willans group were the first group to synthesise copper-NHC complex electrochemically under continuous conditions. The final chapter of this thesis extends this methodology to nickel. Initial studies found that there were problems with the mass balance and a significant amount of material was going missing. A novel series of experiments using a divided cell were used to examine where different parts of the reaction were taking place, this confirmed that free carbenes could be found in solution, as opposed to on the electrode. A raft of techniques were used to investigate the mechanism, demonstrating that the product was being degraded under the reaction conditions. These mechanistic insights were used to tune the reaction conditions, improving the mass balance of the reaction.

## Table of contents

<b>Acknowledgements .....</b>	<b>iii</b>
<b>Abstract .....</b>	<b>v</b>
<b>Table of contents .....</b>	<b>vi</b>
<b>List of figures .....</b>	<b>ix</b>
<b>List of tables .....</b>	<b>xv</b>
<b>List of schemes.....</b>	<b>xvii</b>
<b>List of graphs .....</b>	<b>xix</b>
<b>List of equations .....</b>	<b>xxi</b>
<b>List of abbreviations.....</b>	<b>xxiii</b>
<b>1. Introduction.....</b>	<b>1</b>
1.1. N-heterocyclic carbenes.....	1
1.1.1. Overview of carbenes.....	1
1.1.2. Metal-NHC complexes and catalysis .....	1
1.1.3. Synthesis of metal-NHC complexes .....	7
1.2. Flow chemistry .....	10
1.2.1. Fundamentals of flow chemistry .....	10
1.2.2. Synthesis of organometallic species in flow.....	13
1.3. Electrochemistry.....	17
1.3.1. Fundamentals of electrochemistry .....	17
1.3.2. Electrochemical synthesis of metal complexes.....	20
1.3.3. Electrochemistry in flow.....	24
1.4. Summary and Aims .....	28
<b>2. Electrochemistry in batch .....</b>	<b>29</b>
2.1. Design of a flexible batch reactor for electrochemistry.....	29
2.1.1. Existing batch reactors .....	29
2.1.2. Requirements for an electrochemical batch reactor.....	31
2.1.3. The bottle reactor .....	31
2.1.4. A more robust design for commercialisation .....	33
2.2. Synthesis of ligand precursors .....	34
2.2.1. IMesHX ligand precursors (L1 and L2) .....	35
2.2.2. Other ligand precursors.....	37
2.2.3. Cyclic voltammetry .....	38
2.3. Electrochemical synthesis of organometallic complexes .....	42
2.3.1. Electrochemical procedure in the bottle reactor.....	42

2.3.2.	Synthesis of copper-NHC complexes .....	43
2.3.3.	Synthesis of gold-NHCs .....	47
2.3.4.	Synthesis of iron complexes.....	48
2.4.	Electrochemical synthesis of organic molecules.....	49
2.4.1.	Sulphonamide synthesis .....	49
2.4.2.	Hypervalent iodine reactions .....	51
2.5.	Conclusions and future work .....	52
2.6.	Experimental .....	54
2.6.1.	General considerations .....	54
2.6.2.	Bottle reactor design .....	55
2.6.3.	Ligand synthesis .....	57
2.6.4.	Preparation of metal complexes .....	60
2.6.5.	Sulphonamide synthesis .....	62
2.6.6.	Synthesis of hypervalent iodine species .....	63
<b>3.</b>	<b>Mass transfer within an electrochemical flow reactor.....</b>	<b>64</b>
3.1.	Electrochemical flow reactors .....	64
3.1.1.	Reactor designs .....	65
3.1.2.	Third generation flow reactor.....	69
3.1.3.	Set up of electrochemical reactions in flow.....	70
3.2.	Investigation of different flow paths .....	72
3.2.1.	Initial investigations .....	72
3.2.2.	Modelling mass transfer .....	74
3.3.	Computational fluid dynamics.....	76
3.3.1.	Basic principles of fluid dynamics .....	76
3.3.2.	Simulating an electrochemical flow reactor.....	77
3.4.	The effect of hops on mass transfer .....	82
3.4.1.	Rationalising the effect of hops .....	82
3.4.2.	The happy hopper .....	84
3.5.	A systematic study .....	87
3.5.1.	Design of flow channels .....	87
3.5.2.	Characterisation of the spacers.....	88
3.5.3.	Synthesis of copper species.....	93
3.5.4.	Carboxylation of imidazoliums.....	94
3.6.	Conclusions and future work .....	97
3.7.	Experimental .....	99
3.7.1.	Third generation reactor .....	99

3.7.2.	Copper-NHC reaction.....	101
3.7.3.	Computational fluid dynamics studies .....	104
3.7.4.	Systematic studies .....	116
<b>4.</b>	<b>Continuous electrochemical synthesis of nickel(II)-<i>N</i>-heterocyclic carbene complexes.....</b>	<b>122</b>
4.1.	Synthesis of metal complexes .....	122
4.1.1.	Nickel(II)-NHC complexes .....	123
4.1.2.	Continuous synthesis of copper complexes.....	123
4.2.	Initial studies .....	124
4.2.1.	Translating batch into flow.....	124
4.2.2.	Ligand screen.....	127
4.2.3.	Selectivity of flow vs batch.....	128
4.2.4.	Optimisation in flow .....	132
4.3.	The mystery of the missing material – mechanistic studies .....	134
4.3.1.	Alternating polarity .....	135
4.3.2.	Surface analysis.....	137
4.3.3.	Divided cell experiments .....	142
4.3.4.	Colour analysis.....	147
4.4.	Product degradation .....	153
4.4.1.	Cyclic voltammetry .....	153
4.4.2.	Over-reaction of products.....	154
4.5.	Conclusions and future work .....	156
4.6.	Experimental .....	159
4.6.1.	General considerations .....	159
4.6.2.	Ligand synthesis .....	159
4.6.3.	Chemical synthesis of Ni <sup>II</sup> .....	162
4.6.4.	Electrochemical batch reactions.....	162
4.6.5.	Electrochemical flow reactions .....	163
4.6.6.	Divided cell experiments .....	165
4.6.7.	Colour analysis.....	166
<b>5.</b>	<b>Conclusion .....</b>	<b>168</b>
<b>6.</b>	<b>References .....</b>	<b>170</b>

## List of figures

Figure 1.1: NHCs are stabilised by $\pi$ -donation from the nitrogen atoms into the empty p orbital and the withdrawal of $\sigma$ electron density from the carbene by the nitrogen atoms. NHCs can also be easily tuned through modification of the R groups and heterocycle backbone. <sup>2</sup>	1
Figure 1.2: NHCs donate into $e_g$ orbitals. <sup>2</sup>	2
Figure 1.3: Iron-NHC complexes exhibit a wide variety of geometries. <sup>12,14,15</sup>	3
Figure 1.4: Iron-NHC complex used as a polymerisation catalyst by Grubbs et al. <sup>17</sup>	3
Figure 1.5: Kumada coupling using an iron-NHC as the catalyst. <sup>18</sup>	4
Figure 1.6: Copper-NHC catalysed 'click' reaction for the formation of triazoles. <sup>22</sup>	4
Figure 1.7: Copper-NHC catalysed hydrosilylation developed by the Nolan group. <sup>23</sup>	5
Figure 1.8: A selection of multidentate Ni-NHC complexes used to catalyse Kumada couplings. <sup>3</sup>	5
Figure 1.9: Nickel-NHC catalysed cross coupling of perfluorinated arenes with boronic acids. <sup>31</sup>	6
Figure 1.10: Nickel catalysed C-N cross coupling using Ni-NHC complexes generated in situ. <sup>32</sup>	7
Figure 1.11: Common methods of generating metal-NHC complexes using a base. The carbene can be produced first using a strong base (a) or in situ using a weaker base (b).	7
Figure 1.12: a) Copper-NHC complexes can be produced using the basic metal precursor $\text{Cu}_2\text{O}$ . <sup>36</sup> b) $[\text{Fe}\{\text{N}(\text{SiMe}_3)_2\}_2]$ can act as the base and the metal source when synthesising iron-NHC complexes. <sup>37</sup>	8
Figure 1.13: a) Transmetalation from silver is a common and synthetically easy way to generate metal-NHC complexes. <sup>1</sup> b) Magnesium-NHCs have been used to generate iron-NHCs via transmetalation. <sup>38</sup> c) Transmetalation from indium is an unusual method for producing nickel-NHCs. <sup>39</sup>	9
Figure 1.14: Chen et al have reported the use of metal powders to generate metal-NHC complexes for iron, cobalt, nickel and copper. <sup>41</sup>	10
Figure 1.15: In flow a reaction progresses over the length of the reactor (top). In batch the reaction progresses over time (bottom).	10
Figure 1.16: a) Idealised plug flow with uniform velocity across the channel. b) Laminar flow with a parabolic velocity profile.	11
Figure 1.17: a) Segmented flow is formed when two phases meet at a T-junction. b) Packed bed reactors are often used for heterogeneous catalysts.	12
Figure 1.18: a) Coiled tubular reactor made from 1/16" PTFE tubing. b) One tank of a CSTR; when in use multiple tanks are connected in series.	13
Figure 1.19: Synthesis by transferring magnesium from commercial Grignard reagents. <sup>60,62</sup>	14

Figure 1.20: The synthesis of Grignard reagents in CSTRs (a) and fluidised bed reactors (b). <sup>61,63</sup> .....	15
Figure 1.21: Synthesis of copper(I)-NHCs using a packed bed reactor. <sup>64</sup> .....	16
Figure 1.22: The synthesis of tricarbonyl chromium piano stool complexes in flow is much safer. <sup>65</sup> .....	16
Figure 1.23: Synthesis of iron piano-stool complexes in flow. <sup>66</sup> .....	17
Figure 1.24: Photochemical synthesis of RuCp(MeCN) <sub>3</sub> PF <sub>6</sub> on a gram scale. <sup>67</sup> .....	17
Figure 1.25: A simple electrochemical setup, oxidation occurs at the anode and reduction at the cathode. An electrolyte solution enables the transfer of charge. ....	18
Figure 1.26: A layer of anions forms on the surface of the anode with the concentration of anions and the potential decreasing with the distance from the electrode. ....	19
Figure 1.27: Schematic and photograph of a divided cell, with an ion exchange membrane separating the two chambers. ....	20
Figure 1.28: Scope of metal complexes produced electrochemically, the majority by Tuck et al. ....	21
Figure 1.29: a) General scheme for the electrochemical synthesis of metal complexes. b) A selection of mono- and bi-dentate ligands produced via the cathodic reduction of LH ligand precursors. ....	21
Figure 1.30: a) Metal-NHC complexes produced by the Chen group. <sup>14</sup> b) Cations were used by the Willans group to selectively form mono- or bis-NHC complexes. They were also able to produce complexes with base sensitive substituents, such as esters. <sup>100</sup> .....	22
Figure 1.31: Fe(III) or Fe(II) may be formed selectively by performing the reaction in air or under inert conditions. <sup>98</sup> .....	23
Figure 1.32: Longitudinal (left) and transverse (right) cross sections of electrochemical flow reactors. ....	24
Figure 1.33: The Atobe group exploited laminar flow to avoid the unwanted oxidation of reagents. <sup>113</sup> .....	25
Figure 1.34: Electrochemical birch reactor and the 100 g scale reactor fabricated by the Baran group. <sup>114</sup> Reproduced with permission from AAAS. ....	25
Figure 1.35: The Wirth group generated hypervalent iodine compounds electrochemically and telescoped these into another reaction to act as oxidising agents. <sup>115</sup> .....	26
Figure 1.36: The Willans 2 <sup>nd</sup> generation reactor featured a stacked electrode design and was able to produce Cu(IMes)Cl in 94 %. <sup>19</sup> Reproduced with permission from the Royal Society of Chemistry .....	27
Figure 1.37: A range of complexes could be synthesised electrochemically in flow using the 2 <sup>nd</sup> generation Willans reactor. <sup>112</sup> .....	27
Figure 2.1: Electrochemistry under inert conditions in a three necked flask connected to a Schlenk line (left) and the IKA ElectraSyn 2 (right). ....	30

Figure 2.2: The design of the bottle reactor – a batch reactor for electrochemistry in an undivided cell.....	32
Figure 2.3: The bottle reactor lid, including a broad range of electrodes that can be accommodated.....	33
Figure 2.4: Cross section of the PEEK head piece which uses flat stainless steel electrode contacts and o-rings to create a seal.....	34
Figure 2.5: Ligand precursors to test the bottle reactor. ....	35
Figure 2.6: $^1\text{H}$ NMR spectra of L1 (blue trace, $\text{CDCl}_3$ , 300 MHz) and L2 (red trace, $\text{CD}_3\text{CN}$ , 400 MHz) showing significant deshielding of the NCHN proton when the counter ion is a halide. ....	37
Figure 2.7: a) In a chemical reduction an electron is transferred from the HOMO of the reducing agent into the LUMO of the reductant. b) For electrochemical reductions the energy of the electrons in the electrode can be increased by increasing the applied potential, which then allows the electron to be transferred into the LUMO of the reductant.....	39
Figure 2.8: Voltammograms for analytes that can be reduced reversibly feature two symmetrical peaks with the reduction potential ( $E^0$ ) being halfway between the two peaks. ....	40
Figure 2.9: $^1\text{H}$ NMR spectrum of Cu1, showing the loss of proton a. The spectrum for L1 was taken in $\text{CDCl}_3$ at 300 MHz and C2 was taken in $\text{CDCl}_3$ at 400 MHz. ....	44
Figure 2.10: Molecular structure of Cu1. Ellipsoids are shown at 50% probability level and hydrogen atoms are omitted for clarity. ....	44
Figure 2.11: Copper complexes that have been synthesised in the bottle reactor with the conversions obtained for them as determined by $^1\text{H}$ NMR spectroscopy. <sup>a</sup> Isolated yield. <sup>b</sup> Electrolyte ( $\text{nBu}_4\text{NPF}_6$ , 0.5 equiv) added to solution.....	46
Figure 2.12: Gold complexes that have been synthesised in the bottle reactor with the conversions obtained after $1.2 \text{ F mol}^{-1}$ . <sup>a</sup> Isolated yield after $2.0 \text{ F mol}^{-1}$ . ....	48
Figure 2.13: Iron complexes that have been synthesised in the bottle reactor with the conversions obtained for them. <sup>a</sup> Isolated yield after 2.4 electron equivalents. ....	49
Figure 2.14: Six bottle reactors performing reactions in parallel. ....	51
Figure 3.1: Proposed set up for a catalyst screening platform, with complexes produced electrochemically and telescoped into a reaction of interest. ....	64
Figure 3.2: Previous studies have used flow channel geometries to justify the design of reactors, but have not investigated it in detail. a) Star shaped channel. <sup>160</sup> b) Snaking shaped channel. <sup>169</sup> c) Spiral shaped channel. <sup>159</sup> a and b reproduced with permission from Elsevier. c reproduced under creative commons licensing. ....	66
Figure 3.3: The effect of different channel geometries on the decarboxylative methoxylation of diphenylacetic acid. <sup>161</sup> Figure reproduced under creative commons licensing.....	67



Figure 3.4: Design and set up of the first generation reactor and how glass beads were used to increase tubulance and selectivity. <sup>112</sup> b was reproduced with permission from the Royal Scociety of Chemistry.....	68
Figure 3.5: The second generation reactor had a stacked disk design. <sup>112</sup> Reproduced with permission from the Royal Scociety of Chemistry. ....	69
Figure 3.6: Assembling the third generation reactor: insulating PTFE gasket (1), electrode (2), spacer (3), electrode (4), spacer (5), electrode (6), gasket (7) and the steel housing (8). ....	70
Figure 3.7: Electrochemical synthesis of Cu1. ....	71
Figure 3.8: Set up of the electrochemical flow reactor.....	71
Figure 3.9: The spacers that were tested. Colours correspond to Graph 3.2..	73
Figure 3.10: Laminar flow consists of parallel layers of fluid moving past each other, with the largest velocity found in the centre of channels. ....	76
Figure 3.11: Five flow channels were constructed within COMSOL multiphysics. One wall in each channel was chosen to simulate the surface of the electrode, shown in blue. ....	78
Figure 3.12: Unstructured mesh for steps and square hops. ....	79
Figure 3.13: Velocity fields calculated using Navier-Stokes equations. No eddies or back mixing can be seen. Size of the arrows corresponds to their relative velocity. ....	80
Figure 3.14: Plains perpendicular to the direction of fluid flow (shown in red) were used to obtain the average concentration at intervals along the flow channels. ....	81
Figure 3.15: Representation of a hop in the flow channel. ....	83
Figure 3.16: Diagram CFD results for a) straight channel and b) channel with hops. One side of the flow channel (the 'electrode') is shown in blue. Species diffuse away from this surface into the bulk.....	84
Figure 3.17: The happy hopper spacer. Left: how the straight channels are connected via hops. Right: the layout of the spacers which are used as a pair. ....	85
Figure 3.18: Flow channels used in the systematic study. ....	88
Figure 3.19: The residence time distribution was calculated as the time between 50% relative absorbance and the residence time distributions for the four spacers. ....	89
Figure 3.20: A schematic representation of a typical voltammogram used to calculate the limiting current. <sup>177</sup> .....	91
Figure 3.21: Planes across the channels were used to calculate the mean concentration at intervals along the channel.....	106
Figure 3.22: Dimensions of the straight channel.....	107
Figure 3.23: Straight channel used in the CFD studies.....	107
Figure 3.24: Position of the electrode in the straight channel.....	108

Figure 3.25: Dimensions of the turns used to construct the channel with turns.	109
Figure 3.26: Channel with turns.	110
Figure 3.27: Position of the electrode in the channel with turns.	110
Figure 3.28: Dimensions of the 90° turns used to construct the channel with hops and the channel with stepped turns.	112
Figure 3.29: Channel with hops and channel with stepped turns.	112
Figure 3.30: Position of the electrode in the channel with hops.	113
Figure 3.31: Position of the electrode in the channel with stepped turns.	114
Figure 3.32: Modified second generation reactor.	116
Figure 3.33: Flow channels used in the systematic study.	117
Figure 4.1: Top: $^1\text{H}$ NMR spectrum of Ni11 (400 MHz, $\text{CD}_3\text{CN}$ ), prepared electrochemically in the flow reactor. Bottom: $^1\text{H}$ NMR spectrum of Ni11 (500 MHz, $\text{CD}_3\text{CN}$ ), prepared electrochemically in the bottle reactor and showing multiple sets of peaks.	129
Figure 4.2: Molecular structure of Ni11. Ellipsoids are shown at 50% probability level. Hydrogen atoms and $\text{PF}_6$ counter ions are omitted for clarity.	130
Figure 4.3: Molecular structure of $\text{Ni(11)}_2$ . Ellipsoids are shown at 50% probability level. Hydrogen atoms and $\text{PF}_6$ counter ions are omitted for clarity.	131
Figure 4.4: Solubility studies of L11 (a) and Ni11 (b) in a range of solvents. Green indicates complete dissolution, amber partial dissolution and red little or no dissolution.	133
Figure 4.5: Descriptions of direct current (blue), alternating current (orange) and alternating potential (green). The period is indicated by a red arrow.	135
Figure 4.6: Electrodes examined using SEM.	138
Figure 4.7: ETD (a) and CBS (b) images of an unused electrode, showing scratches from sandpaper and small amounts of organic material (500 x mag.). c) EDX spectrum showing small amounts of carbon and silicon.	139
Figure 4.8: EDT image of the anode (100 x mag.). The top left of the image is outside of the flow channel, while the rest of the image was inside the flow channel, in contact with the reaction solution.	140
Figure 4.9: EDT images of the anode at different points along the flow channel. a) Striations close to the inlet (500 x mag.) b) Pitting starts to occur roughly halfway along the flow channel (500 x mag.). c) Large amounts of pitting was observed near the outlet (1000 x mag.).	140
Figure 4.10: ETD (a) and CBS (b) images of the first cathode (100 x mag.).	141
Figure 4.11: ETD (a) and CBS (b) images of the first cathode showing organic deposits (1000 x mag.). ETD (c) and CBD (d) images of the first cathode showing conical nickel deposits (5000 x mag.).	141

- Figure 4.12: EDT (a) and CBS (b) images of the second cathode, showing large amounts of organic deposition (100 x mag.).....142**
- Figure 4.13: Divided cell experiments: the anodic chamber A contains electrolyte and the cathodic chamber B contains electrolyte and ligand precursor. Electrodes are either copper or nickel, depending upon the experiment.....144**
- Figure 4.14: Images of the first divided cell experiment at the end of the reaction. Chamber A contained electrolyte and chamber B contained electrolyte and ligand precursor. The reaction was carried out using copper electrode and L10 (a) and using nickel electrodes and L11 (b). .....146**
- Figure 4.15: Workflow for the colour analysis of reactions. ....148**
- Figure 4.16: Overlaid cyclic voltammograms of ligand precursors L11 and Ni11 (1 mM). A silver wire was used as pseudo-reference electrode with ferrocene (1 mM) as an internal standard. Experiments were performed with a scan rate of 300 mV s<sup>-1</sup> in acetonitrile with Bu<sub>4</sub>NPF<sub>6</sub> (0.1 M) as a supporting electrolyte. ....154**

## List of tables

Table 2.1: Reduction potentials of ligand precursors. ....	41
Table 2.2: Selected bond lengths and angles for Cu1.....	45
Table 2.3: Yields for the sulphonamide reaction when using different constant potentials and currents.....	51
Table 3.1: Residence times, time to reach steady state and the collection times when the volume of the reactor is 0.5 mL. ....	101
Table 3.2: Chemical shifts for L1 and Cu1. ....	102
Table 3.3: Combined data for A. Volume = 0.463 mL.....	103
Table 3.4: Combined data for B. Volume = 0.512 mL.....	103
Table 3.5: Combined data for C. Volume = 0.520 mL.....	103
Table 3.6: Combined data for D. Volume = 0.512 mL.....	104
Table 3.7: Combined data for E. Volume = 0.486 mL.....	104
Table 3.8: Pressure drop for four of the flow channels.....	105
Table 3.9: Dimensions of the straight channel. ....	108
Table 3.10: Mean concentrations at distances along the straight channel....	109
Table 3.11: Dimensions of the channel with turns. ....	111
Table 3.12: Mean concentrations at distances along the channel with turns.	111
Table 3.13: Dimensions of the channel with hops.....	113
Table 3.14: Mean concentrations at distances along the channel with hops.	114
Table 3.15: Dimensions of the channel with steps. ....	115
Table 3.16: Mean concentrations at distances along the channel with steps. ....	115
Table 3.17: Limiting current and calculated mass transfer coefficient for F.	119
Table 3.18: Limiting current and calculated mass transfer coefficient for G.	119
Table 3.19: Limiting current and calculated mass transfer coefficient for H.	119
Table 3.20: Limiting current and calculated mass transfer coefficient for I.	120
Table 3.21: Mean conversions of L1 to Cu1 for the systematic spacers at 1.8 V with a flow rate of 0.04 mL min <sup>-1</sup> . ....	120
Table 3.22: Combined conversion of L8 to carboxylate and imidazole. ....	121
Table 4.1: Selected bond lengths and angles for Ni11.....	130
Table 4.2: Selected bond lengths and angles for Ni(11) <sub>2</sub> . ....	131
Table 4.3: Solvent screen for the electrochemical synthesis of Ni11. ....	133
Table 4.4: Effects of current and potential on the synthesis of Ni11 in the presence and absence of electrolyte and alternating polarity.....	134

Table 4.5: Summary of the divided cell experiments and the species observed via $^1\text{H}$ NMR spectroscopy and HRMS. For the copper reactions the solution was electrolysed with copper electrodes for $1.2 \text{ F mol}^{-1}$ . For the nickel reactions the solution was electrolysed with nickel electrodes for $2.4 \text{ F mol}^{-1}$ . .....	147
Table 4.6: Testing the stability of Ni11 under different reaction conditions..	155
Table 4.7: Results for the continuous electrochemical synthesis of Ni9.....	163
Table 4.8: Results for the continuous electrochemical synthesis of Ni10.....	164
Table 4.9: Results for the continuous electrochemical synthesis of Ni11.....	164
Table 4.10: Results for the continuous electrochemical synthesis of Ni12...	165
Table 4.11: Results for the continuous electrochemical synthesis of Ni13...	165
Table 4.12: Species observed via HRMS during the divided cell experiments. ....	165
Table 4.13: Summary of the results from the divided cell experiments. ....	166

## List of schemes

Scheme 2.1: Synthesis of L1 and L2 via condensation and anion exchange, with yields. ....	36
Scheme 2.2: Synthesis of L3, L5, L6 and L7 with yields. ....	38
Scheme 2.3: Electrochemical synthesis of Cu(IMes)Cl. ....	42
Scheme 2.4: Electrochemical coupling of amines and thiols to produce sulphonamides. ....	50
Scheme 2.5: Electrochemical synthesis of hypervalent iodine species, stabilised by fluorinated ligands. I9 was made in an analogous manner, using hexafluoroisopropanol. ....	52
Scheme 2.6: The oxidation of hydroquinone was used to as an indirect method to analyse the outcome of the electrolysis. ....	52
Scheme 3.1: Carboxylation of imidazoliums with the conditions used by de Robillard et al. <sup>150</sup> ....	94
Scheme 3.2: Carboxylation of imidazoliums under continuous conditions gives a mixture of products. ....	95
Scheme 3.3: Paired electrosynthesis reported by Amemiya et al. <sup>179</sup> ....	98
Scheme 3.4: Domino oxidation-reduction for the synthesis of nitriles, reported by Hartmer et al. <sup>180</sup> ....	98
Scheme 4.1: a) Synthesis of Ni(II)-NHC complexes using a base. b) Synthesis of Ni(II)-NHC complexes via transmetallation. ....	123
Scheme 4.2: Continuous electrochemical synthesis of copper(I)-NHC complexes. ....	124
Scheme 4.3: Electrochemical synthesis of nickel-NHC complexes conducted by the Chen group. <sup>14</sup> ....	124
Scheme 4.4: Adaptation of Chen's procedure in the bottle reactor using two nickel electrodes. ....	125
Scheme 4.5: Synthesis of Ni9 under potentiostatic conditions. ....	126
Scheme 4.6: Galvanostatic conditions gave full conversion of L9 to Ni9, but a yield of 49% indicating that half of the material was unaccounted for. ....	126
Scheme 4.7: Electrochemical synthesis of a range of Ni(II)-NHC complexes. ....	128
Scheme 4.8: Chemical synthesis of Ni11. ....	132
Scheme 4.9: Proposed mechanism for the formation of metal-NHC complexes where the carbene is free in solution (a) or remains coordinated to the cathode (b). ....	143
Scheme 4.10: Series of divided cell experiments and the expected results. a) Metal ions and carbenes are produced at opposite electrodes and unable to form the product. b) With an APM both electrodes act as anode and cathode. c) Transferring solution between the two chambers. ....	145
Scheme 4.11: Ni11 was pumped through the reactor to test its stability under reaction conditions. ....	154

<b>Scheme 4.12: Reaction conditions for the synthesis of Ni11 that reduce the amount of product degradation. ....</b>	<b>156</b>
---	------------

## List of graphs

Graph 2.1: Overlaid cyclic voltammograms of ligand precursors L1-5 (1 mM). A silver wire was used as pseudo-reference electrode with ferrocene (1 mM) as an internal standard. Experiments were performed with a scan rate of $300 \text{ mV s}^{-1}$ in acetonitrile with $\text{Bu}_4\text{NPF}_6$ (0.1 M) as a supporting electrolyte. ....	41
Graph 2.2: Time course experiments for the formation of Cu1 and Cu2. ....	47
Graph 3.1: Examining the frequency of the polarity flicker and its effect on the long term stability of a reaction. <sup>170</sup> .....	72
Graph 3.2: The different spacers at a range of flow rates. ....	74
Graph 3.3: Estimated mass transfer coefficients ( $k_m$ ) using Equation 1. ....	75
Graph 3.4: Mean concentration of a species along a flow channel. ....	82
Graph 3.5: Estimated mass transfer using Equation 1.1, including the happy hopper. ....	86
Graph 3.6: Different spacers, including the happy hopper at a range of flow rates. ....	87
Graph 3.7: Comparison of symmetrical and asymmetrical models of residence time distributions with experimental values. ....	90
Graph 3.8: Mass transfer coefficients for the four spacers in the systematic study. ....	92
Graph 3.9: Ratio of mass transfer coefficient to energy dispersion rate for the different spacers. ....	93
Graph 3.10: Conversion of L1 to Cu1 in the systematic spacers with an applied potential of 1.8 V and a flow rate of $0.04 \text{ mL min}^{-1}$ . ....	94
Graph 3.11: Experimental RTD with modelled RTD where $D_{ax} = 2.5 \times 10^{-4}$ and the dispersion number ( $N_L$ ) = 0.06. ....	118
Graph 4.1: Time monitoring of the electrochemical synthesis of Ni11. Samples of the outlet were taken at 30 minute intervals. ....	136
Graph 4.2: Relationship between the conversion of Cu1 and the frequency of the APM when 1.8V is applied. Conversion obtained without the APM (87%) is shown in orange. <sup>170</sup> .....	136
Graph 4.3: Relationship between the conversion of Ni11 and the frequency of the APM when 1 mA is applied. Conversion obtained without the APM (4%) is shown in orange. ....	137
Graph 4.4: Top: Colour calibration for the flow reactions. A combined 6 mM solution of Ni11 and L11 were filmed. 1.2 mM of Ni11 corresponds to 20% yield. Bottom: video stills of each concentration. ....	150
Graph 4.5: Colour analysis of the continuous electrochemical synthesis of Ni11: 6 mM, 1 mA, 1/60 Hz, $0.04 \text{ mL min}^{-1}$ . Orange line from calibration corresponds to 20% yield. $^1\text{H}$ NMR analysis showed a yield of 19%. ....	150
Graph 4.6: Colour analysis of the synthesis of Ni11 in a stirred batch reactor. ....	151



Graph 4.7: Colour analysis of the synthesis of Ni11 in an unstirred batch reactor, with regions of interest near the anode (orange), in between the electrodes (blue) and near the cathode (green).....	152
Graph 4.8: Colour analysis of the synthesis of Ni11 in an unstirred batch reactor, with regions of interest near the electrodes (blue) and near the base (orange). ....	153
Graph 4.9: Average potential for half of a period at 1/60 Hz (30 s) when 1 mA is applied to a solution of L11 or Ni11. ....	155
Graph 4.10: Hypothesised trade-off between yield and mass balance. ....	157

## List of equations

- Equation 1.1: An equation showing the relationship between residence time ( $\tau$ ), volume ( $V$ ) and flow rate ( $\dot{V}$ ). .....11**
- Equation 2.1: Equations relating current and time with electron equivalents.  $Q$  = total charge (C),  $n$  = number of electrons transferred per molecule of starting material,  $F$  = Faraday's constant ( $C\ mol^{-1}$ ),  $N$  = amount of starting material (mol),  $I$  = current (A),  $t$  = time (s). .....42**
- Equation 3.1 Calculating the mass transfer coefficient ( $k_m$ ).  $D$  is the diffusion coefficient,  $d_h$  the hydraulic diameter,  $\dot{V}$  the flow rate,  $\nu$  the kinematic viscosity,  $h$  and  $w$  the height and width of the channel respectively,  $L$  the length,  $N$  the number of segments and  $S_c$  the Schmidt number. ....75**
- Equation 3.2: Calculating the Reynolds number ( $Re$ ) where  $\rho$  is the fluid density,  $u$  is the velocity,  $L$  is the length of the channel and  $\mu$  is the kinematic viscosity. ....76**
- Equation 3.3: Newton's second law of motion (top) and its relation to the Navier-Stokes equation (bottom). Where  $m$  is mass,  $a$  is acceleration,  $F$  is force,  $\rho$  is the fluid density,  $p$  is pressure,  $\mu$  is kinematic viscosity,  $u$  is the velocity and  $T$  is the temperature. ....77**
- Equation 3.4: Continuity equation (top) and simplified Navier-Stokes equation (bottom). Where  $u$  is velocity,  $p$  is pressure,  $\mu$  is kinematic viscosity,  $T$  is temperature and  $F$  is force. ....77**
- Equation 3.5: Calculating the concentration. Where  $J_i$  is the mass flux diffusive flux vector,  $u$  is the flow velocity vector,  $c_i$  is the concentration of the species,  $R_i$  is the reaction rate expression and  $D_i$  is the diffusion coefficient (set to  $1 \times 10^{-9}\ m^2\ s^{-1}$ ). .....80**
- Equation 3.6: Symmetrical model for calculating the axial dispersion coefficient ( $D_{ax}$ ) for small  $N_L$  values. Where  $u$  is the average velocity,  $t$  is the time,  $L$  is the length and  $E_t$  is the exit time. ....89**
- Equation 3.7: Asymmetrical model for calculating the axial dispersion coefficient ( $D_{ax}$ ) for large  $N_L$  values. Where  $u$  is the average velocity,  $t$  is the time,  $L$  is the length and  $E_t$  is the exit time. ....89**
- Equation 3.8: Calculating the vessel dispersion number ( $N_L$ ). Where  $Pe_L$  is the Peclet number,  $D_{ax}$  is the axial dispersion coefficient,  $u$  is the average velocity and  $L$  is the length. ....90**
- Equation 3.9: Calculating the mass transfer coefficient ( $k_m$ ) from the limiting current ( $I_{lim}$ ). Where  $n$  is the number of electrons exchanged,  $F$  is the Faraday constant and  $C_B$  is the concentration of the bulk solution.<sup>177</sup> ...91**
- Equation 3.10: Navier-Stokes equation. Where  $\rho$  is the density,  $u$  is the velocity field,  $\mu$  the viscosity,  $P$  is the pressure,  $F$  is the volume force vector (body force in this case). ....105**
- Equation 3.11: Calculating the concentration. Where  $J_i$  is the mass flux diffusive flux vector,  $u$  is the flow velocity vector,  $c_i$  is the concentration of the species,  $R_i$  is the reaction rate expression – here zero- and  $D_i$  is the diffusion coefficient. ....106**

- Equation 3.12: Calculating the axial dispersion coefficient ( $D_{ax}$ ). Where  $u$  is the average velocity,  $t$  is the time,  $L$  is the length and  $E_t$  is the exit time....117**
- Equation 3.13: Calculating the mass transfer coefficient ( $k_m$ ) from the limiting current ( $I_{lim}$ ). Where  $n$  is the number of electrons exchanged,  $F$  is the Faraday constant and  $C_B$  is the concentration of the bulk solution. ....118**
- Equation 4.1: Equation for calculating the required current for an electrochemical flow reaction where  $I$  is the current,  $n$  is the number of electrons required for each substrate,  $F$  is the Faraday coefficient,  $c$  is the concentration and  $\dot{V}$  is the flow rate.<sup>197</sup> .....126**
- Equation 4.2: Calculating  $\Delta E$  using the CIEL\*a\*b\* colour space. ....149**

## List of abbreviations

A	Area
API	Active pharmaceutical ingredient
APM	Alternating polarity microcontroller
c	Concentration
CBS	Circular backscattering detector
CFD	Computational fluid dynamics
COD	1,5-Cyclooctadiene
Cp	Cyclopentadienyl
CSTR	Continuous stirred tank reactor
CV	Cyclic voltammetry
D	Diffusion coefficient
D <sub>ax</sub>	Axial dispersion coefficient
deltaE	colour independent measure of contrast
d <sub>h</sub>	Hydraulic diameter
Dppe	1,2-Bis(diphenylphosphino)ethane
E	Potential or voltage
EDX	Energy dispersive X-ray spectroscopy
ETD	Everhart-Thornley detector
F	Faraday constant
F	Force
Fc	Ferrocene
HOMO	Highest occupied molecular orbital
HRMS	High resolution mass spectrometry
I	Current
ICy	1,3-Dicyclohexyl-imidazol-2-ylidene
IMes	1,3-bis(2,4,6-trimethylphenyl)imidazol-2-ylidene
IPr	1,3-bis(2,4-diisopropylphenyl)imidazol-2-ylidene
IR	Infrared
J	Mass flux vector
k <sub>m</sub>	Mass transfer coefficient
LUMO	Lowest unoccupied molecular orbital
NHC	<i>N</i> -heterocyclic carbene
N <sub>L</sub>	Vessel dispersion number
NMR	Nuclear magnetic resonance
PEEK	Polyetheretherketone
ppm	Parts per million
ppt	Precipitate

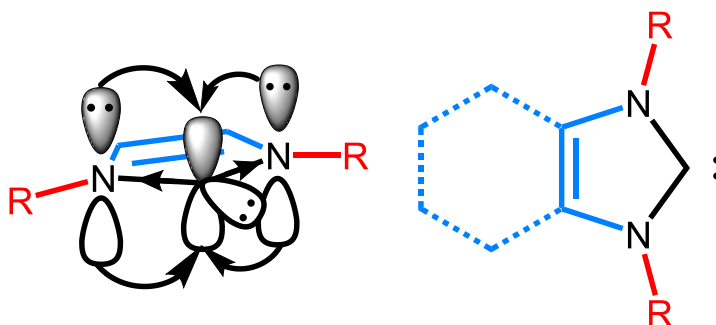
PTFE	Polytetrafluoroethylene
Q	Electron equivalents
R	Resistance
Re	Reynolds number
RT	Room temperature
RTD	Residence time distribution
$S_c$	Schmidt number
SCE	Saturated calomel electrode
SEM	Scanning electron microscopy
T	temperature
t	Time
u	Velocity
UV	Ultra violet
V	Volume
$\dot{V}$	Volumetric flow rate
$\rho$	Density
$\tau$	Residence time
$\mu$	Kinematic viscosity

## 1. Introduction

### 1.1. *N*-heterocyclic carbenes

#### 1.1.1. Overview of carbenes

Carbenes are carbon atoms that have six valence electrons.<sup>1</sup> Carbenes have many applications, particularly as ligands in organometallic chemistry, and are broadly subdivided into classes based upon the electronic state which the carbon atom exists in. *N*-Heterocyclic carbenes (NHCs) are singlet carbenes which are stabilised by being part of a heterocycle, usually a five membered ring. The carbene is an  $sp^2$  hybridised carbon atom which has an empty p orbital and a lone pair of electrons. Adjacent to the carbon atom are one or two heteroatoms, of which at least one is a nitrogen atom. NHCs are stabilised by hyperconjugation through  $\pi$ -donation from the nitrogen atom into the empty p orbital of the carbene. Extra stability is provided by the  $\sigma$ -acceptance of electron density by the nitrogen atom, helping to stabilise the lone pair (Figure 1.1).<sup>1-4</sup>



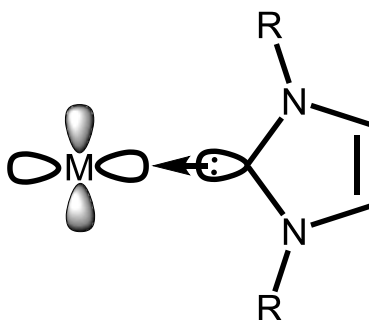
**Figure 1.1:** NHCs are stabilised by  $\pi$ -donation from the nitrogen atoms into the empty p orbital and the withdrawal of  $\sigma$  electron density from the carbene by the nitrogen atoms. NHCs can also be easily tuned through modification of the R groups and heterocycle backbone.<sup>2</sup>

Many varieties of NHC exist with differences in backbone saturation and electronic properties, ring size, number and type of heteroatoms, and heteroatom substituents (Figure 1.1). The backbone (blue in Figure 1.1) mostly governs the electronics, whilst the N-substituents (red in Figure 1.1) are primarily responsible for the sterics.<sup>2</sup> The most common motif is a five membered ring with two nitrogen atoms adjacent to the carbene. Nitrogen atoms are generally included rather than oxygen or sulphur atoms because they can be further substituted.<sup>1</sup>

#### 1.1.2. Metal-NHC complexes and catalysis

The first metal-NHC complexes were prepared independently by Wanzlick and Öfele in 1968.<sup>5,6</sup> In 1991 Arduengo isolated the first free NHC, with bulky adamantyl N-

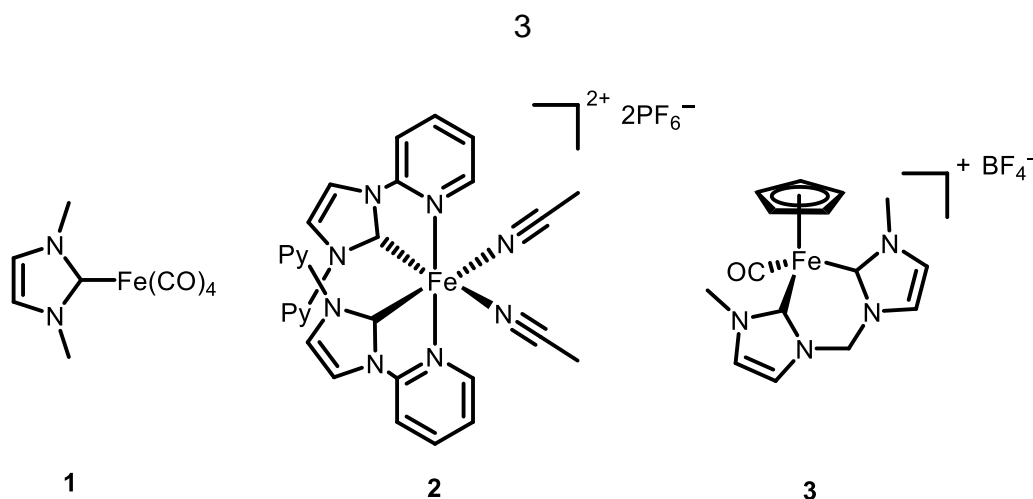
substituents providing kinetic stabilisation.<sup>7</sup> Since these reports, NHCs have become ubiquitous ligands in homogenous transition metal catalysis, perhaps the best known example being Grubbs second generation catalyst for olefin metathesis.<sup>8</sup> They are strong  $\sigma$ -donors as ligands, coordinating to metals across the whole periodic table by donating into one of the  $e_g$  orbitals of a metal centre (Figure 1.2).<sup>9</sup> NHCs are highly versatile with the potential to tune the steric and electronic properties of the ligand almost independently of each other by varying the backbone and N-substituents (Figure 1.1).<sup>2</sup>



**Figure 1.2:** NHCs donate into  $e_g$  orbitals.<sup>2</sup>

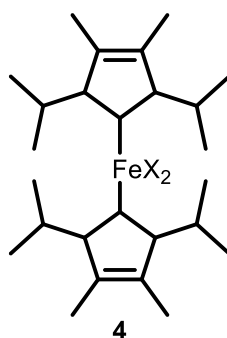
Historically, research in homogenous catalysis has focused on second and third row transition metals, such as ruthenium, iridium and palladium. These metal complexes are relatively easy to synthesise and can be used to catalyse a broad range of transformations. However these metals are relatively rare and expensive as well as being potentially toxic.<sup>10</sup> By contrast, first row transition metals such as iron, nickel and copper are abundant, inexpensive and generally more environmentally benign.<sup>11</sup>

The first iron-NHC was reported in 1969 (**1**, Figure 1.3),<sup>12</sup> though iron-NHC complexes have become more common relatively recently.<sup>10,11,13</sup> The ability of NHCs to act as strong  $\sigma$ -donors combined with their versatile nature has made them useful ligands for iron complexes. In particular, polydentate ligands with multiple NHCs (**2**, Figure 1.3)<sup>14</sup> or hemilabile groups such as pyridines (**3**, Figure 1.3)<sup>15</sup> are popular due to their ability to stabilise iron complexes.<sup>10</sup>



**Figure 1.3:** Iron-NHC complexes exhibit a wide variety of geometries.<sup>12,14,15</sup>

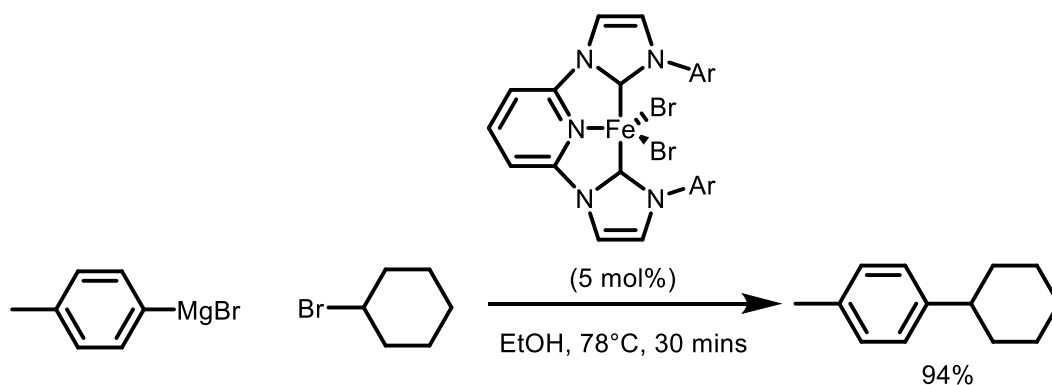
In the past two decades increasing work has been conducted using iron-NHC complexes as catalysts.<sup>16</sup> The first example of an iron-NHC complex as a catalyst was reported by Grubbs *et al* in 2000 (Figure 1.4).<sup>17</sup> The group used complex **4** to catalyse the polymerisation of styrene and methyl methacrylate. Other transformations using iron-NHC catalysts include allylic alkylations, reductions, borylations and hydrosilylations.<sup>10</sup>



**Figure 1.4:** Iron-NHC complex used as a polymerisation catalyst by Grubbs *et al*.<sup>17</sup>

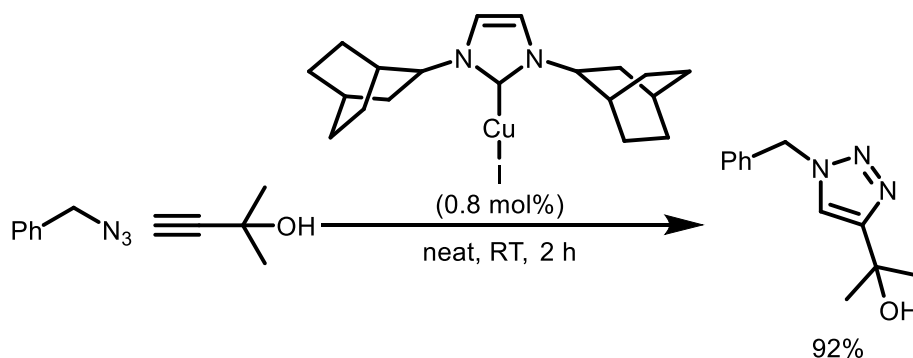
One of the areas that has seen the most publications is Kumada-type cross-couplings.<sup>10</sup> These reactions involve the coupling of a Grignard reagent with an alkyl halide and traditionally uses palladium as a catalyst. In 1971, Kochi *et al* used  $\text{FeCl}_3$  to catalyse this reaction, and in 2006 the Bedford group demonstrated that the use of NHCs as ligands improved the reactivity of the catalyst and the overall yield (Figure 1.5).<sup>18</sup>





**Figure 1.5:** Kumada coupling using an iron-NHC as the catalyst.<sup>18</sup>

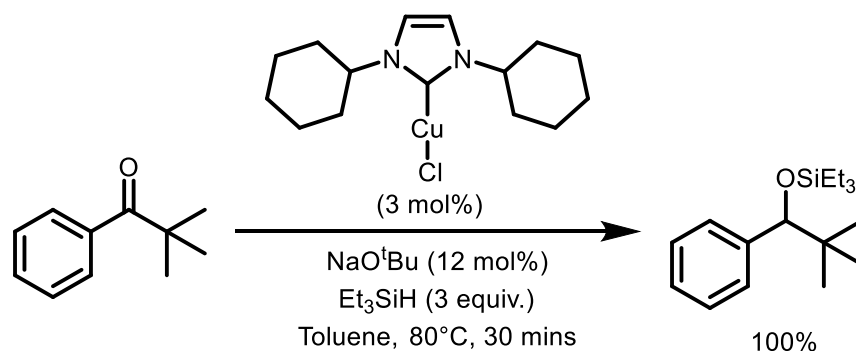
Copper-NHC complexes have received significant interest as catalysts since the turn of the millennium.<sup>19</sup> The synthesis of triazoles from alkynes and azides is one of the best known 'click' reactions, enabling the formation of heterocycles under mild conditions *via* a [3+2] cycloaddition. Since their first use in 2002, copper(I) catalysts have become ubiquitous for these reactions, offering excellent selectivity for the formation of 1,4-disubstituted [1,2,3]-triazoles.<sup>20</sup> The Nolan group have investigated the use of NHCs as ligands, noting that the anion has a significant effect on the reaction with iodides performing much better than chlorides.<sup>21</sup> Whilst most of the complexes gave excellent yields for simple reactions, adamantyl substituents were required for more challenging bulky substrates (Figure 1.6). This gave excellent yields with a catalyst loading of 0.8 mol% and the authors noted that the reaction was able to proceed with loadings of 0.05 mol%, although they did not provide a yield for this.<sup>22</sup>



**Figure 1.6:** Copper-NHC catalysed 'click' reaction for the formation of triazoles.<sup>22</sup>

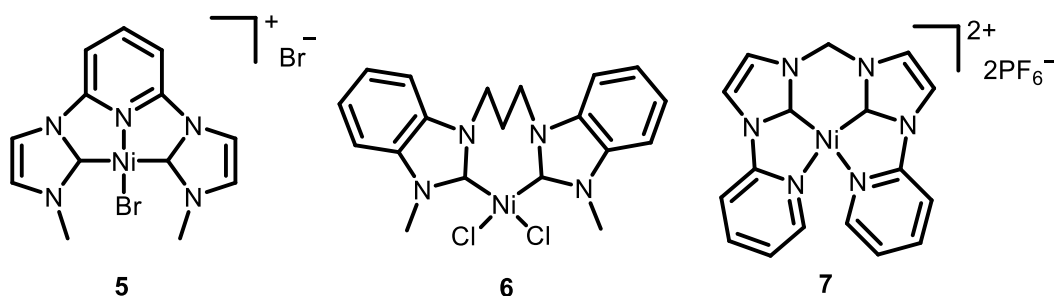
Copper complexes have also been used in hydrosilylations, an important class of reactions that are used to incorporate silicon functional groups into molecules or to reduce organic compounds.<sup>23</sup> Stryker's reagent ( $[(\text{Ph}_3\text{P})_3\text{CuH}]_6$ ) has been widely used for the reduction of carbonyls, however the complex is difficult to handle and is typically used as a stoichiometric reductant.<sup>24</sup> The Nolan group have used NHCs to stabilise

copper hydrides, enabling copper catalysed reactions, obtaining excellent conversions for the hydrosilylation of hindered ketones (Figure 1.7). They found that ICy was the best ligand and they were able to obtain >90% conversions with a relatively low catalyst loading (3 mol%).<sup>25</sup>



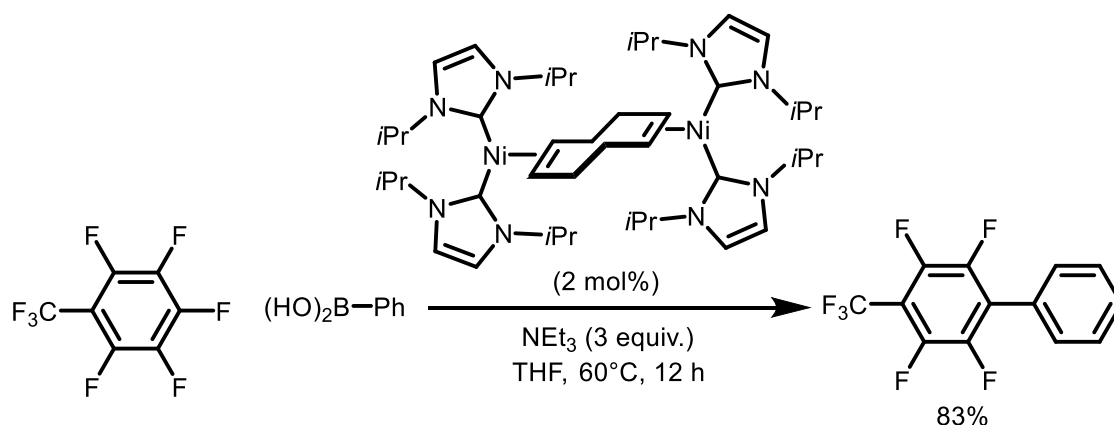
**Figure 1.7:** Copper-NHC catalysed hydrosilylation developed by the Nolan group.<sup>23</sup>

Nickel(II)-NHC complexes have received considerable interest as catalyst for cross coupling reactions due to its position above palladium in the periodic table. Many groups have tried to use nickel as a substitute for palladium. Nickel offers a cheaper and more earth abundant alternative, however it is important to bear in mind the differences between nickel and palladium; nickel is harder than palladium, less electronegative and tends to undergo oxidative addition more easily, enabling the use of electrophiles such as phenol derivatives in cross-couplings which would be unsuitable for use with palladium.<sup>26–28</sup> Conversely reductive elimination steps can be slower, something that can be addressed through the use of strong  $\sigma$ -donating ligands, such as NHCs. NHC ligands are relatively rare for nickel catalysed Suzuki reactions but they are much more popular for nickel catalysed Kumada couplings, with numerous examples of pincer and multidentate Ni-NHC complexes reported to give excellent yields for the coupling of aryl halides with Grignard reagents (Figure 1.8).<sup>3</sup>



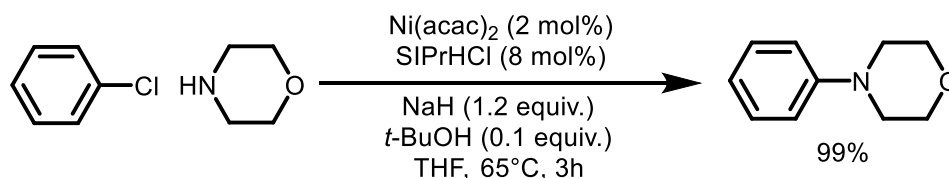
**Figure 1.8:** A selection of multidentate Ni-NHC complexes used to catalyse Kumada couplings.<sup>3</sup>

When considering the formation of a C-C bond the Suzuki reaction is often the first one that springs to mind, enabling the coupling of aryl halides with a boronic acid.<sup>29</sup> One of the first uses of nickel to catalyse these reactions was in 1996 by the Miyaura group. They used nickel phosphine complexes to catalyse the coupling of aryl-chlorides with boronic acids.<sup>30</sup> Up until that point palladium catalysed Suzuki reactions had been limited to aryl-bromides and -iodides, the work by Miyaura highlights the complementary nature of nickel for these reactions. The use of NHCs as ligands has taken longer to establish, with early efforts requiring phosphine co-ligands, long reaction times, high temperatures and high catalyst loadings when compared to their phosphine counterparts.<sup>3,29</sup> NHCs remain an esoteric ligand for nickel catalysed Suzuki reactions, generally being used for challenging transformations. One such example is the coupling of aryl-fluorides and boronic acids, as demonstrated by Schaub *et al.* (Figure 1.9).<sup>31</sup> This group demonstrated the use of a nickel-NHC complex as a catalyst for Suzuki reactions involving perfluorinated arenes. Furthermore, they found that the reaction was selective for the *para* position of functionalised perfluorinated arenes. They were able to obtain good yields with relatively low catalyst loadings (2 mol%) and without the need for phosphine co-ligands.<sup>31</sup>



**Figure 1.9:** Nickel-NHC catalysed cross coupling of perfluorinated arenes with boronic acids.<sup>31</sup>

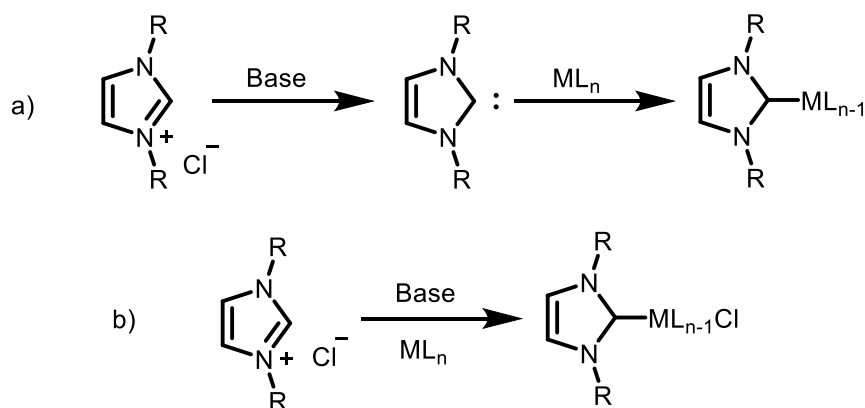
NHCs are a popular ligand for nickel catalysed aminations.<sup>27</sup> The first examples of these reactions was reported in 2001 by the Fort group.<sup>32</sup> They produced Ni(II)-NHC complexes in situ from Ni(acac)<sub>2</sub> and the imidazolium salt SIPrHCl. The coupling of aryl-chlorides to secondary amines was performed under relatively mild conditions (Figure 1.10),<sup>32</sup> more forcing conditions were required for anilines and primary amines.<sup>33</sup> Since then nickel catalysed C-N cross couplings have been extended to the coupling aryl halides, phenol derivatives, allyl halides, alkyl halides and olefins with primary, secondary and cyclic amines, hydrazines and anilines.<sup>27</sup>



**Figure 1.10:** Nickel catalysed C-N cross coupling using Ni-NHC complexes generated *in situ*.<sup>32</sup>

### 1.1.3. Synthesis of metal-NHC complexes

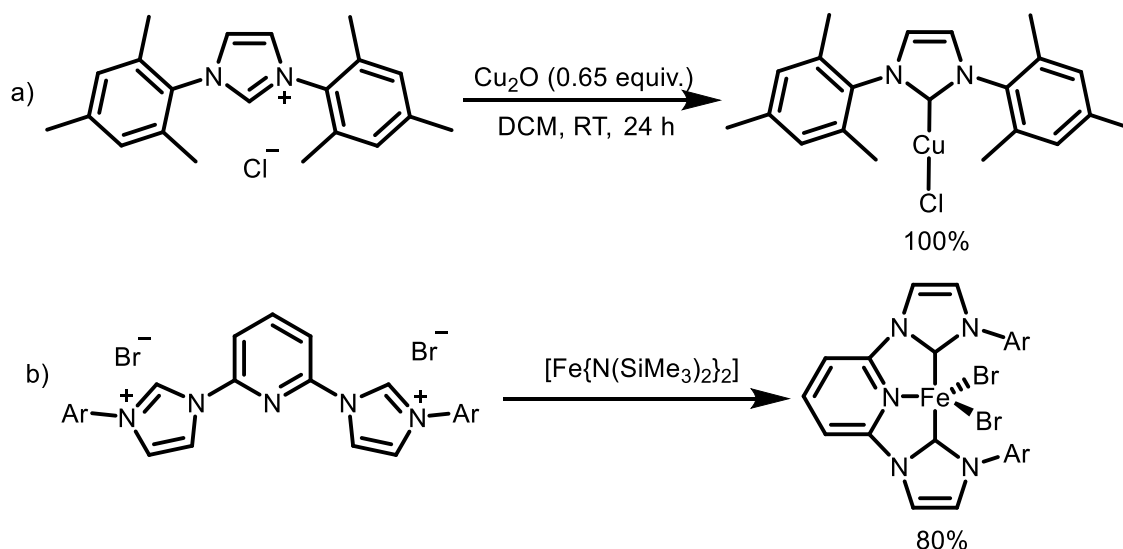
Several strategies have been developed for the synthesis of metal-NHC complexes from imidazolium precursors. Traditional methods involve stoichiometric amounts of base to deprotonate the imidazolium precursor and form the free carbene which can subsequently be reacted with a metal source (a, Figure 1.11).<sup>1,10</sup> Strong bases are required, often sodium hydride or butyl lithium, and the reaction must be carried out under strict inert conditions to prevent the free carbene from reacting with oxygen or water. Alternatively, the imidazolium can be deprotonated *in situ* and the resultant carbene is then able to react directly with the metal source (b, Figure 1.11). This approach allows the use of weaker bases, such as potassium carbonate.<sup>1</sup>



**Figure 1.11:** Common methods of generating metal-NHC complexes using a base. The carbene can be produced first using a strong base (a) or *in situ* using a weaker base (b).

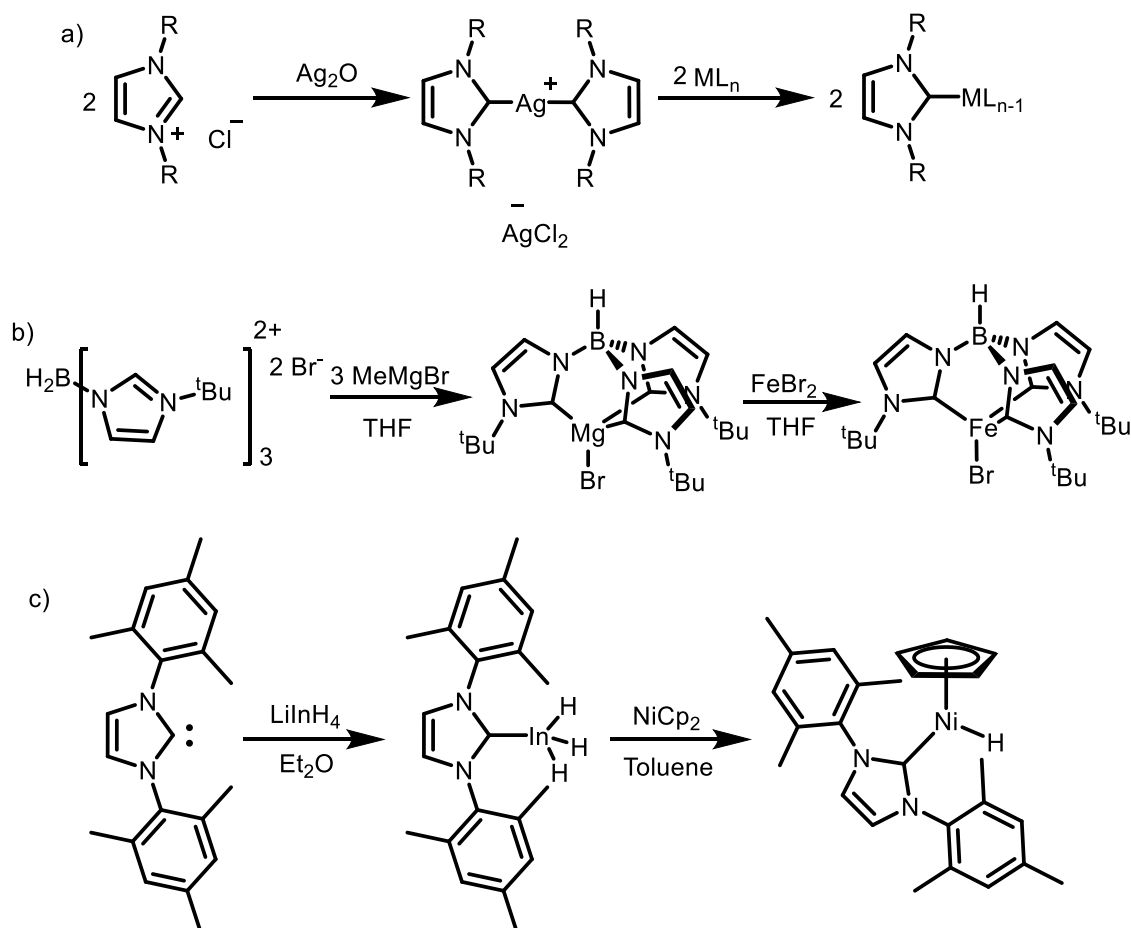
Nickel-NHC complexes are usually prepared by the generation of free carbenes through stoichiometric amounts of base and then subsequent reaction with a source of nickel.<sup>28</sup> These steps can be performed sequentially, isolating the free carbene, or concurrently with the imidazolium reduced *in situ*. Nickel(0) complexes can be produced by using  $\text{Ni(COD)}_2$  as the metal source.<sup>34</sup>  $\text{Ni(COD)}_2$  is very air sensitive; the requirement for a glove box can be circumvented by using paraffin wax capsules containing  $\text{Ni(COD)}_2$  which can be stored on the benchtop.<sup>34</sup> Historically  $\text{Ni(CO)}_4$  was also used, however this should be avoided due to its exceedingly toxic nature.<sup>35</sup> Nickel(II) complexes are synthesised in an analogous fashion but using nickel(II) metal sources such as  $\text{NiCl}_2$  or  $\text{Ni(OAc)}_2$ , which are generally air stable.<sup>28</sup>

Basic metal precursors can be used to generate metal-NHC complexes directly. For example, copper-NHC complexes are often synthesised by reacting an imidazolium salt with  $\text{Cu}_2\text{O}$  (a, Figure 1.12).<sup>36</sup> A similar method produces silver-NHCs from  $\text{Ag}_2\text{O}$ . A common method of generating iron-NHC complexes employs the use of  $[\text{Fe}\{\text{N}(\text{SiMe}_3)_2\}_2]$  (b, Figure 1.12).<sup>10,37</sup> This reagent acts as both the base and metal source to produce iron(II)-NHCs and the volatile amine  $\text{HN}(\text{SiMe}_3)_2$ . The oily green  $[\text{Fe}\{\text{N}(\text{SiMe}_3)_2\}_2]$  is extremely air sensitive and must be freshly prepared, a process which includes purification *via* distillation. In addition to the handling difficulties, the use of  $[\text{Fe}\{\text{N}(\text{SiMe}_3)_2\}_2]$  is often associated with the production of iron(III) side products, which due to their paramagnetic nature, can make the analysis of Fe(II)-NHCs challenging.<sup>10</sup>



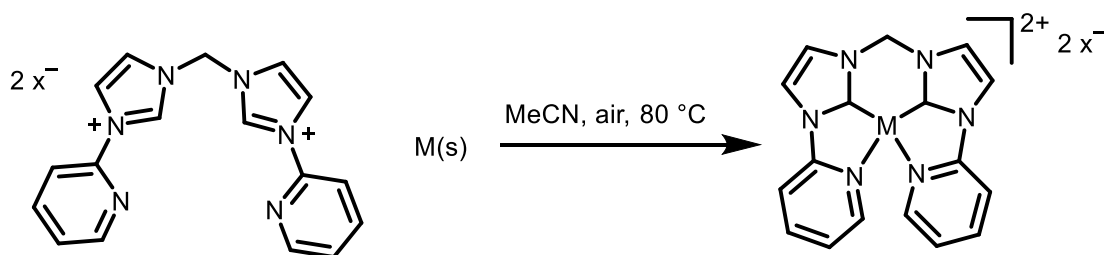
**Figure 1.12:** a) Copper-NHC complexes can be produced using the basic metal precursor  $\text{Cu}_2\text{O}$ .<sup>36</sup> b)  $[\text{Fe}\{\text{N}(\text{SiMe}_3)_2\}_2]$  can act as the base and the metal source when synthesising iron-NHC complexes.<sup>37</sup>

Another popular method of metal-NHC formation is the transmetalation from a silver-NHC.<sup>1</sup> The imidazolium precursor is first reacted with silver oxide to form a silver-bis(NHC) complex. The silver complex is subsequently reacted with the metal source, producing the desired metal-NHC complex and silver halide as the by product (a, Figure 1.13). The formation of the silver halide is the driving force for the transmetalation due to high lattice energy and its generally insoluble nature, which also allows the silver halide to be filtered off. The silver complexes have the advantage that they are generally air stable, although they are usually light sensitive. Chen *et al* have produced iron-NHCs using this method and Smith *et al* have transmetalated to iron from magnesium-NHC complexes (b, Figure 1.13).<sup>14,38</sup> There is one example of a nickel(II)-NHC hydride complex being prepared *via* transmetallation from an indium complex (c, Figure 1.13).<sup>39</sup>



**Figure 1.13:** a) Transmetalation from silver is a common and synthetically easy way to generate metal-NHC complexes.<sup>1</sup> b) Magnesium-NHCs have been used to generate iron-NHCs *via* transmetalation.<sup>38</sup> c) Transmetalation from indium is an unusual method for producing nickel-NHCs.<sup>39</sup>

Recently, new synthetic pathways to metal-NHCs that utilise less harsh conditions have been developed by Chen's group. The group reported the use of metal powders for the synthesis of metal-NHC complexes, with the metal being oxidised in air (Figure 1.14).<sup>40,41</sup> These reactions are very slow as the metal powder must be first oxidised, and the presence of air can lead to oxidation of the carbene to form imidazolone by products. Ni-NHC complexes produced in this way have been used to produce palladium, platinum, cobalt and ruthenium complexes *via* transmetalation.<sup>42</sup> The same group also demonstrated the first use of electrochemistry to make metal-NHC complexes (Section 1.3.2).<sup>14</sup>

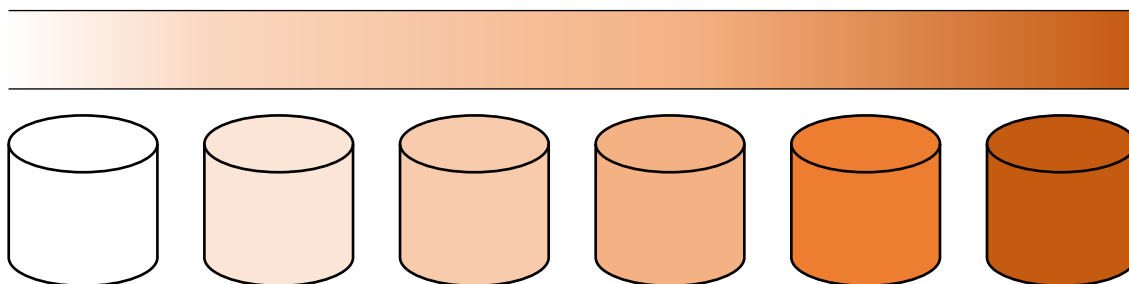


**Figure 1.14:** Chen *et al* have reported the use of metal powders to generate metal-NHC complexes for iron, cobalt, nickel and copper.<sup>41</sup>

## 1.2. Flow chemistry

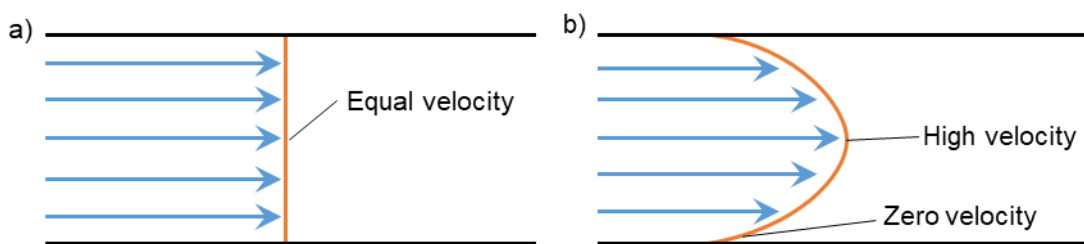
### 1.2.1. Fundamentals of flow chemistry

Flow chemistry is widely used in industry and has seen an increase in uptake among academics in the past few decades.<sup>43</sup> One of the main advantages, particularly for industry, is that it is a continuous process. The reaction solution flows through a tube, as opposed to batch reactions which are conducted in a single vessel such as a round bottom flask. In batch reactors a reaction progresses over time, with the composition of the entire vessel changing. By contrast, a reaction in a flow reactor proceeds along the length of the tube (Figure 1.15).<sup>44</sup> This means that the composition at any single point in the reactor remains the same, enabling reagents to be added at very specific points in a reaction.



**Figure 1.15:** In flow a reaction progresses over the length of the reactor (top). In batch the reaction progresses over time (bottom).

This is described by the idealised 'plug flow' model which assumes that there is a uniform flow rate and that mixing only occurs across the diameter of the reactor *via* diffusion (a, Figure 1.16). In reality the flow rate is not uniform in a tubular reactor, with the fastest flow rate in the centre of the tube and the slowest flow rate along the sides leading to a parabolic velocity profile (b, Figure 1.16). Diffusion also occurs longitudinally.<sup>45</sup> The residence time ( $\tau$ ) is the average time which a molecule spends within the reactor and is controlled by the volume of the reactor (the length of tube) and the flow rate (Equation 1.1).



**Figure 1.16:** a) Idealised plug flow with uniform velocity across the channel. b) Laminar flow with a parabolic velocity profile.

$$\tau = \frac{V}{\dot{V}}$$

**Equation 1.1:** An equation showing the relationship between residence time ( $\tau$ ), volume ( $V$ ) and flow rate ( $\dot{V}$ ).

Conducting chemistry under continuous conditions can have a number of advantages. Firstly, flow reactors have a much larger surface area to volume ratio than batch reactors.<sup>46</sup> This means that heat transfer is drastically improved, something which can make highly exothermic reactions safer due to the increased rate of cooling which may be applied, this is especially true when scaling up such reactions.<sup>46</sup> Equally, for reactions that require a large amount of heat, flow chemistry can be beneficial. Not only is the heat transfer excellent for flow reactors but reactions are usually performed under pressure, allowing solvents to be heated above their atmospheric boiling points. This avoids the use of high boiling point solvents and is easier to scale up than similar methods such as microwave reactors which typically operate on a small scale.<sup>47</sup>

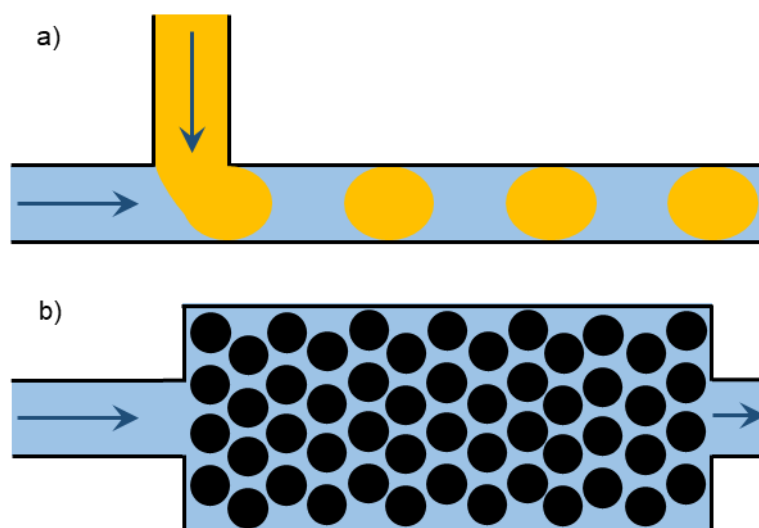
The ability to scale up reactions is typically the reason why industrial chemists turn to flow. By performing a reaction continuously the requirement for downtime between batches is eliminated, improving the space-time yield of a process. This is particularly true if multi-step reactions are telescoped together.<sup>48</sup> In addition, continuous processes are useful when a reaction involves hazardous intermediates because only a small amount is present at any one time.<sup>49,50</sup>

The large surface area to volume ratio can also be used to improve photo- and electrochemical reactions. In photochemistry the energy from photons is used to generate excited intermediates. In batch, one of the key challenges is getting enough photons into a reaction. Photons are absorbed by the reaction mixture, resulting in the amount of photons decreasing with the path length making photochemistry difficult to perform in batch at scale. Flow reactors greatly reduce the path length, thereby increasing the photon flux of a reaction.<sup>51</sup> Electrochemistry will be explored in detail in Section 1.3.3.



Mass transfer is an important consideration for reactions. Lab-scale flow reactors typically operate with laminar flow conditions, where mass transfer is governed by diffusion.<sup>52</sup> Given the narrow diameter of these types of reactors mass transfer is not usually a problem for homogenous reactions, and if it is then static mixers such as meshes or baffles can be employed.<sup>53</sup> Efficient mixing becomes a much more pressing concern for multiphasic reactions, something that flow chemistry can be used to address.<sup>54</sup>

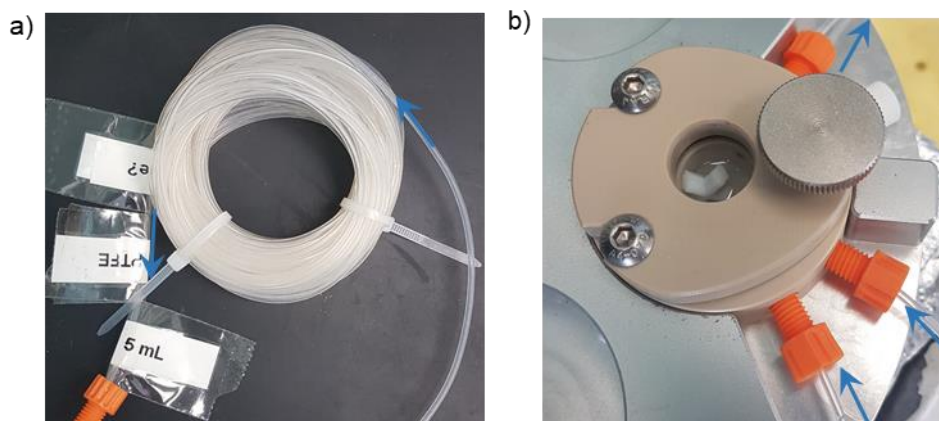
Segmented or 'slug' flow is often used for gas-liquid and liquid-liquid reactions. A T-piece brings together two immiscible reaction streams (a, Figure 1.17).<sup>46</sup> Build-up of pressure differences between the two streams results in a slug flow, with alternating droplets of each phase along the tubing. This creates a large surface area between the two phases, improving mass transfer between them.<sup>52</sup> For liquid-solid reactions a packed bed reactor is often used. A tube or cartridge is filled with solid material, for example a heterogeneous catalyst, and the liquid phase is flowed through this (b, Figure 1.17).<sup>46</sup>



**Figure 1.17:** a) Segmented flow is formed when two phases meet at a T-junction. b) Packed bed reactors are often used for heterogeneous catalysts.

Most laboratory flow chemistry is conducted using tubular reactors (a, Figure 1.18). These consist of plastic or steel tubing with a typical internal diameter of 1/16" (most tubing diameters are sold in inches). The length of tubing may be varied and is usually coiled around a heat source or a lamp. Chip reactors (microreactors) are low volume flow reactors that have flow channels machined into a plate of steel or ceramic. In some instances, particularly when suspensions are involved, tubular reactors may be impractical. Continuous Stirred Tank Reactors (CSTRs) are well suited to multiphasic reactions.<sup>55</sup> These consist of a series of batch reactors that are stirred and connected by

tubing (b, Figure 1.18). This gives excellent mass transfer due to the active stirring, whilst remaining continuous as the reaction mixture flows from one tank to the next.



**Figure 1.18:** a) Coiled tubular reactor made from 1/16" PTFE tubing. b) One tank of a CSTR; when in use multiple tanks are connected in series.

Although it might not be suitable for every reaction, flow chemistry is a useful tool for the modern synthetic chemist.<sup>54</sup> It enables the safe handling of hazardous intermediates and the use of high temperatures and pressures. Although they can be more expensive and challenging to set up, experiments conducted in flow are often more reproducible, have a higher throughput and are more amiable to scaling up.<sup>46,47</sup> The use of pumps and inline analysis allows flow systems to be automated readily without the need for liquid or solid handling robots, enabling reactions to be optimised or for kinetics to be investigated autonomously.<sup>48,56,57</sup>

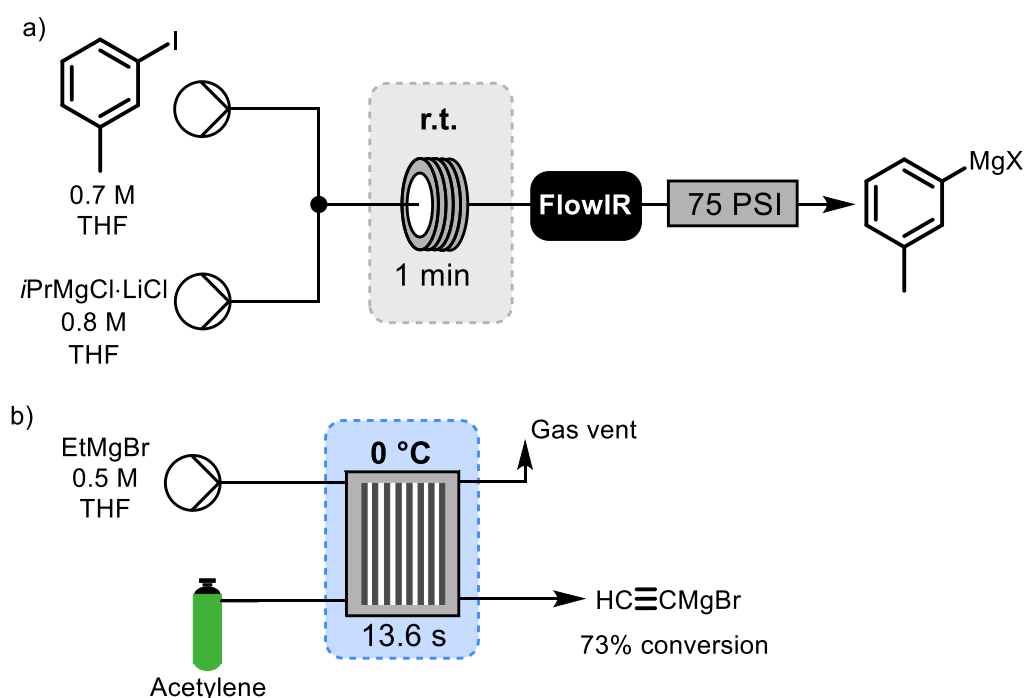
### 1.2.2. Synthesis of organometallic species in flow

Compared to the wealth of organic reactions performed in flow, the contributions of the organometallic community have been quite modest.<sup>58,59</sup> Many organometallic complexes are air and moisture sensitive, making them challenging to handle. Flow chemistry has been used for the on demand synthesis of sensitive reagents and this approach could be beneficial for organometallic species, telescoping Grignard reagents or transition metal catalysts into reactions.

Grignard reagents are important for Kumada cross-coupling reactions. Some common Grignards are available commercially, but more complex reagents need to be made in-house through the reaction of an alkyl or aryl halide with magnesium. These reactions are strongly exothermic and the Grignards produced are often pyrophoric. Several groups have developed continuous processes for the synthesis of Grignard reagents to address these safety concerns.<sup>60–63</sup> By conducting it in flow the surface area to volume ratio is increased, thereby increasing the rate of cooling which may be applied. Furthermore by producing the Grignard in flow, only a small amount of pyrophoric

material is present at any one time. These examples have often used in-line analysis which is a useful tool, especially for highly reactive species, such as Grignard reagents.

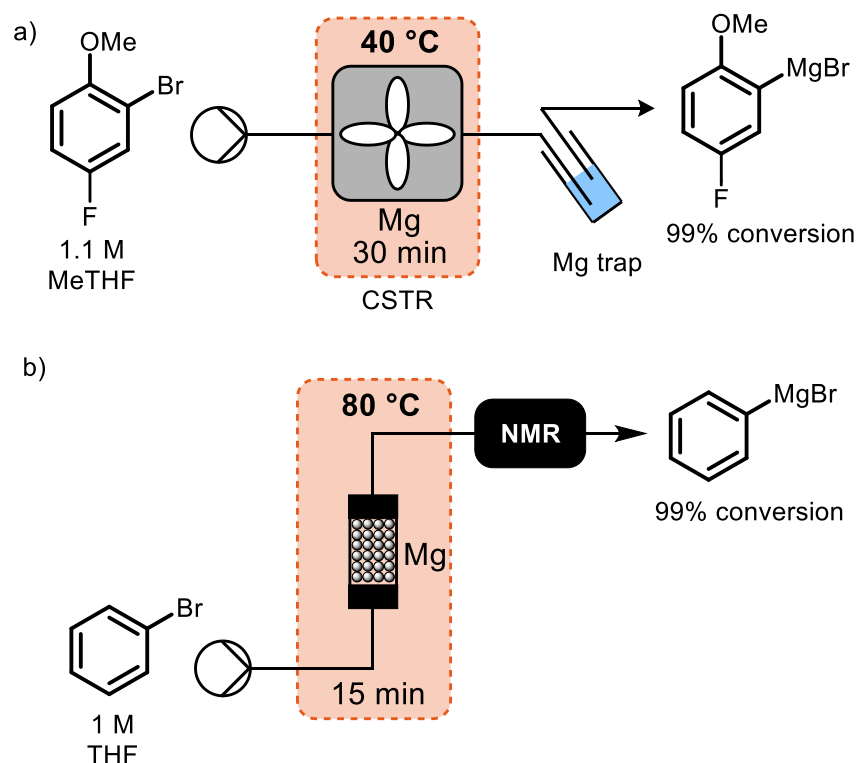
One of the challenges with these reactions is the multiphasic nature of them. The Ley group addressed this by using solutions of commercially available Grignards and combining them with aryl halides in a flow reactor, thereby transferring the magnesium from the commercial Grignard into the aryl halide of interest (Figure 1.19 a). This was monitored using in-line IR spectroscopy.<sup>60</sup> Deng *et al* used a similar method for the synthesis of ethynyl-MgBr. To produce this Grignard they reacted commercial EtMgBr with acetylene in a falling film microreactor (Figure 1.19 b). EtMgBr enters at the top of the reactor and 'falls' to the bottom of the reactor whilst acetylene is added at the bottom of the reactor and bubbles up the reactor to a gas vent.<sup>62</sup> This provides excellent, and consistent, gas-liquid contact. Although useful for the controlled synthesis of less common Grignards by transfer of magnesium between species, neither of these examples address the issue of making Grignards in the first place.



**Figure 1.19:** Synthesis by transferring magnesium from commercial Grignard reagents.<sup>60,62</sup>

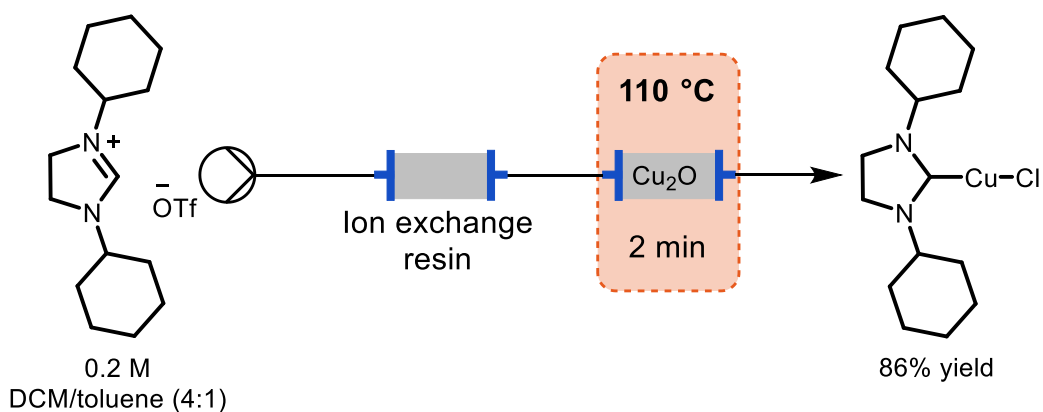
In 2016 two groups reported the synthesis of Grignards from magnesium and aryl halides.<sup>61,63</sup> Kopach *et al*, from Eli Lilly, used continuous stirred tank reactors (CSTRs) to produce Grignard reagents (a, Figure 1.20). These reactors were intermittently charged with magnesium and used a series of settling pipes and traps to prevent magnesium particulates from entering downstream processes. An in situ IR probe was used to monitor the formation of Grignard species.<sup>61</sup> Goldbach *et al* used a fluidised bed reactor of magnesium to produce Grignard reagents which were monitored using in-line

NMR spectroscopy (b, Figure 1.20). This reactor was charged with magnesium and placed vertically and solvent pumped upwards at a sufficient velocity to prevent the particles settling, providing superior mass and heat transfer to a packed bed reactor.<sup>63</sup>



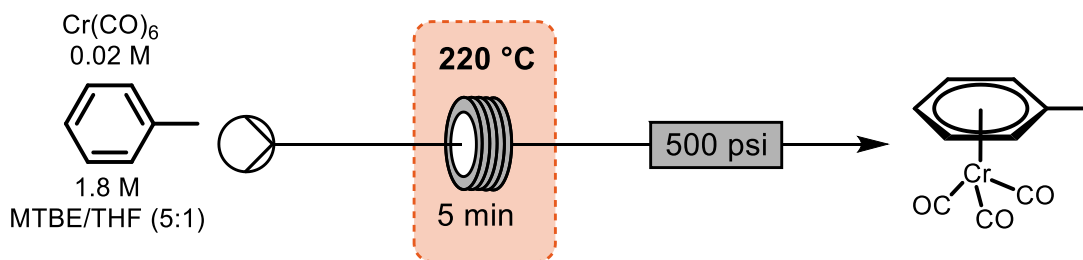
**Figure 1.20:** The synthesis of Grignard reagents in CSTRs (a) and fluidised bed reactors (b).<sup>61,63</sup>

The McQuade group described the first example of copper-NHC synthesis in flow.<sup>64</sup> They flowed solutions of imidazoliums through a pack bed reactor of  $\text{Cu}_2\text{O}$ , producing a range of copper-NHC complexes, many of which are challenging to make in batch (Figure 1.21). The  $\text{Cu}_2\text{O}$  required a solid diluent and the group found that molecular sieves slightly improved the yield, presumably because they also removed any water in the system. Of interest was their use of an ion exchange column to change the counter ion of imidazoliums salts. Sometimes the synthetic path to a ligand limits the choice of counter ion and the use of an ion exchange column to circumvent this issue could be useful. One of the key drawbacks was the lack of long term stability, the reactor was only capable of producing 2.5 mmol of complex, limiting its use as a catalyst dispensing system for platforms that operate continuously.<sup>64</sup>



**Figure 1.21:** Synthesis of copper(I)-NHCs using a packed bed reactor.<sup>64</sup>

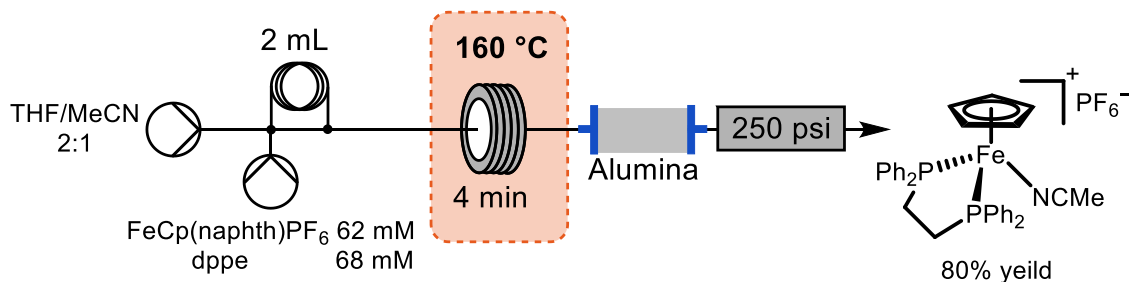
$\text{Cr}(\text{CO})_3$  piano-stool complexes are of interest because the  $\text{Cr}(\text{CO})_3$  group enables the facile nucleophilic substitution of an arene. These type of complexes can be very challenging to make due to the high temperatures required, taking several days when heated in an open vessel and presenting a significant hazard when performed under pressure. In fact Leadbeater noted that “in our hands, the synthesis of (arene) $\text{Cr}(\text{CO})_3$  complexes using this sealed vessel approach has been met with vessel failure more times than it has been successful”.<sup>65</sup> The Leadbeater group used flow chemistry to heat their  $\text{Cr}(\text{CO})_6$  in the presences of arenes to generate piano-stool complexes. By using stainless steel tubing and a 500 psi back pressure regulator they were able to conduct their reaction at  $220\text{ }^\circ\text{C}$  and obtain isolated yields of 71% (Figure 1.22). Despite the high temperatures and pressures this offers a much safer path to these complexes than conventional methods.<sup>65</sup>



**Figure 1.22:** The synthesis of tricarbonyl chromium piano stool complexes in flow is much safer.<sup>65</sup>

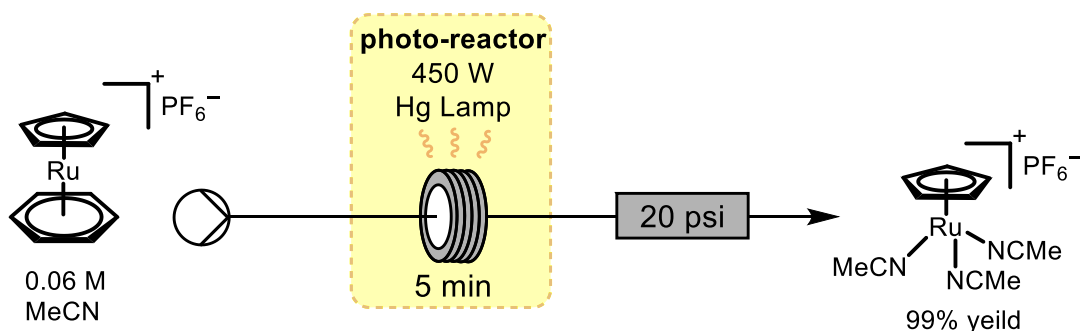
The Renaud group turned to flow chemistry to reduce the reaction time for the synthesis of Fe piano-stool complexes.<sup>66</sup> They used  $\text{Fe}(\text{Cp})(\text{naphthalene})$  as a starting material, displacing the naphthalene with a bisphosphine ligand and a coordinating acetonitrile. In some instances a precipitate was observed and this was removed through the use of an alumina column (Figure 1.23). The authors noted that the continuous production of iron complex would be of interest for catalysis, but they did not attempt to run the reaction for an extended period of time.<sup>66</sup> The alumina column presented no problem for them, but

during prolonged use it could become blocked or increase the pressure sufficiently for the pumps to stall.



**Figure 1.23:** Synthesis of iron piano-stool complexes in flow.<sup>66</sup>

$\text{RuCp}(\text{MeCN})_3\text{PF}_6$  is usually prepared from ruthenium sandwich complexes *via* photolysis on a small scale. The Jamison group wanted to produce this complex on a gram scale for catalytic studies and turned to flow to address the issue of light transmittance (Figure 1.24).<sup>67</sup> The larger surface area to volume ratio of flow reactors mean that, when the tubing is transparent, a higher and more even photon flux can be achieved. The group were able to get full conversion to  $\text{RuCp}(\text{MeCN})_3\text{PF}_6$  and improve the throughput from  $0.158 \text{ g h}^{-1}$  in batch to  $1.56 \text{ g h}^{-1}$  in flow.



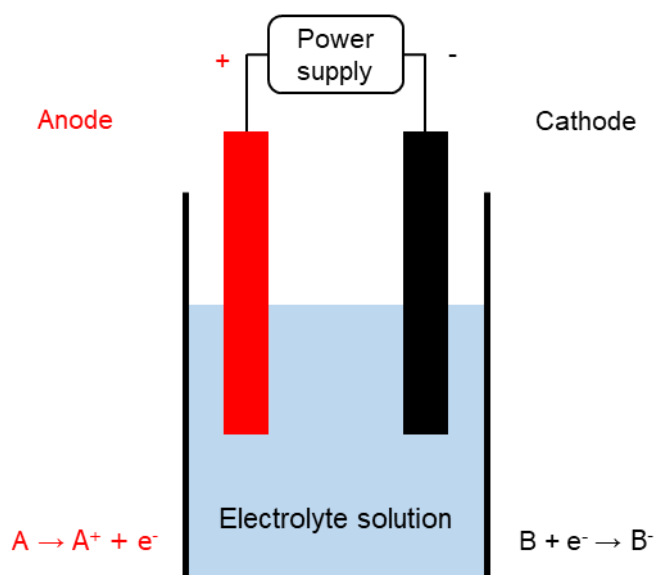
**Figure 1.24:** Photochemical synthesis of  $\text{RuCp}(\text{MeCN})_3\text{PF}_6$  on a gram scale.<sup>67</sup>

### 1.3. Electrochemistry

#### 1.3.1. Fundamentals of electrochemistry

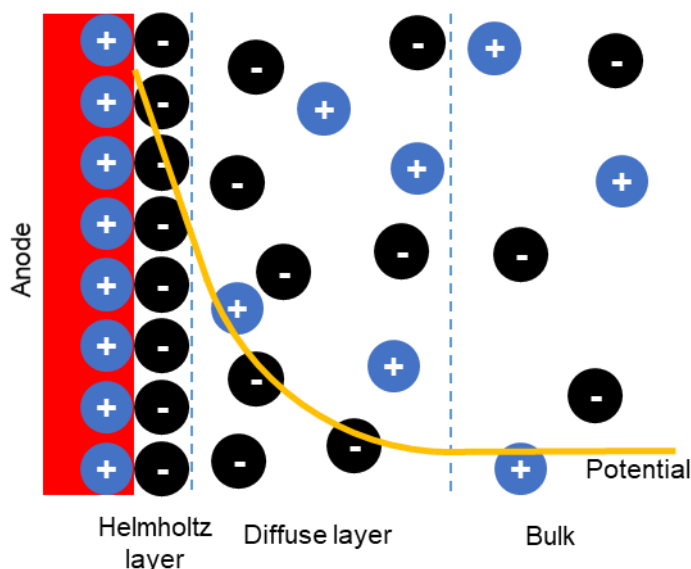
Electrochemistry is predominantly used in organic synthesis as a means of oxidising or reducing compounds without the use of harsh reagents. Electrochemistry offers an atom efficient means of performing these transformations.<sup>49,68</sup> In its simplest form an electrochemical set up requires only a power supply and two electrodes which are placed in a solution containing an electrolyte to transport the charge (Figure 1.25). Oxidation can occur at the positive electrode (the anode) and reduction can occur at the negative electrode (the cathode). The working electrode refers to the electrode where the reaction

of interest is taking place, whilst the other electrode is often called the counter electrode.<sup>69</sup> A reaction always occurs at the counter electrode to enable the transfer of charge, and is usually the electrolysis of solvent. The reactions are heterogeneous as they take place on the surface of the electrode, therefore one of the key limitations is the surface area of the electrode.<sup>49</sup> Consequently good mass transfer is important, to bring the reactant into contact with the electrode and enable the product to move away from the electrode and into the bulk solution.



**Figure 1.25:** A simple electrochemical setup, oxidation occurs at the anode and reduction at the cathode. An electrolyte solution enables the transfer of charge.

At the surface of the electrode is an electrochemical double layer, sometimes called a Helmholtz layer, formed from a charged electrode and the species of opposite polarity forming a layer next to the electrode.<sup>70</sup> For example anions would form a layer of negative charge at the surface of the positively charged anode. Further away from the electrode a diffuse layer is found where the concentration of anions decreases, along with the potential, until the bulk solution is reached (Figure 1.26).<sup>71,72</sup>



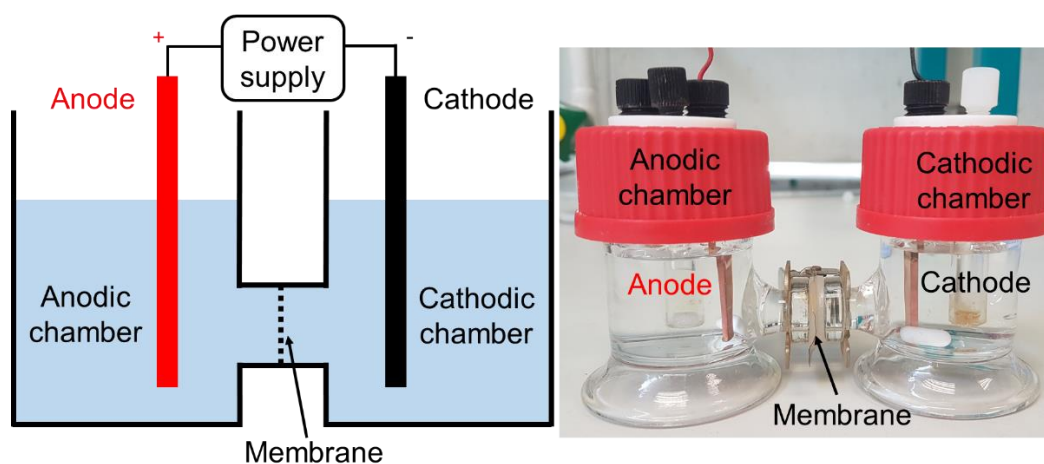
**Figure 1.26:** A layer of anions forms on the surface of the anode with the concentration of anions and the potential decreasing with the distance from the electrode.

Electrochemical vessels are referred to as cells and can be undivided or divided. Undivided cells are the simplest and are best used when the reaction at the counter electrode does not affect the reaction of interest. The simplest reaction involves the direct oxidation or reduction of one of the reagents at one electrode and solvent degradation at the opposite electrode.<sup>70,73</sup> Electrocatalysed reactions use a mediator to transfer electrons from the electrode to the reagents.<sup>70,73</sup> This usually lowers the overpotential (the potential applied that is above the amount required theoretically),<sup>74</sup> which can be useful if the reagents reduction potential falls outside of the solvent's electrochemical window. Furthermore, the homogenous nature of the mediators comes with the benefits of homogenous catalysis, such as selectivity.

In some instances two reactions of interest can be paired, with one occurring at the anode and the other at the cathode.<sup>49,70,75</sup> This avoids the problem of undesirable reactions and increases the faradaic efficiency (the proportion of electrons that take part in the desired reaction) as both electrodes are working electrodes. The two products may then react with one another to form a final product. An example of this is the synthesis of metal-NHC complexes. This is a slightly unusual situation as the anode is not only sacrificial, but also one of the reagents. It provides a simple synthetic route to metal-NHC complexes especially as the imidazolium salt also acts as the electrolyte.<sup>14</sup> Domino-oxidation-reduction reactions work with a similar principle, with both electrodes acting as working electrodes. Here a single reagent is oxidised and subsequently reduced (or *vice versa*).<sup>70</sup>



Where an undesirable reaction at the counter electrode cannot be avoided the cell can be divided by an ion exchange membrane, allowing small ions (such as  $H^+$ ) to transfer charge across the cell, but separating the two reactions from each other (Figure 1.27).<sup>69</sup> Divided cells are usually more expensive and typically require very high concentrations of electrolyte. This is because of the large distances between the electrodes and the presence of the membrane which greatly increases the resistance of the cell.



**Figure 1.27:** Schematic and photograph of a divided cell, with an ion exchange membrane separating the two chambers.

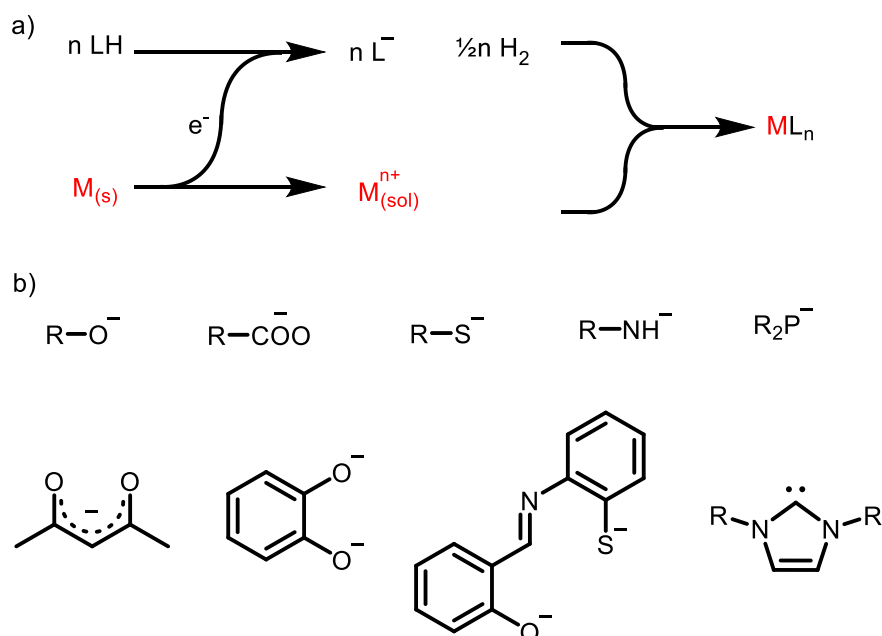
### 1.3.2. Electrochemical synthesis of metal complexes

The electrochemical synthesis of metal complexes is generally regarded as a niche technique, however it was used throughout much of the 70s, 80s and 90s by a number of groups.<sup>76–82</sup> Between them a plethora of complexes were produced, with metals from the entire first row (except scandium), half the second row, and a few examples from the third row, f-block and groups 13 and 14 (Figure 1.28).<sup>83–86</sup> The first contemporary examples of the electrochemical synthesis of metal complexes was in 1975, with work from Eisenbach, Lehmkuhl and Tuck focused on halide and alkoxide ligands.<sup>87–89</sup> The Tuck group went on to be the main proponent of electrochemical synthesis, extending the scope of metals and ligands and using it to produce anionic, cationic and neutral complexes.<sup>89–91</sup>

Group →	1	2	3	4	5	6	7	8	9	10	11	12	13	14	15	16	17	18
↓ Period																		
1	1 H																	2 He
2	3 Li	4 Be											5 B	6 C	7 N	8 O	9 F	10 Ne
3	11 Na	12 Mg											13 Al	14 Si	15 P	16 S	17 Cl	18 Ar
4	19 K	20 Ca	21 Sc	22 Ti	23 V	24 Cr	25 Mn	26 Fe	27 Co	28 Ni	29 Cu	30 Zn	31 Ga	32 Ge	33 As	34 Se	35 Br	36 Kr
5	37 Rb	38 Sr	39 Y	40 Zr	41 Nb	42 Mo	43 Tc	44 Ru	45 Rh	46 Pd	47 Ag	48 Cd	49 In	50 Sn	51 Sb	52 Te	53 I	54 Xe
6	55 Cs	56 Ba		72 Hf	73 Ta	74 W	75 Re	76 Os	77 Ir	78 Pt	79 Au	80 Hg	81 Tl	82 Pb	83 Bi	84 Po	85 At	86 Rn
7	87 Fr	88 Ra		104 Rf	105 Db	106 Sg	107 Bh	108 Hs	109 Mt	110 Ds	111 Rg	112 Cn	113 Nh	114 Fl	115 Mc	116 Lv	117 Ts	118 Og
Lanthanides				57 La	58 Ce	59 Pr	60 Nd	61 Pm	62 Sm	63 Eu	64 Gd	65 Tb	66 Dy	67 Ho	68 Er	69 Tm	70 Yb	71 Lu
Actinides				89 Ac	90 Th	91 Pa	92 U	93 Np	94 Pu	95 Am	96 Cm	97 Bk	98 Cf	99 Es	100 Fm	101 Md	102 No	103 Lr

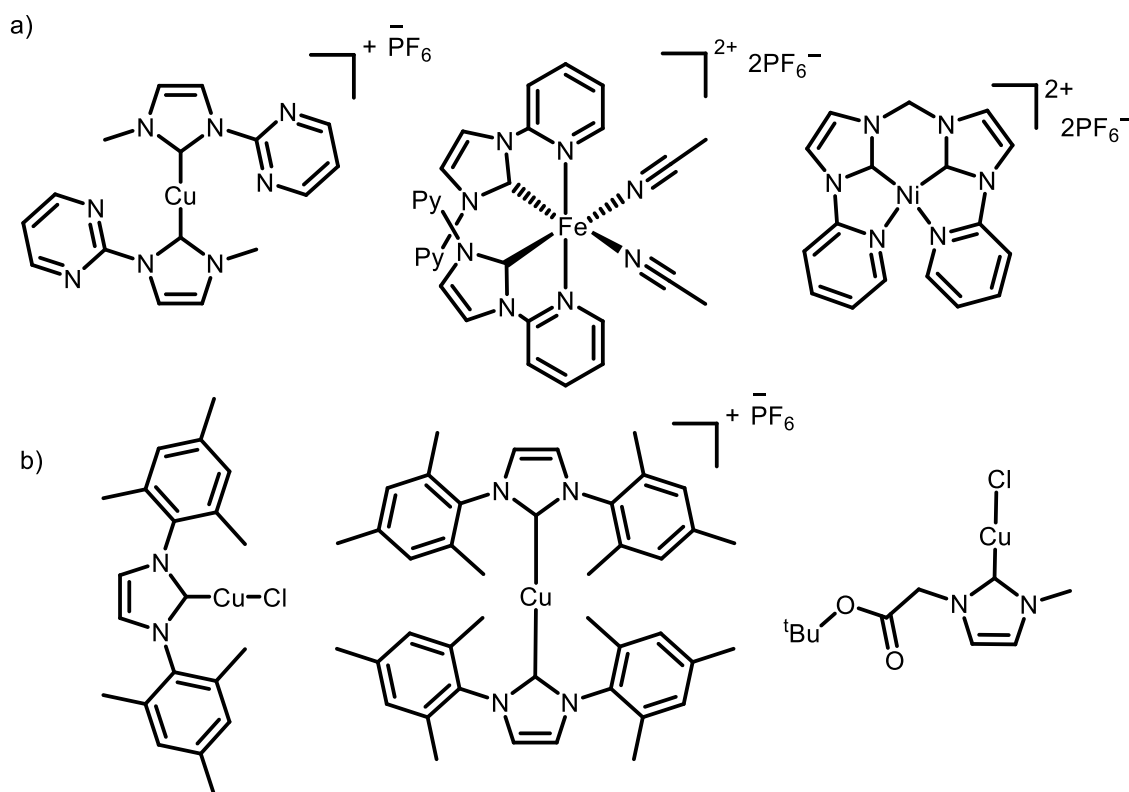
**Figure 1.28:** Scope of metal complexes produced electrochemically, the majority by Tuck *et al.*

A wide range of ligands can be generated from LH ligand precursors (Figure 1.29, b). This has included alkoxides,<sup>87</sup> acacs,<sup>92</sup> carboxylates,<sup>93</sup> phosphides,<sup>94</sup> thiols,<sup>95</sup> amines,<sup>96</sup> catechols,<sup>97</sup> salens<sup>98</sup> and NHCs.<sup>14,99</sup> The reaction proceeds *via* the cathodic reduction of the ligand precursor, generating the ligand and hydrogen gas as a by-product. This occurs simultaneously with the oxidation of a sacrificial anode, producing metal ions in solution. The ligands are then able to coordinate to the metal ions (Figure 1.29, a).<sup>79,80</sup>



**Figure 1.29:** a) General scheme for the electrochemical synthesis of metal complexes. b) A selection of mono- and bi-dentate ligands produced *via* the cathodic reduction of LH ligand precursors.

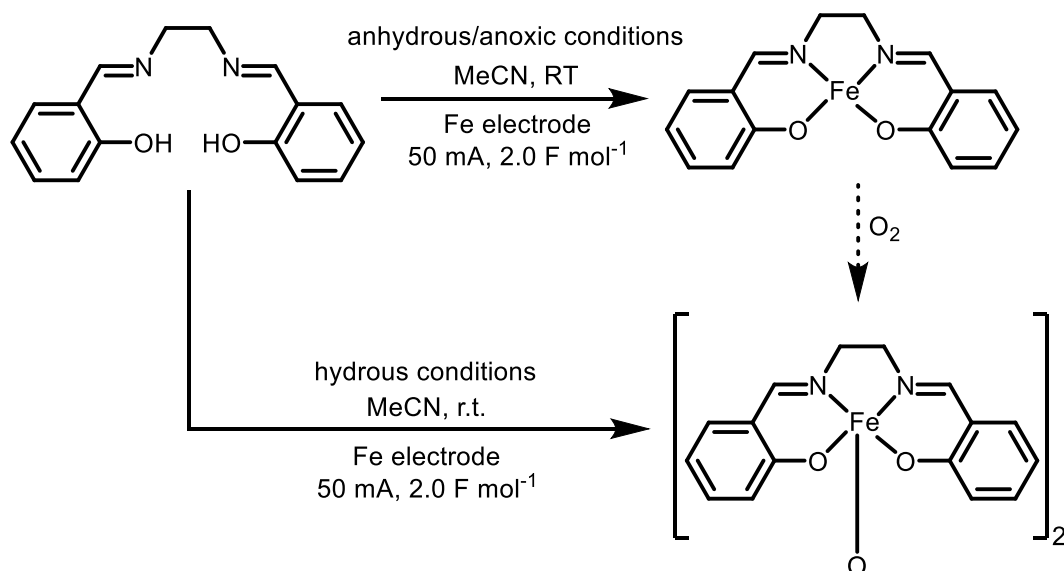
NHCs are a relatively recent addition to this methodology. The Chen group first explored the electrochemical synthesis of metal-NHC complexes in 2011, producing a series of copper(I), iron(II) and nickel(II) complexes (Figure 1.30, a).<sup>14</sup> This group used a platinum cathode to reduce the imidazoliuim (which also acts as the electrolyte), forming a carbene. Metal ions were then produced at a sacrificial anode. The Willans group have extended this to copper(I) complexes with bulky ligands and demonstrated that mono- or bis-NHC complexes may be produced selectively depending on the anion (Figure 1.30, b).<sup>99</sup> The use of coordinating anions such as halides results in the synthesis of mono-NHC complexes, while non-coordinating anions, such as  $\text{PF}_6^-$ , result in bis-NHC complexes. This method has advantages over traditional methods of metal-NHC synthesis; the use of expensive or air sensitive reagents is avoided, it is much more atom economical and is performed at room temperature in the absence of a base, allowing base sensitive groups to be tolerated.



**Figure 1.30:** a) Metal-NHC complexes produced by the Chen group.<sup>14</sup> b) Cations were used by the Willans group to selectively form mono- or bis-NHC complexes. They were also able to produce complexes with base sensitive substituents, such as esters.<sup>100</sup>

This broad strategy has enabled the synthesis of a range of complexes, including those featuring multidentate ligands.<sup>82,96,98</sup> Other, non-reducible, ligands may also be added to the reaction to help stabilise complexes.<sup>82,101</sup> Generally the complex formed is in the lowest oxidation state for that metal, which allows the facile synthesis of low-oxidation state complexes, something that can be challenging using chemical methods.<sup>76,77,79,82</sup>

Further oxidation of metal centres usually occurs in solution by reaction with oxygen.<sup>82</sup> For example, Chapman *et al* were able to produce Fe(III) or Fe(II) salen complexes selectively by conducting the reaction in air or under inert conditions respectively (Figure 1.31), something that they extended to Mn(II) and Mn(IV) complexes.<sup>98</sup> There are a few examples of further electrochemical oxidation.<sup>102,103</sup>



**Figure 1.31:** Fe(III) or Fe(II) may be formed selectively by performing the reaction in air or under inert conditions.<sup>98</sup>

These reactions are usually performed in an undivided batch reactor, often using acetonitrile as the solvent.<sup>80</sup> Acetonitrile has a broad electrochemical window and helps to stabilise many complexes. In principle any metal electrode may be used as the sacrificial anode, with the choice of electrode specifying which metal is in the complex. In practice the choice is limited by the material properties (and cost) of the metal in question. Here a rudimentary knowledge of redox potentials can be beneficial. For example, pure manganese is very brittle, making it unsuitable as an electrode. However it may be alloyed with nickel to produce a more suitable material. Manganese has a more negative reduction potential (-1.185 V, compared to -0.257 V for nickel)<sup>104</sup> indicating that it is easier to oxidise than nickel and Mn(II) ions will be generated preferentially. This was exploited by Chapman *et al*, who used manganese-nickel alloy electrodes to produce Mn(II)-salen complexes with no evidence of nickel impurities.<sup>98</sup> Similarly, in the course of this thesis chromium impurities have been observed when using stainless steel anodes. This can be avoided through the use of pure iron electrodes.

The reaction conditions are generally mild, being conducted at room temperature, and it is unusual to observe by products.<sup>77</sup> Often products precipitate and if not diethyl ether will usually trigger precipitation, enabling simple work ups.<sup>77</sup> This is particularly important when supporting electrolytes are used as electrolytes are often removed *via* extraction

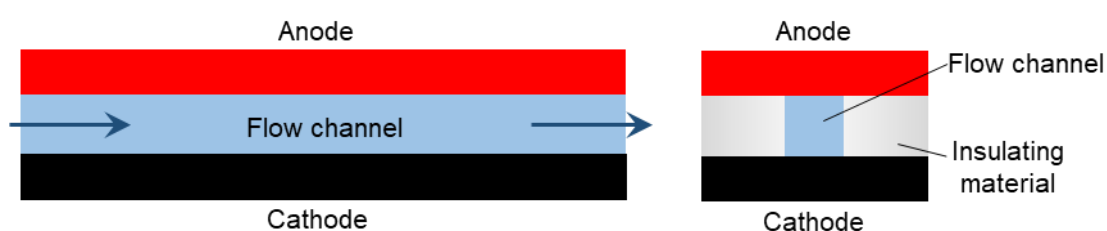
with water. Many low-oxidation state metal complexes are very air and moisture sensitive, making aqueous washes impractical. In the past perchlorate salts were often used as an electrolyte, these are usually avoided due to the explosive hazards associated with their use.<sup>82</sup>

Despite the broad scope of electrochemistry to produce metal complexes it has not been widely adopted. Perhaps this is because it is primarily confined to the first row and during the late 20<sup>th</sup> century most homogenous catalysis was performed with second and third row metals. However, as the synthetic community pivots towards first row transition metals for catalysis, electrochemistry may become more popular for the synthesis of these complexes, especially if it is able to produce such complexes on demand; allowing catalysts to be dispensed into reactions directly.

### 1.3.3. Electrochemistry in flow

There are numerous examples of groups using electrochemistry in flow and it has several advantages over conventional electrochemistry.<sup>105–107</sup> The inter-electrode distance is much smaller, leading to less resistance which can remove the need for a supporting electrolyte and thus simplify the work up and improving the atom economy.<sup>43,49,68,108</sup>

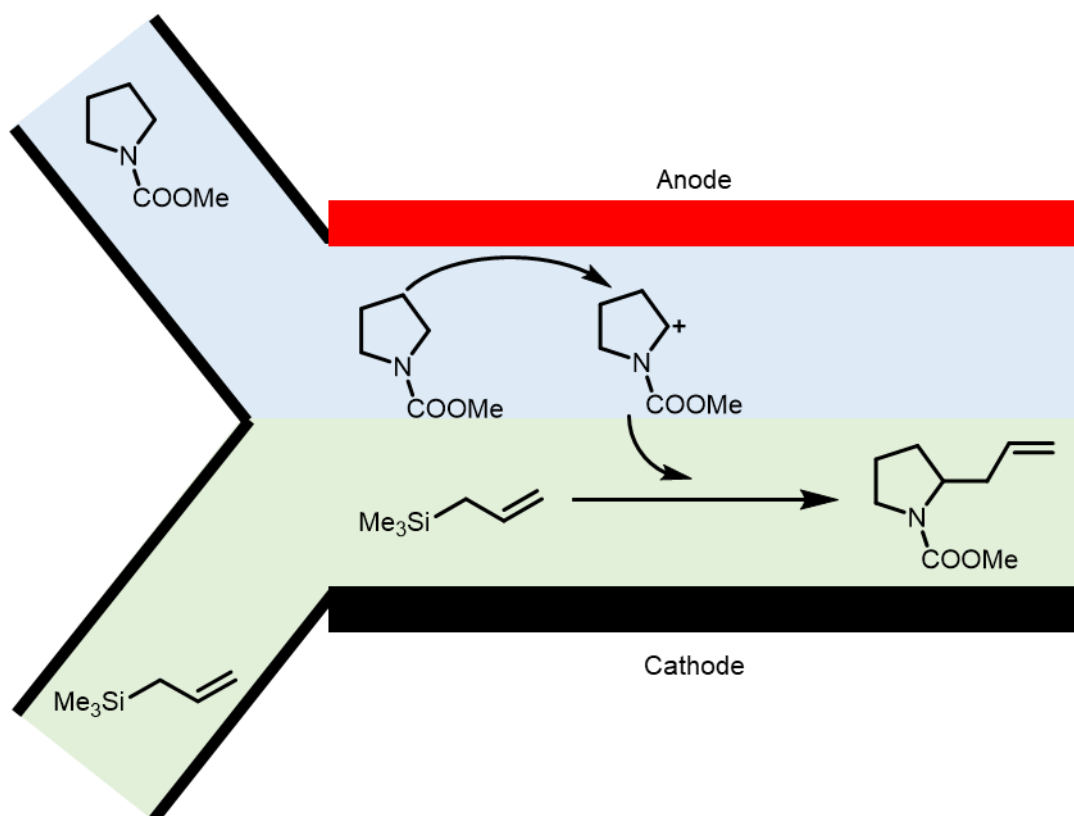
The majority of electrochemical flow reactors used for synthesis follow the same basic design principles, two plate electrodes held apart by an insulating material with a flow channel cut into it (Figure 1.32). The specific details might vary; some are designed to be used with recirculating flow,<sup>109</sup> others for single pass reactions,<sup>110</sup> some allow reactions to be performed in parallel<sup>111</sup> and some are modular allowing the volume to be changed.<sup>112</sup>



**Figure 1.32:** Longitudinal (left) and transverse (right) cross sections of electrochemical flow reactors.

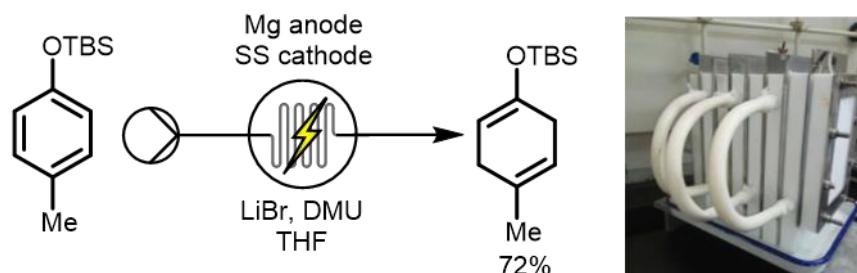
Most electrochemical flow reactors are dominated by laminar flow. The Atobe group took advantage of laminar flow for the electrolysis of *N*-(methoxycarbonyl)pyrrolidine.<sup>113</sup> Their reactor had two inlets, resulting in parallel flows. The pyrrolidine is oxidised at the anode, forming a cation which migrates to the cathodic side of the flow channel where it reacts with an alkene to form the product. The parallel laminar flow prevents the oxidation of the alkene, because its movement across the flow channel is governed by diffusion. By

contrast the cation migrates across the channel more quickly as a result of electrostatic forces.<sup>113</sup>



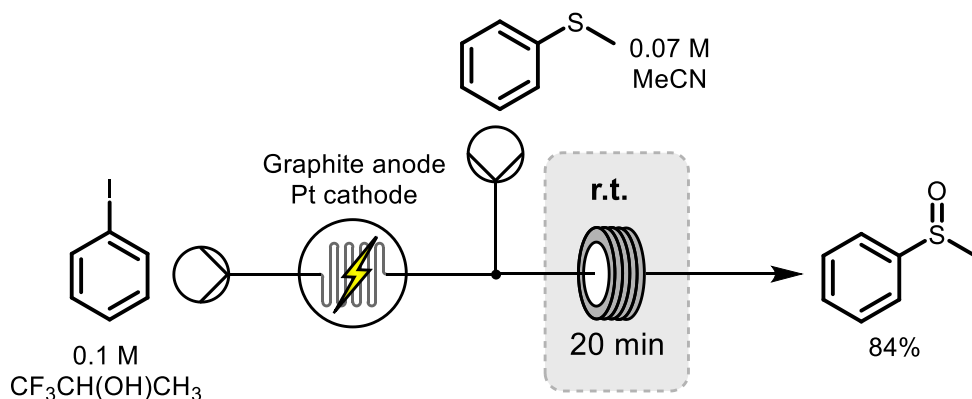
**Figure 1.33:** The Atobe group exploited laminar flow to avoid the unwanted oxidation of reagents.<sup>113</sup>

Scaling up electrochemical processes in batch is challenging because as the distance between electrodes increases, so too does the potential required. This can cause selectivity issues and result in solvent degradation. Consequently flow chemistry is widely used in industry to scale up electrochemical reactions.<sup>108</sup> In 2019 the Baran group demonstrated a modular electrochemical flow reactor that was able to scale up a Birch reaction to a 100 g scale using magnesium anodes and stainless steel cathodes (Figure 1.34).<sup>114</sup>



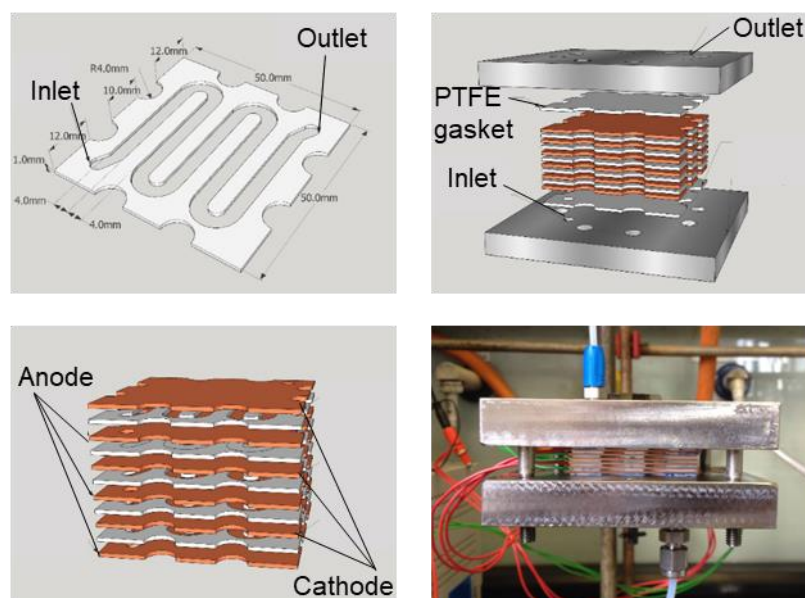
**Figure 1.34:** Electrochemical birch reactor and the 100 g scale reactor fabricated by the Baran group.<sup>114</sup> Reproduced with permission from AAAS.

The Wirth group have used electrochemistry to generate hypervalent iodine reagents.<sup>115</sup> These compounds are useful for selective oxidations, however they can be unstable and quickly decompose. Furthermore their chemical synthesis requires stoichiometric amounts of chemical oxidants. The Wirth group were able to produce these reagents electrochemically using a flow reactor with platinum and graphite electrodes from iodobenzene and fluorinated solvents. The hypervalent iodine species were then telescoped into a coiled reactor to act as oxidants for a range of substrates (Figure 1.35).<sup>115</sup>

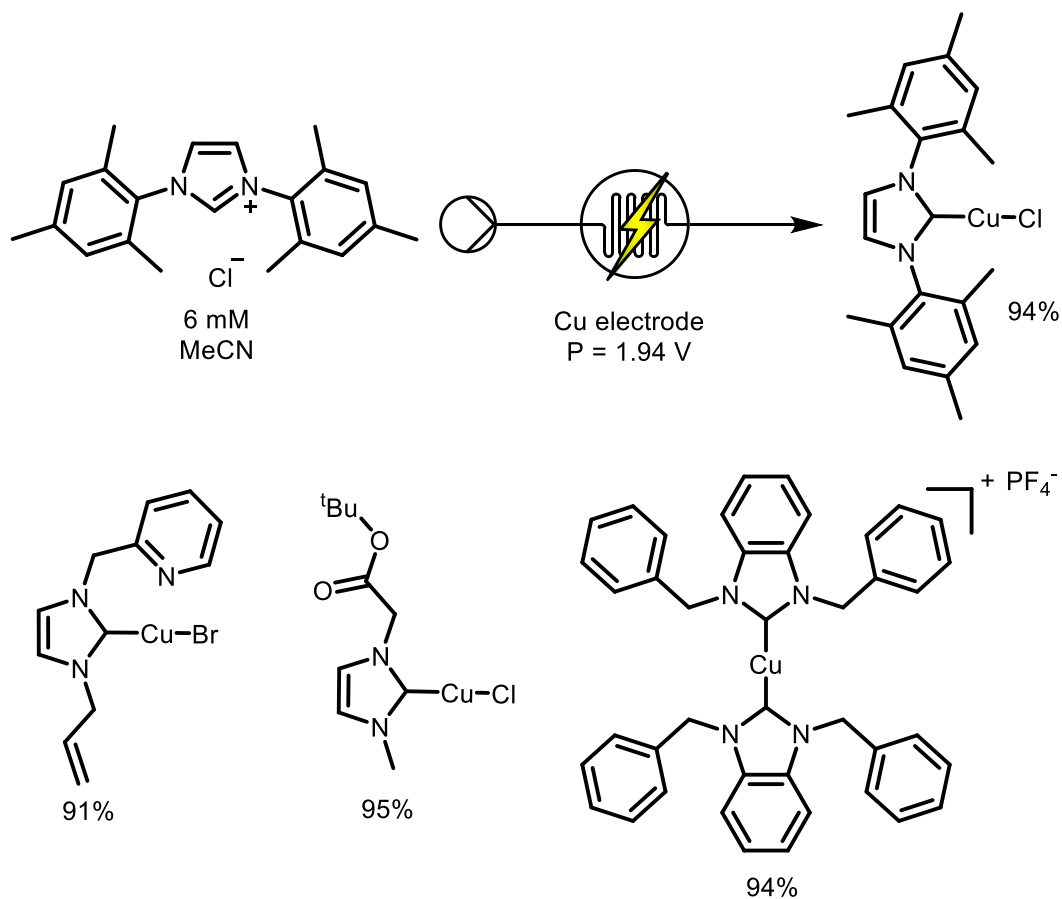


**Figure 1.35:** The Wirth group generated hypervalent iodine compounds electrochemically and telescoped these into another reaction to act as oxidising agents.<sup>115</sup>

The Willans group are the only group to have synthesised organometallic compounds electrochemically in flow (Figure 1.36).<sup>112</sup> The group have synthesised a range of copper-NHC complexes and used the synthesis of  $\text{Cu}(\text{IMes})\text{Cl}$  as a model reaction. The imidazolium precursor was pumped through the reactor whilst a constant potential of 1.94 V was applied.  $\text{Cu}(\text{IMes})\text{Cl}$  was formed with a yield of 94% in a single pass and no bis-NHC complex was observed. A variety of copper-NHC complexes were synthesised, including some with base sensitive N-substituents (Figure 1.37).<sup>112</sup>



**Figure 1.36:** The Willans 2<sup>nd</sup> generation reactor featured a stacked electrode design and was able to produce Cu(IMes)Cl in 94 %.<sup>19</sup> Reproduced with permission from the Royal Society of Chemistry



**Figure 1.37:** A range of complexes could be synthesised electrochemically in flow using the 2<sup>nd</sup> generation Willans reactor.<sup>112</sup>



## 1.4. Summary and Aims

Electrochemistry is currently experiencing a revival and offers a green method for performing oxidations and reductions, avoiding the use of harsh reagents. It allows the atom efficient synthesis of organometallic compounds, in particular the relatively straight forward synthesis of NHC complexes with first row transition metals, avoiding difficult to handle reagents such as  $\text{Fe}[\text{N}(\text{SiMe}_3)_2]_2$ .

Metal-NHC complexes are widely used as catalysts and there has been a desire to move towards first row metals due to their relative abundance and potential for lower toxicity when compared to second and third row elements such as platinum and ruthenium. However, many first row metal complexes are synthetically challenging to produce using traditional chemical methodologies. Electrochemistry has the potential to offer a simpler synthetic route to these new catalysts, increasing their accessibility and hopefully their use. Due to the sensitivity of many organometallic complexes it is necessary to conduct these electrochemical reactions under inert conditions. One aspect of this project is the design and utilisation of a simple and flexible batch reactor for air sensitive electrochemistry, with the aim of making such reactions cheaper and easier for the non-expert to perform.

Many first row complexes which are used in catalysis are difficult to handle and store, presenting a barrier to their adoption. The Willans group have previously demonstrated that copper-NHC complexes can be produced on demand through the use of an electrochemical flow reactor, allowing catalysts to be dispensed directly into reactions.<sup>112</sup> Part of this project examines the effects of mass transfer within a miniaturised version of the previous electrochemical flow reactor and how the mass transfer can be manipulated to improve the performance of the reactor.

A significant portion of this work looks at extending the studies conducted by the Willans group to other metals such as nickel, enabling the synthesis of nickel-NHC complexes electrochemically. These complexes have received considerable interest as catalysts for cross couplings and consequently the ability to telescope such complexes into reactions would be of considerable interest.

## 2. Electrochemistry in batch

Within our group we are focussed on the synthesis of metal complexes for catalytic and biomedical applications, and have found that many of these can be prepared efficiently using electrochemical synthetic techniques. However, due to the air sensitive nature of some of this chemistry it is desirable to have a batch reactor to enable electrochemistry under inert conditions, whilst remaining standardised and highly versatile. This chapter describes the development and production of such a reactor, which has been used to perform organic and inorganic transformations, as well as analytical electrochemistry. This has been enabled through a flexible and well defined design. The reactor is based upon a commercially available vial with an adapted lid and features a fixed interelectrode distance which is crucial for reproducibility, along with the ability to accommodate a variety of interchangeable electrode materials making it suitable for a range of applications.

### 2.1. Design of a flexible batch reactor for electrochemistry

#### 2.1.1. Existing batch reactors

During the last decade synthetic electrochemistry has received renewed interest as an enabling technology that typically provides a mild and atom efficient method for performing chemical transformations.<sup>69,108,116–121</sup> This well-understood redox mode of activation, coupled with broad applicability has resulted in the development of a raft of new methodologies in organic synthesis.<sup>69,116,119</sup> Although it has been exploited to a lesser degree, electrochemistry can offer a simple route to inorganic and organometallic complexes, in particular complexes featuring metal centres with low oxidation states.<sup>77,79,82,122</sup> In these instances, the ligand precursor is reduced at the cathode and a sacrificial anode is oxidised to release a metal ion which can then coordinate to the ligand. Recently, this methodology has been extended to the preparation of complexes featuring *N*-heterocyclic carbenes (NHCs) as ligands, offering a synthetic pathway to complexes featuring ligands that have base sensitive groups incorporated within them.<sup>14,98,99,112</sup> Whilst many of the benefits of electrosynthesis have been realised in these new synthetic strategies, there remains a bottleneck to widespread adoption. One reason for this impediment derives from a lack of simple, well defined and reproducible setups.<sup>123–126</sup>

There are numerous examples of homemade electrochemical reactors, incorporating both divided and non-divided cells.<sup>125–128</sup> Although this has allowed the development of efficient methodologies, reproducibility remains an issue, especially when transferring experimental procedures between laboratories.<sup>49</sup> Three-necked round bottom flasks

have been used in many laboratories, including the Willans group,<sup>99</sup> with the central neck connecting the flask to a Schlenk line and the outer two necks each having a suba-seal fitted (Figure 2.1). A wire passed through each suba-seal connects the electrodes to a power supply. Although this proved an effective set up, one of the key limitations was an inability to precisely adjust the distance between the electrodes and the depth of electrode in solution, these parameters typically have a significant effect on reaction outcome.<sup>129</sup> Consequently any results using this method are less reproducible because the resistance and current density varies between experiments.

More recently, several commercial reactors have been developed which provide a constant interelectrode distance,<sup>130</sup> however a common issue with these reactors is the inability to perform transformations under inert atmospheres or the flexibility to adapt them to different reaction set ups. Arguably the most common commercial reactor is the Electrasyn 2.0;<sup>130</sup> a batch reactor produced by IKA in collaboration with the Baran group. The reactor keeps the distance between electrodes constant, however the reactor cannot be connected to a Schlenk line (Figure 2.1).



**Figure 2.1:** Electrochemistry under inert conditions in a three necked flask connected to a Schlenk line (left) and the IKA ElectraSyn 2 (right).

Currently the electrosynthesis community has limited access to standardised, flexible and affordable electrochemical batch reactors.<sup>123</sup> Herein, the design and development of a simple, yet highly versatile batch reactor (the bottle reactor) is reported. This reactor has been used for the synthesis of air sensitive organometallic and inorganic complexes, as well as for the fast optimisation of an organic transformation. Cyclic voltammetry has also been performed in the reactor, showcasing the versatility of the set up. It is hoped that this reactor will increase the accessibility of electrochemistry by providing an inexpensive reactor.

### 2.1.2. Requirements for an electrochemical batch reactor

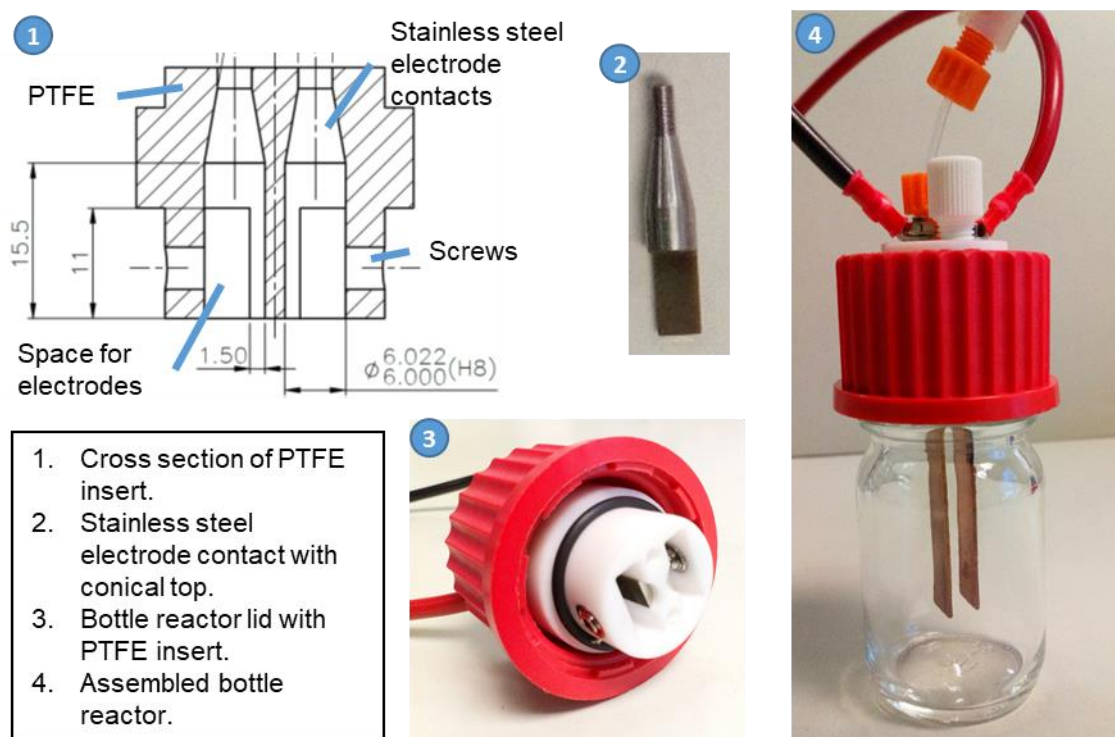
The ideal electrochemical batch reactor should fulfil several requirements:

- Fixed distance between electrodes to ensure reproducible resistance and current density in the reaction.
- Accommodate a broad range of electrode materials, thereby increasing the flexibility of the reactor and the range of reactions it can be used for.
- Be easily connected to a range of power supplies using readily available connectors to enable synthesis using a simple power supply or cyclic voltammetry with a potentiostat.
- The ability to attach to a Schlenk line so that it may be placed under vacuum and an inert atmosphere to enable air sensitive intermediates and products to be synthesised.
- Ports for adding and removing solutions, and with the ability to carry out *in situ* analysis.

### 2.1.3. The bottle reactor

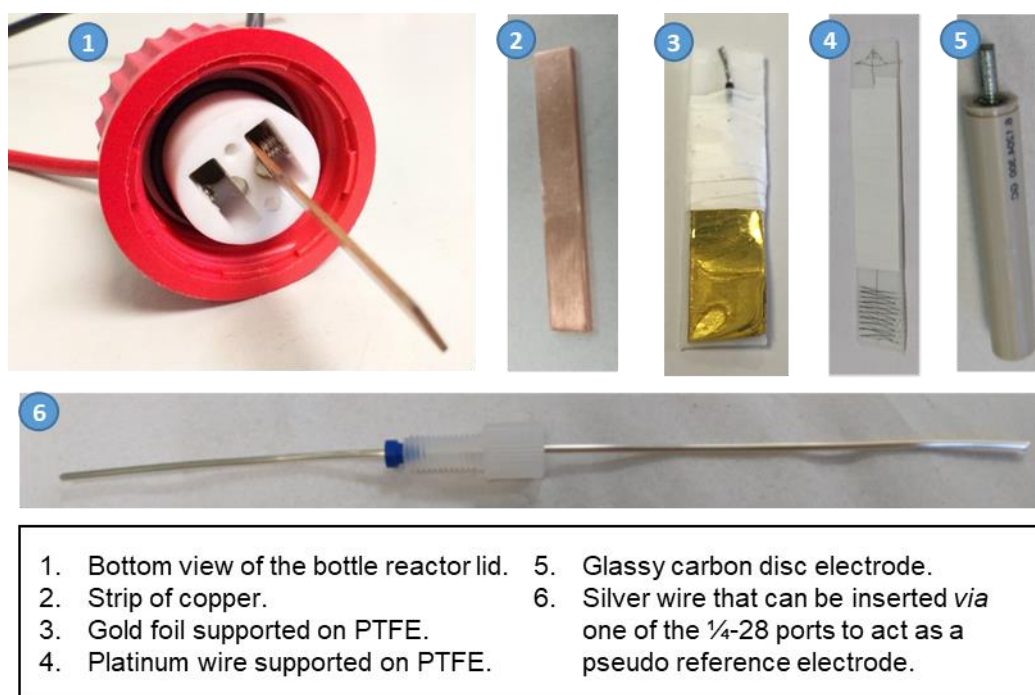
In collaboration with Professor Nikil Kapur (School of Mechanical Engineering), an electrochemical batch reactor was designed (Figure 2.2). The vessel is based upon commercially available vials with an adapted lid. The lid features a commercial cap with a hole cut in it and a polytetrafluoroethylene (PTFE) insert. PTFE was chosen because it is exceedingly resistant to chemicals and deforms easily when subject to compression,<sup>131,132</sup> enabling seals to be created without the use of o-rings. The PTFE insert has an extrusion which overlaps with the rim of the vial, such that when the cap is screwed into place a tight seal is created between the vial and the PTFE.

The PTFE insert has four holes machined into it; two have a ¼-28 thread added to them to make two ports allowing standard fittings to be screwed into the lid. This enables the reactor to be attached to a Schlenk line through one of the ports *via* a short piece of tubing with a Luer fitting on the other end. The other port can be fitted with a blank fitting which can be removed to allow the addition of solvents or the removal of samples. The solution can also be removed from the bottle reactor using a cannula made from tubing and a ¼-28 fitting. Alternatively, one of the ports can be used to insert a silver wire to act as a pseudo reference electrode and also allows the possibility of *in situ* analysis, such as IR or UV-vis, if a probe is inserted through one of the ports (Figure 2.3).



**Figure 2.2:** The design of the bottle reactor – a batch reactor for electrochemistry in an undivided cell.

The remaining two holes have a cone shape machined into them and complementary stainless steel electrode contacts were fashioned (Figure 2.2); when screwed into place the stainless steel is pulled up and into the PTFE. PTFE is a very soft plastic and is able to deform easily around the conical electrode contacts to create a good seal.<sup>131</sup> The top of the steel contacts are joined to cables that can be connected to a power supply. Grooves were made in the PTFE to allow electrodes to be placed in contact with the stainless steel contacts. A small grub screw in the wall of each groove can be tightened to hold the electrodes in place, thereby allowing electrodes up to 5 mm thick to be used, whilst maintaining a 4 mm interelectrode distance (Figure 2.3). This facilitates the use of a wide array of electrodes including strips of metal or carbon, as well as commercial electrodes. Foils or wires of expensive materials, such as gold or platinum, can be supported on strips of PTFE (Figure 2.3); allowing maximum use of the material whilst maintaining structural integrity and avoiding the use of plated electrodes which, depending on their design, can become unusable after scratching or chipping of the surface and are therefore unsuitable as sacrificial anodes. The first thread insert used to hold the grub screw worked initially, but after repeated use was found to twist out of the PTFE. This thread was subsequently replaced with a larger insert to improve the robustness of the reactor.



**Figure 2.3:** The bottle reactor lid, including a broad range of electrodes that can be accommodated.

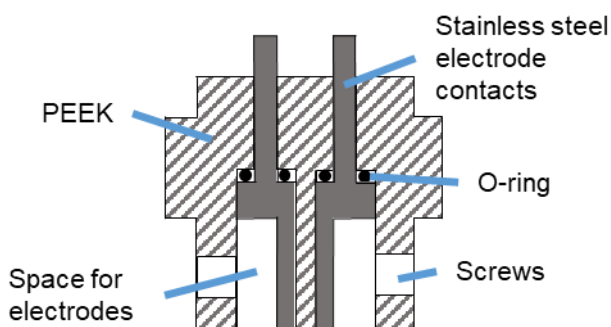
The ability to maintain a reproducible and constant interelectrode gap, whilst ensuring high flexibility of electrode materials, was of great importance during the design process. The distance between the electrodes remains constant to increase reproducibility of reactions, whilst allowing a broad range of electrode materials, with an assortment of shapes, thicknesses and lengths to be accommodated. Furthermore, the electrodes are able to connect to a range of commercially available power supply units using simple, readily available connectors to permit use of the reactor with a simple power supply unit or a potentiostat.

#### 2.1.4. A more robust design for commercialisation

One of the key drawbacks of the PTFE bottle reactor was the tendency for the thread insert holding the grub screws to twist out of the PTFE head piece. The initial thread insert was replaced with an insert that had a larger surface area. Although this was effective in extending the working lifespan of the reactor, the setup remained troublesome and required regular tweaking and maintenance. Asynt had expressed an interest in commercialising the bottle reactor and it was decided that a more robust reactor that demanded less maintenance would be needed for commercialisation.

It was anticipated that a harder plastic would reduce the incidence of threads twisting out of the insert. Polyether ether ketone (PEEK) is almost as chemically inert as PTFE and is much harder and therefore easier to machine.<sup>133</sup> However, the PTFE bottle reactor relied upon how easy it is to deform PTFE to create a good seal around the stainless steel contacts and the rim of the vial. PEEK requires much larger forces to deform and

consequently the PEEK insert was designed to use o-rings to provide the seal (Figure 2.4). The stainless steel contacts, and the holes which they are inserted into, were altered to have a flat shape as opposed to conical. This allows an o-ring to sit in-between the electrode contact and the headpiece to create a seal. It was anticipated that the o-rings were semi-consumables that needed to be replaced periodically. It was anticipated that the PEEK insert would be significantly more robust as it is more simple to replace an o-ring than a thread insert.

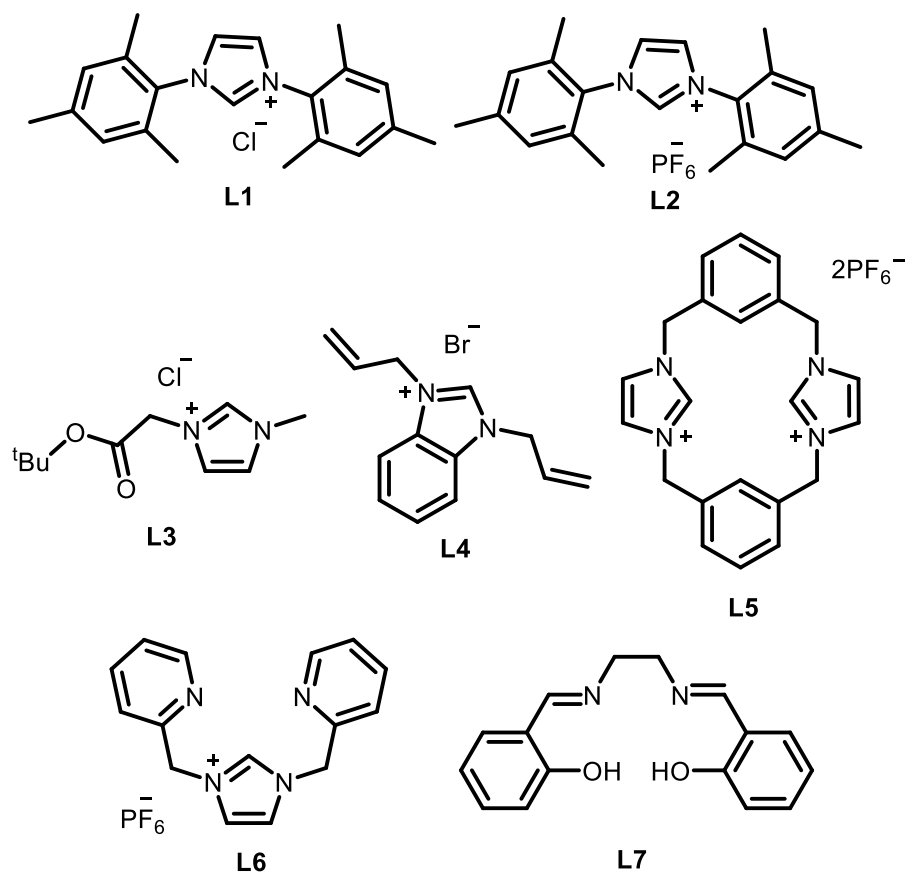


**Figure 2.4:** Cross section of the PEEK head piece which uses flat stainless steel electrode contacts and o-rings to create a seal.

## 2.2. Synthesis of ligand precursors

To test the PTFE bottle reactor, a range of metal complexes were synthesised from a range of ligand precursors with different functional groups (Figure 2.5). Metal complexes have been electrochemically synthesised previously from these ligand precursors and, as such, they were chosen to evaluate the efficacy of the bottle reactor and to allow a direct comparison to previously reported results.<sup>14,98,99,112,134</sup> Copper electrodes were to be used with **L1** to **L5**. **L1** and **L2** were chosen as 1,3-bis(2,4,6-trimethylphenyl)imidazol-2-ylidene (IMes) is a common ligand for metal-NHC complexes, with **L1** being expected to produce the mono-NHC copper(I) complex and **L2** the cationic bis-NHC copper(I) complex due to the non-coordinating nature of the hexafluorophosphate anion.<sup>99</sup> **L3** and **L4** feature base sensitive groups (ester and allyl respectively) and would be unsuitable as ligand precursors if traditional methods of metal-NHC synthesis, involving the use of strong base, were used.<sup>99,112</sup> These ligand precursors were chosen to highlight the advantages and complementary nature of the electrochemical methodology. The macrocyclic ligand precursor **L5** was selected as a more challenging ligand, whilst **L6** and **L7** were prepared for the use with iron electrodes. The use of **L7** to form iron-salen complexes has been reported before,<sup>98</sup> whilst it was expected that **L6** could be used to make a coordinatively saturated iron(II)-bis(NHC) complex.



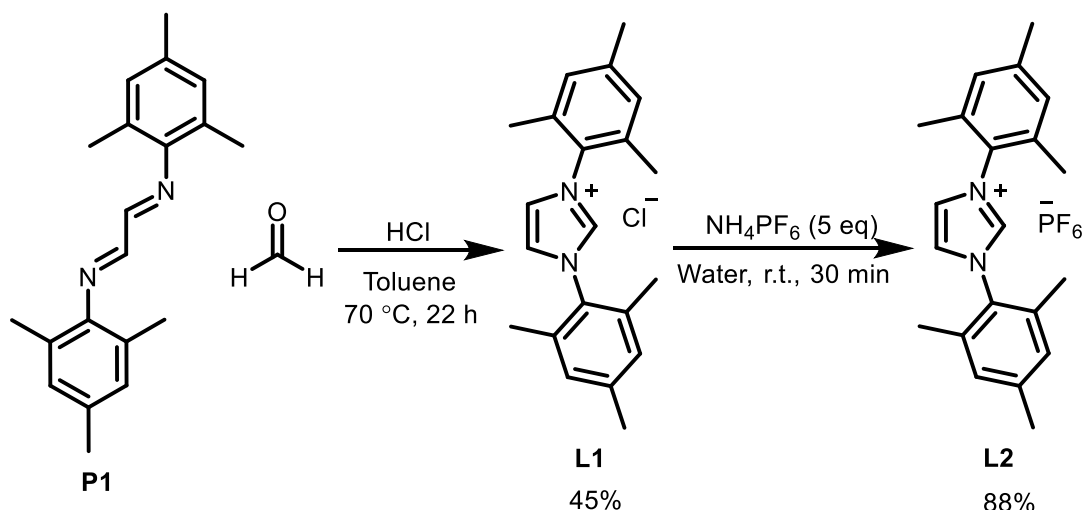


**Figure 2.5:** Ligand precursors to test the bottle reactor.

### 2.2.1. IMesHX ligand precursors (L1 and L2)

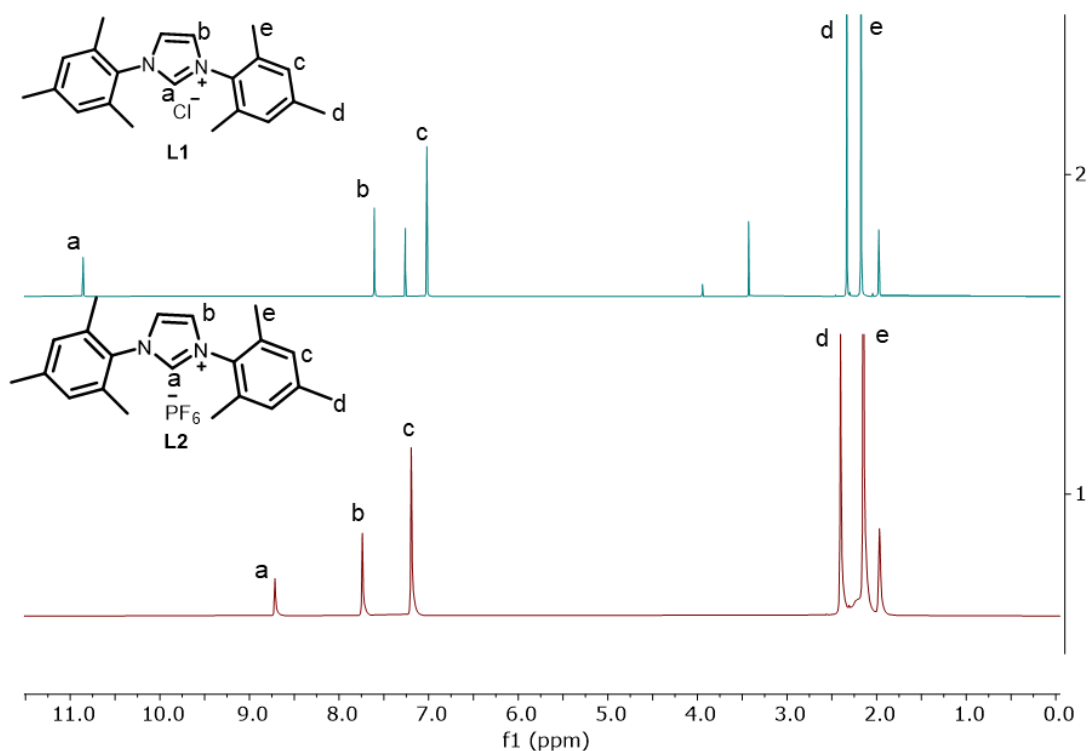
The diimine precursor (**P1**) was prepared using an adapted literature procedure, by reacting 2,4,6-trimethylaniline and glyoxal in the presence of an acid catalyst.<sup>112</sup> **P1** was then used to synthesise **L1** *via* a condensation reaction with paraformaldehyde in anhydrous toluene on a multi-gram scale. A portion of **L1** was used to produce **L2** through an anion exchange with  $\text{NH}_4\text{PF}_6$  (Scheme 2.1).<sup>112</sup>





**Scheme 2.1:** Synthesis of **L1** and **L2** via condensation and anion exchange, with yields.

All of the ligands were characterised using high resolution mass spectrometry (HRMS), proton nuclear magnetic resonance spectroscopy ( $^1\text{H}$  NMR) and proton decoupled carbon nuclear magnetic resonance spectroscopy ( $^{13}\text{C}\{^1\text{H}\}$  NMR). HRMS was used to confirm the molecular weight of the cationic fragment of the imidazolium salts, whilst the  $^1\text{H}$  and  $^{13}\text{C}\{^1\text{H}\}$  NMR spectra were compared to literature data.<sup>98,99,112</sup> NHC precursors feature a distinctive singlet between 8.5 and 11 ppm in their  $^1\text{H}$  NMR spectra, corresponding to the C2 proton. In instances where the imidazolium has a halide counter ion, the singlet can be found further downfield within this range due to a H-bonding interaction between the C2 proton and the halide.<sup>135</sup> By contrast, the C2 proton (proton 'a', Figure 2.6) in imidazoliums with non-coordinating anions is less de-shielded and is observed to be less downfield. For example, the C2 proton in **L1** is observed at 10.70 ppm, whilst in **L2** it is found at 8.70 ppm, providing a useful way to determine if an anion exchange reaction has been successful (Figure 2.6).



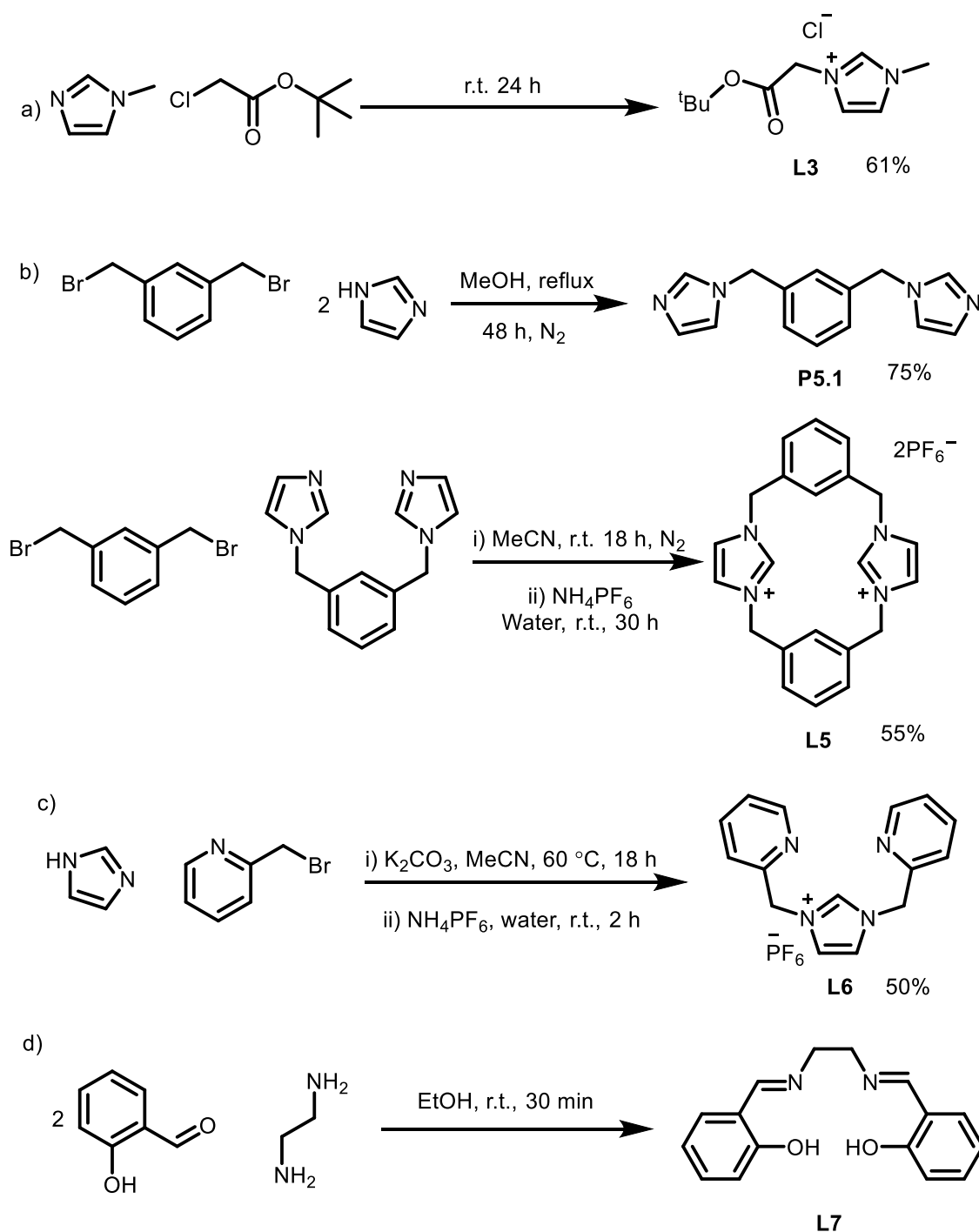
**Figure 2.6:**  $^1\text{H}$  NMR spectra of **L1** (blue trace,  $\text{CDCl}_3$ , 300 MHz) and **L2** (red trace,  $\text{CD}_3\text{CN}$ , 400 MHz) showing significant deshielding of the  $\text{NCHN}$  proton when the counter ion is a halide.

### 2.2.2. Other ligand precursors

**L3** was prepared by the reaction of *N*-methylimidazole with *tert*-butyl chloroacetate in a neat reaction (Scheme 2.2, a). Due to the extremely hygroscopic nature of **L3** it was recrystallised under anhydrous conditions and stored in the glove box. **L4** was prepared by Dr Benjamin Lake, a previous member of the Willans group.

**L5** was synthesised by initially heating 1,3-bis(bromomethyl)benzene to reflux with a large excess of imidazole. The resultant intermediate (**P5.1**) was added slowly to a solution of 1,3-bis(bromomethyl)benzene to produce the cyclophane with bromide anions (**P5.2**). An anion exchange delivered **L5** (Scheme 2.2, b).

**L6** was synthesised by heating imidazole with two equivalents of 2-bromomethylpyridine in the presence of potassium carbonate to give the imidazolium bromide salt that underwent an anion exchange to yield **L6** (Scheme 2.2, c). **L7** was prepared through the condensation of salicylaldehyde with ethylenediamine (Scheme 2.2, d).



**Scheme 2.2:** Synthesis of **L3**, **L5**, **L6** and **L7** with yields.

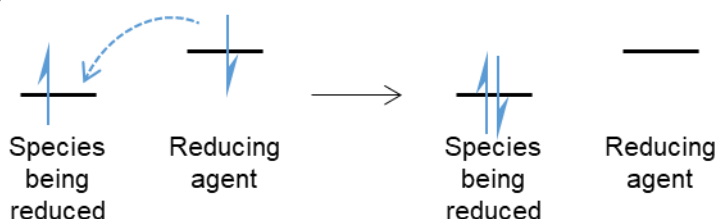
### 2.2.3. Cyclic voltammetry

Cyclic voltammetry is a common technique within inorganic chemistry that is used to examine the redox potentials of species.<sup>136</sup> When a species is reduced, an electron is transferred into its lowest unoccupied molecular orbital (LUMO). If done chemically the electron originates from the highest occupied molecular orbital (HOMO) of the reducing agent; whether the reaction occurs depends upon the energy difference between these two orbitals. The HOMO of the reducing agent must be higher than the LUMO of the

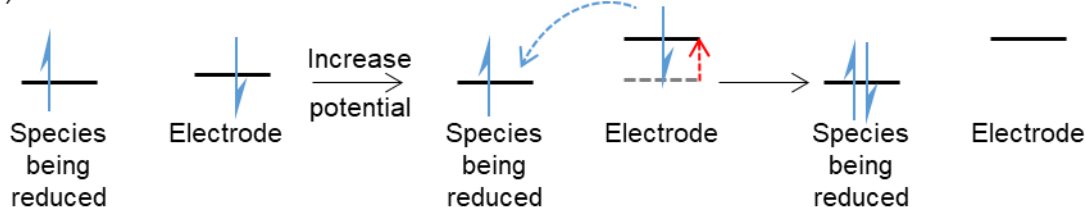
species being reduced for the reaction to be thermodynamically favourable and proceed (Figure 2.7, a).

An analogous process occurs when reductions are conducted electrochemically. An electron is transferred from the electrode material to the species being reduced. The electron from the electrode must have sufficient energy to be higher than the LUMO of the species being reduced and the energy of this electron is determined by the potential applied to the cell.<sup>137</sup> When the potential is sufficiently high, so that an electron from the electrode is higher in energy than the LUMO of the species being reduced, an electron is transferred to that species and consequently a current can be observed (Figure 2.7, b). This phenomenon can be used analytically to obtain information on the potential required to oxidise or reduce chemical species. It is from this that the term reduction potential is obtained, which is simply the potential which must be applied for a species to be reduced. The reduction potential can give mechanistic insights to chemical systems as well as helping to understand electrochemical systems.<sup>136</sup>

a) Chemical reduction



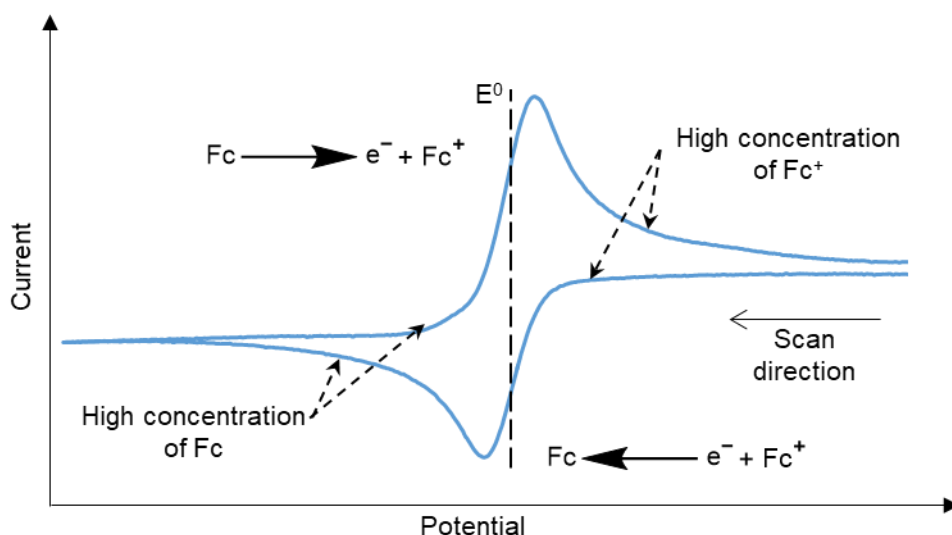
b) Electrochemical reduction



**Figure 2.7:** a) In a chemical reduction an electron is transferred from the HOMO of the reducing agent into the LUMO of the reductant. b) For electrochemical reductions the energy of the electrons in the electrode can be increased by increasing the applied potential, which then allows the electron to be transferred into the LUMO of the reductant.

The reduction potential of a species can be measured using cyclic voltammetry. When conducting these experiments three electrodes are used; typically a glassy carbon working electrode, a platinum counter electrode and a reference electrode.<sup>137</sup> An argon saturated electrolyte solution, in which the analyte is dissolved, is subject to repeated cycles between two potentials using a triangular waveform, for example from -2.5 V to +2.5 V and back to -2.5V. In a reversible process, such as the reduction of  $\text{Fc}^+$  to  $\text{Fc}$  and the subsequent oxidation of  $\text{Fc}$  to  $\text{Fc}^+$ , a 'duck' shaped voltammogram is obtained with the redox potential, or  $E^0$ , being the potential half way between the two peaks (Figure 2.8).<sup>138</sup>

The 'duck' shape originates from a combination of the Nernst equation and mass transfer. It is important to note that the solution is not stirred. During a cyclic voltammetry experiment the potential is decreased and an increase in the current is observed once the potential is sufficient to transfer an electron to the oxidised form of the analyte, for example reducing  $\text{Fc}^+$  to  $\text{Fc}$ . A more negative potential increases the rate of electron transfer and therefore the current. Simultaneously the concentration of  $\text{Fc}^+$  near the surface of the electrode decreases as the  $\text{Fc}^+$  is reduced to  $\text{Fc}$ , creating a diffusion layer of  $\text{Fc}$  near the electrode surface, thereby limiting the amount of  $\text{Fc}^+$  which can diffuse towards the electrode and leading to the current dropping.<sup>139</sup> This diffusion limited current gives a CV its 'duck' shape. The opposite is true when the potential is reversed, with the initial concentration of  $\text{Fc}$  near the electrode being high and then decreasing as it is oxidised back to  $\text{Fc}^+$ , leading to a symmetrical curve in the reverse direction (Figure 2.8).<sup>136,138</sup>

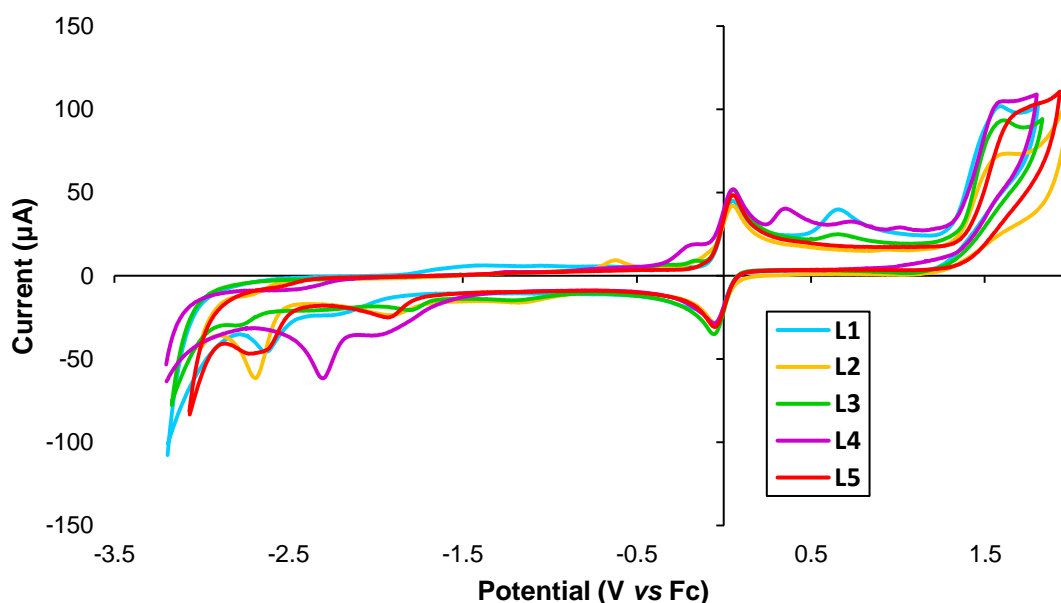


**Figure 2.8:** Voltammograms for analytes that can be reduced reversibly feature two symmetrical peaks with the reduction potential ( $E^0$ ) being halfway between the two peaks.

Cyclic voltammetry using the bottle reactor was conducted to examine the reduction potentials of the ligand precursors **L1-5**. Each ligand precursor was dissolved in an electrolyte solution and ferrocene was used as an internal standard. A silver wire was inserted into the bottle reactor through one of the ports to act as a pseudo-reference electrode so that the applied potential can be accurately measured, whilst the other port was used to bubble argon through the solution.

All of the ligand precursors featured an irreversible reduction between -2.2 and -2.9 V versus ferrocene (Graph 2.1 and Table 2.1), corresponding to the reduction of the ligand precursor. The reduction potentials for the imidazolium salts were all between -2.62 V and -2.84 V. By contrast the less electron rich benzimidazolium, **L4**, had a reduction

potential at -2.29 V. This can be attributed to the benzene ring on the backbone of **L4**, which acts to withdraw electron density from the imidazole ring.<sup>140</sup> This would be expected to make **L4** easier to reduce at the C2 position because it would be able to accept an electron more readily. Other notable features in the voltammograms include peaks at +0.66 V for **L1** and **L3**, which correspond to the oxidation of Cl<sup>-</sup>.<sup>136</sup> **L4** features several peaks between -0.18 V and 1.01 V which are likely to be associated with the oxidation of Br<sup>-</sup>,<sup>136</sup> as well as the allyl groups on the *N*-substituents.<sup>141</sup> By contrast **L2** and **L5** have no peaks in this region.



**Graph 2.1:** Overlaid cyclic voltammograms of ligand precursors **L1-5** (1 mM). A silver wire was used as pseudo-reference electrode with ferrocene (1 mM) as an internal standard. Experiments were performed with a scan rate of 300 mV s<sup>-1</sup> in acetonitrile with Bu<sub>4</sub>NPF<sub>6</sub> (0.1 M) as a supporting electrolyte.

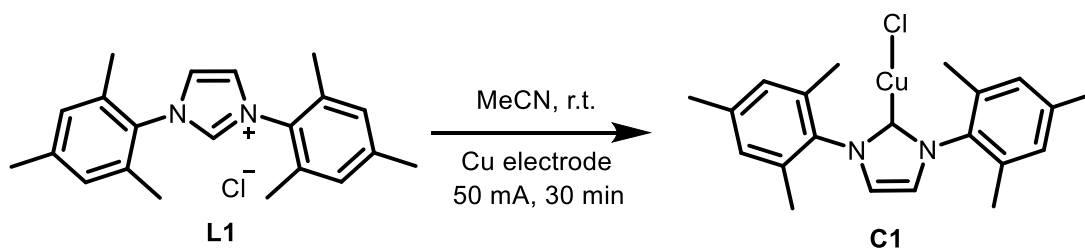
Ligand precursor	Reduction potential (V vs SCE)
<b>L1</b>	-2.62
<b>L2</b>	-2.84
<b>L3</b>	-2.74
<b>L4</b>	-2.29
<b>L5</b>	-2.69

**Table 2.1:** Reduction potentials of ligand precursors.

## 2.3. Electrochemical synthesis of organometallic complexes

### 2.3.1. Electrochemical procedure in the bottle reactor

The bottle reactor lid was assembled with the appropriate electrodes and 1 mmol of the ligand precursor was weighed into the reactor which was then placed under argon on a Schlenk line. Anhydrous acetonitrile (15 mL) was added to the reactor and stirred until all of the ligand precursor had dissolved, whereupon a power supply was used to apply a constant current for 1.2 electron equivalents (Scheme 2.3). Galvanostatic conditions were used so that the amount of electrons transferred into the reaction could be controlled, allowing comparison between the different ligands and previous studies.



**Scheme 2.3:** Electrochemical synthesis of Cu(IMes)Cl.

Electron equivalents, F, refers to the number of electrons used in a reaction in an analogous way to the stoichiometry of other reagents in reactions. For example, the reduction of an imidazolium to a NHC requires one electron. Therefore, for 1 mmol of starting material 1 mmol of electrons will be needed, this is 1 F. If 2 mmol of electrons were provided then that would be 2 F mol<sup>-1</sup>. The amount of electron equivalents can be calculated from the current and the time elapsed using Equation 2.1, which is derived from Faraday's law.

$$Q = nFN$$

$$t = \frac{Q}{I}$$

$$\therefore t = \frac{nFN}{I}$$

**Equation 2.1:** Equations relating current and time with electron equivalents. Q = total charge (C), n = number of electrons transferred per molecule of starting material, F = Faraday's constant (C mol<sup>-1</sup>), N = amount of starting material (mol), I = current (A), t = time (s).

After 1.2 F mol<sup>-1</sup> the reaction mixture was filtered through Celite. For the majority of the complexes this was done by transferring the reaction mixture *via* cannula onto a bed of Celite that had been placed under an atmosphere of argon and filtering it into a Schlenk tube. For the more air sensitive complexes, **Cu3** and **Fe6** for example, the reaction

mixture was transferred to an ampoule and then filtered through Celite pipettes in the glovebox.

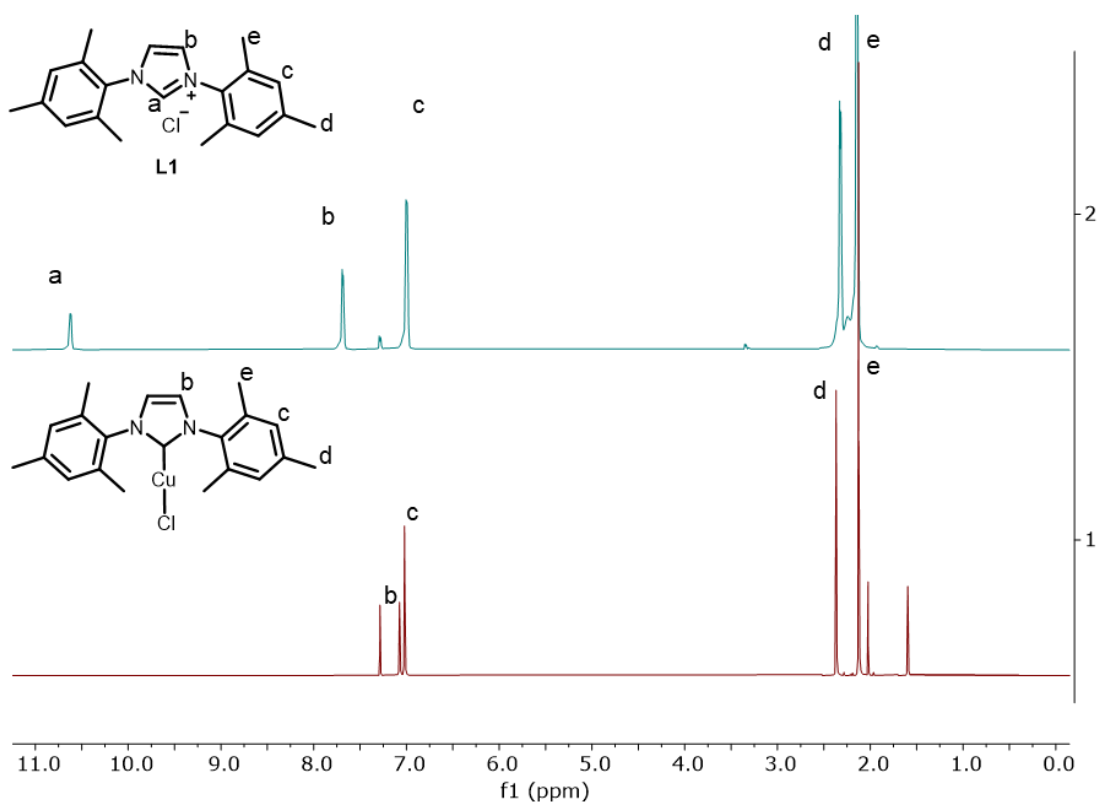
Once filtered, a portion of the eluent (~1 mL) was transferred to a small ampoule and the solvent was removed under vacuum. The solid residue was then dissolved in an appropriate deuterated solvent for analysis by  $^1\text{H}$  NMR spectroscopy to calculate the conversion based upon the integrals of the ligand precursor and the complex, as obtained from the literature.<sup>98,99,112,134,142</sup> Working up reactions that have highly air sensitive products typically leads to a significantly lower yield than might otherwise be expected. This is due to the extra manipulations required to work up and purify the product, involving techniques such as cannula filtration, which usually lead to the loss of material. The aim of this study was to assess the ability of the bottle reactor to perform numerous and repeated electrochemical reactions under inert conditions. Consequently, the conversion of starting material to product was chosen to be analysed, to separate the experimental set up of the bottle reactor from the work up. In some instances, the remaining reaction mixture was recrystallised under anhydrous conditions to obtain an isolated yield, for example novel complexes such as **Au3**.

### 2.3.2. Synthesis of copper-NHC complexes

Initial testing of the bottle reactor was performed by the preparation of a range of copper-NHC complexes which require the use of inert atmospheres and anhydrous solvents. The electrochemical synthesis of metal-NHC complexes has been reported previously.<sup>14,99,112</sup> This process requires the oxidation of a sacrificial anode, which releases metal ions into solution and the cathodic reduction of imidazolium salts to produce metal-NHC complexes *via* highly reactive carbene intermediates. These carbenes are extremely sensitive to the presence of oxygen and water, which results in the formation of imidazolone side products.<sup>14</sup> Consequently, keeping the reaction under inert conditions is of paramount importance.

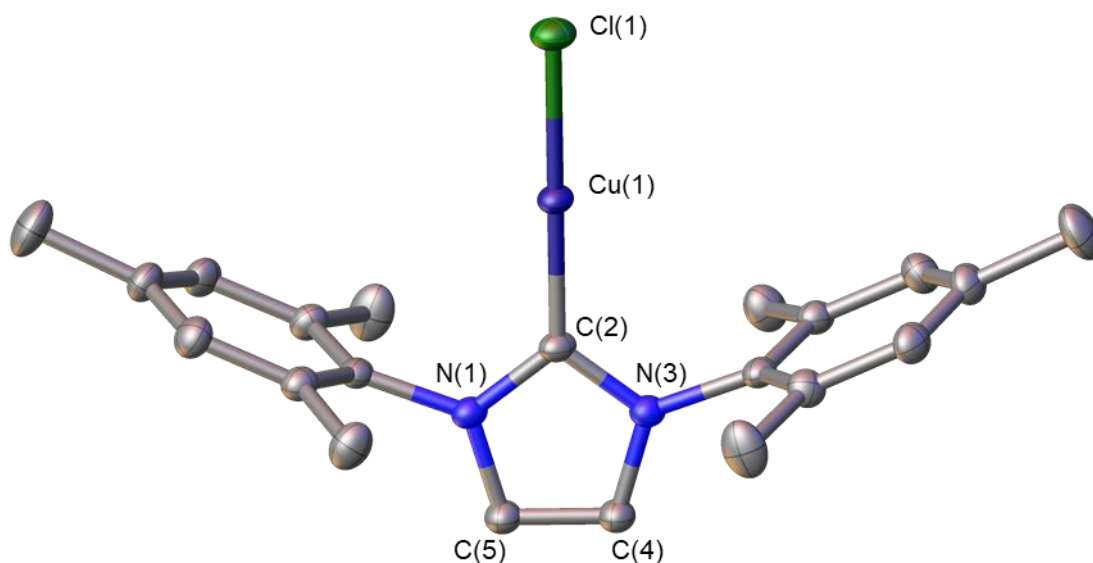
The synthesis of the well documented **Cu1** was chosen to begin with as it is a complex that can be easily synthesised from ligand precursor **L1**.<sup>99</sup> A constant current of 50 mA was applied to a solution of ligand precursor **L1** (0.05 M) for 1.2 electron equivalents and **Cu1** was isolated in 95% yield after recrystallisation. **Cu1** was characterised using  $^1\text{H}$  and  $^{13}\text{C}\{^1\text{H}\}$  NMR spectroscopy, HRMS and single crystal X-ray crystallography. The masses of the expected adducts were observed in the HRMS. The NMR spectra corresponded to literature values and showed the loss of the characteristic C2 proton from the ligand precursor at 10.70 ppm, as would be expected (Figure 2.9).<sup>99</sup> The protons on the imidazolium backbone are also observed to be less de-shielded when complexed, whilst the signals for protons on the mesityl rings remained largely unchanged (Figure 2.9).





**Figure 2.9:**  $^1\text{H}$  NMR spectrum of **Cu1**, showing the loss of proton a. The spectrum for **L1** was taken in  $\text{CDCl}_3$  at 300 MHz and **C2** was taken in  $\text{CDCl}_3$  at 400 MHz.

Single crystals of **Cu1** were grown by vapour diffusion of diethyl ether into a concentrated solution of **Cu1** in acetonitrile (Figure 2.10). The unit cell, bond lengths and angles were consistent with previously reported structures (Table 2.2).<sup>143</sup> The copper complex exhibits a linear geometry with the plane of the mesityl rings perpendicular to that of the imidazolium.



**Figure 2.10:** Molecular structure of **Cu1**. Ellipsoids are shown at 50% probability level and hydrogen atoms are omitted for clarity.

Atoms	Bond lengths (Å) and angles (deg)
Cu(1)-Cl(1)	2.0981(17)
Cu(1)-C(2)	1.873(8)
Cl(1)-Cu(1)-C(2)	180.0
N(1)-C(2)	1.354(6)
C(2)-N(3)	1.354(6)
N(1)-C(2)-N(3)	104.4(7)

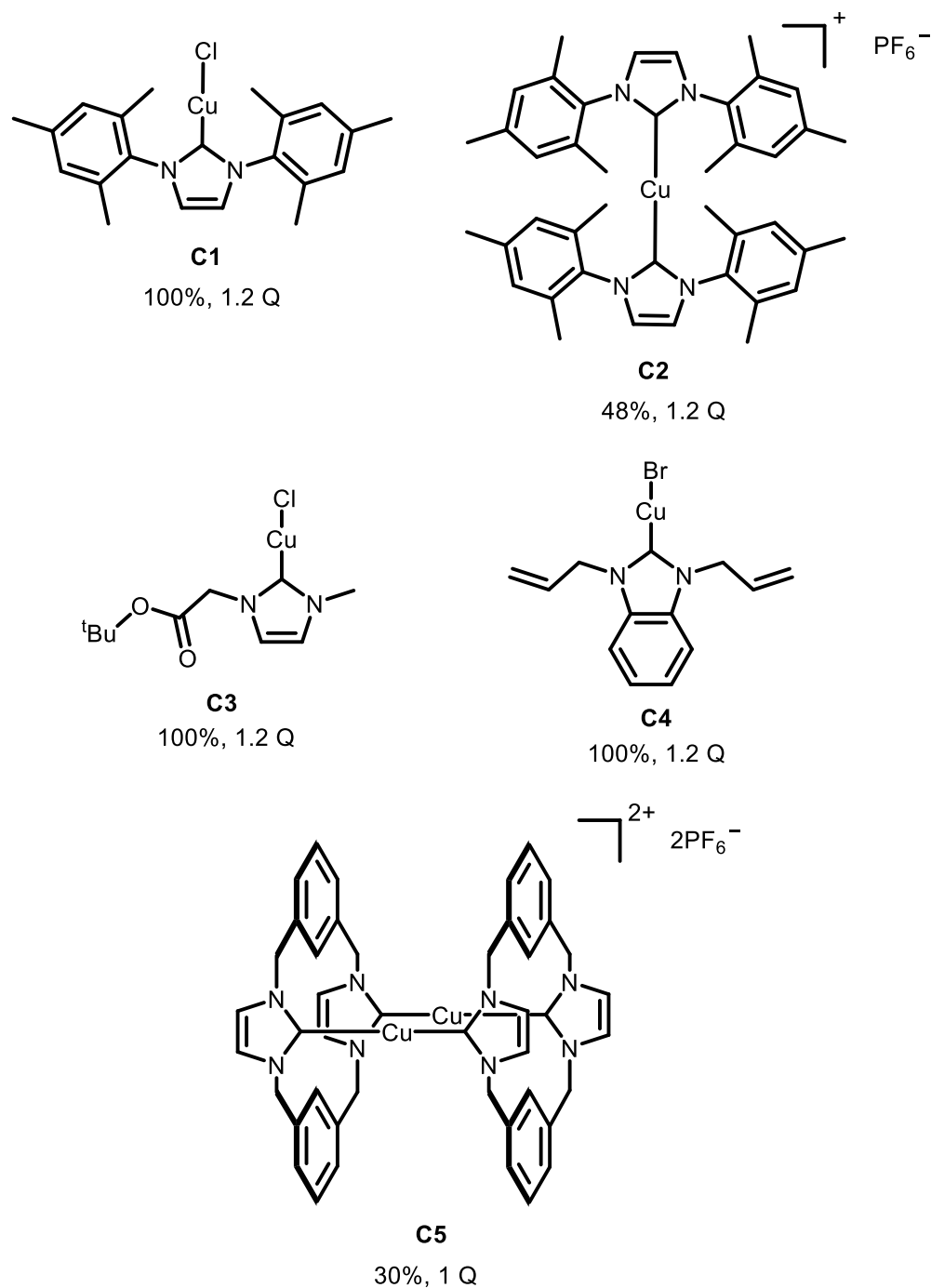
**Table 2.2:** Selected bond lengths and angles for **Cu1**.

A range of 5 copper-NHC complexes were prepared by applying a constant current to a solution of the ligand precursor (1 mmol) in anhydrous acetonitrile for 1.2 electron equivalents, with the ligand precursor acting as both the starting material and the electrolyte (Figure 2.11). Consequently, as the concentration of the imidazolium decreases the resistance of the cell increases, resulting in an increase in the potential. Typically the potential at the start of a reaction is approximately 5 V and this increases to 20-25 V as the reaction proceeds and the imidazolium is consumed.

Complete conversion of **L1** to the neutral mono-NHC complex **Cu1** was obtained. **L2** features the same imidazolium cation as **L1**, but has a non-coordinating  $\text{PF}_6^-$  anion which led to a 60% conversion to **Cu2**, the expected cationic bis-NHC complex.<sup>99</sup> The non-coordinating nature of the anion results in a second NHC ligand coordinating to the Cu(I) centre. The lower conversion of ligand precursors with  $\text{PF}_6^-$  anions to complexes compared to halide anions is consistent with previously reported results which have found that the electrochemical synthesis of cationic, (bis)NHC-copper(I) complexes typically require higher electron equivalents to reach full conversion.<sup>99,112</sup>

When the precursor was replaced with **L3** or **L4** complete conversion was observed after 1.2 electron equivalents. **L3** and **L4** feature base-sensitive ester and allyl groups respectively and this highlights the complementary nature of the electrochemical approach to traditional chemical methods using strong bases. **Cu3** and **Cu4** would be impossible to synthesise using strong bases.<sup>99</sup> When cyclophane derived bis-imidazolium salt **L5** was subject to electrolysis for 1.2 electron equivalents an 85% conversion to the dicationic, dinuclear complex **Cu5** was observed, as expected from previous reports.<sup>99</sup> Due to the poor solubility of **L5**, the synthesis of **Cu5** was conducted

on a 0.5 mmol scale and supporting electrolyte was required to compensate for the poor conductivity of the solution.

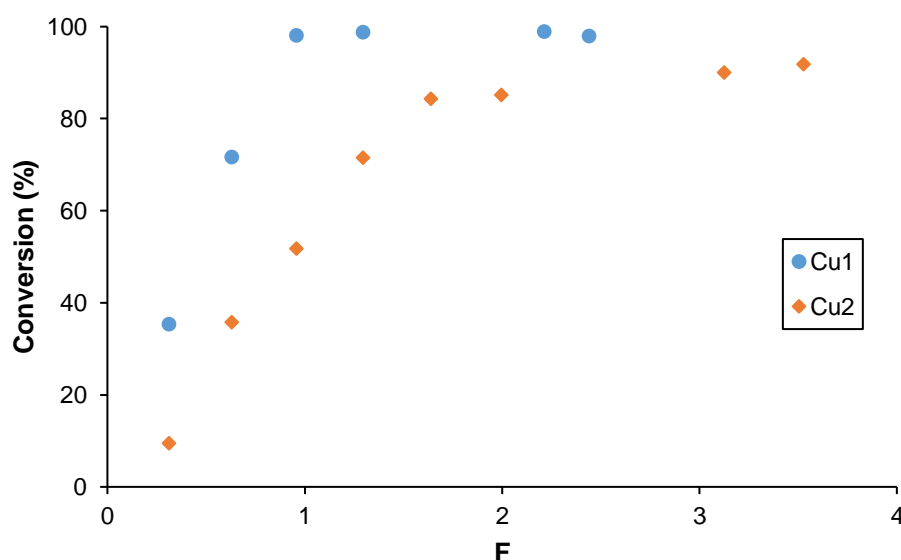


**Figure 2.11:** Copper complexes that have been synthesised in the bottle reactor with the conversions obtained for them as determined by  $^1\text{H}$  NMR spectroscopy. <sup>a</sup>Isolated yield. <sup>b</sup>Electrolyte ( $n\text{Bu}_4\text{NPF}_6$ , 0.5 equiv) added to solution.

Time course experiments were conducted to investigate the different rates of formation of mono- and bis-NHC complexes from **L1** and **L2** (Graph 2.2). These ligands were chosen as the complexes which they produce are relatively air stable, remaining intact in solution for several hours, thereby greatly simplifying the process and increasing the

number of time points which could be taken. The ligand precursors were dissolved in acetonitrile and a constant current of 50 mA was applied. Aliquots were removed at regular intervals through one of the ports and analysed using  $^1\text{H}$  NMR spectroscopy, whilst the other port remained connected to the Schlenk line, providing a positive pressure of argon. None of the samples showed any evidence of imidazolone side products, demonstrating that samples can be taken from reaction mixtures, whilst maintaining an inert atmosphere.

The formation of **Cu1** is fast, with full conversion being reached after 1 F. Interestingly, almost immediately after 1 F had elapsed a green precipitate started to form, suggesting that the additional electrons were forming some form of copper(II) species. Formation of **Cu2** was significantly slower, with a conversion of 85% after 1.6 F which rose only slightly more, to 92%, after 3.5 electron equivalents. Slower formation of **Cu2** could be attributed to either mass transfer limitations because two carbenes must come into contact with a copper ion.<sup>99</sup>



**Graph 2.2:** Time course experiments for the formation of **Cu1** and **Cu2**.

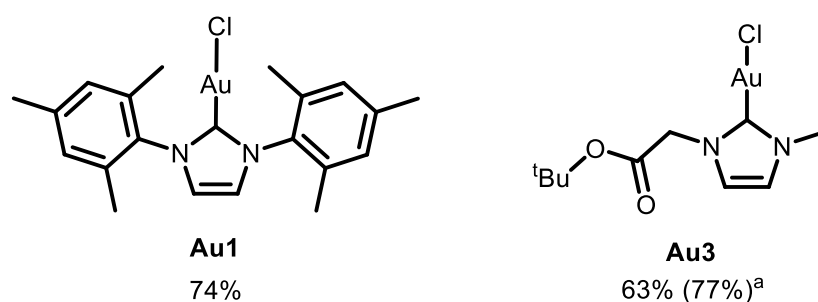
### 2.3.3. Synthesis of gold-NHCs

The electrochemical synthesis of metal-NHC complexes can be translated to other metals with relative ease because the bottle reactor provides large flexibility with regards to the electrodes that can be used with it. **L1** and **L3** were tested using a gold anode and stainless steel cathode to produce **Au1** and **Au3** (Figure 2.12) by Madeleine Woodward. Commercial 'gold' electrodes are often stainless steel electrodes with gold plated onto them. This is perfectly adequate for synthetic organic chemistry providing the gold plating is not chipped or damaged, where the choice of electrodes is generally based upon their reactivity and the over potential required. However, plated electrodes are unsuitable for

electrochemical methodologies where the anode is sacrificial. Loss of the gold plating during the reaction could expose the stainless steel underneath and consequently lead to the synthesis of a range of unintended complexes. Consequently, high purity gold foil was utilised and supported on strips of PTFE, with a wire running from the foil up to the top of the strip to form a contact with the steel electrode contacts.

When **L1** was subjected to 1.2 electron equivalents using a gold anode and stainless steel cathode, a conversion of 74% to the expected mono-NHC product was observed. Interestingly, a significant amount (10%) of bis-NHC complex was produced in this reaction, contrasting with the analogous reaction using copper electrodes. Gold(I)-NHC complexes are often isostructural with copper(I)-NHC complexes,<sup>134</sup> however in this instance a subtle blend of steric and electronic affects might enable the formation of bis-NHC complexes. The larger size of the gold cation could produce less steric hindrance. In addition, gold(I) is softer than copper(I) and therefore might be expected to bond less strongly to hard chloride ligands which, combined with a reduction in steric hindrance, could go some way to explaining why the formation of **Au1** is less selective than its copper counterpart.

Conversely when **L3** was electrolysed with gold and stainless steel electrodes no bis-NHC product was observed, only the neutral mono-NHC complex. **Au3** is isostructural to **Cu3**, although conversion of **L3** to the gold complex was significantly lower (63%) than to the analogous copper complex (>99%). As **Au3** is a novel complex it was fully isolated after 2 electron equivalents and characterised using HRMS, <sup>1</sup>H and <sup>13</sup>C{<sup>1</sup>H} NMR spectroscopy.



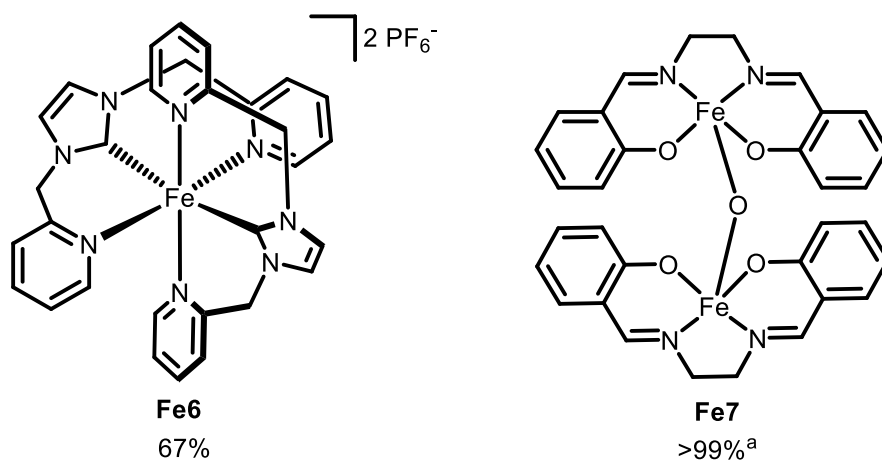
**Figure 2.12:** Gold complexes that have been synthesised in the bottle reactor with the conversions obtained after 1.2 F mol<sup>-1</sup>. <sup>a</sup>Isolated yield after 2.0 F mol<sup>-1</sup>.

### 2.3.4. Synthesis of iron complexes

The current state of the art for the synthesis of iron(II)-NHC complexes utilises the [Fe{N(SiMe<sub>3</sub>)<sub>2</sub>}]<sub>2</sub> precursor, however this reagent is exceedingly air sensitive, challenging to prepare and often results in iron(III) impurities being present in the product.<sup>10,37</sup> Electrochemistry offers a promising alternative approach towards this class of

organometallic complexes. Iron(II)-NHC complexes are often extremely air sensitive, consequently ligand precursor **L6** was chosen as it yields **Fe6** (Figure 2.13); a coordinatively saturated octahedral complex which is slightly less sensitive than other iron(II)-(bis)NHC complexes and can be analysed using  $^1\text{H}$  NMR spectroscopy. A constant current was applied to an acetonitrile solution containing **L6** (0.05 M) for 1.2 electron equivalents using iron foil electrodes to provide **Fe6** with 67% conversion.

A salen ligand, **L7**, was used in conjunction with iron electrodes to showcase the versatility of the reactor. Initially, commercial stainless steel electrodes were used, however this led to the observation of chromium impurities *via* HRMS. The reduction potential of  $\text{Cr}^{3+}$  to  $\text{Cr}_{(\text{s})}$  is -0.74 V, compared -0.44 V for the reduction potential of  $\text{Fe}^{2+}$  to  $\text{Fe}_{(\text{s})}$ .<sup>136</sup> Consequently the chromium in the stainless steel electrode is oxidised to  $\text{Cr}^{3+}$  at the same time as the oxidation of the iron in the electrode. This highlights the importance of electrode selection, particularly sacrificial electrodes where the composition of the electrode must be carefully considered, and demonstrates the benefits of having a reactor which can accommodate a wide range of electrodes. For the subsequent synthesis of **Fe7**, iron foil electrodes were used to apply a constant current to **L7** for 2.4 electron equivalents (**L7** must be reduced twice) in air to form the iron(III)-salen complex **Fe7** with a yield of 99% (Figure 2.13).



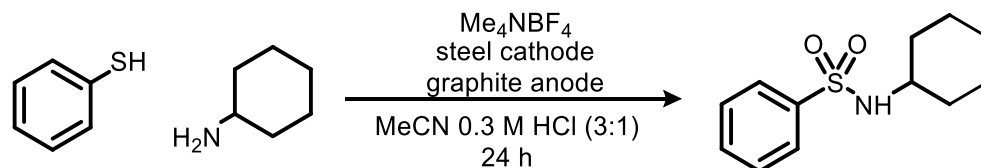
**Figure 2.13:** Iron complexes that have been synthesised in the bottle reactor with the conversions obtained for them. <sup>a</sup>Isolated yield after 2.4 electron equivalents.

## 2.4. Electrochemical synthesis of organic molecules

### 2.4.1. Sulphonamide synthesis

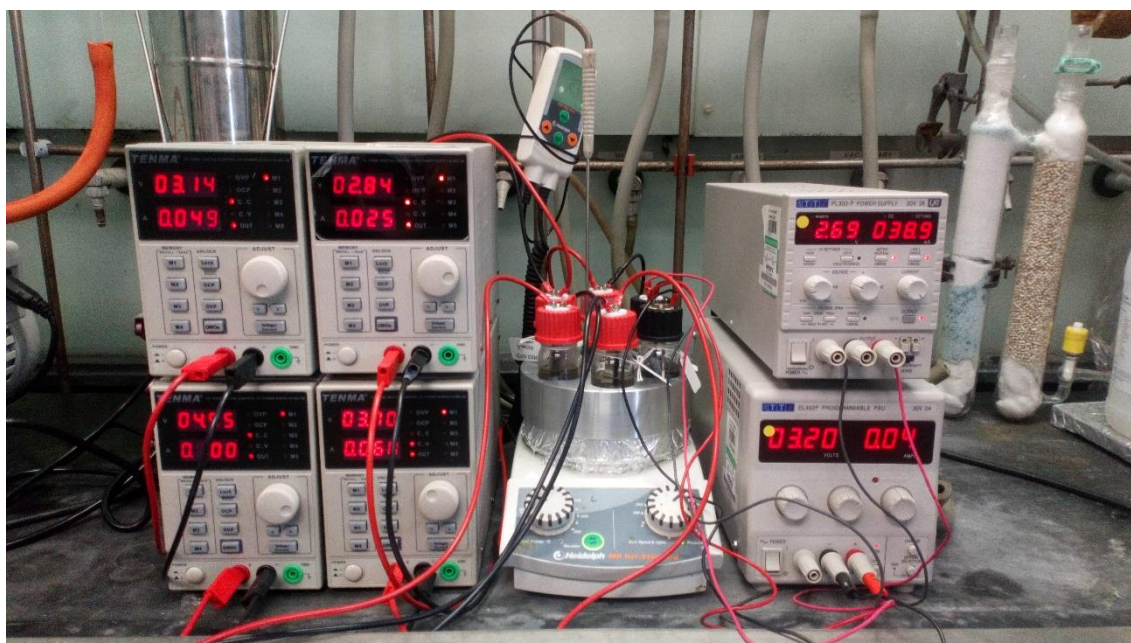
In order to demonstrate the broad applicability of the bottle reactor to a range of transformations, two organic reactions were reproduced. The first was the synthesis of sulphonamides which involves the oxidative coupling of amines and thiols with hydrogen gas being the only by-product (Scheme 2.4). This reaction was developed by the Noël

group and, whilst the majority of their work was conducted in flow, they did a number of reactions in batch.<sup>128</sup> The Noël group used a potential of 3.7 V and achieved a yield of 55%, however no product was observed *via* <sup>1</sup>H NMR spectroscopy when attempting to repeat the reaction in the bottle reactor under the same conditions. This discrepancy is not entirely unsurprising given that the Noël set up had a larger interelectrode gap of 7 mm compared to the bottle reactor of 4 mm.<sup>128</sup> Consequently the smaller interelectrode gap of the bottle reactor and the resulting lower resistance would be expected to significantly alter the reaction conditions and outcome.



**Scheme 2.4:** Electrochemical coupling of amines and thiols to produce sulphonamides.

A parallel plate made of aluminium was used to quickly optimise the reaction, performing six reactions simultaneously (Figure 2.14). Potentiostatic and galvanostatic conditions were tested with reactions performed in duplicate, demonstrating the reproducibility of the bottle reactor (Table 2.3). It was found that decreasing the potential to 3.2 V increased the yield to 51% and a further increase to 58% was observed when using a constant current of 20 mA, a yield which is comparable to that obtained by Noël.<sup>128</sup> A lower current of 10 mA was applied for twice the amount of time to provide the same number of electron equivalents, although this resulted in a lower yield. The successful optimisation of this synthetic organic electrochemical reaction demonstrates the bottle reactor's versatility and highlights the requirement of having an experimental set-up that is well defined to enhance inter-laboratory reproducibility. Had Noël not mentioned the interelectrode gap that they used the re-optimisation of this reaction would likely have taken significantly longer.



**Figure 2.14:** Six bottle reactors performing reactions in parallel.

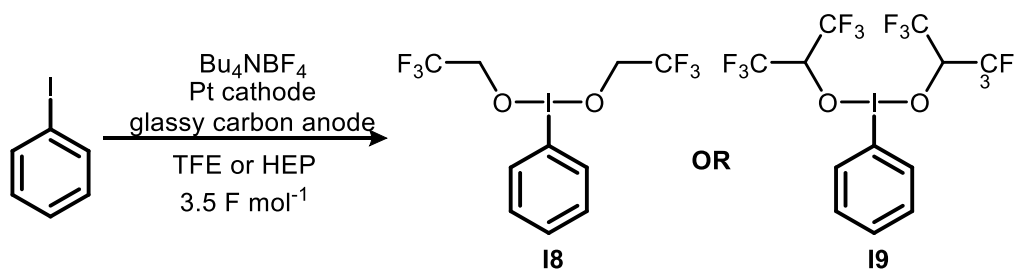
Potential or current	Yield 1 (%)	Yield 2 (%)	Average (%)
3.7 V	<2	-	-
3.4 V	41	37	39
3.2 V	48	54	51
20 mA	56	60	58
10 mA	40	-	-

**Table 2.3:** Yields for the sulphonamide reaction when using different constant potentials and currents.

### 2.4.2. Hypervalent iodine reactions

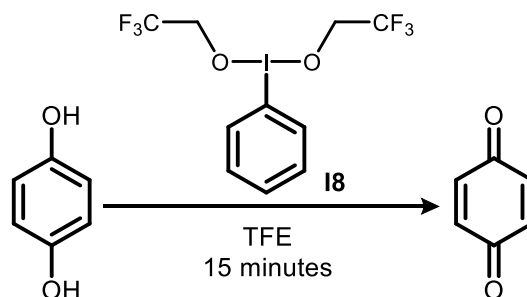
There is considerable interest in hypervalent iodine as mild and selective oxidising agents in organic chemistry.<sup>144–147</sup> Historically, the synthetic route to hypervalent iodine species has been through stoichiometric chemical oxidants, such as hydrogen peroxide.<sup>147</sup> More recently there have been several studies looking at the use of electrochemistry to produce hypervalent iodine species.<sup>148,149</sup> The Wirth group developed a procedure for the synthesis of hypervalent iodine species in flow from the anodic oxidation of iodobenzene, which is then stabilised by fluorinated ligands (Scheme 2.5).<sup>115</sup>





**Scheme 2.5:** Electrochemical synthesis of hypervalent iodine species, stabilised by fluorinated ligands. **19** was made in an analogous manner, using hexafluoroisopropanol.

This reaction was attempted in batch in the bottle reactor using a platinum cathode and glassy carbon anode to electrolyse a solution of iodobenzene in either trifluoroethanol (TFE) or hexafluoroisopropanol (HFIP) using  $n\text{Bu}_4\text{NBF}_4$  as supporting electrolyte. Hypervalent iodine species such as **18** or **19** are only stable in solution and consequently yields were obtained *via*  $^1\text{H}$  NMR spectroscopy, using nitrobenzene as an internal standard which was added after electrolysis to avoid the oxidation of nitrobenzene during electrolysis. When using HFIP a yield of 21% was obtained, by contrast TFE gave a significantly higher yield of 55%. The yield of **18** was further investigated *via* a subsequent oxidation of hydroquinone to benzoquinone mediated by **18** because both of these species are stable (Scheme 2.6). After **18** had been synthesised electrochemically the current was removed and hydroquinone was added to the solution. This yielded benzoquinone with a conversion of 75% and a yield of 20% (using nitrobenzene as an internal standard), a somewhat sibiylne result. It is not clear where this discrepancy originated. As such, the optimisation of this transformation was not pursued further.



**Scheme 2.6:** The oxidation of hydroquinone was used to as an indirect method to analyse the outcome of the electrolysis.

## 2.5. Conclusions and future work

A new flexible and standardised electrochemical batch reactor enabling both organic and inorganic transformations and analytical electrochemistry has been designed, developed and tested. This has enabled the synthesis of an assortment of organometallic species, some of which are exceedingly air sensitive. In addition, the batch reactor has been used

to perform organic reactions in parallel, allowing the quick optimisation of a literature procedure. This highlighted the importance of well-defined systems, although it is unnecessary for all reactions to use standardised equipment it is very helpful (if not essential) for reactors to be well defined and described to enhance reproducibility. Cyclic voltammetry can also be performed in the reactor. The design of this reactor is inexpensive and versatile, enabling its reproduction by synthetic chemists.

The extensive use and rigorous testing of the bottle reactor has highlighted a key limitation of the design, namely the robustness of the thread insert for the screws which hold the electrodes. As a consequence, the PTFE insert has been redesigned to be made from a harder PEEK, which should prevent the thread inserts twisting out of place. The new design will need to be tested thoroughly before it is commercialised by Asynt. It is anticipated that the bottle reactor will increase the accessibility of electrochemistry to the synthetic chemistry community.

The bottle reactor would be particularly suited to reactions requiring inert or specialised atmospheres, such as CO or CO<sub>2</sub>.<sup>150</sup> The ability of the bottle reactor to accommodate electrodes with a wide range of dimensions also makes it suited to studies looking at the fabrication of electrodes which may be unlikely to fit in commercial reactors which are usually designed to be used with bespoke electrodes.

Currently the design of the bottle reactor may only be used with vessels that have a GL32 thread. It would be relatively straightforward to increase the diameter of the insert to accommodate a larger vessel for the scale-up of reactions. Equally, tall narrow vessels could be of use for photo-electrochemistry with longer electrodes as these would provide a relatively large surface area to volume ratio which is useful for photochemistry.

## 2.6. Experimental

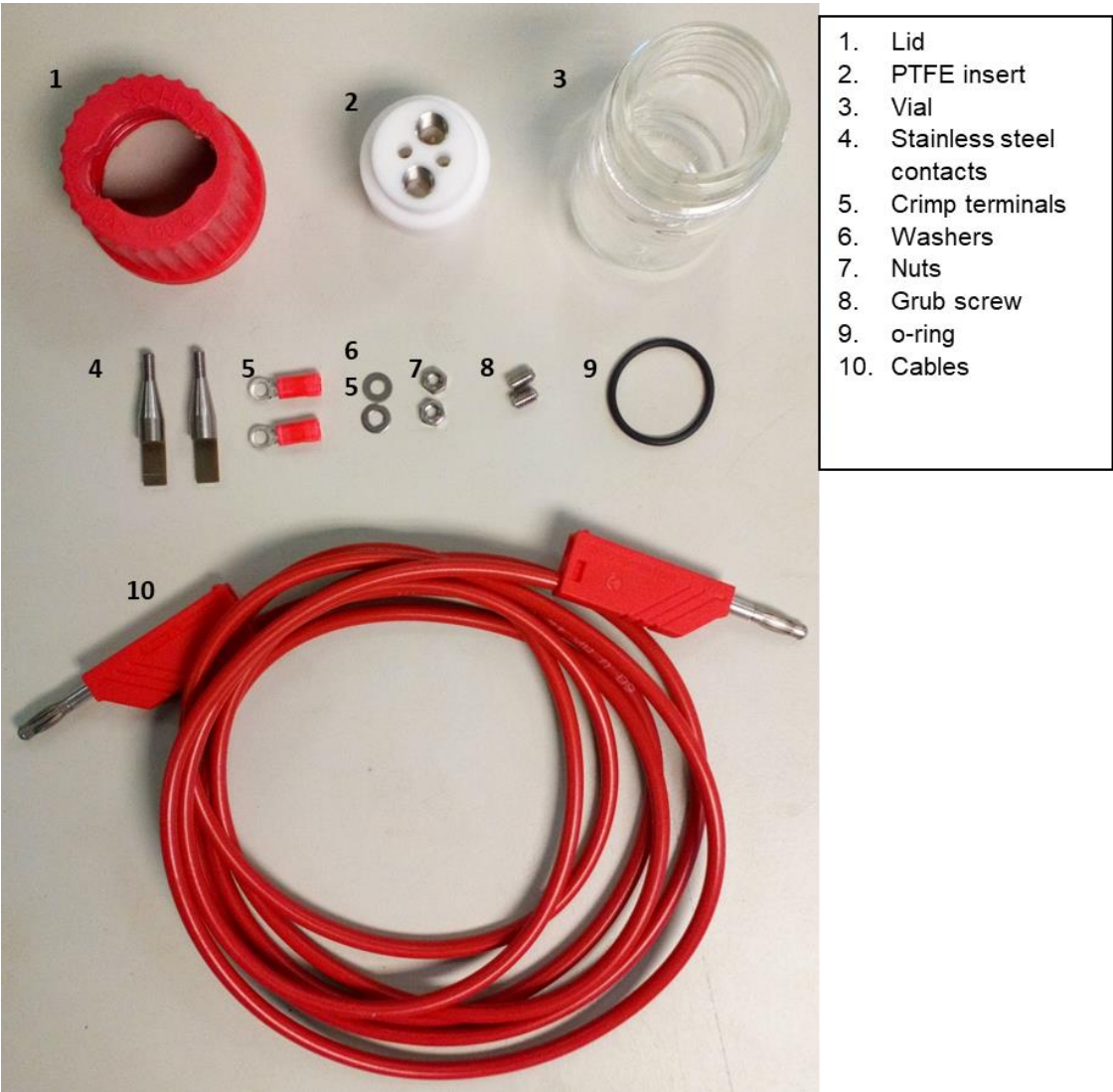
### 2.6.1. General considerations

NMR data were obtained on either a Bruker A500 (CH dual cryoprobe) or Bruker Ascend 400 spectrometer.  $^1\text{H}$  NMR and  $^{13}\text{C}\{^1\text{H}\}$  NMR chemical shifts were referenced against residual solvent peaks. Spin-spin coupling constants  $J$  are given in Hz and refer to apparent multiplicities rather than true coupling constants. Data is reported as: chemical shift, multiplicity and integration. Carbon shifts are reported to the nearest 0.1 ppm. Carbons in an identical environment giving one signal are not indicated further. Mass spectra were collected on a Bruker Daltonics (micro TOF) instrument operating in electrospray mode. Elemental Analyses were performed by Mr Stephen Boyer at London Metropolitan University. Unless otherwise noted all reagents employed in these studies were used as received from Sigma-Aldrich, Fluorochem, Fischer Scientific or Acros Organics and used without purification. Anhydrous solvents were dried in a Dow-Grubbs solvent system by passing over activated alumina to remove water, copper catalyst to remove oxygen, and molecular sieves to remove any remaining water. Toluene and DCM were freeze-pump-thaw degassed, while other solvents were degassed by purging with argon.

All crystals were obtained by recrystallisation from MeCN/ Et<sub>2</sub>O. Data was collected at 120 K on crystals mounted on a Hampton Scientific cryoloop using a SuperNova, Dual, Cu at home/near, Atlas. The structures were solved by direct methods with SHELXT, refined using full-matrix least-squares routines against  $F^2$  with SHELXL, and visualized using OLEX2.<sup>151,152</sup> All non-hydrogen atoms were refined anisotropically. All hydrogen atoms were placed in calculated positions and refined using a riding model with fixed C–H distances of 0.95 Å ( $sp^2\text{CH}$ ), 1.00 Å (CH), 0.99 Å (CH<sub>2</sub>), 0.98 Å (CH<sub>3</sub>). The thermal parameters of all hydrogen atoms were estimated as  $U_{\text{iso}}(\text{H}) = 1.2U_{\text{eq}}(\text{C})$  except for CH<sub>3</sub> where  $U_{\text{iso}}(\text{H}) = 1.5U_{\text{eq}}(\text{C})$ .

Cyclic voltammetry of **L1-5** was performed at room temperature in the bottle reactor using a Metrohm, DropSens,  $\mu\text{STAT}$  400 potentiostat and data acquired with DropView 8400 software. Experiments were performed in anhydrous, degassed MeCN (1 mM),  $n\text{Bu}_4\text{NPF}_6$  (0.1 M) supporting electrolyte (scan rate of 300 mV s<sup>-1</sup>), with a Metrohm glassy carbon disk (1 mm) working electrode, platinum wire counter electrode, and silver wire pseudo-reference electrode. Ferrocene (Fc) was added as an internal standard (1 mM,  $\text{Fc}^+/\text{Fc}$  at +0.380 V vs SCE) to reference experiments.

2.6.2. Bottle reactor design



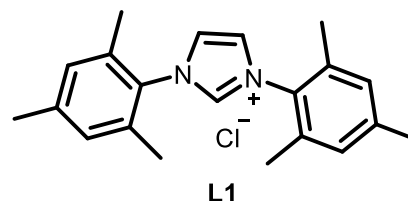
No.	Item	Supplier	Part no.	Notes
1	Lid	Duran	29 227 08 08	GL32 thread two extra semi-circular holes filed out
2	PTFE insert	School of Mechanical Engineering, University of Leeds		Technical drawings attached as a pdf, CAD files available upon request
	Thread inserts	RS PRO	175-0421	for ¼-28 fittings

	Thread inserts	RS PRO	175-0422	for grub screws to hold electrodes
<b>3</b>	Vial	Menke	24-0030-32-20-20-17	volume: 30 mL, thread size: GL32
<b>4</b>	Stainless steel electrode contacts	School of Mechanical Engineering, University of Leeds		technical drawings attached as a pdf, CAD files available upon request
<b>5</b>	Crimp terminal	RS PRO	FVW S1.25-M3(LF)	M3 stud size 0.25 -1.65 mm <sup>2</sup> wire size
<b>6</b>	Washers	RS PRO	560-338	Steel, M3
<b>7</b>	Nuts	RS PRO	483-0861	Steel, M3
<b>8</b>	Grub screw	RS PRO	137-742	Stainless steel, M4, Hex socket set
<b>9</b>	o-ring	Simply Bearings	BS019	1.78 mm section, 20.35 mm bore Viton rubber o-ring
<b>10</b>	Cables	Onecall	72-13842	cut in half to make two cables
-	Blank fitting	Cole-Parmer	P-316	flat bottom ¼-28 plug fitting
-	Orange fitting	Cole-Parmer	002103	flangeless fitting ¼-28, 1/16"
-	ferrule	Cole-Parmer	008FT16	ferrule 1/16"
-	Tubing	Polyflon	K6A0079040X	1/16" PFA tubing
-	Luer adapter	Cole-Parmer	P-628	female Luer to female ¼-28

## 2.6.3. Ligand synthesis

### 2.6.3.1. L1

Trimethylaniline (25 mL, 178 mmol) was dissolved in methanol (100 mL) and acetic acid (2 mL) was added. Glyoxal (12 mL, 105 mmol) was added dropwise and the solution was stirred for 24 hours, leading to a red solution with a yellow precipitate. The precipitate was filtered under vacuum and washed with cold methanol to leave the diimine precursor to **L1**. The diimine was placed under nitrogen in a large round bottomed flask and dissolved in anhydrous toluene (~150 mL). Paraformaldehyde (2.5 g, 83 mmol) was dissolved in a solution of hydrochloric acid in dioxane (20 mL, 4 M) and added to the toluene solution which was heated to 70 °C for 22 hours. A brown precipitate formed and was filtered under vacuum before being washed with ethyl acetate to give an off white powder which was recrystallised from acetonitrile and diethyl ether to deliver **L1** as colourless crystals (15.23 g, 38 mmol, 45%).



$^1\text{H}$  NMR (501 MHz,  $\text{CDCl}_3$ )  $\delta$  10.89 (s, 1H,  $\text{NCHN}$ ), 7.59 (s, 2H,  $\text{Imid}_{\text{backbone}}$ ), 7.03 (s, 4H, ArH), 2.34 (s, 6H,  $\text{CH}_3$  *o*- $\text{CH}_3$ ), 2.18 (s, 12,  $\text{CH}_3$  *p*- $\text{CH}_3$ ) ppm.

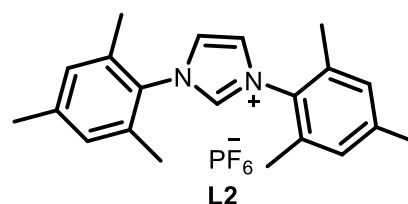
$^{13}\text{C}\{^1\text{H}\}$  NMR (126 MHz,  $\text{CDCl}_3$ )  $\delta$  141.5 (CH), 140.0 (C), 134.2 (C), 130.7 (C), 130.1 (CH), 124.4 (CH), 21.3 ( $\text{CH}_3$ ), 17.8 ( $\text{CH}_3$ ) ppm.

HRMS (ESI+):  $m/z$  305.2036  $[\text{M}-\text{Cl}]^+$ , calcd. 305.2012.

Consistent with data previously reported.<sup>112</sup>

### 2.6.3.2. L2

IMes·HCl (**L1**) (2.9 g, 5.9 mmol) was dissolved in water (50 mL) and a solution of  $\text{NH}_4\text{PF}_6$  (5.0 g, 66.8 mmol) in water (100 mL) was slowly added, leading to a white precipitate. The slurry was stirred for a further 30 minutes, before being filtered and washed with water. The white solid was then dried under vacuum to deliver the product (2.33 g, 5.2 mmol, 88%).



$^1\text{H}$  NMR (400 MHz,  $\text{MeCN}-d_3$ )  $\delta$  8.69 (s, 1H,  $\text{NCHN}$ ), 7.71 (s, 2H,  $\text{Imid}_{\text{backbone}}$ ), 7.16 (s, 4H, ArH), 2.37 (s, 6H,  $\text{CH}_3$  *o*- $\text{CH}_3$ ), 2.12 (s, 12H,  $\text{CH}_3$  *p*- $\text{CH}_3$ ) ppm.

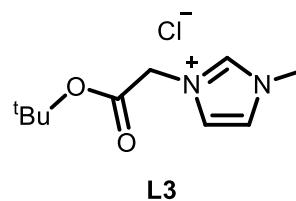
$^{13}\text{C}\{^1\text{H}\}$  NMR (101 MHz,  $\text{MeCN}-d_3$ )  $\delta$  142.6 (CH), 138.3 (C), 135.6 (C), 131.7 (C), 130.6 (CH), 125.9 (CH), 21.2 ( $\text{CH}_3$ ), 17.5 ( $\text{CH}_3$ ) ppm.

HRMS (ESI+):  $m/z$  305.2216  $[\text{M}-\text{PF}_6]^+$ , calcd. 305.2012.

Consistent with data previously reported.<sup>112</sup>

### 2.6.3.3. L3

*Tert*-butyl chloroacetate (3.75 mL, 26 mmol) and *N*-methylimidazole (2 mL, 25 mmol) were placed in a sealed Schlenk tube and stirred for 24 hours to give a viscous colourless reaction mixture. The semi-solid was recrystallised with DCM/ pentane to give a white powder which was filtered and washed with diethyl ether. The resultant hygroscopic white powder rapidly became a viscous colourless oil. The crude oil of **L3** was placed under nitrogen and washed with anhydrous diethyl ether (2 x 40mL) before being recrystallised with anhydrous DCM and hexane. The solution was filtered off and the remaining solid was dried under vacuum before being stored in the glove box as a white solid (4.03 g, 15 mmol, 61%).



$^1\text{H}$  NMR (501 MHz, DMSO- $d_6$ )  $\delta$  9.43 (s, 1H, NCHN), 7.83 (s, 1H, Imid<sub>backbone</sub>), 7.82 (s, 1H, Imid<sub>backbone</sub>), 5.27 (s, 2H, CH<sub>2</sub>), 3.93 (s, 3H, CH<sub>3</sub>), 1.43 (s, 9H, *t*Bu) ppm.

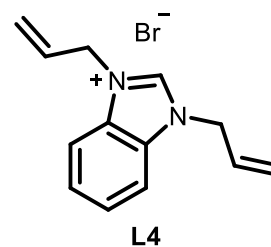
$^{13}\text{C}\{^1\text{H}\}$  NMR (126 MHz, DMSO- $d_6$ )  $\delta$  165.9 (C), 137.8 (CH), 123.7 (CH), 123.2 (CH), 82.9 (C), 49.9 (CH<sub>2</sub>), 35.87 (CH<sub>3</sub>), 27.7 (CH<sub>3</sub>) ppm.

HRMS (ESI<sup>+</sup>):  $m/z$  197.1287 [M-Cl]<sup>+</sup>, calcd. 197.1285, 141.0669 [M-*t*Bu-Cl+H]<sup>+</sup>, calcd. 141.0659.

Consistent with data previously reported.<sup>112</sup>

### 2.6.3.4. L4

Allyl bromide (8.0 mL, 94 mmol) was added to a suspension of benzimidazole (4.7 g, 40 mmol) and NaHCO<sub>3</sub> (10 g) in acetonitrile (100 mL). The mixture was stirred at room temperature for 7 days, after which the mixture was filtered under vacuum to give a yellow crystalline solid. The solid was recrystallised in acetonitrile to leave large off-white crystals (4.4 g, 16 mmol, 39%).



$^1\text{H}$  NMR (500 MHz, Chloroform- $d$ )  $\delta$  11.41 (s, 1H, NCHN), 7.78 – 7.69 (m, 2H, ArH), 7.66 – 7.57 (m, 2H, ArH), 6.20 – 6.05 (m, 2H, CH=CH<sub>2</sub>), 5.55 – 5.43 (m, 4H, CH=CH<sub>2</sub>), 5.32 (d,  $J$  = 6.0 Hz, 4H, NCH<sub>2</sub>) ppm.

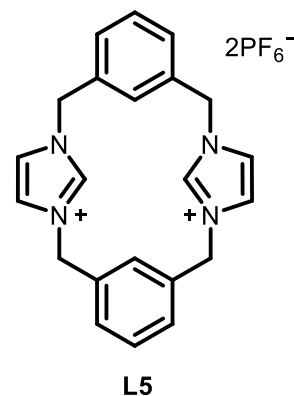
$^{13}\text{C}\{^1\text{H}\}$  NMR (126 MHz, CDCl<sub>3</sub>)  $\delta$  143.0 (CH), 131.5 (C), 129.6 (CH), 127.3 (CH), 122.1 (CH), 113.8 (CH<sub>2</sub>), 50.3 (CH<sub>2</sub>) ppm.

HRMS (ESI<sup>+</sup>):  $m/z$  199.1238 [M-Br]<sup>+</sup>, calcd. 199.1230.

Consistent with data previously reported.<sup>99</sup>

### 2.6.3.5. L5

1,3-Bis(bromomethyl)benzene (2.50 g, 9.41 mmol) was dissolved in anhydrous acetone (100 mL). A solution of 1,3-bis(imidazole-1-ylmethyl)benzene (2.30 g, 9.41 mmol) in anhydrous acetone (100 mL) was added dropwise over 4 hours at room temperature. The mixture was further stirred for 18 hours, upon which a colourless precipitate had formed, which was collected by vacuum filtration and washed with cold acetone (2 x 40 mL) and diethyl ether (2 x 40 mL) to leave the diimidazolium bromide as a microcrystalline colourless solid (2.70 g). The diimidazolium bromide (1.2 g, 2.40 mmol) was dissolved in methanol and a solution of ammonium hexafluorophosphate (3.90 g, 24.1 mmol) in methanol was added in a single portion and stirred for 2 hours. The resultant colourless precipitate was collected by vacuum filtration and washed with cold methanol (3 x 30 mL) followed by diethyl ether (3 x 30 mL) and dried *in vacuo* to deliver the product as a microcrystalline colourless solid.



$^1\text{H}$  NMR (501 MHz,  $\text{DMSO}-d_6$ )  $\delta$  9.23 (s, 2H,  $\text{NCHN}$ ), 7.83 (d,  $J = 1.6$  Hz, 4H,  $\text{Imid}_{\text{backbone}}$ ), 7.61 – 7.56 (m, 4H, ArH), 7.56 – 7.51 (m, 2H, ArH), 6.94 (s, 2H, ArH), 5.44 (s, 8H,  $\text{CH}_2$ ) ppm.

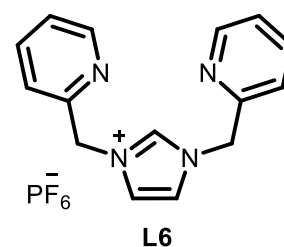
$^{13}\text{C}\{^1\text{H}\}$  NMR (126 MHz, DMSO)  $\delta$  136.2 (CH), 136.1 (CH), 129.5 (CH), 129.0 (CH), 125.5 (CH), 123.2 (C), 51.8 ( $\text{CH}_2$ ) ppm.

HRMS (ESI+):  $m/z$  171.0912 [ $\text{M}-2\text{PF}_6$ ] $^{2+}$ , calcd. 171.0917, 341.1766 [ $\text{M}-2\text{PF}_6\text{-H}$ ] $^+$ , calcd. 341.1761, 487.1497 [ $\text{M}-\text{PF}_6$ ] $^+$ , calcd. 487.1481.

Consistent with data previously reported.<sup>112</sup>

### 2.6.3.6. L6

Imidazole (1.0 g, 14.7 mmol), 2-(bromomethyl)pyridine hydrobromide (4.17 g, 29.4 mmol) and potassium carbonate (4.06 g, 58.8 mmol) were combined under an atmosphere of nitrogen before anhydrous acetonitrile (20 mL) was added. The resulting reaction mixture was maintained at 60 °C with constant stirring for 18 h. Then, the reaction mixture was concentrated under reduced pressure to ~10 mL and diethyl ether (50 mL) was added to precipitate the imidazolium bromide intermediate which was collected by filtration and washed with diethyl ether (2 x 10 mL). The precipitate was dissolved in water with constant stirring (30 mL) and ammonium hexafluorophosphate (2.40 g, 29.4 mmol) was added. The





resulting suspension was stirred for 1 h, then the resulting brown precipitate was collected by filtration and washed with diethyl ether (2 x 10 mL) to deliver the product as a brown amorphous solid (1.36 g, 3.37 mmol, 23%).

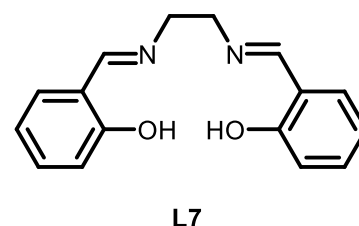
$^1\text{H}$  NMR (400 MHz, DMSO- $d_6$ )  $\delta$  9.42 (s, 1H), 8.56 (s, 2H), 7.90 (td,  $J$  = 7.7, 1.8 Hz, 2H), 7.81 (s, 2H), 7.49 (d,  $J$  = 7.8 Hz, 2H), 7.41 (dd,  $J$  = 7.5, 4.9 Hz, 2H), 5.62 (s, 4H) ppm.

$^{13}\text{C}$  NMR (126 MHz, DMSO- $d_6$ )  $\delta$  150.1, 138.0, 124.1, 123.8, 123.0, 53.6, 40.0 ppm.

HRMS (ESI+):  $m/z$  251.1301,  $[\text{M}]^+$  calcd. 253.1291.

### 2.6.3.7. L7

Salicylaldehyde (4.5 mL, 41 mmol) was dissolved in ethanol (50 mL) and ethylenediamine (1.5 mL, 22 mmol) was added, immediately turning the solution a bright yellow colour and forming a precipitate. The mixture was stirred for 30 minutes, after which it was cooled to 0 °C and filtered under vacuum. The bright yellow solid was washed with cold ethanol and diethyl ether to give *N,N*-bis(salicylidene)ethylenediamine as a bright yellow solid (4.96 g, 18.5 mmol, 84%).



$^1\text{H}$  NMR (400 MHz, Chloroform- $d$ )  $\delta$  13.22 (s, 2H, OH), 8.36 (s, 2H, CH=N), 7.32-7.26 (m, 2H, ArH), 7.25-7.20 (m, 2H, ArH), 6.98-6.90 (m, 2H, ArH), 6.89-6.83 (m, 2H, ArH), 3.94 (s, 4H, CH<sub>2</sub>) ppm.

$^{13}\text{C}\{^1\text{H}\}$  NMR (101 MHz, CDCl<sub>3</sub>)  $\delta$  166.6 (C), 161.1 (C), 132.5 (CH), 131.6 (CH), 118.8 (CH), 118.8 (CH), 117.1 (CH), 59.9 (CH<sub>2</sub>) ppm.

HRMS (ESI+):  $m/z$  269.1296  $[\text{M}+\text{H}]^+$  calcd. 269.1290.

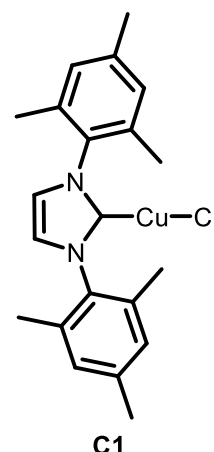
## 2.6.4. Preparation of metal complexes

### 2.6.4.1. General procedure

A bottle reactor vial was charged with the ligand precursor (1 mmol), then the reactor was assembled and placed under an atmosphere of argon. MeCN (anhydrous, 15 mL) was added and Cu, Au or Fe electrodes were used to apply a constant current of 50 mA for 40 minutes ( $1.2 \text{ F mol}^{-1}$ ) from a Tenma bench top power supply (72-10480 from Farnell). A sample of approximately 0.5 mL was taken at the end of the reaction and filtered through Celite after which the solvent was removed under reduced pressure. The resultant solid was redissolved in a suitable deuterated solvent and analysed using  $^1\text{H}$  NMR spectroscopy. Integrals for the complex and ligand were used to calculate the conversion.

### 2.6.4.2. Cu1

**L1** (0.34 g, 1 mmol) was placed into the bottle reactor under argon and dissolved in anhydrous acetonitrile (15 mL). Copper electrodes were used to apply a constant current of 50 mA for 40 min (1.2 F mol<sup>-1</sup>). The reaction mixture was filtered through Celite and the solvent removed under vacuum to give the copper complex as a white solid (0.383 g, 0.95 mmol, 95%). Suitable crystals were grown by the vapour diffusion of diethyl ether into a concentration solution of the complex in acetonitrile.



<sup>1</sup>H NMR (400 MHz, Chloroform-d) δ 7.05 (s, 2H, Imidbackbone), 7.00 (s, 4H, ArH), 2.34 (s, 6H, CH<sub>3</sub>-ortho), 2.10 (s, 13H, CH<sub>3</sub>-para), 2.00 (d, J = 1.6 Hz, 1H).

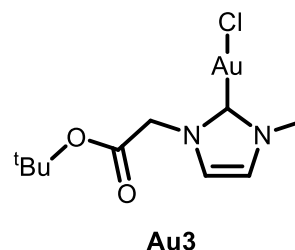
<sup>13</sup>C{<sup>1</sup>H} NMR (101 MHz, CDCl<sub>3</sub>) δ 139.50, 135.10, 134.55, 129.49, 122.28, 21.12, 17.77.

HRMS (ESI<sup>+</sup>): m/z 305.2009 [ligand]<sup>+</sup> calcd. 305.2012, 408.1514 [M-Cl+MeCN]<sup>+</sup> calcd. 408.1496, 671.3183 [M-Cl+ligand]<sup>+</sup> calcd. 671.3170.

Consistent with data previously reported.<sup>99</sup>

### 2.6.4.3. Au3

As **Au3** is unreported in the literature the reaction was repeated for 2 electron equivalents to drive the reaction to completion. **L3** (0.34 g, 1 mmol) was placed into the bottle reactor under argon and dissolved in anhydrous acetonitrile (15 mL). A gold anode and steel cathode was used to apply a constant current of 50 mA for 80 min (2 F mol<sup>-1</sup>). The mixture was filtered through Celite and the solvent was removed under vacuum to give the copper complex as a pale gold solid (0.329 g, 0.77 mmol, 77%).



<sup>1</sup>H NMR (400 MHz, CDCl<sub>3</sub>) δ 7.04 (d, J = 2.0 Hz, 1H, Imid<sub>backbone</sub>), 6.98 (d, J = 2.0 Hz, 1H, Imid<sub>backbone</sub>), 4.86 (s, 2H, CH<sub>2</sub>), 3.83 (s, 3H, CH<sub>3</sub>), 1.48 (s, 9H, tBu) ppm.

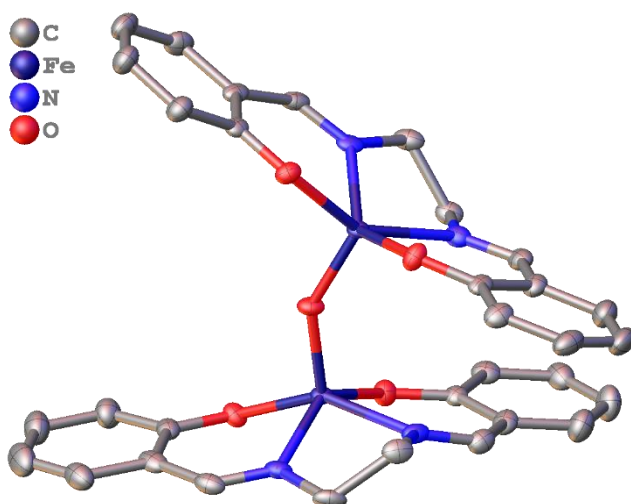
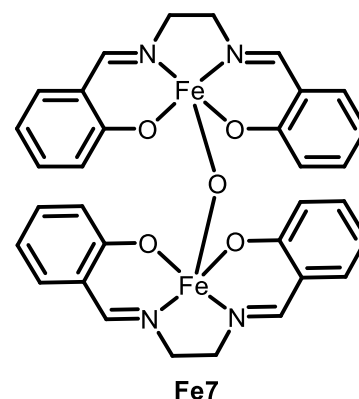
<sup>13</sup>C{<sup>1</sup>H} NMR (101 MHz, CDCl<sub>3</sub>) δ 172.8 (C), 166.2 (C), 122.0 (CH), 122.0 (CH), 84.1 (C), 52.5 (CH<sub>2</sub>), 38.4 (CH<sub>3</sub>), 28.1 (CH<sub>3</sub>) ppm.

HRMS (ESI<sup>+</sup>): m/z 434.1131 [M-Cl+MeCN]<sup>+</sup> calcd. 434.1137, 378.0504 [M-Cl+MeCN-tBu+H]<sup>+</sup> calcd. 378.0511.

#### 2.6.4.4. Fe7

Due to the paramagnetic nature of **Fe7** the complex was fully isolated after being electrolysed using an iron electrode in air for 1.2 electron equivalents. Suitable crystals were grown by the vapour diffusion of diethyl ether into a concentration solution of the complex in acetonitrile.

HRMS (ESI+):  $m/z$  322.0411  $[M-Fe-L-O]^+$ , calcd. 322.0405.

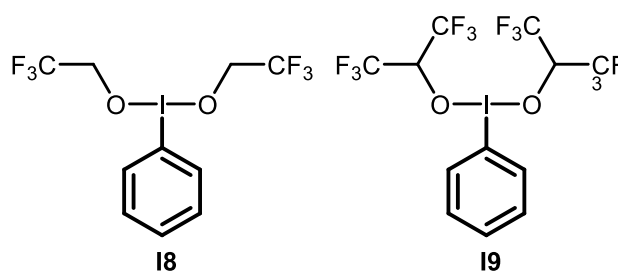


#### 2.6.5. Sulphonamide synthesis

A bottle reactor vial was charged with tetramethylammonium tetrafluoroborate (32 mg, 0.2 mmol), MeCN (15 mL) and aqueous HCl (0.3 M, 5 mL). Then cyclohexylamine (0.345 mL, 3 mmol) and thiophenol (0.205 mL, 2 mmol) were added. The bottle reactor lid was fitted with an IKA graphite anode and an IKA stainless steel cathode and a potential difference was applied for the specific time (potentiostatic or galvanostatic). After completion the reaction mixture was diluted with water (10 mL) and extracted with EtOAc (3 x 20 mL). The combined organic layers were washed with brine (20 mL), dried over  $MgSO_4$  and filtered. The solvent was removed under reduced pressure to deliver the crude product as a light brown oil. To that 2,4,6-trimethoxybenzene (internal standard, 112 mg, 0.66 mmol) and  $CDCl_3$  (3 mL) were added to form a homogeneous solution which was analysed by  $^1H$  NMR spectroscopy.

### 2.6.6. Synthesis of hypervalent iodine species

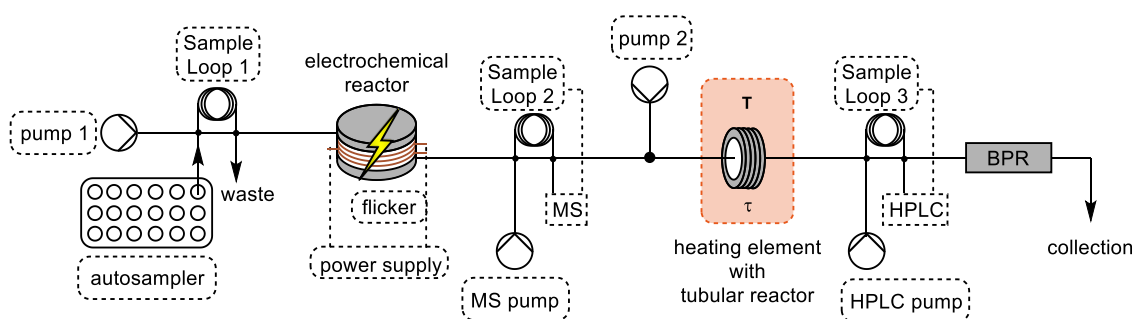
Iodobenzene (110  $\mu$ L, 1 mmol) and  $n\text{Bu}_4\text{NBF}_4$  (330 mg, 1 mmol) were placed in the bottle reactor in air and dissolved in trifluoroethanol (20 mL) to form **18** or hexafluoroisopropanol (20 mL) to form **19**. A glassy carbon



anode (IKA) and platinum plated cathode (IKA) were used to apply a current of 50 mA for 2 hours (XX F mol<sup>-1</sup>) resulting in a yellow solution with no precipitate. Hydroquinone (112 mg, 1 mmol) was added and the reaction stirred for 30 minutes, with the solution turning orange. The mixture was quenched with a saturated aqueous solution of  $\text{Na}_2\text{S}_2\text{O}_3$  (50 mL) and an extraction was performed using EtOAc (3 x 25 mL). The combined organic layers were washed with water (25 mL) and brine (25 mL), dried with  $\text{MgSO}_4$  and filtered before removing the solvent under reduced pressure. Nitrobenzene (internal standard, 105  $\mu$ L) was added, the residue was dissolved in  $\text{CDCl}_3$  and analysed using  $^1\text{H}$  NMR spectroscopy to give a yield of 20% and a conversion of 75%.

### 3. Mass transfer within an electrochemical flow reactor

Conducting electrochemistry in flow has several advantages over conducting it in batch, including a small interelectrode gap and an increased surface area to volume ratio.<sup>70</sup> Previous work within the Willans group has established the electrochemical generation of copper-NHC complexes in flow,<sup>112</sup> and work has now turned to look at telescoping these complexes into other reactions to act as catalysts with the aim of building a catalyst screening platform (Figure 3.1). In order for this to be successful, the electrochemical flow reactor must be well understood and this chapter explores how changing the geometries of flow channels can alter the mass transfer within such reactors and affect the reaction outcomes.



**Figure 3.1:** Proposed set up for a catalyst screening platform, with complexes produced electrochemically and telescoped into a reaction of interest.

#### 3.1. Electrochemical flow reactors

Emerging technologies have been hailed in the chemistry community as a means of exploring new reactivity and increasing the accessibility or productivity of existing reactions. Electrochemistry and flow chemistry are two ‘emerging technologies’ that are well established and widely used by industry.<sup>153,154</sup> Perhaps ‘maturing technology’ might be a better agnomen given the return of flow chemistry and electrochemistry to the laboratory over the past two decades and the ensuing multitude of new reactions which has broadened their applicability.<sup>46,50,69,116,155</sup> Many of these emerging technologies complement one another, for example the combination of electro and photochemistry can lead to the generation of excited radicals with relative ease.<sup>156</sup> Similarly, flow chemistry can greatly improve the efficiency of electro and photochemistry.<sup>108,157</sup>

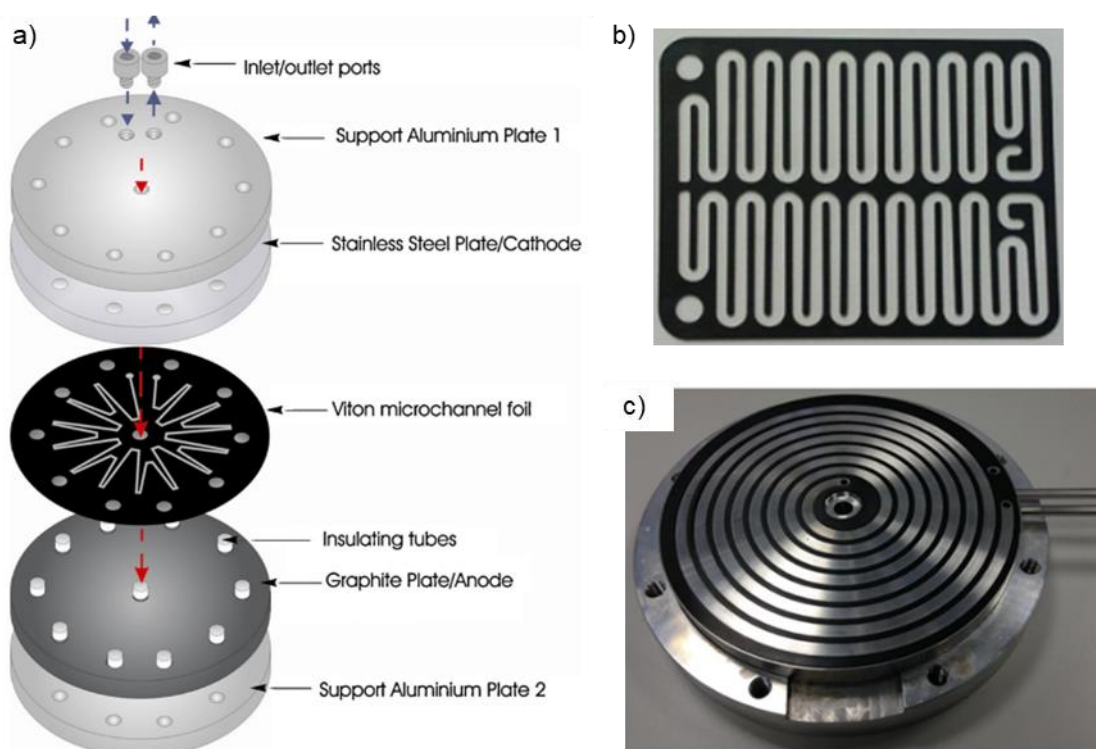
The much smaller interelectrode gap in flow cells reduces the amount of electrolyte needed, in some cases eliminating the need for it completely, thereby increasing the atom efficiency of the reaction.<sup>158</sup> Furthermore, electrochemistry is a heterogeneous process and consequently the efficiency can be greatly increased by exploiting the large

surface area to volume ratio of flow reactors.<sup>108</sup> The movement of species to and from a surface, the mass transfer, is of considerable importance during heterogeneous reactions,<sup>139</sup> but despite this it is often overlooked by the synthetic chemistry community. Combine this with the relative youth of flow electrochemistry and it is not surprising that whilst considerable work has been conducted in performing electrochemical reactions in flow, relatively few studies have been published which consider how the design of a reactor effects the mass transfer of species within it. Mass transfer comprises of three components: diffusion, a slow process where species move from areas of high concentration to areas of low concentration; migration, where charged species are moved due to electrostatic forces and convection, where species are moved as a result of the movement of the fluid. Convection is typically what people are referring to when they discuss 'mixing'.

Laminar flow normally dominates in microreactors,<sup>46,54</sup> with turns providing a potential source of turbulence to aid mixing. Although other groups have used the layout of flow channels to rationalise the design of electrochemical flow reactors,<sup>159,160</sup> only one study has directly compared designs.<sup>161</sup> Instead, the design of reactors has focused on practicalities such as reducing the footprint of reactors or performing reactions in parallel.<sup>112,162,163</sup>

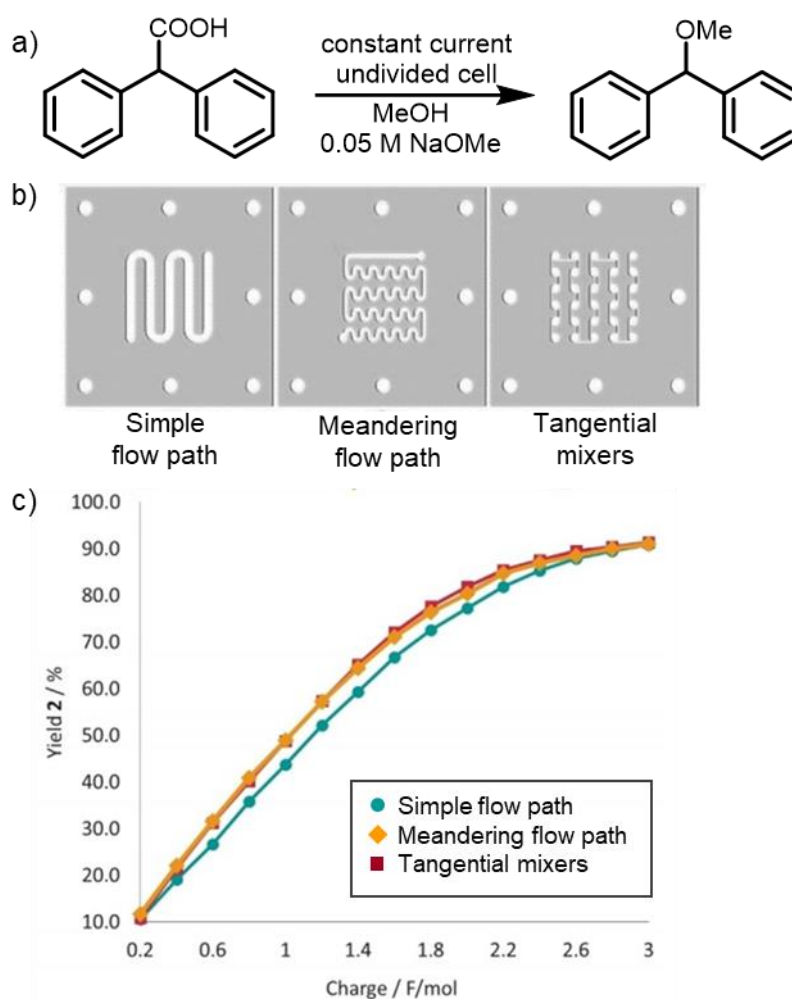
### 3.1.1. Reactor designs

Most work on mass transfer in electrochemical flow reactors has focused on using obstructions, such as meshes or beads to increase the mass transfer by introducing turbulence.<sup>164–168</sup> These endeavours have been successful, however they add unnecessary complications to experimental set-ups, requiring the careful placement of turbulence promoters in-between electrodes for them to be effective. Ideally the mass transfer could be controlled by changing the shape or layout of flow channels. Several studies have used this idea to justify the design of their reactors.<sup>159,160,169</sup> Pletcher *et al* have designed numerous cells including one with a 'star' shaped flow path and one with a 'snaking' channel to disrupt the flow and increase mass transfer (Figure 3.2, a and b).<sup>160,169</sup> The same group also designed a spiral shaped reactor to reduce the disruption to flow regimes caused by corners (Figure 3.2, c).<sup>159</sup>



**Figure 3.2:** Previous studies have used flow channel geometries to justify the design of reactors, but have not investigated it in detail. a) Star shaped channel.<sup>160</sup> b) Snaking shaped channel.<sup>169</sup> c) Spiral shaped channel.<sup>159</sup> a and b reproduced with permission from Elsevier. c reproduced under creative commons licensing.

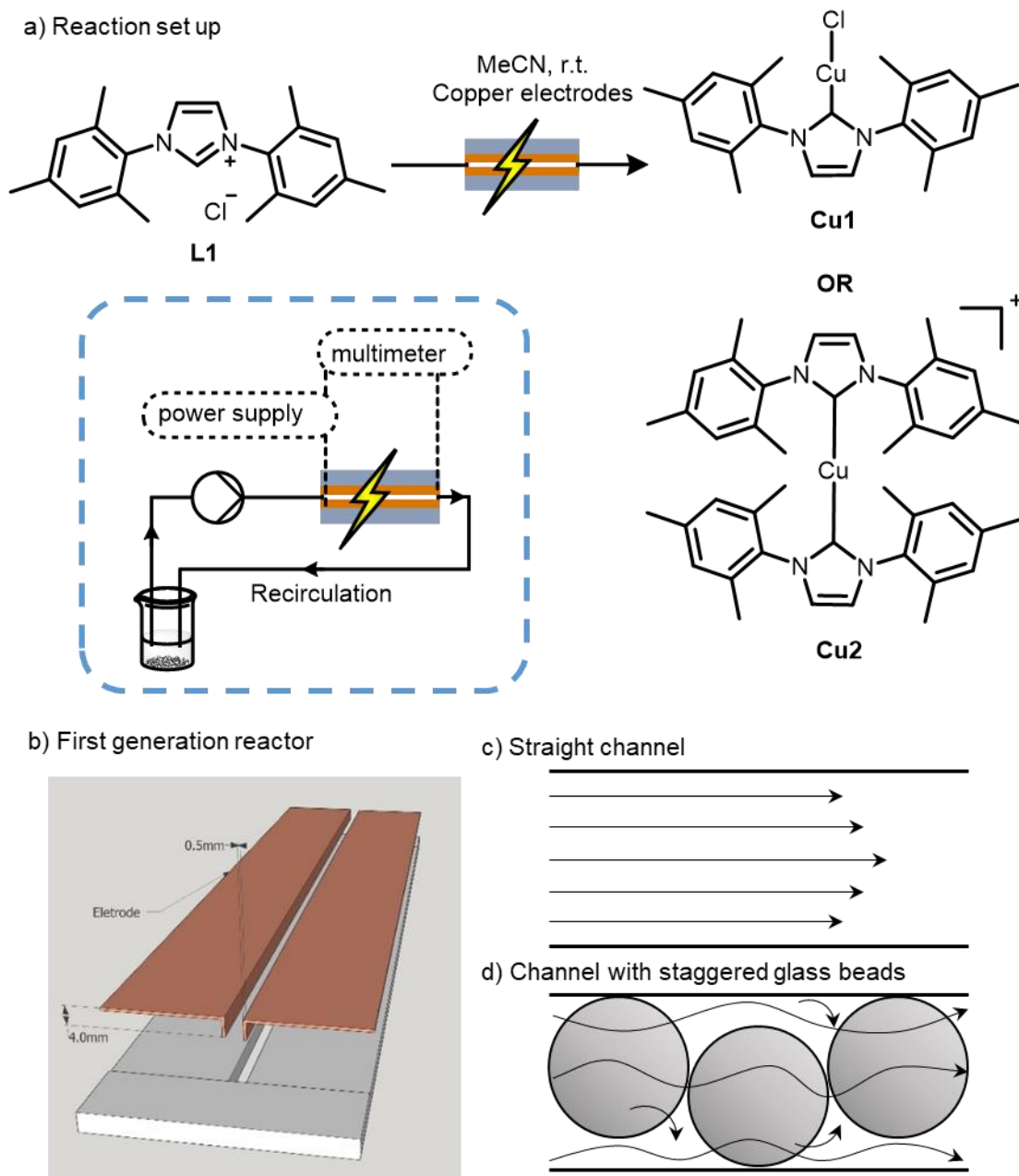
In 2021 Jud *et al* designed and fabricated a flow reactor for conducting electrochemical reactions in a single pass.<sup>161</sup> The group used the decarboxylative methoxylation of diphenylacetic acid as a model reaction and were able to obtain nearly full conversion in a single pass. They also tested three different flow channels, finding that channels with meandering paths or tangential mixers provided a small increase in yield, despite having a smaller electrode surface areas than the simple flow path (Figure 3.3). This was attributed to extra mixing.



**Figure 3.3:** The effect of different channel geometries on the decarboxylative methoxylation of diphenylacetic acid.<sup>161</sup> Figure reproduced under creative commons licensing.

The first electrochemical flow reactors to be used in the synthesis of organometallic complexes were made by the Willans group.<sup>112</sup> This first generation reactor consisted of a linear PTFE flow channel (190.0 mm x 4.0 mm x 2.5 mm) with two copper electrodes 2.5 mm apart (Figure 3.4, b). The formation of Cu(IMes)Cl (**Cu1**) was chosen as benchmark reaction to optimise the reaction conditions due to the air stable and diamagnetic nature of **Cu1** which allowed reaction monitoring using <sup>1</sup>H NMR spectroscopy. The reaction mixture was recirculated through the reactor and it was observed that the product contained a mixture of **Cu1** and the corresponding bis-NHC product (**Cu2**), along with some CuCl<sub>2</sub> (Figure 3.4, a). This was attributed to the large distance between the two electrodes, along with poor mass transfer. To rectify this, glass beads (2.0 mm outer diameter) were packed in a staggered fashion within the flow channel and this led to the formation of **Cu1** as the only product (Figure 3.4, c and d).<sup>112</sup> Evidently mass transfer can have a significant effect on the selectivity of reactions and whether side-products are observed.

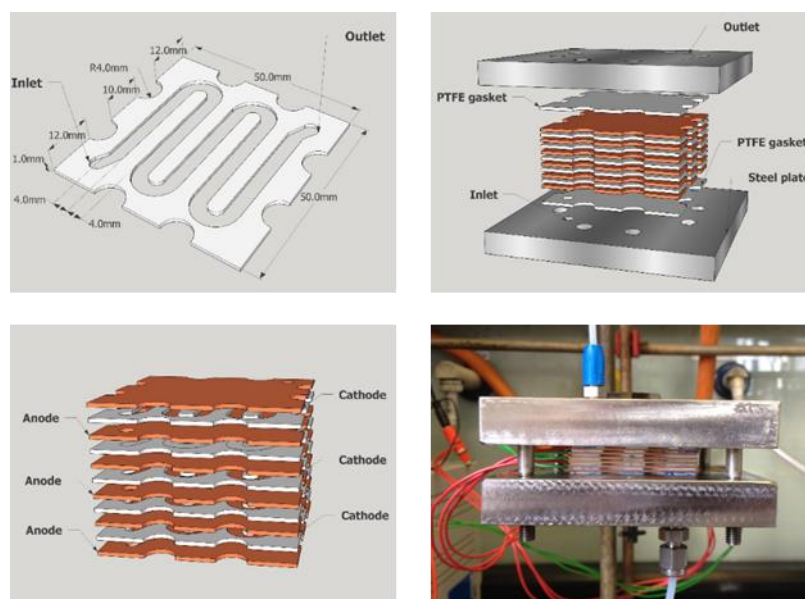




**Figure 3.4:** Design and set up of the first generation reactor and how glass beads were used to increase turbulence and selectivity.<sup>112</sup> b was reproduced with permission from the Royal Society of Chemistry

The first generation reactor had a faradaic efficiency of 67% and the group aimed to further increase this as well as be able to generate copper-NHC complexes in a single pass, without the need for recirculating reaction solutions. The second generation reactor was designed to give a high electrode surface area to volume ratio, with copper plates alternating with PTFE spacers (Figure 3.5). The spacers had sinuous flow channels to reduce the footprint of the reactor and were 1 mm thick. The smaller inter-electrode gap resulted in a higher faradaic efficiency when compared to the first generation reactor. The modular design of the stacked disk reactor also allowed the volume to be changed. With five spacers, a volume of 4 mL, and a residence time of 6 minutes **Cu1** could be

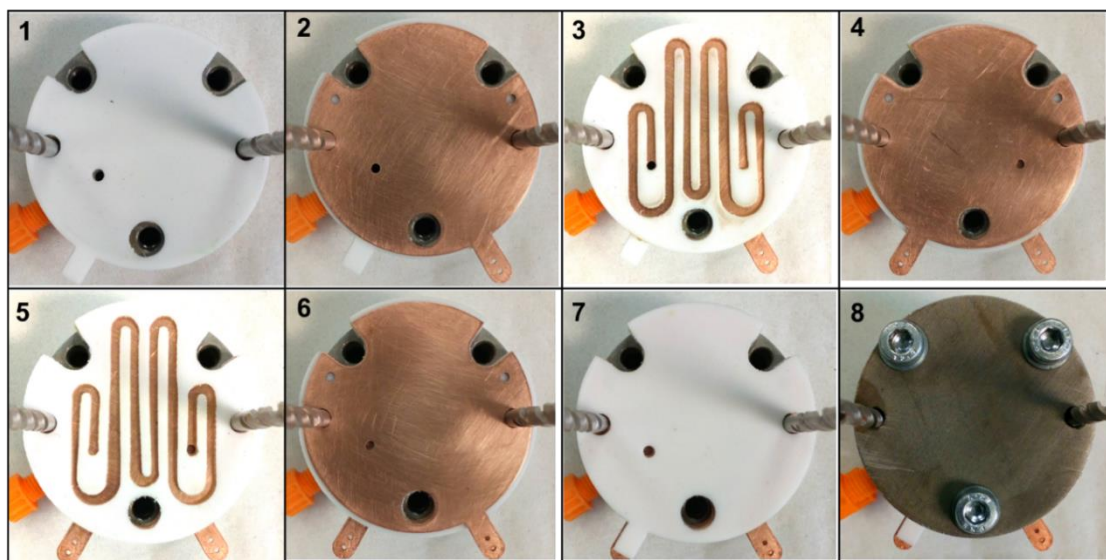
formed in 97% yield in a single pass with a faradaic efficiency of 93%, a significant improvement of the first generation reactor.<sup>112</sup>



**Figure 3.5:** The second generation reactor had a stacked disk design.<sup>112</sup> Reproduced with permission from the Royal Society of Chemistry.

### 3.1.2. Third generation flow reactor

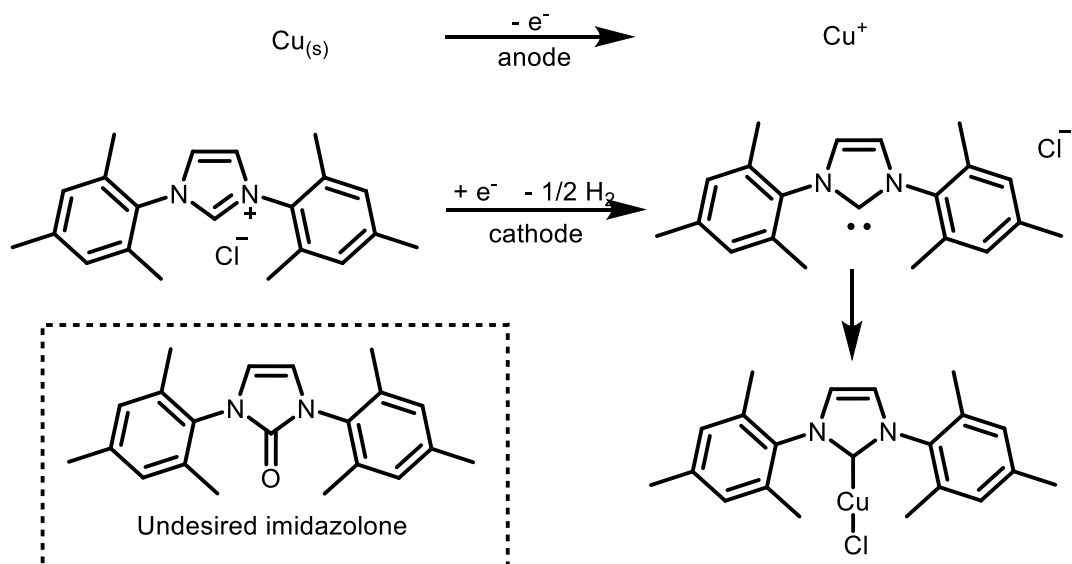
The second generation flow reactor used by Chapman *et al*,<sup>112</sup> although effective, did have a relatively large volume (4 mL). Because the long term aim of this project is to incorporate an electrochemical flow reactor as part of a high throughput screening platform, it was desirable to have a reactor which had a relatively small volume, to enable the screening process to be faster and use less material. As a result, Professor Nikil Kapur (School of Mechanical Engineering, University of Leeds) designed a third generation reactor in collaboration with the Willans group. Like the second generation reactor it features stacked electrodes which alternate between cathode and anode with PTFE spacers in between (Figure 3.6). The volume can be varied by changing the number of PTFE spacers that are used, with one normal spacer giving a volume of approximately 0.5 mL. The shape of the flow channel in the PTFE spacer can also be varied, something which is discussed in section 3.2.



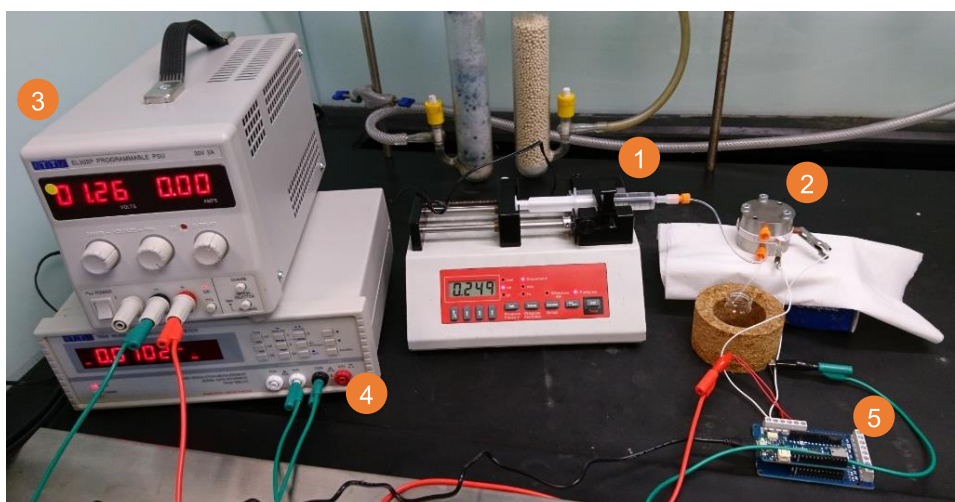
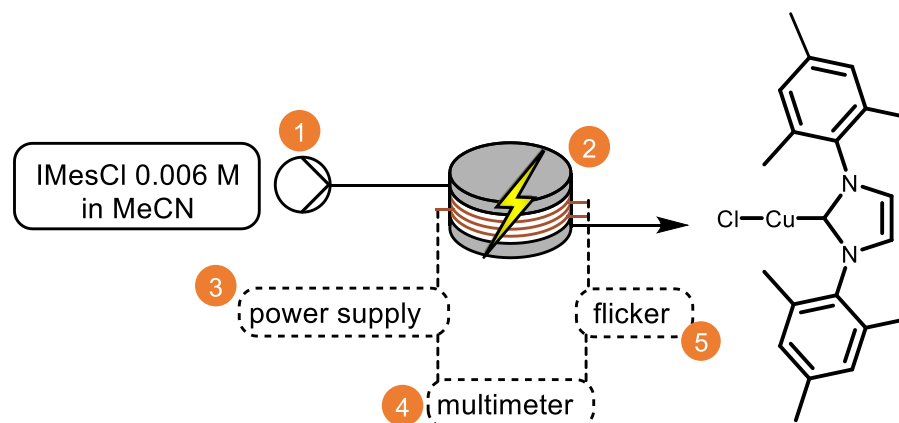
**Figure 3.6:** Assembling the third generation reactor: insulating PTFE gasket (1), electrode (2), spacer (3), electrode (4), spacer (5), electrode (6), gasket (7) and the steel housing (8).

### 3.1.3. Set up of electrochemical reactions in flow

The electrochemical synthesis of **Cu1** provides a useful model reaction because the ligand can be prepared on a large scale and the resulting complex is air stable, thereby simplifying the set up and allowing a diverse range of conditions to be tested. In the electrochemical reactor, **L1** is reduced at the cathode to generate the carbene, which subsequently reacts with a copper ion which has been formed by oxidation of the anode to produce **Cu1** (Figure 3.7).<sup>112</sup> Throughout these studies a 6 mM solution of **L1** in anhydrous acetonitrile was used. This solution was prepared under argon to try and reduce the formation of imidazolones which are formed when free carbenes react with oxygen. The solution was transferred into a syringe and pumped through the reactor using a syringe pump. A power supply was connected to the electrode and a multimeter enabled the current to be monitored (Figure 3.8). Darkening of the electrodes, possibly due to deposition, was observed following reactions. Consequently, the electrodes were sanded down and cleaned with acetone, water and hydrochloric acid after each reaction.



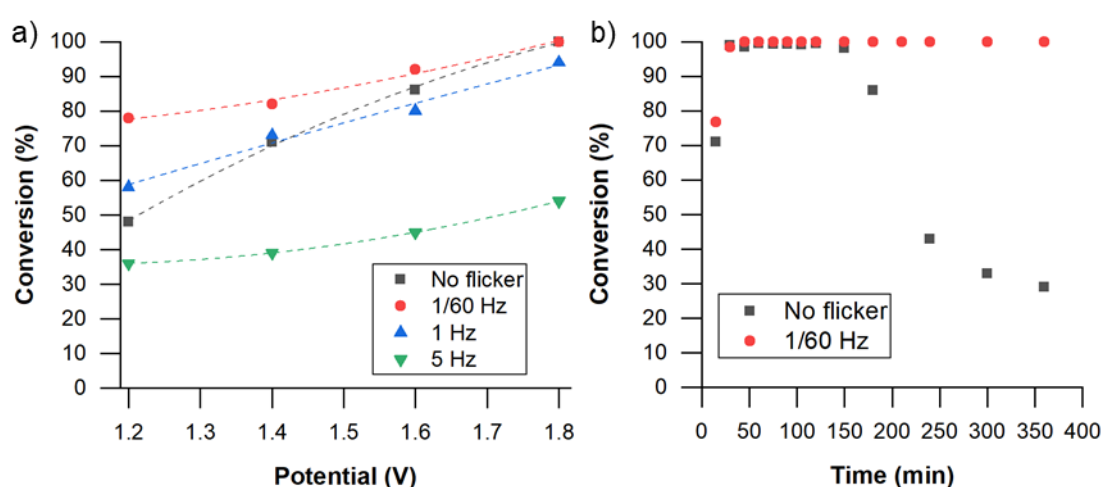
**Figure 3.7:** Electrochemical synthesis of **Cu1**.



**Figure 3.8:** Set up of the electrochemical flow reactor.

Initial optimisation work was conducted by Dr Christiane Schotten, another member of the Willans group, demonstrating that using a 6 mM concentration of ligand precursor

and a flow rate  $0.034 \text{ mL min}^{-1}$  would provide full conversion of **L1** to **Cu1** when two normal spacers (volume =  $0.92 \text{ mL}$ ) were used and a constant potential of  $1.8 \text{ V}$  was applied. It was found that using a constant potential gave more consistent results compared to using a constant current. A polarity flicker was added in series after work by Dr Christiane Schotten demonstrated that alternating the polarity of the electrodes at a low frequency ( $1/60 \text{ Hz}$ ) increased the conversion (Graph 3.1, a) and increased the stability of the reactor over long periods of time (Graph 3.1, b),<sup>170</sup> an important consideration for a screening platform. The flicker is an Arduino circuit that alternates the polarity of the electrodes, it is thought that this reduces deposition and fouling of the electrodes and helps to prevent short circuits within the reactor.



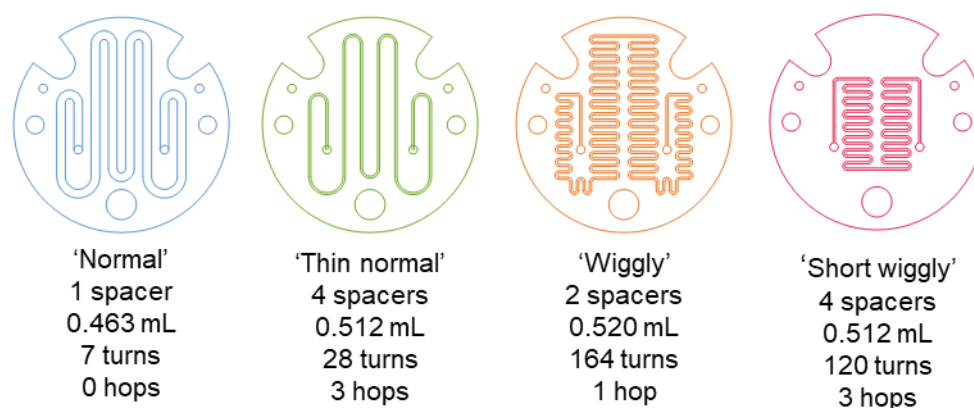
**Graph 3.1:** Examining the frequency of the polarity flicker and its effect on the long term stability of a reaction.<sup>170</sup>

## 3.2. Investigation of different flow paths

### 3.2.1. Initial investigations

To explore whether the shape of flow channels had an impact on the outcome of a reaction, four spacers with different flow paths were initially investigated (Figure 3.9). All had the same depth ( $1 \text{ mm}$ ), but the width and number of turns were varied. The 'normal' spacer had 7 turns and a width of  $2 \text{ mm}$ . A thinner, 'thin normal' version with a width of  $0.5 \text{ mm}$  and 7 turns was also tested. Four 'thin normal' spacers were needed to give a comparable volume to one 'normal' spacer. To increase the number of turns a 'wiggly' spacer with 82 turns ( $0.5 \text{ mm}$  width) and a 'short wiggly' spacer with 30 turns ( $0.5 \text{ mm}$  width) were investigated. Two 'wiggly' spacers and four 'short wiggly' spacers were required to give a volume of approximately  $0.5 \text{ mL}$ . Whenever multiple spacers were

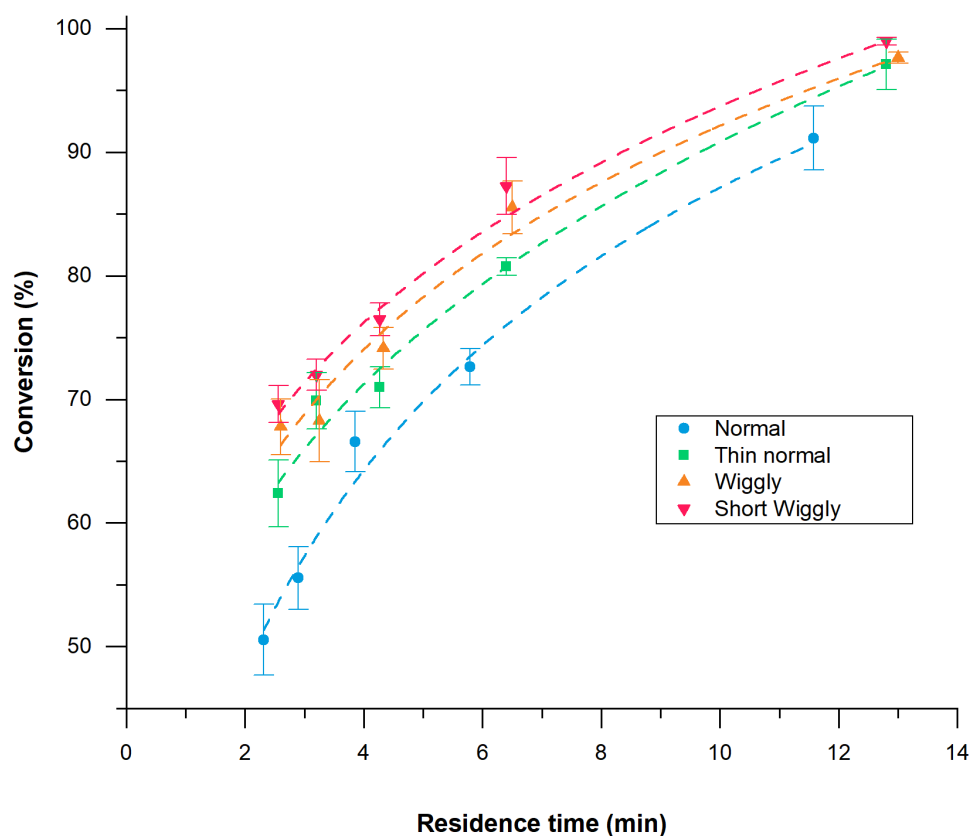
used the flow path must pass through an electrode, as shown in Figure 3.6, in what will be referred to as a 'hop'.



**Figure 3.9:** The spacers that were tested. Colours correspond to Graph 3.2.

The synthesis of **Cu1** was examined using the different flow channels at a range of flow rates. Two residence times were allowed to elapse to ensure that steady state had been reached before the eluent was collected for one residence time. The solvent was then removed under vacuum and the remaining white solid dissolved in deuterated chloroform.  $^1\text{H}$  NMR spectroscopy was used to calculate the conversion from the integrals of the imidazolium salt and the copper-NHC complex at  $\delta$  7.62 ppm (s, 2H) and 7.00 ppm (s, 4H) respectively. Each reaction was performed a minimum of three times and a mean of the conversion at each flow rate was calculated for each spacer. This was plotted against the residence time and the standard error calculated for each point (Graph 3.2). Although there is some overlap in errors, the general trend is that the 'short wiggly' spacer gave the best conversion, followed by the 'wiggly', 'thin normal' and then the 'normal' spacer gave the lowest conversion. The differences in conversion which were observed are likely to arise from the different geometries of the spacers which could affect the mass transfer within the reactor.





**Graph 3.2:** The different spacers at a range of flow rates.

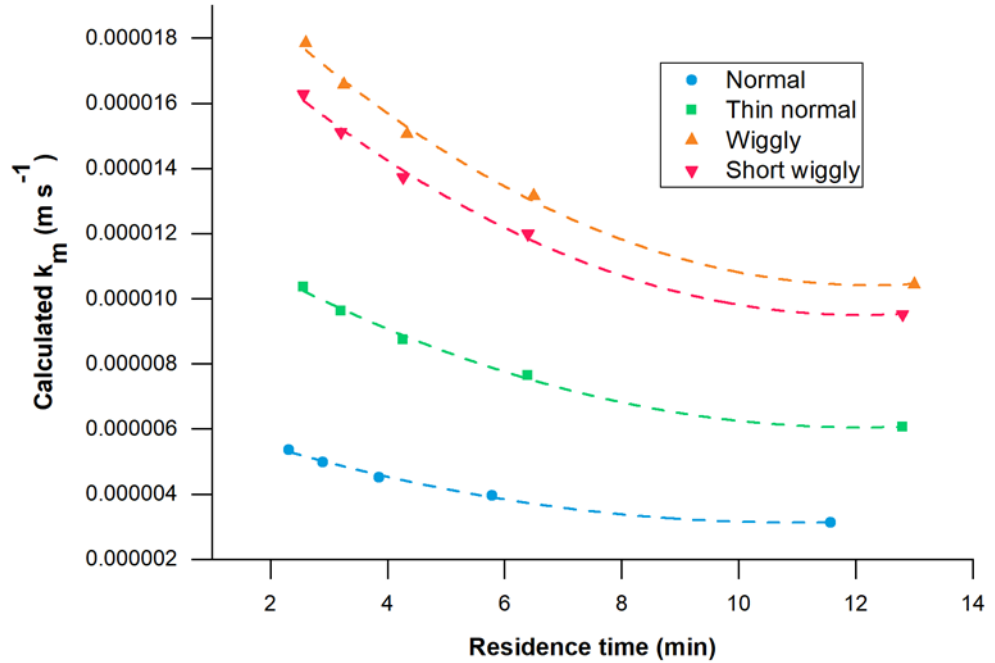
### 3.2.2. Modelling mass transfer

Equation 3.1 was used to estimate which spacer provides the most efficient mass transfer. Equation 3.1 uses the dimensions of a flow channel, along with the flow rate and diffusivity constants to estimate the mass transfer coefficient. It is based upon a similar equation used by Colli *et al* which used  $L$  instead of  $L/N$ .<sup>164</sup> Mass transfer is highest directly after the flow has been disturbed, such as after a segmented electrode as demonstrated by Colli *et al*.<sup>171</sup> If the turns in our system disturb the flow, and thereby influence mass transfer, then this could be approximated by dividing the length of the flow channel into segments. The number of segments ( $N$ ) would be equal to the number of straight sections or the number of turns plus one. This gives Equation 3.1, which assumes that each turn provides perfect mixing. This assumption is unlikely to be true, but should provide a qualitative estimate to rank the efficiency of each flow channel.

$$k_m = 1.85 \frac{D}{d_h} \left( \frac{d_h^2 \cdot \dot{V}}{\nu h w \frac{L}{N} S_c} \right)^{\frac{1}{3}}$$

**Equation 3.1** Calculating the mass transfer coefficient ( $k_m$ ).  $D$  is the diffusion coefficient,  $d_h$  the hydraulic diameter,  $\dot{V}$  the flow rate,  $\nu$  the kinematic viscosity,  $h$  and  $w$  the height and width of the channel respectively,  $L$  the length,  $N$  the number of segments and  $S_c$  the Schmidt number.

The results of this simple mass transfer model are summarised in Graph 3.3 and show that the 'wiggly' spacer is expected to perform the best as this has the highest number of turns (164 for 2 spacers), followed the 'short wiggly' (120 turns for 4 spacers) and then the 'thin normal' (28 turns, 4 spacers) and the 'normal' (7 turns, 1 spacers). In contrast to experimental results, this simple model under predicts the performance of the 'short wiggly' spacer. The primary difference is that this spacer has a small individual volume, meaning that several spacers must be used to have a comparable volume. The consequence of this is that the flow path passes through the electrode more often. Equation 3.1 treats any change in direction of the flow path as equivalent; the effect of a turn being equal to that of passing through an electrode. The discrepancy between the predicted mass transfer (Graph 3.3) and the conversion (Graph 3.2) would suggest that any mass transfer induced by passing through the electrode is not equivalent to the mass transfer caused by a turn.



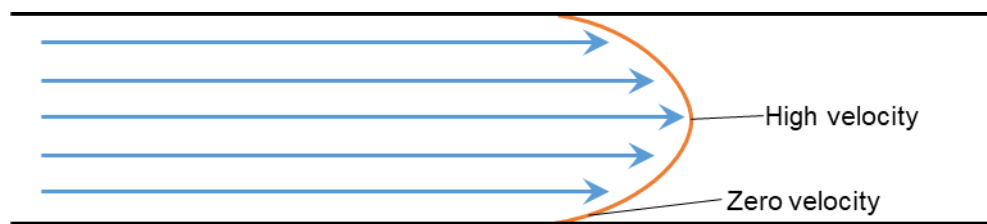
**Graph 3.3:** Estimated mass transfer coefficients ( $k_m$ ) using Equation 1.



### 3.3. Computational fluid dynamics

#### 3.3.1. Basic principles of fluid dynamics

Fluid dynamics is a discipline which studies and describes the behaviour of fluids. Broadly speaking, fluid flow can be categorised as either laminar or turbulent. In laminar flow fluid particles maintain a constant velocity relative to the other particles, resulting in layers of fluid sliding past each other (Figure 3.10), consequently mixing usually occurs *via* diffusion. By contrast turbulent flow is highly irregular, with fluid particles having different velocities resulting in the formations of eddies and a non-uniform flow regime which aids mixing.<sup>172</sup>



**Figure 3.10:** Laminar flow consists of parallel layers of fluid moving past each other, with the largest velocity found in the centre of channels.

The Reynolds number of a fluid can be used to estimate whether laminar or turbulent flow dominates. This dimensionless number describes the ratio of inertial forces to viscous forces (Equation 3.2).<sup>173</sup> If the Reynolds number is less than 2000 then the flow is usually assumed to be laminar. Consequently if the flow channel has small dimensions or the fluid is flowing slowly laminar flow is likely to dominate.

$$Re = \frac{\rho u L}{\mu}$$

**Equation 3.2:** Calculating the Reynolds number ( $Re$ ) where  $\rho$  is the fluid density,  $u$  is the velocity,  $L$  is the length of the channel and  $\mu$  is the kinematic viscosity.

The type of flow (*i.e.* turbulent or laminar), along with the type of fluid (incompressible like a liquid or compressible like a gas), is important in determining how we describe the motion of a fluid. The Navier-Stokes equations govern how fluids move and are built upon Newton's second law of motion (Equation 3.3).<sup>173</sup> Conventionally, this is written in the form  $ma = F$ ; where the mass and acceleration components are governed by the density and velocity of the fluid (the inertial forces) and the force is a combination of the pressure, the viscous forces and any external forces applied to the fluid. Depending on

the circumstances the Navier-Stokes equations cannot always be solved, but it can be simplified using assumptions based upon the type of flow and the type of fluid.

$$ma = F$$

$$\rho \left( \frac{\delta u}{\delta t} + u \cdot \nabla u \right) = -\nabla p + \nabla \cdot \left( \mu (\nabla u + (\nabla u)^T) - \frac{2}{3} \mu (\nabla \cdot u) I \right) + F$$

**Equation 3.3:** Newton's second law of motion (top) and its relation to the Navier-Stokes equation (bottom). Where  $m$  is mass,  $a$  is acceleration,  $F$  is force,  $\rho$  is the fluid density,  $p$  is pressure,  $\mu$  is kinematic viscosity,  $u$  is the velocity and  $T$  is the temperature.

For example the Navier-Stokes equations are always accompanied by a continuity equation which says that mass is conserved. If the fluid is incompressible, which is the case for most liquids, then the continuity equation can be simplified to  $\nabla \cdot u = 0$ . This also allows  $\frac{2}{3} \mu (\nabla \cdot u) I$  to be removed from the Navier-Stokes equation. If the flow is laminar then it is assumed that the inertial forces are inconsequential when compared to the viscous forces and they can therefore also be ignored. In the instance of the electrochemical flow reactors examined in this chapter both of these are the case, allowing the Navier-Stokes equation to be simplified to Equation 3.4.<sup>173</sup>

$$\nabla \cdot u = 0$$

$$0 = -\nabla p + \nabla \cdot \left( \mu (\nabla u + (\nabla u)^T) \right) + F$$

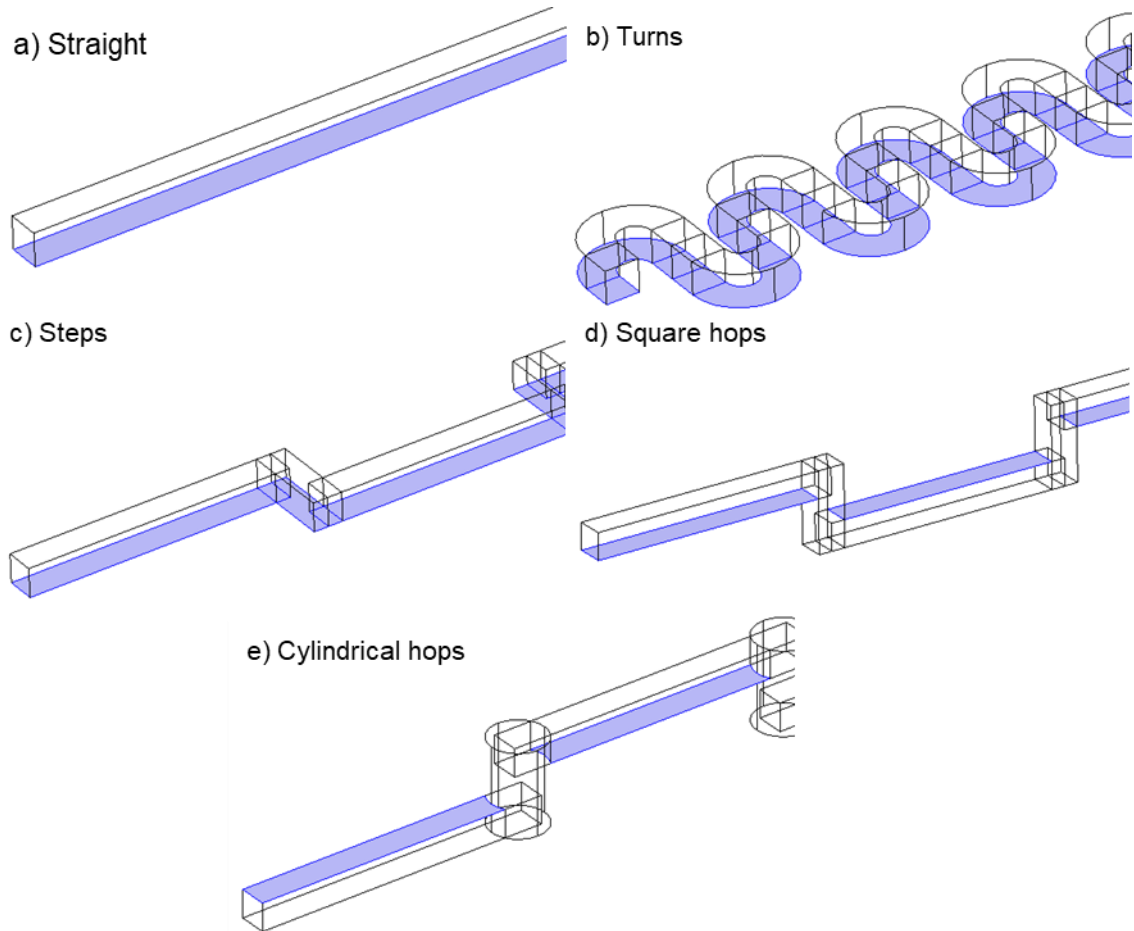
**Equation 3.4:** Continuity equation (top) and simplified Navier-Stokes equation (bottom). Where  $u$  is velocity,  $p$  is pressure,  $\mu$  is kinematic viscosity,  $T$  is temperature and  $F$  is force.

### 3.3.2. Simulating an electrochemical flow reactor

Fluid flow can be modelled computationally using computational fluid dynamics (CFD) and is often conducted using commercially available software. COMSOL multiphysics was used in the study to construct virtual flow channels, simulate fluid flow through them and visualise the results.

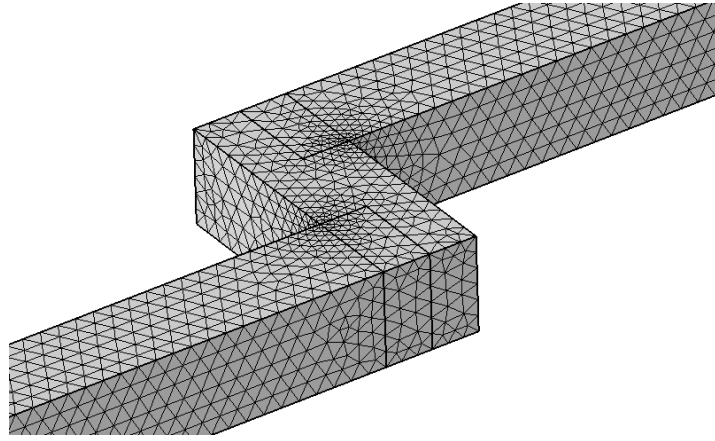
Five flow channels were constructed; a straight channel, a channel with s-shaped turns, a channel with right angled stepped turns, a channel with square hops and a channel with cylindrical hops, each with a channel height and width of 1 mm (Figure 3.11). The straight channel was a simple cuboid, 100 mm in length while the channel with turns featured twenty 180° turns and a path length of 100 mm. The geometric shape of the channels with stepped turns and square hops were identical, the only difference being

which surface was modelled as an electrode; ten stepped turns were connected with straight sections, giving a path length of 120 mm. This was to try and distinguish between the shape of the channel and the act of passing through an electrode. The cylindrical hops had the same basic shape as the square hops, but with cylinders connecting the straight sections instead of cuboids. This was to replicate the flow paths in section 3.2 which had wider holes when passing through an electrode. Consequently the volume was 159 cm<sup>3</sup>, slightly larger than the volume of the square hops (120 cm<sup>3</sup>) although the mean path length remained the same.



**Figure 3.11:** Five flow channels were constructed within COMSOL multiphysics. One wall in each channel was chosen to simulate the surface of the electrode, shown in blue.

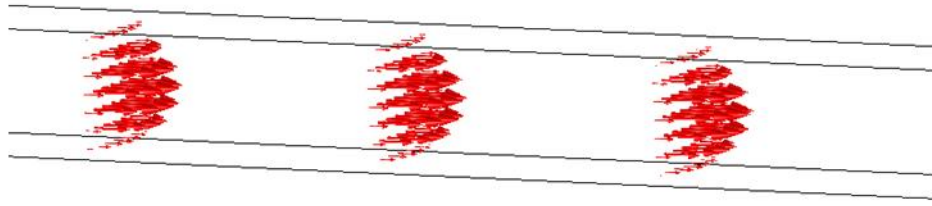
An unstructured mesh was generated for each channel. This is where the channel geometry is divided into a network of polyhedra, enabling each polyhedron to be solved individually (Figure 3.12). The main advantage of using an unstructured mesh is that the size of the polyhedra may be changed so that greater resolution can be achieved at points of interest (*i.e.* at corners or close to the boundaries) without unnecessarily increasing the amount of computing power required for the rest of the model.



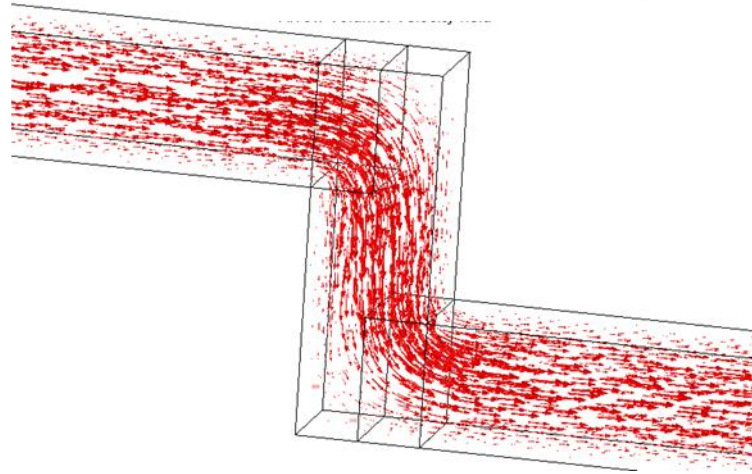
**Figure 3.12:** Unstructured mesh for steps and square hops.

The 'laminar flow' and 'transport of dilute species' packages within COMSOL were used to model the fluid flow within the flow channels. To do this, velocity fields were modelled using Navier-Stokes equations assuming that the flow was at steady state. A 'no slip' condition was applied to the wall, meaning the velocity of fluid next to the walls would be treated as  $0 \text{ m s}^{-1}$ , whilst the inlet was set to an initial velocity of  $0.001 \text{ m s}^{-1}$  with a fully developed flow. Visualisation of the fluid flow shows clear laminar flow with a well-developed parabolic profile (Figure 3.13). The ability of eddies to form at sharp corners during laminar flow has been demonstrated,<sup>174</sup> however no evidence of this was observed during the CFD.

a) Straight



b) Step and square hops



**Figure 3.13:** Velocity fields calculated using Navier-Stokes equations. No eddies or back mixing can be seen. Size of the arrows corresponds to their relative velocity.

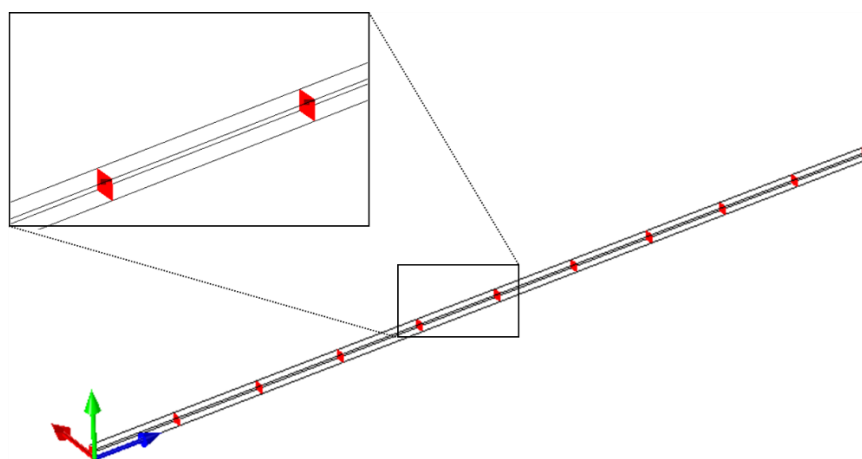
The 'transport of dilute species' package was used to simulate species leaving the surface of an electrode. To do this one wall of the channel (shown in blue, Figure 3.11) was set to a concentration of  $1 \text{ mol m}^{-3}$ , whilst the initial concentration of the inlet was set to  $0 \text{ mol m}^{-3}$ . The remaining boundaries were to set to have no flux. Equation 3.5 was used to model the concentration within the channel using velocity fields produced from the Navier-Stokes equation (Equation 3.4). The bottom wall of the straight channel, the channel with turns and the stepped turns was used to act as the electrode. For the square hops and the cylindrical hops the wall acting as an electrode was alternated between the top and bottom wall each time the channel passed through a hop.

$$\nabla \cdot J_i + u \cdot \nabla c_i = R_i$$

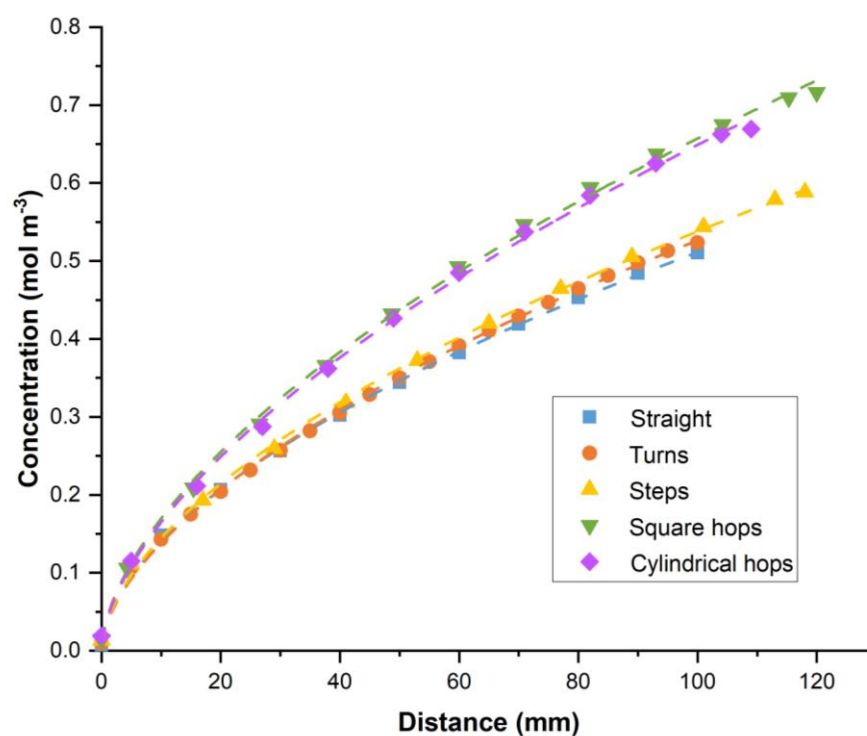
$$J_i = -D_i \nabla c_i$$

**Equation 3.5:** Calculating the concentration. Where  $J_i$  is the mass flux diffusive flux vector,  $u$  is the flow velocity vector,  $c_i$  is the concentration of the species,  $R_i$  is the reaction rate expression and  $D_i$  is the diffusion coefficient (set to  $1 \times 10^{-9} \text{ m}^2 \text{ s}^{-1}$ ).

To obtain the concentration of the species in the bulk solution planes were cut across the channel at regular intervals and the average concentration for the surface of each plane was calculated (Figure 3.14). The concentration was then plotted against the distance along each flow channel (Graph 3.4). The straight channel, turns and stepped turns all performed similarly, with a concentration of between 0.51 and 0.54 mol m<sup>-3</sup> at 100 mm along the channel. However the two channels with hops were calculated to have a much higher concentration in the bulk solution with 0.67 and 0.66 mol m<sup>-3</sup> for the square hops and cylindrical hops respectively at 100 mm. The slightly lower concentration seen for the cylindrical hops is due to the smaller surface area of the electrode; 91 mm<sup>2</sup> for the square hops compared to 75 mm<sup>2</sup> for the cylindrical hops. This further supports the hypothesis that hops increase the effective mass transfer coefficient, facilitating the removal of material from the electrode surface and into the bulk solution.



**Figure 3.14:** Plains perpendicular to the direction of fluid flow (shown in red) were used to obtain the average concentration at intervals along the flow channels.

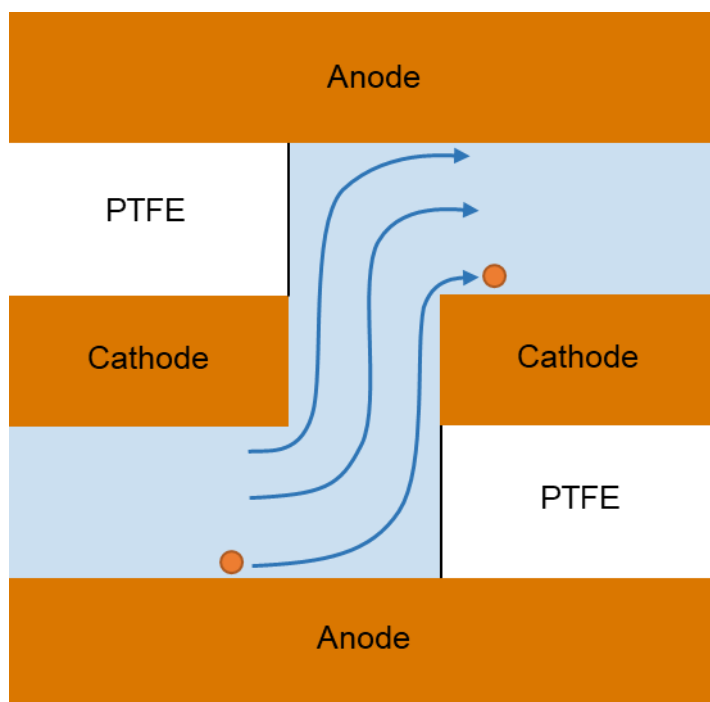


**Graph 3.4:** Mean concentration of a species along a flow channel.

### 3.4. The effect of hops on mass transfer

#### 3.4.1. Rationalising the effect of hops

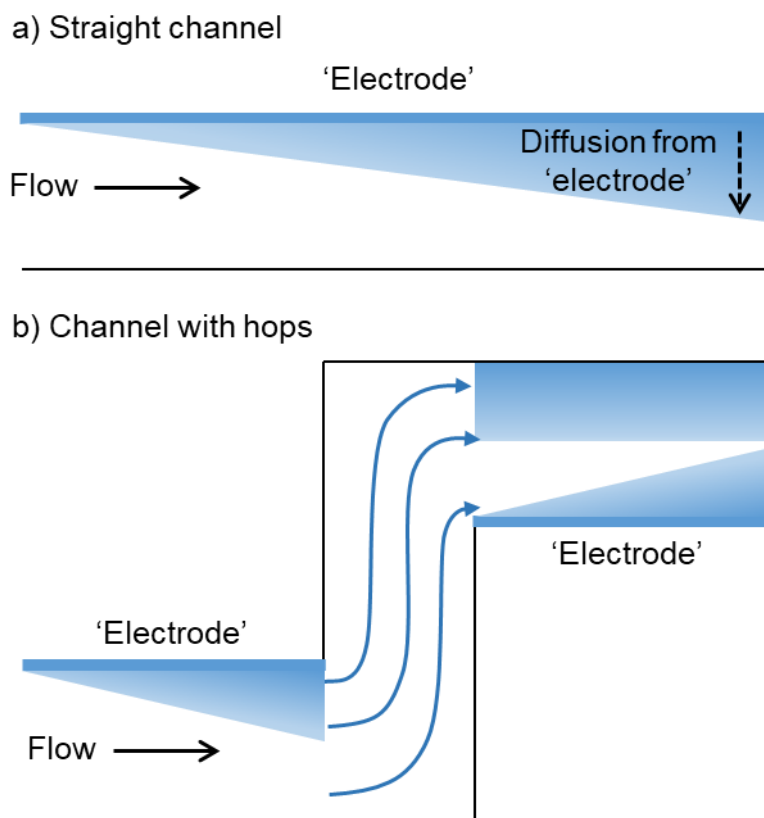
Electrochemistry is a heterogeneous process which does not occur uniformly in a flow channel as it can only occur at the surfaces of the electrodes which make up the top and bottom of the channel.<sup>108,139,157</sup> For the synthesis of **Cu1**, the intermediates produced at each electrode must come into contact with each other. The exact mechanism for this is currently unknown, however it is likely that mass transfer across the channel and between the two electrodes will be important (Figure 3.15).



**Figure 3.15:** Representation of a hop in the flow channel.

All of the flow channels tested in section 3.2.1 had a varying number of turns which were shown through CFD to increase the efficiency of mass transfer, although to a lesser extent than when the solution passed through the electrode in a 'hop'. Small Reynolds numbers, due to the dimensions of the reactor, mean that laminar flow dominates. In passing through a hop, the solution in contact or in proximity to the bottom electrode remains at the bottom of the flow channel, but is now in contact with the electrode of opposite polarity and *vice versa* (Figure 3.15). Consequently metal ions produced at the anode quickly come into close proximity with the cathode and the carbene generated there. A further effect, which is observed in the CFD models, is that of concentration gradients (Figure 3.16). In the model, one surface has a concentration of 1 (shown in blue) and the solution entering the channel has a concentration of 0. Therefore at the beginning of the channel there is a large concentration gradient. This gradient decreases along the channel as the concentration of the bulk solution near to the blue surface increases. After a hop the blue surface is brought into contact with solution that has a low concentration, resulting in a large concentration gradient and increasing the rate of diffusion.

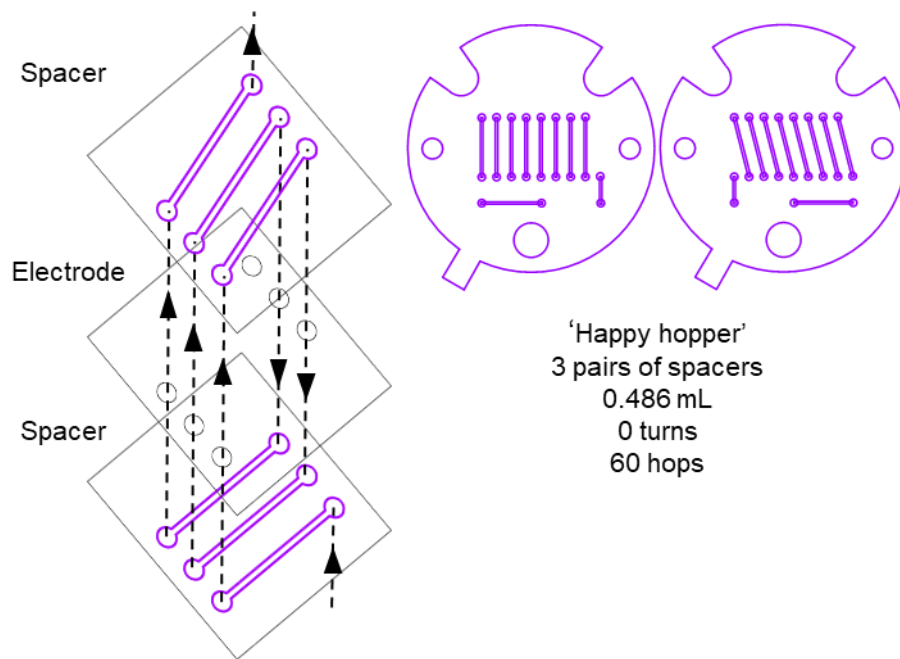




**Figure 3.16:** Diagram CFD results for a) straight channel and b) channel with hops. One side of the flow channel (the 'electrode') is shown in blue. Species diffuse away from this surface into the bulk.

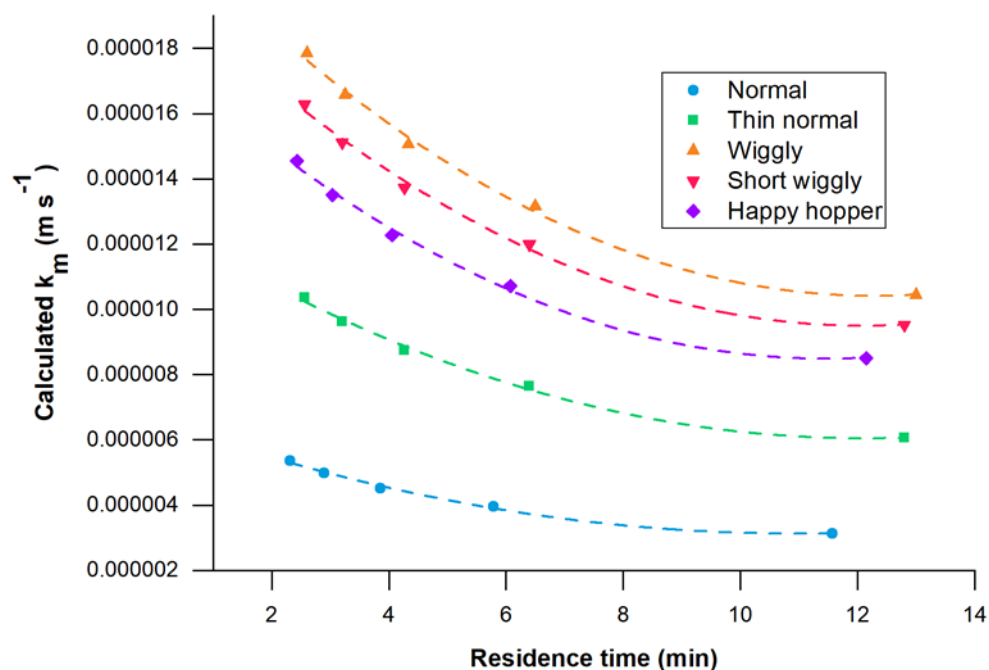
### 3.4.2. The happy hopper

To test whether extra hops improved the conversions obtained from the reactor a new flow path was designed which only featured hops in the absence of turns. The original hopper had a narrow channel width and more than eighty hops. This led to a large pressure drop and consequently required the reactor to be bolted together with significantly more force than was required for the other spacers to prevent it leaking. This led to the deformation of the PTFE channels, such that the channels become blocked and made the original hopper unusable. It was redesigned to have a smaller number of hops and with wider channels (0.5 mm). This happy hopper was a less extreme version of the original hopper and consisted of a pair of PTFE spacers that each had ten straight channels connected to each other by a series of hops (Figure 3.17). Three pairs of happy hopper spacers gave a volume of approximately 0.5 mL, allowing its performance to be compared with the other spacers.



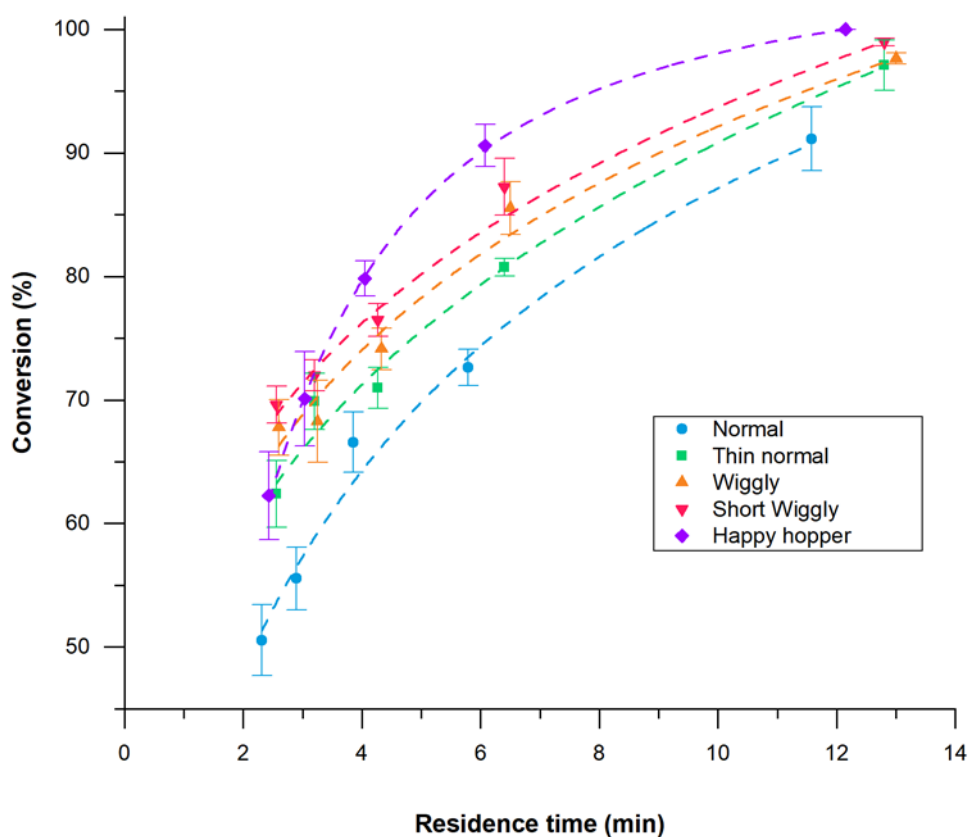
**Figure 3.17:** The happy hopper spacer. Left: how the straight channels are connected via hops. Right: the layout of the spacers which are used as a pair.

The happy hopper was added to the simple model for mass transfer and based upon three pairs having 60 hops, the happy hopper would be expected to have inferior mass transfer when compared to the short wiggly spacer. As discussed in section 3.2.2, this model assumes hops and turns are equal with respect to mass transfer and consequently it would not be surprising for the happy hopper to display an improved experimental performance with respect to the other spacers despite poor performance in the simple mass transfer model.



**Graph 3.5:** Estimated mass transfer using Equation 1.1, including the happy hopper.

The production of **Cu1** was used to evaluate the efficiency of mass transfer of the happy hopper in the same way as the other four spacers by varying the flow rate (Graph 3.6). At the slowest flow rate of  $0.04 \text{ mL min}^{-1}$  full conversion was obtained, as determined by  $^1\text{H}$  NMR spectroscopy, higher than that of the other spacers. This trend continued, with higher conversions observed at longer residence times. At shorter residence times (and faster flow rates) a lower conversion was observed. The exact reason for this is unclear, but could conceivably be due to the time scale of the reaction. If the polarity of the electrode is alternated more quickly than the reaction can take place then a drop in conversion would be expected. The mechanism, and by extension the rates for this reaction are poorly understood and consequently it is unclear whether this effect is responsible for the reduction in conversion or alternative effects are at play.



**Graph 3.6:** Different spacers, including the happy hopper at a range of flow rates.

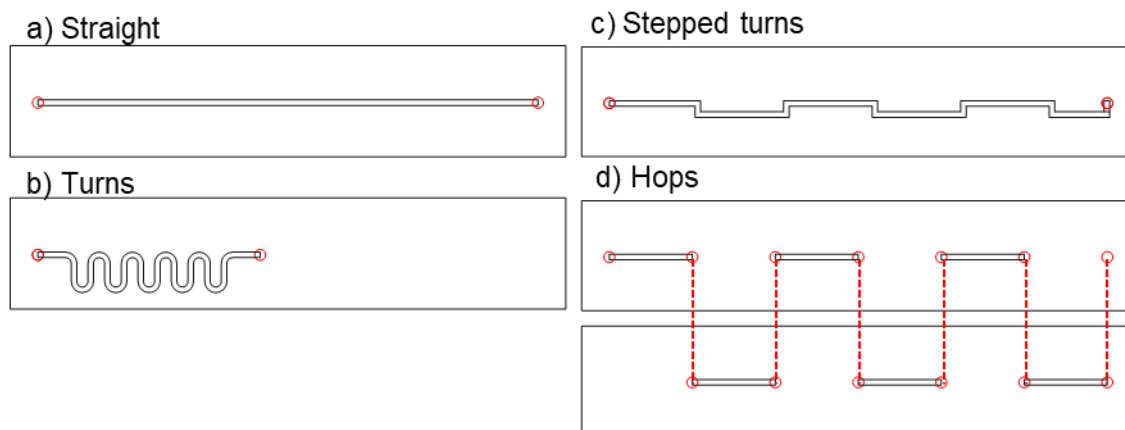
### 3.5. A systematic study

#### 3.5.1. Design of flow channels

Initial investigations used flow paths that varied from one another with regards to channel width, the number of turns and the number of hops. This was due to the design of the third generation reactor which was made with the synthesis of organometallic complexes in mind, consequently disentangling the effects of hops and turns was challenging. A more systematic approach would allow the effects that hops and turns have on mass transfer to be examined independently from one another. This was conducted with help of Sarah Boyall, a summer student in the Willans group.

Four flow paths were designed to have the same volume (0.090 mL), length (90.0 mm) and cross sectional area of flow path (1.0 mm x 1.0 mm) to make them easily comparable (Figure 3.18). These flow paths were laser cut into pieces of PTFE to be used as spacers in a reactor which had the same stacked plate design as the second and third generation reactors. A straight channel with no hops or turns was designed as the control. One channel had five 's-shaped' turns and another five hops, where the channel passed through the electrode. A fourth 'stepped turns' channel was designed with 5 dog-leg turns

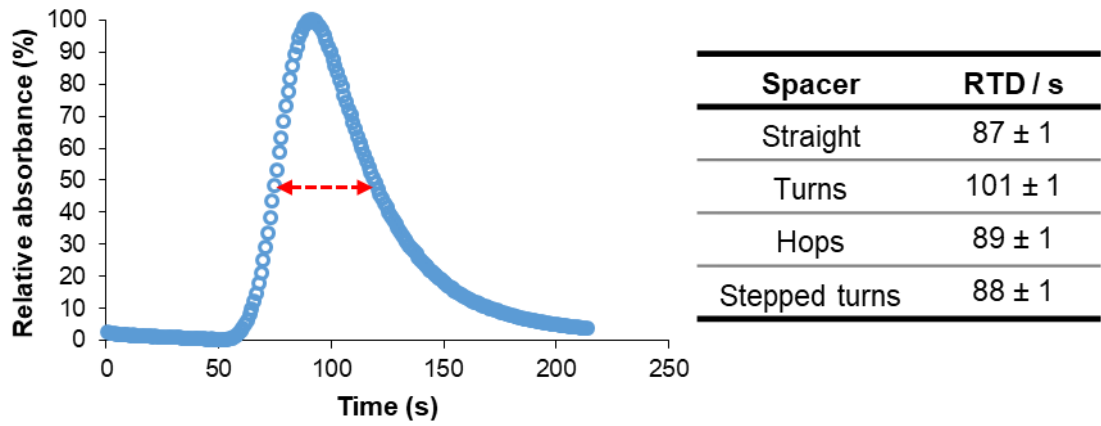
to provide the same shape and dimensions of the hops spacer, but without passing through the electrode. The stepped turn channel was designed as a control to see if any difference in the hops channel was due to the shape of the hops or the act of passing through the electrode.



**Figure 3.18:** Flow channels used in the systematic study.

### 3.5.2. Characterisation of the spacers

The residence time distribution of the four spacers were obtained by pumping acetonitrile through the reactor and using valves to introduce short pulses of methylene blue in acetonitrile into the reactor. The absorbance of the solution leaving the reactor was then measured using an inline UV-Vis spectrometer. The residence time distribution was calculated as the time between 50% relative absorbance over an average of four runs (Figure 3.19). The residence time distributions for the straight, hops and stepped turn spacers were identical, suggesting that the shape of the hops has little to no effect on back mixing. The residence time distribution was significantly longer for the turns spacer, however this is not unexpected. The volume of the turns spacer is the same as the other spacers, so the amount of time that reaction solutions are in contact with the electrodes should be the same, however another flow channel (which is insulated from the electrodes) is required to bring the solution to the outlet. Consequently the residence time distribution of the turns spacer is anticipated to be comparable to the other spacers when the solution is in contact with the electrodes.



**Figure 3.19:** The residence time distribution was calculated as the time between 50% relative absorbance and the residence time distributions for the four spacers.

Diffusion and back mixing both contribute to the longitudinal spread of a tracer in a tubular reactor, which is characterised by the axial dispersion coefficient ( $D_{ax}$ ).<sup>175</sup> An estimate of the axial dispersion coefficient can be obtained by fitting a model to experimental data. When the Reynolds number is less than 100 two models may be used, a symmetrical model (Equation 3.6) which is most appropriate when axial dispersion is small and an asymmetric model (Equation 3.7) when axial dispersion is high.<sup>176</sup> The amount of axial dispersion is described by the vessel dispersion number ( $N_L$ ),  $N_L$  is in turn calculated from the axial dispersion coefficient (Equation 3.8). As  $D_{ax}$  and  $N_L$  are both unknown it is customary to fit both models and select the one which corresponds to the experimental data the closest, from this  $N_L$  may be calculated.<sup>176</sup> The asymmetric model was most similar to that obtained for the four spacers investigated in this study (Graph 3.7), giving an  $N_L$  of 0.06 and an axial dispersion coefficient of  $2.5 \times 10^{-4} \text{ m}^2 \text{ s}^{-1}$ . The large value of  $N_L$  would suggest that some back mixing does occur, however the similarities in residence time distributions across the different spacers indicates that there is an equal amount of back mixing in each spacer.

$$N_L < 0.01: E_{t,ADM} = \sqrt{\frac{u^3}{4\pi D_{ax}L}} \exp\left[-\frac{(L-ut)^2}{4D_{ax}L}\right]$$

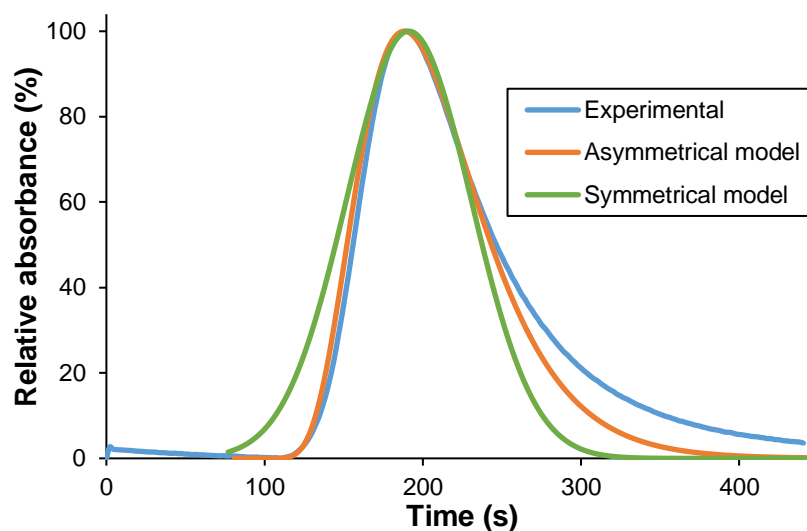
**Equation 3.6:** Symmetrical model for calculating the axial dispersion coefficient ( $D_{ax}$ ) for small  $N_L$  values. Where  $u$  is the average velocity,  $t$  is the time,  $L$  is the length and  $E_t$  is the exit time.

$$N_L > 0.01: E_t = \frac{u}{\sqrt{4\pi D_{ax}t}} \exp\left[-\frac{(L-ut)^2}{4D_{ax}t}\right]$$

**Equation 3.7:** Asymmetrical model for calculating the axial dispersion coefficient ( $D_{ax}$ ) for large  $N_L$  values. Where  $u$  is the average velocity,  $t$  is the time,  $L$  is the length and  $E_t$  is the exit time.

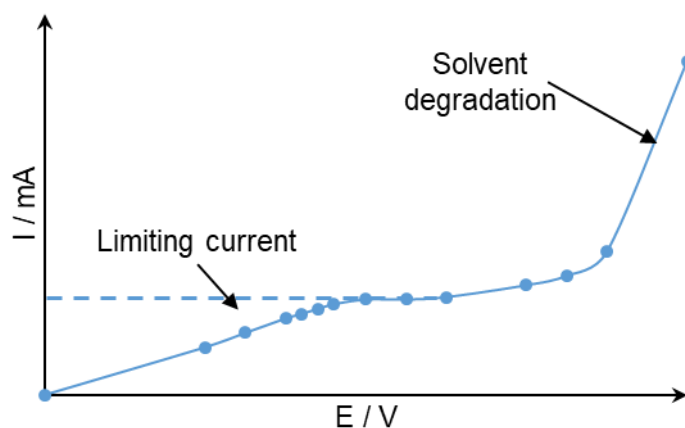
$$N_L = \frac{1}{Pe_L} = \frac{D_{ax}}{uL}$$

**Equation 3.8:** Calculating the vessel dispersion number ( $N_L$ ). Where  $Pe_L$  is the Peclet number,  $D_{ax}$  is the axial dispersion coefficient,  $u$  is the average velocity and  $L$  is the length.



**Graph 3.7:** Comparison of symmetrical and asymmetrical models of residence time distributions with experimental values.

Mass transfer coefficients can be calculated in electrochemical flow reactors by using the limiting current method.<sup>177</sup> When an electrochemical reaction is taking place there is the transfer of electrons, which can be observed as a current. By increasing the potential, the rate of the electrochemical step is increased and consequently the current. When the mass transfer of species to the electrode surface becomes the rate limiting step the current plateaus despite an increase in the potential (Figure 3.20). From this the mass transfer coefficient may be calculated (Equation 3.9).<sup>27</sup> An aqueous solution of  $K_3Fe(CN)_6$  and  $K_4Fe(CN)_6$  with a supporting electrolyte was used. Initially copper electrodes were used, however a suitable voltammogram could not be obtained and blue deposits were observed, consistent with the electrochemical formation of Prussian blue.<sup>178</sup>



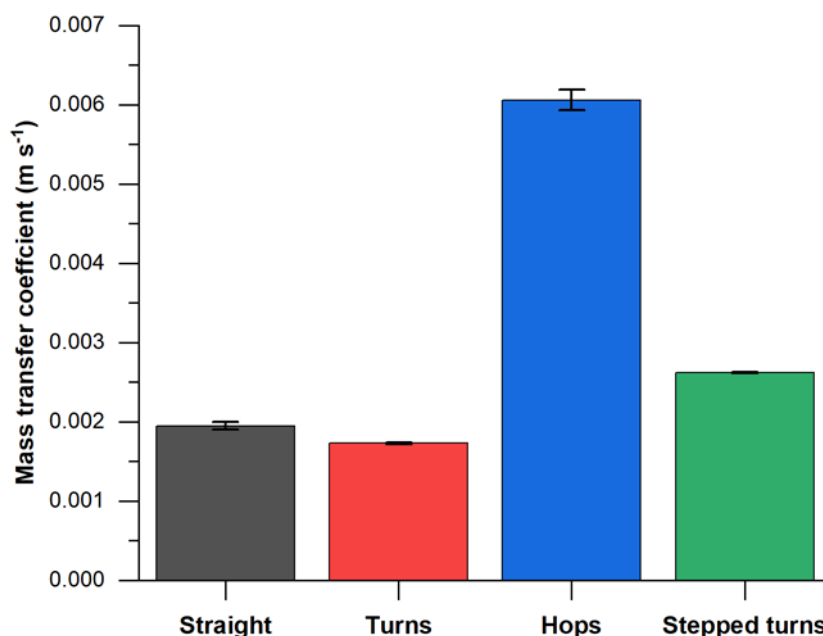
**Figure 3.20:** A schematic representation of a typical voltammogram used to calculate the limiting current.<sup>177</sup>

$$k_m = \frac{I_{lim}}{nFAC_B}$$

**Equation 3.9:** Calculating the mass transfer coefficient ( $k_m$ ) from the limiting current ( $I_{lim}$ ). Where  $n$  is the number of electrons exchanged,  $F$  is the Faraday constant and  $C_B$  is the concentration of the bulk solution.<sup>177</sup>

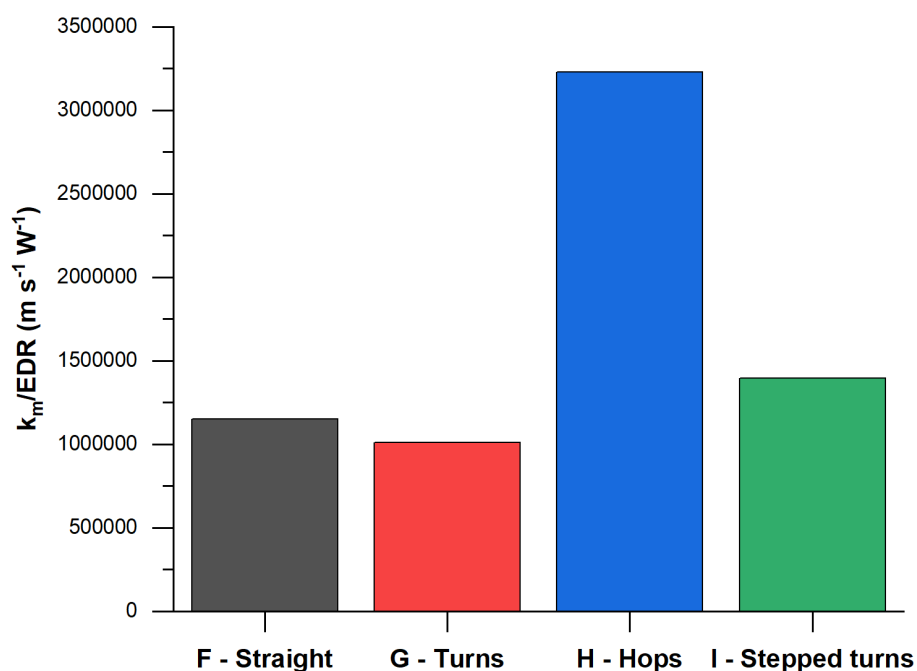
The copper electrodes were replaced with graphite electrodes and the solution passed through it whilst the potential was slowly increased. A plateau was only observed when a low flow rate ( $0.04 \text{ ml min}^{-1}$ ) was used, suggesting that mass transfer is not the rate limiting step at higher flow rates. The straight, turns and stepped turned spacers all had nearly identical mass transfer coefficients. By contrast the hops spacer had a mass transfer coefficient 5 times higher, demonstrating that hops do increase mass transfer significantly (Graph 3.8). Importantly the stepped turns spacer's mass transfer coefficient was comparable to both the straight and turns spacer confirming that the increased mass transfer coefficient of the hops spacer is not due to the shape of it.





**Graph 3.8:** Mass transfer coefficients for the four spacers in the systematic study.

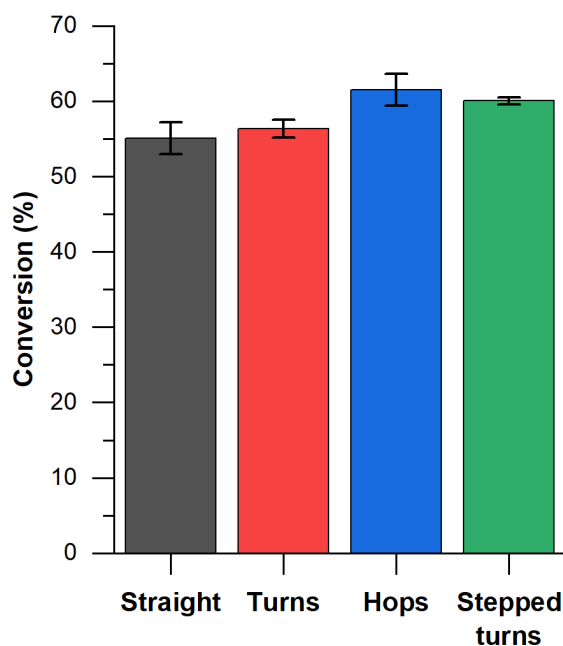
When scaling up reactors the energy input (*via* pumping power due to pressure drop) is of considerable importance. To investigate this the energy dispersion rate was calculated using pressure drops obtained from the CFD studies; these were scaled to reflect the slightly shorter channel lengths. The channels with steps and hops had a slightly higher pressure drop, resulting in an energy dispersion rate 10% higher. The ratio between mass transfer coefficients and energy dispersion rates was calculated, with hops providing a threefold increase when compared to turns, offsetting the slight increase in energy requirements (Graph 3.9). This also demonstrates that the increase in effective mass transfer is due to the hops themselves and how the position of the electrode changes relative to the channel, as opposed to any changes in the flow regime.



**Graph 3.9:** Ratio of mass transfer coefficient to energy dispersion rate for the different spacers.

### 3.5.3. Synthesis of copper species

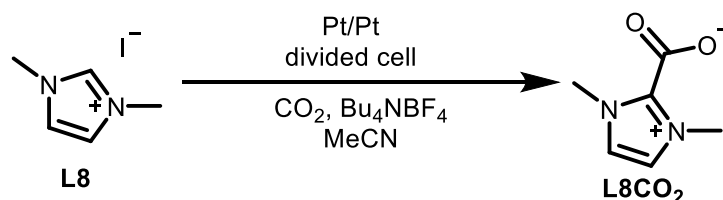
To probe whether the increase in mass transfer coefficient translated into more efficient reactions, **Cu1** was synthesised in the systematic flow channels. Only a small increase in the conversion was observed for the hops spacer at  $0.04 \text{ mL min}^{-1}$  (Graph 3.10), suggesting that the production of **Cu1** is not mass transfer limited in this reactor. The limiting current method for calculating mass transfer coefficients uses  $\text{K}_3\text{Fe}(\text{CN})_6$  in excess and consequently only considers the reaction at one of the electrodes.<sup>177</sup> By contrast, the synthesis of **Cu1** involves species generated at both electrodes coming into contact with one another and this additional complexity might explain why an increase in the conversion to **Cu1** is not observed for the hops spacer.



**Graph 3.10:** Conversion of **L1** to **Cu1** in the systematic spacers with an applied potential of 1.8 V and a flow rate of 0.04 mL min<sup>-1</sup>.

#### 3.5.4. Carboxylation of imidazoliums

The carboxylation of imidazoliums was chosen as a simpler version of the synthesis of **Cu1** to examine whether channel geometries can change the outcome of a reaction. The idea was to look at the formation of free carbenes at the cathode by trapping them *via* reaction with dissolved CO<sub>2</sub>. This reaction was previously reported by de Robillard *et al.*<sup>150</sup> They investigated the carboxylation of a range of non-bulky imidazoliums by reducing the imidazoliums to carbenes at the cathode and then reacting the carbenes with CO<sub>2</sub>. De Robillard *et al* conducted this reaction in a divided cell using platinum electrodes and a supporting electrolyte. CO<sub>2</sub> was bubbled through the reaction whilst the imidazolium was electrolysed (Scheme 3.1).<sup>150</sup>

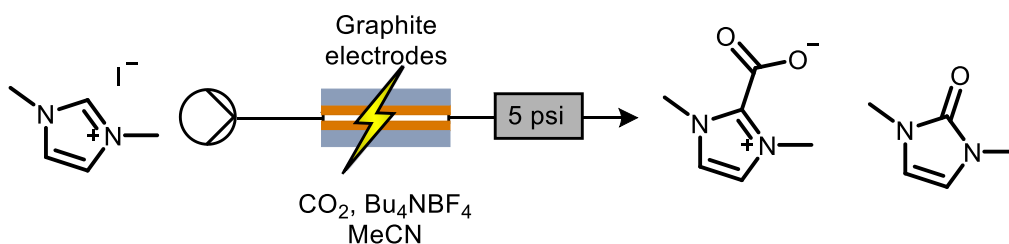


**Scheme 3.1:** Carboxylation of imidazoliums with the conditions used by de Robillard *et al.*<sup>150</sup>

The bottle reactor was used for initial investigations looking at transferring de Robillard *et al.*'s methodology into a non-divided cell. Dimethyl imidazolium iodide (**L8**) was

electrolysed in the bottle reactor without an electrolyte using graphite electrodes whilst CO<sub>2</sub> was bubbled through the solution. <sup>1</sup>H NMR spectroscopy showed a conversion of 33%. Although this is significantly lower than previously reported (77%)<sup>150</sup> the conditions are more suitable for a flow reaction; the reaction can be conducted in an undivided cell and graphite electrodes can be used instead of platinum. **L1** was also tried in the bottle reactor, but this gave no product, possibly due to its bulky nature.

To transfer the reaction into flow the reaction solutions were prepared under argon and then CO<sub>2</sub> was bubbled through the solution for 30 minutes to saturate the solution and once in the reactor a back pressure regulator was required to keep the CO<sub>2</sub> in solution (Scheme 3.2). Initial attempts using graphite electrodes found that the results were not very reproducible, with the conversion varying by large amounts. To try to solve this the cathode was swapped for a copper electrode because metal electrodes are generally easier to clean in a consistent way. Similarly potentiostatic conditions were found to be more reliable than galvanostatic conditions.



**Scheme 3.2:** Carboxylation of imidazoliums under continuous conditions gives a mixture of products.

Interestingly when conducting the reaction in flow two products are observed along with the starting material. One is the desired carboxylate, the other is thought to be an imidazolone. Although it is unclear where the oxygen is coming from, it should not matter too much as, like the carboxylate, the imidazolone is also formed from the carbene. Consequently the combined conversion of the carboxylate and imidazolone will still provide information for how much of **L8** is being reduced to form a carbene.

The outlet of the reactor was sampled at regular intervals after two residence times had elapsed to try and ascertain whether steady state has been reached. Steady state was not reached for any of the spacers; the conversion increased over time until between 60 and 80 minutes before reducing again. This could suggest that something is happening at the surface of the electrode which is reducing the effectiveness of the reaction.

Whilst running the time course experiments it was noted that the reactions remained poorly reproducible, despite changing the electrodes, with the current varying

considerably. To try and rectify this electrolyte was added back into the reaction to try and ensure that the solution had a constant resistance during the reaction. This helped greatly and allowed the reaction to be reproducible, although steady state could still not be reached. The aim of this study was to examine the channel geometry, rather than the surface chemistry of the electrodes. Consequently the lack of a steady state wasn't of huge concern as long as steady state wasn't reached in a reproducible way. All four spacers gave conversions of approximately 30%, suggesting that this reaction is not limited by mass transfer.

### 3.6. Conclusions and future work

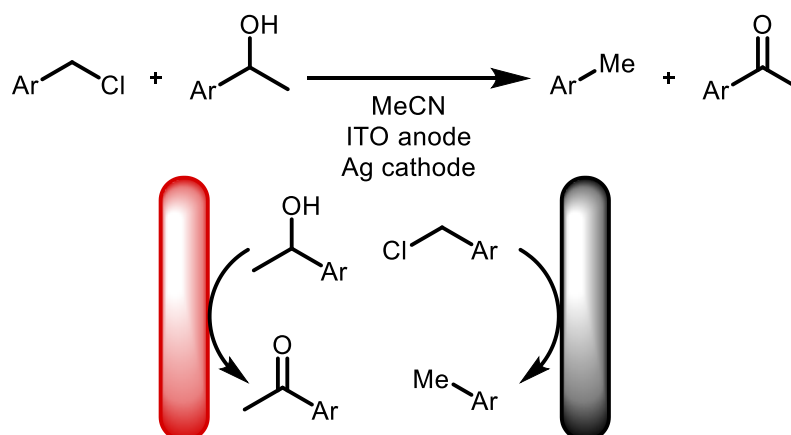
Five different flow channels have been used to investigate the efficiency of mass transfer within an electrochemical flow reactor. These results, combined with CFD modelling have demonstrated that turns and hops both increase the efficiency of mass transfer, but that hops have a greater effect possibly due to improved rates of diffusion. The improved performance of the hops could also be attributed to a 'reverse mass transfer', where the opposite electrode is brought close to the intermediates, as opposed to moving the intermediates across the channel to reach the other electrode. Furthermore, the increase in mass transfer has been exploited to give full conversion of **L1** to **Cu1** within an electrochemical flow reactor, whilst maintaining a small reactor volume. This underscores the importance of considering mass transfer when designing flow reactors, especially if the reaction has heterogeneous components.

A more systematic study was also conducted and the mass transfer coefficients for four spacers were obtained empirically, demonstrating that hops do increase mass transfer and that the increase is due to the nature of the hops, as opposed to the additional energy input from the (relatively modest) increase in pumping power required and that hops do not change the flow regime. However the increase in mass transfer did not correspond with an increase in the conversion of **Cu1**, possibly due to the added complexity of this reaction. A simpler reaction was used to further investigate this, where the carbene generated at the cathode reacts with carbon dioxide. This reaction, which was previously reported, was modified so that it could be conducted under continuous conditions. However no difference was observed between the different spacers suggesting that the reaction is not limited by mass transfer, at least in this reactor. Several products were produced when graphite and copper electrodes were used, furthermore the reaction was demonstrated to be unstable over time. Both of these observations suggest that some interesting surface chemistry is going on. Future studies could look at using glassy carbon electrodes to try and enable steady state to be reached.

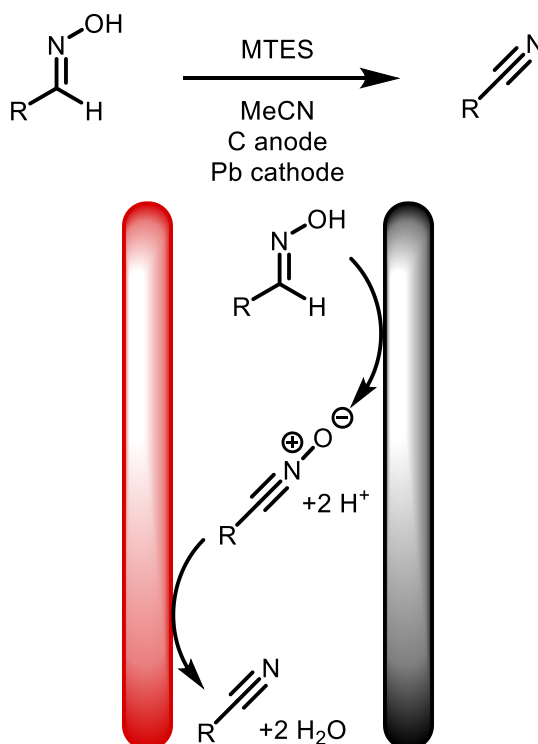
Previous studies within the group have demonstrated that alternating the polarity can be beneficial for reactions, however one of the limitations of this is that it requires both electrodes to be made of the same material.<sup>170</sup> When the polarity is alternated the position of each electrode changes, similar to when a solution passes through a hop. Hops could be used to provide similar benefits to alternating polarity for reactions where it is not possible to have identical electrodes, for example in organic electrochemical reactions where the anode and cathode are often made from different materials. Incorporating hops into the design of a reactor could be of particular benefit for organic

reactions where both electrodes are involved (i.e. the counter reaction is either useful or essential, as opposed to solvent degradation).

Hops could be used for paired electrosynthesis, or redox combined electrochemical reactions such as those reported by Amemiya *et al* (Scheme 3.3) and Hartmer *et al* (Scheme 3.4) respectively.<sup>179,180</sup> Reactions such as Hartmer *et al*'s synthesis of nitriles would benefit from being conducted in flow due to the small interelectrode gap, allowing species to diffuse between electrodes more quickly. This could be further enhanced by the use of hops to replenish the concentration of starting materials near the anode and then 'moving' the cathode closer to the intermediates that formed at the anode.



**Scheme 3.3:** Paired electrosynthesis reported by Amemiya *et al*.<sup>179</sup>



**Scheme 3.4:** Domino oxidation-reduction for the synthesis of nitriles, reported by Hartmer *et al*.<sup>180</sup>

### 3.7. Experimental

NMR data were obtained on either a Bruker AVneo 500 (CH dual cryoprobe) or Bruker Ascend 400 spectrometer.  $^1\text{H}$  NMR and  $^{13}\text{C}\{^1\text{H}\}$  chemical shifts were referenced against residual solvent peaks. Mass spectra were collected on a Bruker Daltonics (micro TOF) instrument operating in the electrospray mode. Elemental Analyses were performed by Mr Stephen Boyer at London Metropolitan University.

Where stated, reactions were carried out under an inert atmosphere of dry nitrogen or argon, using standard Schlenk line or glovebox technique. Anhydrous solvents were dried by passing over activated alumina to remove water and copper catalyst to remove oxygen *via* the Dow-Grubbs solvent system. They were collected onto activated molecular sieves to remove any remaining water. Acetonitrile was degassed with argon. All reagents were used as supplied, without further purification.

Flexible graphite sheets were donated by Dr Itziar Penafiel from the University of Manchester.

#### 3.7.1. Third generation reactor

##### 3.7.1.1. Reactor manufacture and assembly

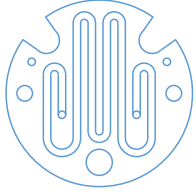

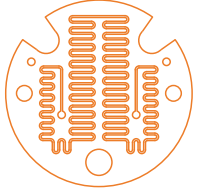
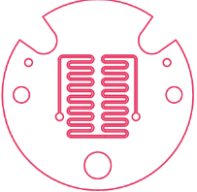
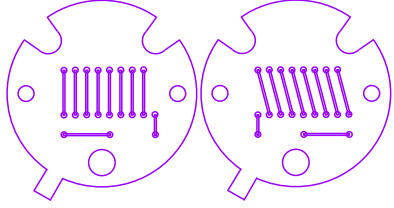
The third generation electrochemical flow reactor was machined out of stainless steel by the workshop in the School of Mechanical Engineering at the University of Leeds. Electrodes and spacers were designed on Corel Draw. Copper electrodes were laser cut by Laser Master (Redruth, TR16 6HY) from C160 copper sheet with a thickness of 0.9 mm. Spacers were laser cut by Laser Web (Barnsley, S71 3HS) from PTFE sheets with a thickness of 1 mm.

The third generation reactor features stacked electrodes which alternate between cathode and anode with PTFE spacers in between (Figure 3.6). PTFE gaskets insulate the stainless steel housing and M5 bolts are used to sandwich the reactor together. The volume can be varied by changing the number of PTFE spacers that are used, with one A spacer giving a volume of approximately 0.5 mL.



### 3.7.1.2. Spacer design

Five spacers (**A-E**) were designed (Figure 2.3a). All had a thickness of 1 mm, whilst the width and number of turns in each spacer was varied. Volumes were calculated from the area of the flow channels.

Spacer	A	B	C	D	E
					
Channel width	2 mm	0.5 mm	0.5 mm	0.5 mm	0.5 mm
Number of turns	7	7	82	30	0
Volume	0.463 mL	0.128 mL	0.260 mL	0.128 mL	0.162 (pair)
Number of spacers to get 0.5 mL	1	4	2	4	3 pairs
Turns per 0.5 mL	7	28	164	120	0
Hops per 0.5 mL	0	3	1	3	60

### 3.7.2. Copper-NHC reaction

#### 3.7.2.1. General procedure for the synthesis of Cu1

The electrochemical synthesis of Cu(IMes)Cl (**Cu1**) from IMesHCl (**L1**) is a well-established reaction that has been used by our group as a model reaction previously.<sup>112,170</sup> **L1** was prepared *via* literature procedures.<sup>181</sup> 6mM solutions of **L1** in anhydrous acetonitrile were prepared under argon to avoid the formation of imidazolones. The solution was transferred to a syringed and pumped through the reactor using a syringe pump. A constant potential of 1.8 V was applied using a Tenma bench top power supply (72-10480 from Farnell) with a multimeter and alternating polarity microcontroller (Arduino MKZERO with Arduino MKR relay proto shield) set to 1/60 Hz in series.<sup>170</sup>

Two residence times were allowed to elapse for the reactor to reach steady state (Table 3.1), before the eluent was collected for one residence time in a round bottomed flask in air. The solvent was removed under vacuum and the remaining white solid dissolved in deuterated chloroform. <sup>1</sup>H NMR spectroscopy was used to calculate the conversion from the integrals of the imidazolium salt and the copper-NHC complex at  $\delta$  7.59 ppm (s, 2H, Imid<sub>backbone</sub>) and 7.00 ppm (s, 4H, ArH) respectively.

$\dot{V}$ / mL min <sup>-1</sup>	$\tau$ / min	Wait time / min	Collection time / min
0.04	12.50	25	10
0.08	6.25	15	5
0.12	4.17	10	4
0.16	3.13	8	3
0.20	2.50	6	2

**Table 3.1:** Residence times, time to reach steady state and the collection times when the volume of the reactor is 0.5 mL.

Proton	L1 (ppm)	Cu1 (ppm)
NCHN	10.89	-
Imid <sub>backbone</sub>	7.59	7.05

<i>ArH</i>	7.03	7.00
<i>p</i> -CH <sub>3</sub>	2.18	2.34
<i>o</i> -CH <sub>3</sub>	2.34	2.10

**Table 3.2:** Chemical shifts for **L1** and **Cu1**.

In between each reaction the reactor was disassembled and the electrodes cleaned. The copper electrodes were cleaned by rinsing with acetone, sandpapering, washing with HCl (~3 M) and rinsed a second time with acetone.

### 3.7.2.2. Different spacer experiments

The general electrochemical flow procedure was followed, using different spacers each with a volume of approximately 0.5 mL at a range of flow rates. Numerous experiments were conducted using different batches of **L1** and anhydrous acetonitrile. Each reaction was performed a minimum of two times and a mean of the conversion at each flow rate was calculated for each spacer. This was plotted against the residence time and the standard error calculated for each point.

Residence time	A (1 spacer)				
	11.58	5.79	3.86	2.89	2.32
Conversion	97.3	69.2	61.7	49.2	41.3
	88.9	70.3	61.5	51.9	51.3
	97.1	76.5	56.0	60.9	52.3
	96.8	74.5	64.5	60.2	57.3
	81.2		63.2		
	85.6		65.9		
			67.0		
			65.2		
			83.6		
			81.6		
			62.3		
Mean	91.1	72.6	66.6	55.5	50.6
SD	6.3	3.0	8.0	5.1	5.8
Standard error	2.6	1.5	2.4	2.5	2.9

**Table 3.3:** Combined data for **A**. Volume = 0.463 mL.

	B (4 spacers)				
Residence time	12.80	6.40	4.27	3.20	2.56
Conversion	100.0	82.2	69.2	75.2	68.9
	94.2	80.8	67.0	68.7	59.8
		79.3	76.1	65.8	58.4
			71.6		
Mean	97.1	80.7	71.0	69.9	62.4
SD	2.9	1.2	3.4	3.9	4.7
Standard error	2.0	0.7	1.7	2.3	2.7

**Table 3.4:** Combined data for **B**. Volume = 0.512 mL.

	C (2 spacers)				
Residence time	13.00	6.50	4.33	3.25	2.60
Conversion	96.7	81.0	68.3	60.6	61.0
	97.2	91.1	78.3	74.4	66.0
	97.6	82.3	73.0	69.7	75.7
	99.1	91.7	69.9		65.4
		81.7	75.8		70.8
			79.6		
Mean	97.6	85.5	74.1	68.3	67.8
SD	0.9	4.8	4.1	5.7	5.0
Standard error	0.4	2.1	1.7	3.3	2.2

**Table 3.5:** Combined data for **C**. Volume = 0.520 mL.

	D (4 spacers)				
Residence time	12.80	6.40	4.27	3.20	2.56
Conversion	98.6	83.7	74.1	73.8	66.0
	99.4	92.8	74.1	70.2	72.1
		85.3	80.4		70.7

	77.3				
Mean	99.0	87.3	76.5	72.0	69.6
SD	0.4	4.0	2.6	1.8	2.6
Standard error	0.3	2.3	1.3	1.3	1.5

**Table 3.6:** Combined data for **D**. Volume = 0.512 mL.

	E (3 pairs of spacers)				
Residence time	12.15	6.08	4.05	3.04	2.43
Conversion	100.0	94.7	82.5	60.7	57.6
	100.0	88.2	80.4	74.6	58.2
	100.0	88.9	76.6	75.0	71.0
Mean	100.0	90.6	79.8	70.1	62.3
SD	0.0	2.9	2.5	6.6	6.2
Standard error	0.0	1.7	1.4	3.8	3.6

**Table 3.7:** Combined data for **E**. Volume = 0.486 mL.

### 3.7.3. Computational fluid dynamics studies

Computational fluid dynamics (CFD) were conducted using the laminar flow and transport of diluted species packages within Comsol Multiphysics 5.5. This uses the finite element method<sup>182</sup> to solve the Navier Stokes equations (for flow) and the advection-diffusion equation for modelling the transport of species within the electro-chemical reactor. The steps in this are (i) define a geometry; (ii) assign inlet, outlet and wall boundary conditions; (iii) solve the steady state flow field; (iv) define the inlet concentration and wall concentration; (v) solve the advection-diffusion equation with the flow field being defined by step iii; (vi) calculate the mean concentration at positions down the channel; (vii) rank the mass transport from the channel wall to the bulk flow as a function of geometry.

The approach where one surface is held at a concentration of 1 (with the others at 0) does not explicitly model the electrochemical process, but it does capture the transport of material away from the electrode surface under the limit of mass transport. This allows

comparative evaluation of the mass transfer characteristics of the flow cell design, whilst considerably simplifying the modelling process, when compared to a full kinetic model.

Throughout the simulation the reference pressure and temperature were set to 1 atmosphere and 293.15 K respectively. The fluid was modelled as water with a density of  $997 \text{ kg m}^{-3}$  and a viscosity of  $0.001 \text{ Pa S}$ . The species had diffusion coefficients of  $1 \times 10^{-9} \text{ m}^2 \text{ s}^{-1}$ .

### 3.7.3.1. Modelling fluid flow

The velocity fields were modelled using the laminar flow equations for a steady state flow. using the Navier-Stokes equation and conservation of mass:

$$\rho(u \cdot \nabla)u = \nabla P + \mu \nabla \cdot [\nabla u + \nabla u^T] + F$$

$$\rho \nabla \cdot u = 0$$

**Equation 3.10:** Navier-Stokes equation. Where  $\rho$  is the density,  $u$  is the velocity field,  $\mu$  the viscosity,  $P$  is the pressure,  $F$  is the volume force vector (body force in this case).

The inlet boundary was set to a velocity of  $0.001 \text{ m s}^{-1}$  with a flat inflow velocity. The outlet was set to suppress backflow and the remaining walls had a no-slip boundary condition applied to them. The pressure drop was calculated for four of the channels.

Channel	P inlet / Pa	P outlet / Pa	P drop / Pa
Straight	2.8256	0.0026	2.8230
Turns	2.8605	0.0030	2.8575
Steps	3.1301	0.0028	3.1273
Hops	3.1295	0.0028	3.1267

**Table 3.8:** Pressure drop for four of the flow channels.

### 3.7.3.2. Simulating material transport from the electrode

The transport of dilute species package within Comsol was used to simulate the flux of a chemical species leaving the surface of an electrode. To do this, one wall of the channel was set to a concentration of  $1 \text{ mol m}^{-3}$  (shown a blue surface in Figure 3.11) with the

inlet concentration of fluid set to 0 mol m<sup>-3</sup>. The remaining boundaries, apart from the outlet, were set to have no flux transport across them.

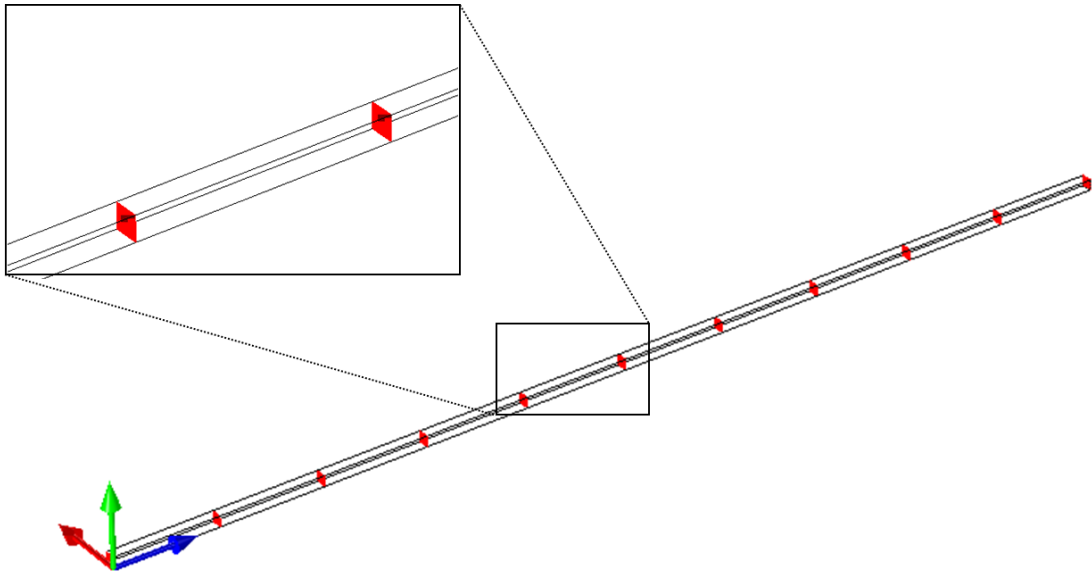
The transport of material away from this electrode into the bulk is as a result of advection (with the flow field calculated using equation 4.1) and diffusion with Equation 3.11, the advection-diffusion equation is used to calculate the movement of the solute.

$$\nabla \cdot J_i + u \cdot \nabla c_i = R_i$$

$$J_i = -D_i \nabla c_i$$

**Equation 3.11:** Calculating the concentration. Where  $J_i$  is the mass flux diffusive flux vector,  $u$  is the flow velocity vector,  $c_i$  is the concentration of the species,  $R_i$  is the reaction rate expression – here zero- and  $D_i$  is the diffusion coefficient.

The concentration was then reported as an average concentration from a series of planes taken normal to the flow at positions down the channel (Figure 3.21). The mean concentration captures the mass transfer away from his surface, with the flow parameters and channel geometry influencing this rate.



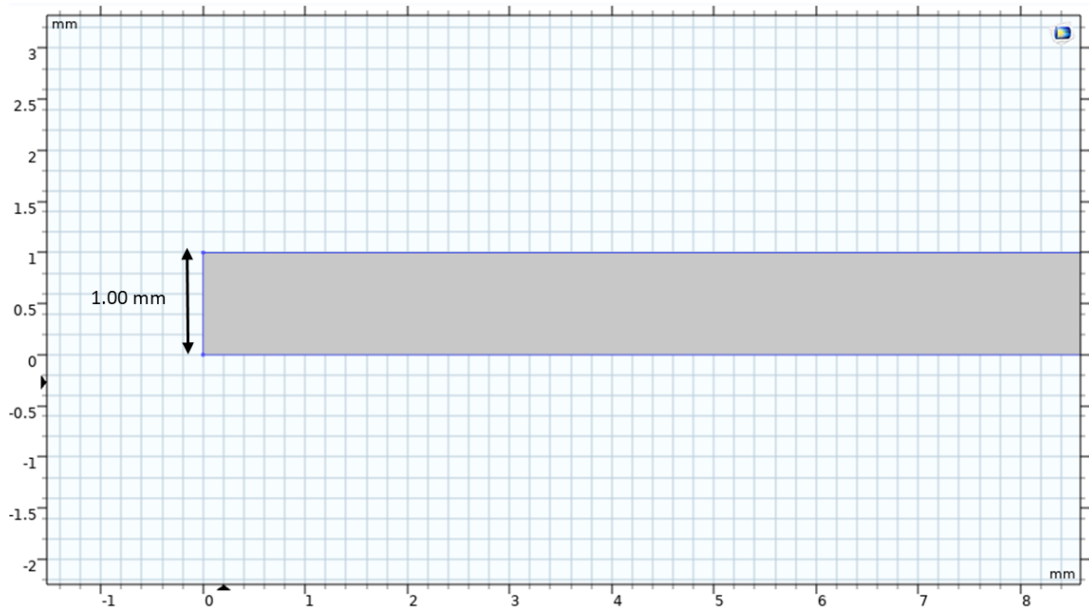
**Figure 3.21:** Planes across the channels were used to calculate the mean concentration at intervals along the channel.

### 3.7.3.3. Flow channel designs

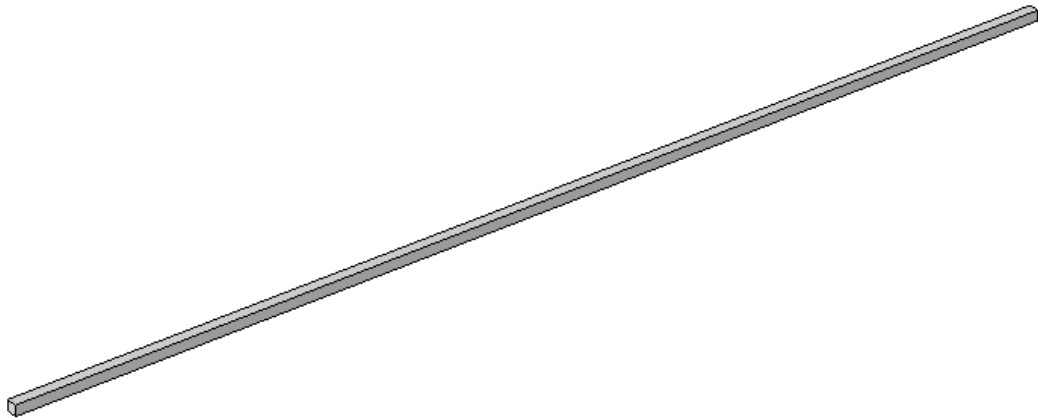
Five flow channels were modelled. All had a depth and width of 1 mm. The fluid properties were taken as water at 25° C. Once constructed the mesh was generated using physics-controlled mesh with the element size set to normal.

### 3.7.3.3.1. Straight channel

The straight channel was a simple cuboid 1 mm x 1 mm x 100 mm. 495368 elements were used to construct the mesh.



**Figure 3.22:** Dimensions of the straight channel.

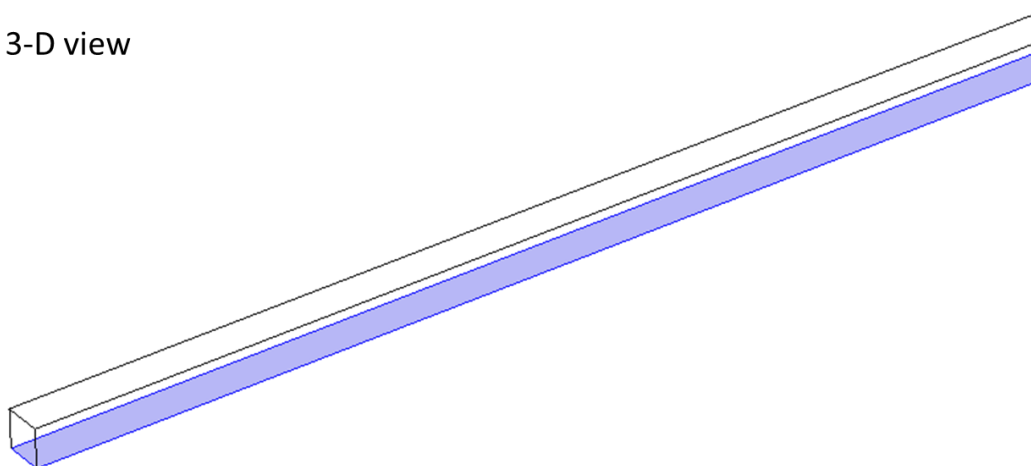


**Figure 3.23:** Straight channel used in the CFD studies.

The bottom wall of the straight channel was used to act as the electrode (shown in blue).



a) 3-D view



b) Top view



**Figure 3.24:** Position of the electrode in the straight channel.

<b>Height / mm</b>	<b>1</b>
<b>Width / mm</b>	<b>1</b>
<b>Length / mm</b>	<b>100</b>
<b>Electrode area / mm<sup>2</sup></b>	<b>100</b>
<b>Volume / mm<sup>3</sup></b>	<b>100</b>

**Table 3.9:** Dimensions of the straight channel.

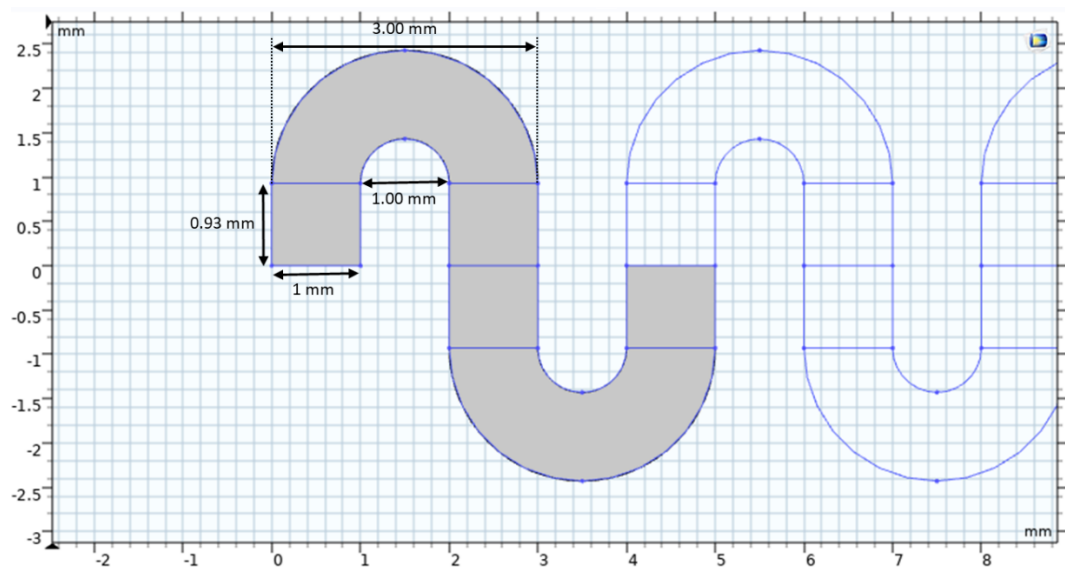
Distance / mm	Mean concentration / mol m <sup>-3</sup>
0	0.007
10	0.148
20	0.206
30	0.257

40	0.302
50	0.344
60	0.382
70	0.419
80	0.453
90	0.484
100	0.510

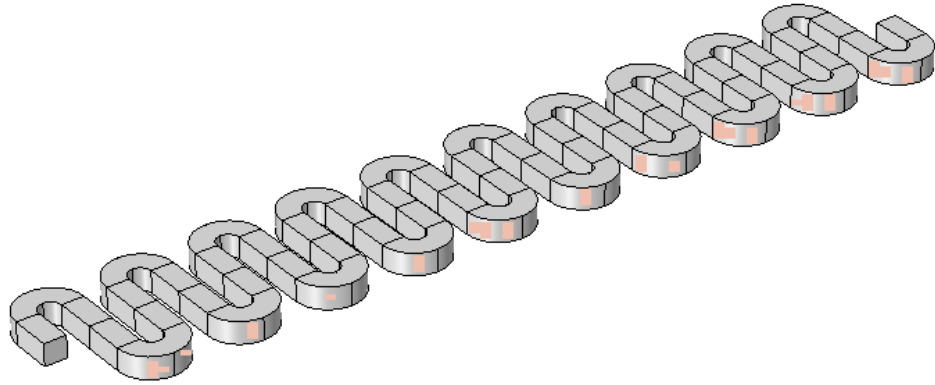
**Table 3.10:** Mean concentrations at distances along the straight channel.

### 3.7.3.3.2. Channel with turns

The channel with turns was constructed in a 2D plane from 10 repeating units, with a channel width of 1 mm and centre-line path length of 100 mm. This was extruded by 1 mm in the z-direction (out of the page) to give a flow channel with square cross section (1 mm by 1 mm). 303356 elements were used to construct the mesh.



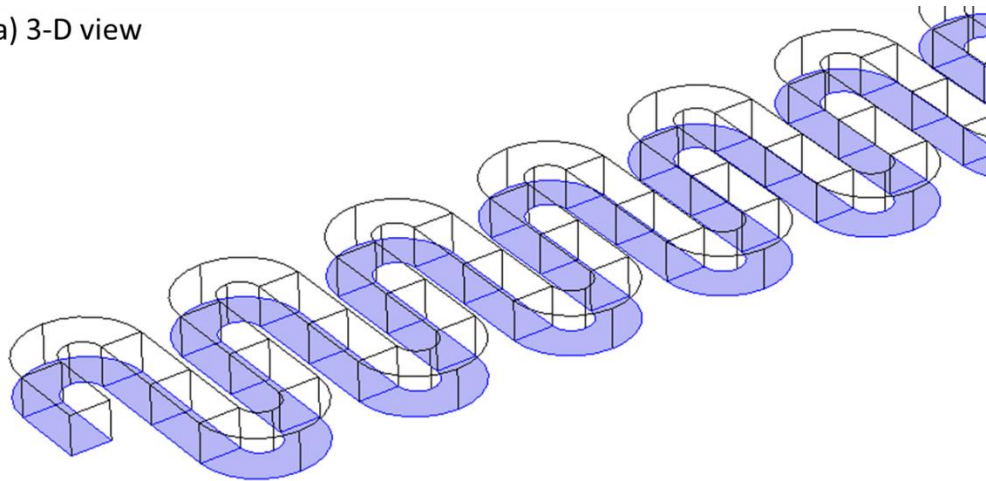
**Figure 3.25:** Dimensions of the turns used to construct the channel with turns.



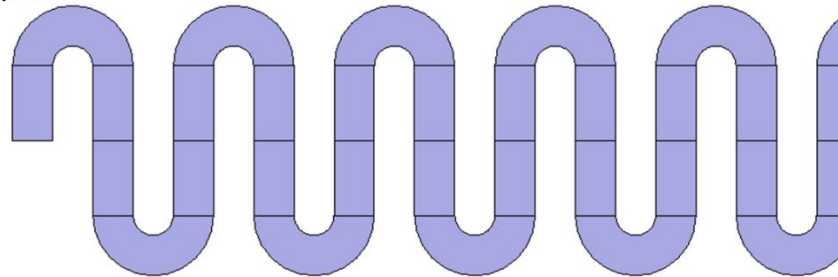
**Figure 3.26:** Channel with turns.

The bottom wall of the channel with turns was used to act as the electrode (shown in blue).

a) 3-D view



b) Top view



**Figure 3.27:** Position of the electrode in the channel with turns.

Height / mm	1
Width / mm	1
Length / mm	100
Electrode area / mm <sup>2</sup>	100
Volume / mm <sup>3</sup>	100

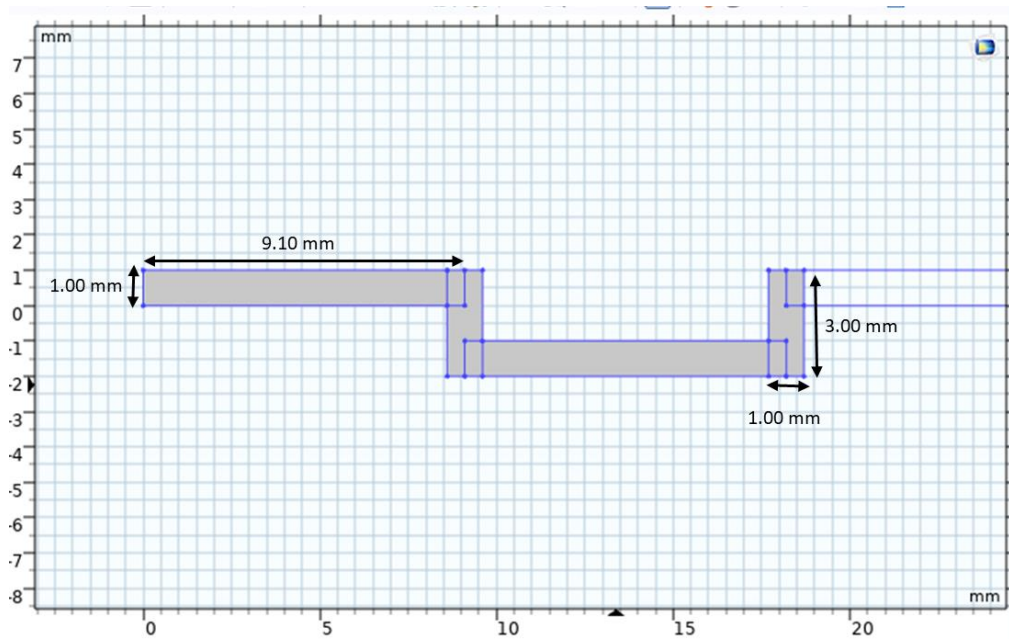
**Table 3.11:** Dimensions of the channel with turns.

Distance / mm	Mean concentration / mol m <sup>-3</sup>
0	0.010
5	0.107
10	0.143
15	0.175
20	0.204
25	0.232
30	0.257
35	0.282
40	0.305
45	0.329
50	0.350
55	0.371
60	0.391
65	0.411
70	0.429
75	0.447
80	0.464
85	0.481
90	0.497
95	0.513
100	0.523

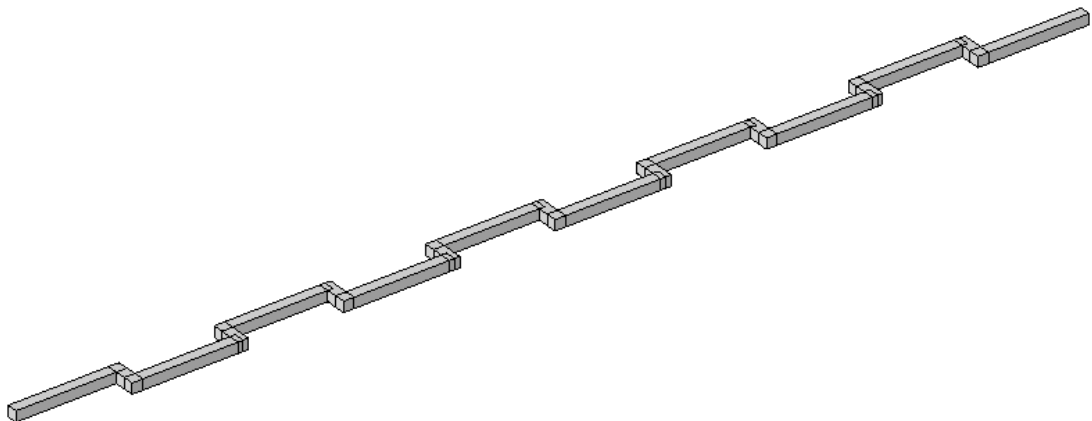
**Table 3.12:** Mean concentrations at distances along the channel with turns.

### 3.7.3.3.3. Channel with hops

The channel with turns was constructed in a 2D plane from 10 repeating units, with a channel width of 1 mm and centre-line path length of 120 mm. This was extruded by 1 mm to give a flow channel with square cross section (1 mm by 1 mm). 387120 elements were used to construct the mesh.



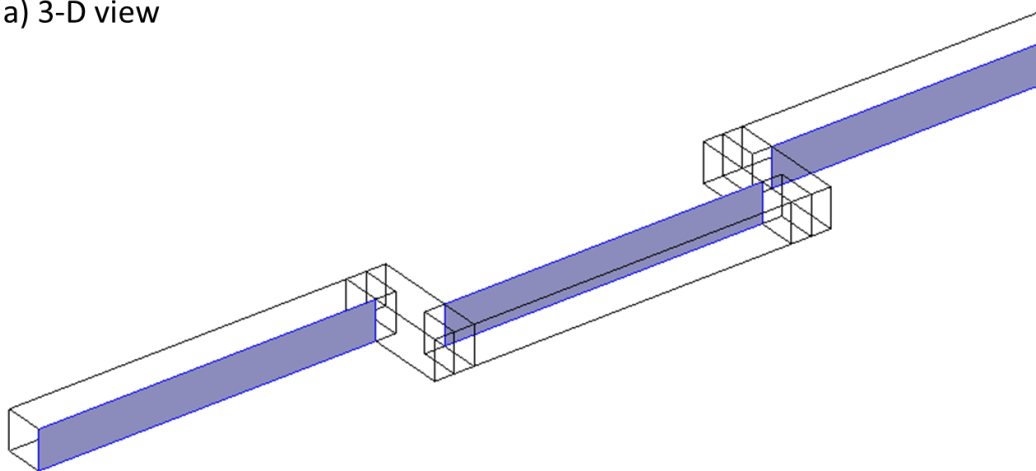
**Figure 3.28:** Dimensions of the 90° turns used to construct the channel with hops and the channel with stepped turns.



**Figure 3.29:** Channel with hops and channel with stepped turns.

The channel with hops had the electrode such that it alternated which side of the channel it was on every time the channel went through a dogleg.

a) 3-D view



b) Top view



**Figure 3.30:** Position of the electrode in the channel with hops.

Height / mm	1
Width / mm	1
Length / mm	120
Electrode area / mm <sup>2</sup>	91
Volume / mm <sup>3</sup>	120

**Table 3.13:** Dimensions of the channel with hops.

Distance / mm	Mean concentration / mol m <sup>-3</sup>
0	0.014
4.3	0.106
15.4	0.209

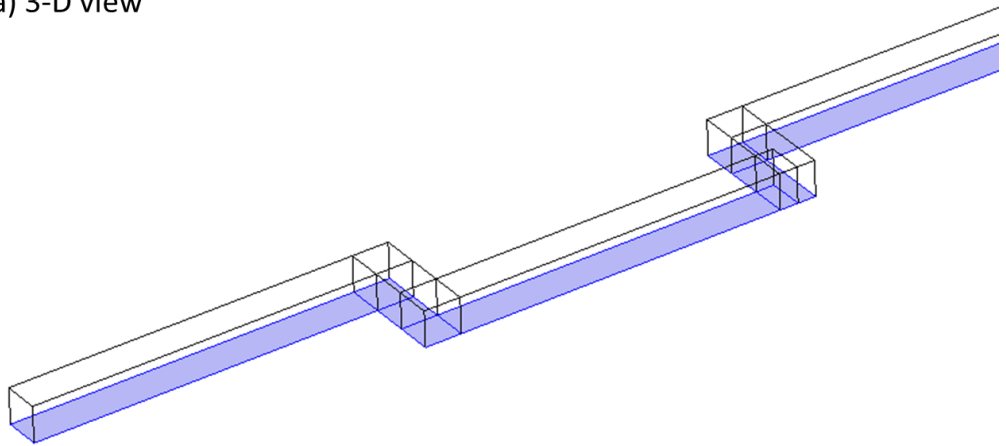
26.5	0.291
37.6	0.366
48.7	0.432
59.8	0.493
70.9	0.547
82	0.594
93.1	0.637
104.2	0.675
115.3	0.709
120	0.716

**Table 3.14:** Mean concentrations at distances along the channel with hops.

#### 3.7.3.3.4. Channel with stepped turns

The geometries of the channel with steps is the same as the one with hops, but the electrode remains on the same side of the channel. This was to distinguish between the shape of the channel with hops (i.e. 90° turns) with the position of the electrode.

a) 3-D view



b) Top view



**Figure 3.31:** Position of the electrode in the channel with stepped turns.

Height / mm	1
Width / mm	1
Length / mm	120
Electrode area / mm <sup>2</sup>	120
Volume / mm <sup>3</sup>	120

**Table 3.15:** Dimensions of the channel with steps.

Distance / mm	Mean concentration / mol m <sup>-3</sup>
0	0.015
4.3	0.105
15.4	0.182
26.5	0.246
37.6	0.300
48.7	0.350
59.8	0.398
70.9	0.442
82	0.481
93.1	0.519
104.2	0.552
115.3	0.584
120	0.592

**Table 3.16:** Mean concentrations at distances along the channel with steps.



### 3.7.4. Systematic studies

#### 3.7.4.1. Reactor and spacer design

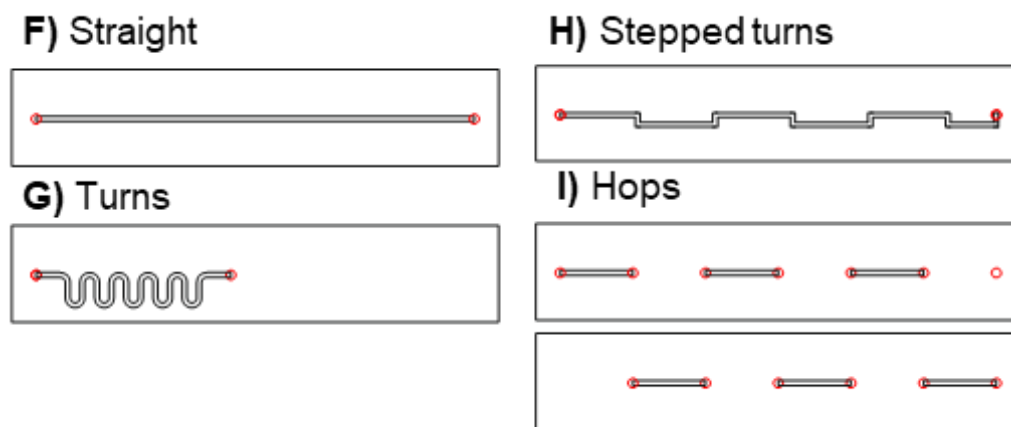
One of our old second generation reactors<sup>112</sup> was adapted by the workshop in the School of Mechanical Engineering at the University of Leeds by machining two ¼-28 fittings 90 mm apart.



**Figure 3.32:** Modified second generation reactor.

Graphite electrodes were cut from graphite foil purchased from Alfa Aesar (43083, 1 mm thick). Spacers were laser cut by Laser Web (Barnsley, S71 3HS) from PTFE sheets with a thickness of 1 mm. 4 spacers were designed so that they had width and depth of 1 mm. Each channel had a path length of 90 mm, giving a volume of 90 mm<sup>3</sup>. Volumes were calculated from the area of the flow channels using Coral Draw.

A straight channel (**F**) was included as a control. A channel with turns (**G**) was made to test what effect adding turns had. **H** was included to test the effect of 90° turns and to compare with the channel with hops. **H** and **I** have very similar geometries the difference is that **H** remains within two electrodes, whilst **I** passes through an electrode in a series of hops.



**Figure 3.33:** Flow channels used in the systematic study.

### 3.7.4.2. Residence time distributions

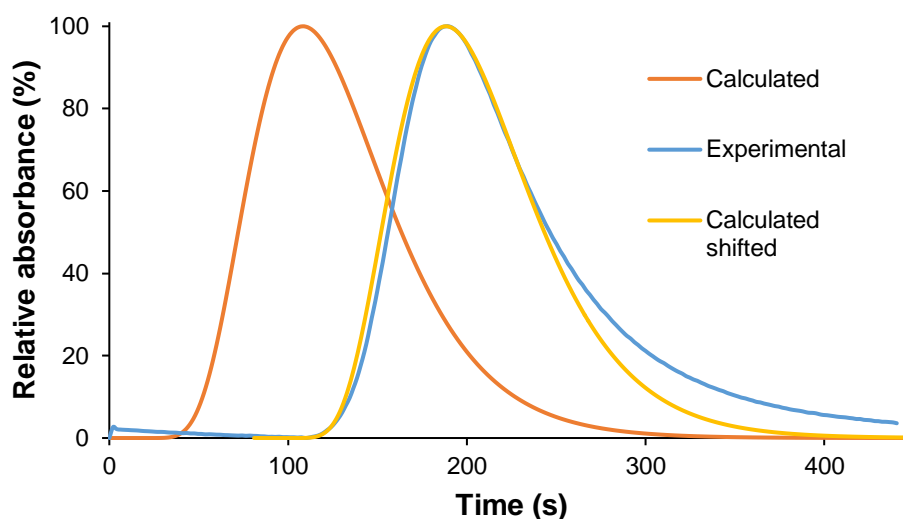
A solution of methylene blue (20 mg, 0.063 mmol) in acetonitrile (100 mL) was pumped into a 15  $\mu\text{L}$  sample loop and then pumped through the reactor with a solution of acetonitrile at a flow rate of  $0.04 \text{ mL min}^{-1}$ . A UV/Vis spectrometer was then used to measure the absorbance, at 600 nm, of the solution leaving the reactor and a graph was plotted of absorbance against time. This was repeated 4 times and an average residence time distribution was taken for each spacer. This was found by taking the points where the graph showed 50% absorbance at each side of the peak and the RTD was the time between these points.

**F**, **H** and **I** all have the same RTD, suggesting that there is no back mixing. **G** has a longer RTD due to the shape of the flow channel. **G** has the same volume and electrode surface area as the other spacers, however due to the meandering flow channel the outlet is only 40 mm away from the inlet. Consequently a straight channel 50 mm in length was needed to carry the solution to the outlet of the reactor. This channel was insulated from the electrodes and therefore should have no impact on the electrochemistry but it will increase the RTD because more diffusion can occur.

The axial dispersion coefficient ( $D_{ax}$ ) was calculated using Equation 3.12 **Error! Reference source not found.**,<sup>176</sup> giving a good fit to the experimental curves when  $D_{ax}$  was  $2.5 \times 10^{-4} \text{ m}^2 \text{ s}^{-1}$  (Graph 3.11). The asymmetric model was used because the dispersion number ( $N_L$ ) is greater than 0.01.

$$E_t = \frac{u}{\sqrt{4\pi D_{ax} t}} \exp \left[ -\frac{(L - ut)^2}{4D_{ax} t} \right]$$

**Equation 3.12:** Calculating the axial dispersion coefficient ( $D_{ax}$ ). Where  $u$  is the average velocity,  $t$  is the time,  $L$  is the length and  $E_t$  is the exit time.



**Graph 3.11:** Experimental RTD with modelled RTD where  $D_{ax} = 2.5 \times 10^{-4}$  and the dispersion number ( $N_L$ ) = 0.06.

### 3.7.4.3. Mass transfer coefficients

Mass transfer coefficients can be calculated in electrochemical flow reactors by using the limiting current method and Equation 3.13.

$$k_m = \frac{I_{lim}}{nFAC_B}$$

**Equation 3.13:** Calculating the mass transfer coefficient ( $k_m$ ) from the limiting current ( $I_{lim}$ ). Where  $n$  is the number of electrons exchanged,  $F$  is the Faraday constant and  $C_B$  is the concentration of the bulk solution.

A solution of potassium hexacyanoferrate (II) trihydrate (2.11 g, 5 mmol), potassium hexacyanoferrate (III) (3.29 g, 10 mmol) and sodium carbonate (5.30 g, 50 mmol) in water (100 mL) was prepared and pumped through a reactor with graphite electrodes at a flow rate of  $0.04 \text{ mL min}^{-1}$ . The current was recorded at increasing voltages and a graph of current against voltage was plotted to determine the limiting current of the spacer. These were then used to calculate the mass transfer coefficient for the spacers and could be compared to calculated values.

#### 3.7.4.3.1. Straight channel

Run Number	Limiting Current / mA	$k_m / \text{m s}^{-1}$
2	1.7682	0.00204
3	1.6138	0.00186
4	1.7038	0.00196
Average	1.6953	0.00195

Std Dev.	0.0776	0.00009
Std Error in mean	0.0448	0.00005

**Table 3.17:** Limiting current and calculated mass transfer coefficient for **F**.

#### 3.7.4.3.2. Channel with turns

Run No.	Limiting Current / mA	km
2	1.5000	0.00173
3	1.4996	0.00173
4	1.5140	0.00174
Average	1.5045	0.00173
Std. Dev.	0.0082	9.44394E-06
Std. Error in Mean	0.0047	5.45246E-06

**Table 3.18:** Limiting current and calculated mass transfer coefficient for **G**.

#### 3.7.4.3.3. Channel with stepped turns

Run Number	Limiting Current / mA	km / m s <sup>-1</sup>
1	2.3064	0.00266
2	2.0986	0.00242
6	2.3610	0.00272
7	2.1428	0.00247
8	2.4516	0.00282
Average	2.2721	0.00262
Std. Dev.	0.1484	0.00017
Std. Error in Mean	0.0664	0.00008

**Table 3.19:** Limiting current and calculated mass transfer coefficient for **H**.

#### 3.7.4.3.4. Channel with hops

Run No.	Limiting Current / mA	$K_m / m s^{-1}$
2	5.3000	0.00610
3	5.5400	0.00638
4	5.0200	0.00578
5	5.1800	0.00597
Average	5.2600	0.00606
Std. Dev.	0.2191	0.00025
Std. Error in Mean	0.1265	0.00013

**Table 3.20:** Limiting current and calculated mass transfer coefficient for **L**.

#### 3.7.4.4. Synthesis of **Cu1**

The synthesis of **Cu1** in the systematic reactor was performed in an analogous manner to the general procedure (3.7.2.1). A 6 mM solution of **L1** in anhydrous acetonitrile was prepared under argon and pumped through the assembled reactor. 1.8 V was applied without alternating the polarity. Two residence times (5 mins) were allowed to elapse for the reactor to reach steady state. Eluent was collected for 10 mins due to the small volume of the reactor, to ensure that there was sufficient material for analysis.

Channel	Mean conversion / %	Error
Straight	55.12	2.12
Turns	56.34	1.16
Hops	61.48	2.12
Stepped turns	60.04	0.44

**Table 3.21:** Mean conversions of **L1** to **Cu1** for the systematic spacers at 1.8 V with a flow rate of 0.04 mL min<sup>-1</sup>.

### 3.7.4.5. CO<sub>2</sub> reactions

For batch reaction **L8** (0.23 g, 1 mmol) was placed in the bottle reactor under argon and dissolved in anhydrous acetonitrile. CO<sub>2</sub> was bubbled through the solution for 15 minutes before graphite electrodes were used to apply a current of 50 mA for 1 hour (2 F mol<sup>-1</sup>), whilst CO<sub>2</sub> was bubbled through the solution. Analysis by <sup>1</sup>H NMR showed a conversion of 33%

For flow reactions **L8** (0.67 g, 3 mmol) and Bu<sub>4</sub>NBF<sub>4</sub> (0.50 mmol, 1.5 g) were placed under argon and dissolved in anhydrous acetonitrile (60 mL). CO<sub>2</sub> was bubbled through the solution for 30 mins. The systematic reactor was assembled with graphite electrode and a 5 PSI back pressure regulator. The solution was pumped through the reactor at a flow rate of 0.04 mL min<sup>-1</sup> and a potential of 3.0 V was applied. A mixture of carboxylate and imidazolone product were observed using <sup>1</sup>H NMR.

Channel	Mean conversion / %	Error
Straight	32.5	0.5
Turns	34.0	2.0
Hops	30.5	1.5
Stepped turns	30.5	2.5

**Table 3.22:** Combined conversion of **L8** to carboxylate and imidazole.

## 4. Continuous electrochemical synthesis of nickel(II)-*N*-heterocyclic carbene complexes

In recent years there has been renewed interest in first row metals as homogenous catalysts, however complexes of these metals can be difficult to synthesise due to the often air sensitive nature of the intermediates and the complexes themselves. The Willans group have previously reported an electrochemical flow reactor that has been used to synthesise copper(I)-*N*-heterocyclic carbene (NHC) complexes and telescoped the copper species directly into reactions to act as catalysts.<sup>112</sup> This chapter focuses on extending this methodology to nickel(II) complexes. Several different analytical and experimental techniques have been used to explore the reaction mechanism, including surface analysis, cyclic voltammetry, divided cell experiments and the use of alternating polarity. Mechanistic insights have subsequently been used to optimise the synthesis of nickel(II)-NHC complexes.

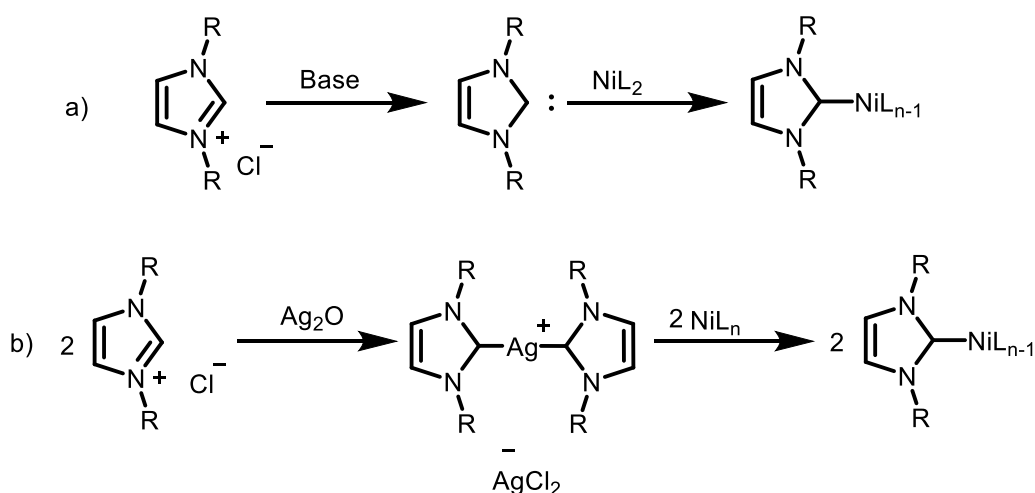
### 4.1. Synthesis of metal complexes

This work aimed to extend the electrochemical synthesis of copper-NHC complexes to other first row metals such as iron and nickel. Initial work with iron(II)-NHCs was found to be challenging due to the presence of iron(III) impurities in the product, making analysis very difficult. It was thought that studies on nickel-NHCs would help our understanding of the iron reaction because both nickel and iron require the metal to be oxidised twice and the ligand to be reduced twice. Furthermore, the synthesis of nickel(II)-NHCs is a worthwhile endeavour in its own right. They have a large potential as homogenous catalysts and the ability to synthesise them on demand would be exceedingly useful, increasing the through put and enabling catalysts to be telescoped into reactions.<sup>27–29,183</sup> Although nickel(II) complexes are not usually air sensitive, unlike iron(II), making them under continuous conditions would be highly beneficial from a safety perspective.

Although one must be careful when generalising about metal toxicities,<sup>184</sup> it is widely accepted that nickel presents more of a hazard than other base metals (with the exception of cobalt).<sup>185,186</sup> The International Council for Harmonisation limits its levels in active pharmaceutical ingredients (APIs) to 20 ppm for oral administration, compared with 300 ppm for copper.<sup>187</sup> Of particular concern is the use of nickel catalysts at a plant scale, which typically involves the *in-situ* generation of nickel species from powdered nickel salts.<sup>184</sup> This poses a significant risk to plant operators,<sup>188</sup> a risk which could be avoided through the on-demand synthesis of nickel complexes from solid nickel electrodes.

### 4.1.1. Nickel(II)-NHC complexes

The current state of the art for the synthesis of nickel(II)-NHC complexes may be broadly subdivided into four synthetic methodologies. The first method uses stoichiometric amounts of base to deprotonate the imidazolium, where upon it can coordinate to a source of nickel (a, Scheme 4.1).<sup>1,28</sup> These steps can be performed sequentially or concurrently. Typical sources of nickel(II) include  $\text{NiCl}_2$  and  $\text{Ni}(\text{OAc})_2$ . Alternatively, the imidazolium salt can be reacted with  $\text{Ag}_2\text{O}$  to form a silver-NHC. The NHC can then be transmetallated from the silver to a nickel complex (b, Scheme 4.1).<sup>189</sup>



**Scheme 4.1:** a) Synthesis of Ni(II)-NHC complexes using a base. b) Synthesis of Ni(II)-NHC complexes via transmetalation.

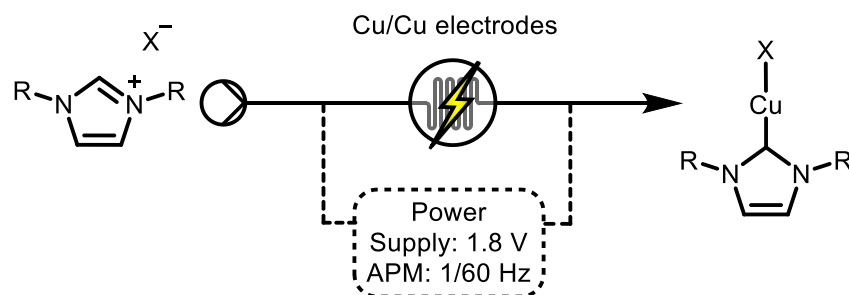
More recently the Chen group have developed several novel methodologies for the synthesis of metal-NHCs. Powdered nickel can be reacted with an imidazolium in air to produce Ni(II)-NHC complexes.<sup>41</sup> However this reaction is very slow and can lead to the formation of imidazolone side products. The same group also developed an electrochemical methodology which is discussed in more detail in Section 4.2.1.<sup>14</sup>

### 4.1.2. Continuous synthesis of copper complexes

The Willans group have successfully synthesised copper(I) complexes electrochemically using electrochemical flow reactors (Scheme 4.2).<sup>112,170,190</sup> These complexes are typically very air sensitive, consequently the ability to make them on-demand and dispense them into reactions to act as catalysts is highly attractive. This occurs *via* the cathodic reduction of the ligand precursor and the production of metal ions at a sacrificial anode. This methodology has been found to be highly effective, generating a range copper complexes with excellent yields (>95%) in a single pass and without any undesired side products.<sup>170</sup> If copper(I)-NHC complexes are required, this is the method that the author would recommend; neutral or cationic complexes may be produced



selectively with ease, even without prior expertise in organometallic or electrochemical synthesis.

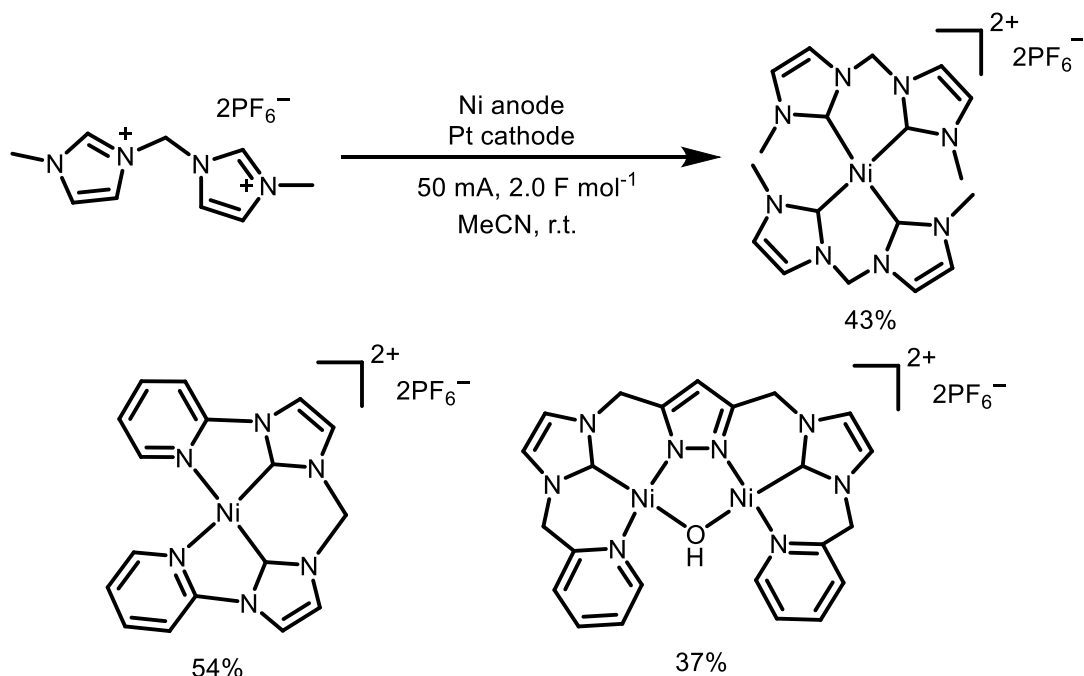


**Scheme 4.2:** Continuous electrochemical synthesis of copper(I)-NHC complexes.

## 4.2. Initial studies

### 4.2.1. Translating batch into flow

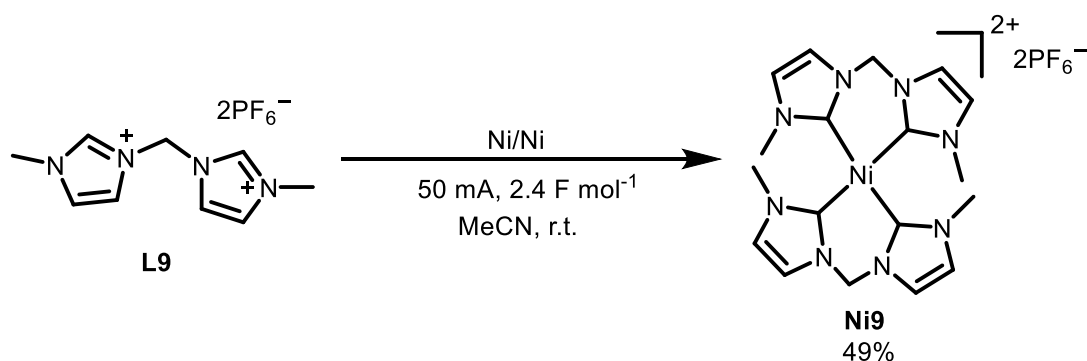
The electrochemical synthesis of nickel(II)-NHC complexes was first reported by the Chen group.<sup>14</sup> They produced three nickel complexes by using a platinum cathode to reduce the imidazolium precursor and a sacrificial anode made of nickel. They obtained moderate yields for these reactions, producing mono-, bis- and tetrakis-NHC complexes (Scheme 4.3).



**Scheme 4.3:** Electrochemical synthesis of nickel-NHC complexes conducted by the Chen group.<sup>14</sup>

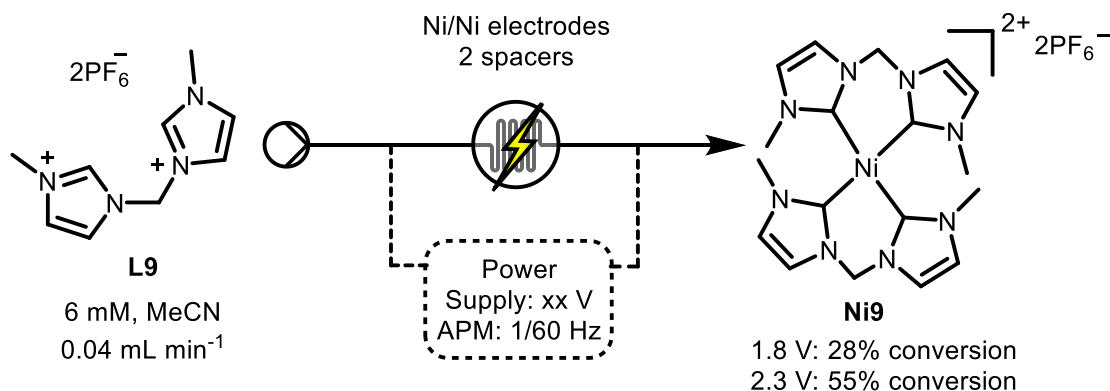
Chen's reaction was reproduced in batch using the bottle reactor. In anticipation of conducting this reaction in flow the platinum cathode was swapped for a nickel one to simplify the reaction, as well as reduce the cost and enable the use of an alternating

polarity. A solution of **L9** in anhydrous acetonitrile was electrolysed under galvanostatic conditions (50 mA) for  $2.4 \text{ F mol}^{-1}$ , as per the general procedure used within the group (Scheme 4.4).<sup>181</sup> Over the course of the reaction the applied potential rose from 5.7 V to 12 V, similar to the preparation of other metal-NHC complexes in batch. The imidazolium salt acts as the electrolyte as well as the starting material, resulting in the resistance of the solution increasing as the reaction progresses and the electrolyte is consumed. **Ni9** was produced with a conversion of 49% by  $^1\text{H}$  NMR spectroscopy, with a spectrum that was consistent with previous reports.<sup>14</sup> In addition, the diamagnetic nature and dark orange colour of the solution is consistent with the formation of a nickel(II) square planar complex.<sup>191–193</sup>



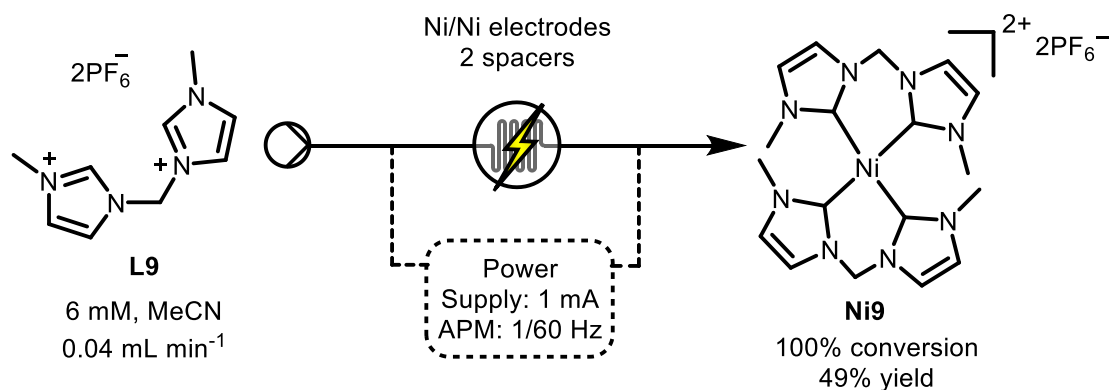
**Scheme 4.4:** Adaptation of Chen's procedure in the bottle reactor using two nickel electrodes.

Once it had been established that **Ni9** could be produced with two nickel electrodes the electrochemical flow reactor described in chapter 3 was used to generate **Ni9** under continuous conditions. As a starting point the optimised conditions for the synthesis of **Cu1** were used (Scheme 4.5).<sup>170,194,195</sup> The flow reactor was assembled with three nickel electrodes and two 'normal' spacers (giving a volume of approximately 1 mL) and a 6 mM solution of **L9** was pumped through at a flow rate of  $0.04 \text{ mL min}^{-1}$  whilst a constant potential of 1.8 V was applied with an alternating polarity microcontroller (APM) in series. This gave an encouraging conversion of 28%. By increasing the potential to 2.3 V a higher conversion of 55% could be obtained. It was thought that the reaction could be monitored using inline UV-Vis spectroscopy. However, a sample of the outlet proved to be too strongly absorbing, requiring a 100-fold dilution for a spectrum to be obtained, rendering inline analysis with UV-Vis spectroscopy impractical.



**Scheme 4.5:** Synthesis of **Ni9** under potentiostatic conditions.

Galvanostatic conditions were found to give full conversion when a constant current of 1 mA was applied (Scheme 4.6). Using a constant current also allows the amount of electrons put into a reaction to be controlled by using Equation 4.1.<sup>70,196,197</sup> Trimethoxybenzene (TMB) was used as an external standard to check the mass balance of the reaction. Surprisingly this did not correspond to the conversion; a yield of 47% was achieved using these reaction conditions, indicating that a significant amount of material was unaccounted for. **Ni9** is a tetrakis square planar complex comprising of two bis-NHC ligands. Consequently, for each complex, four reductions must occur to produce four carbene centres and two oxidations to produce one Ni<sup>2+</sup> ion. As a yield of approximately 50% was obtained it was thought that the lack of charge balance in the product might be responsible in some way (with the remaining charge possibly generating some other species). To test this hypothesis a number of different ligands were screened.



**Scheme 4.6:** Galvanostatic conditions gave full conversion of **L9** to **Ni9**, but a yield of 49% indicating that half of the material was unaccounted for.

$$I = nF c \dot{V}$$

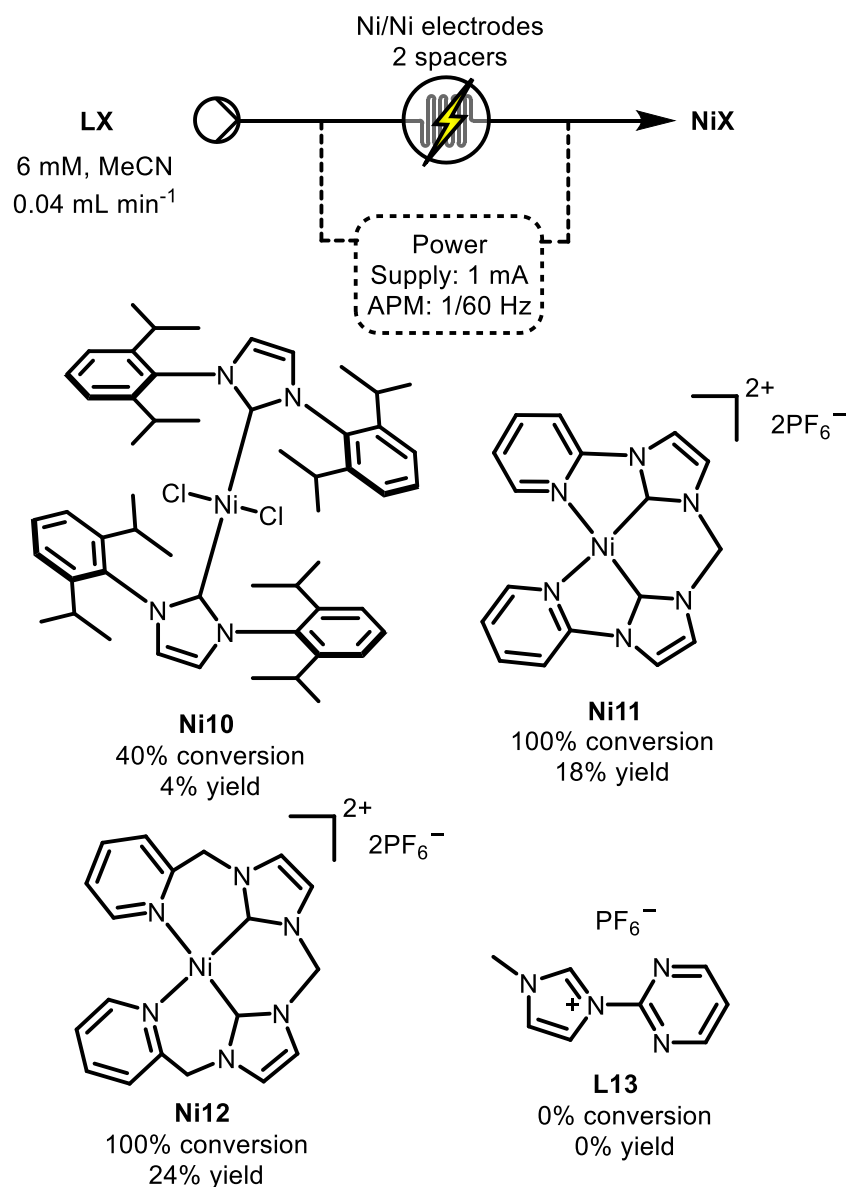
**Equation 4.1:** Equation for calculating the required current for an electrochemical flow reaction where  $I$  is the current,  $n$  is the number of electrons required for each substrate,  $F$  is the Faraday coefficient,  $c$  is the concentration and  $\dot{V}$  is the flow rate.<sup>197</sup>

#### 4.2.2. Ligand screen

**L10** is a popular ligand for catalysis and it was anticipated that it would produce **Ni10**, a coordinatively unsaturated complex, which might be catalytically active. Unfortunately a conversion of 40% was obtained with a yield of 4% (Scheme 4.7). Due to the large steric bulk of the *N*-substituents only two NHCs are able to coordinate to the nickel centre. Whilst this complex has good charge balance, its coordinatively unsaturated nature might mean that it is less stable under the reaction conditions.

**L11** had been used by Chen's group to generate Ni-NHC complexes electrochemically in batch. By pumping **L11** through the electrochemical flow reactor **Ni11** could be synthesised with full conversion and a yield of 18% (Scheme 4.7). It was anticipated that by exchanging the pyridyl *N*-substituents for the more flexible picolyl substituents of **L12** that a higher yield might be obtained due to the macrocycle being less strained. A moderate increase of the yield to 24% was obtained for **Ni12** (Scheme 4.7).

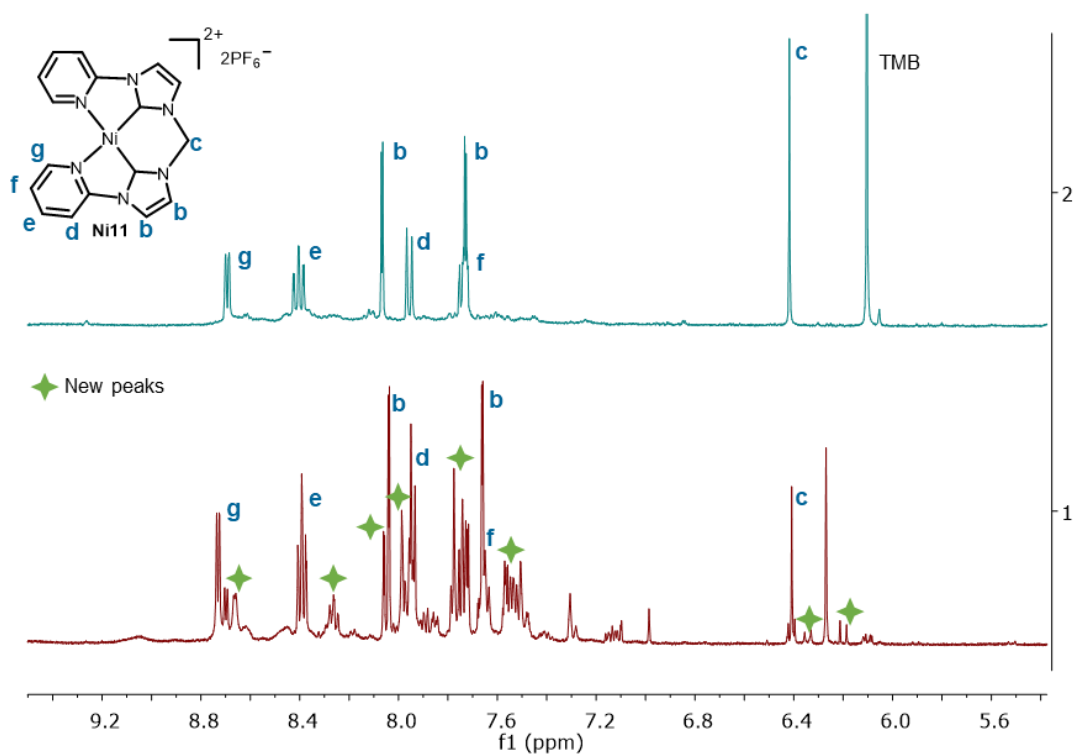
**L9**, **L11** and **L12** are all multidentate ligands which might help to stabilise any nickel complex which is forming. **L13** was tested to see if it was the bis-NHC motif or the general multidentate nature of ligands which helped the formation of Ni-NHC complexes. No product was observed and only a small amount of starting material was recovered, meaning that even more material was going missing (Scheme 4.7). This also demonstrates that the bis-NHC motif is required to produce a meaningful amount of complex. **L11** was chosen to conduct further studies because it is easier to synthesise than **L12** and exhibits better charge balance than **L9**.



**Scheme 4.7:** Electrochemical synthesis of a range of Ni(II)-NHC complexes.

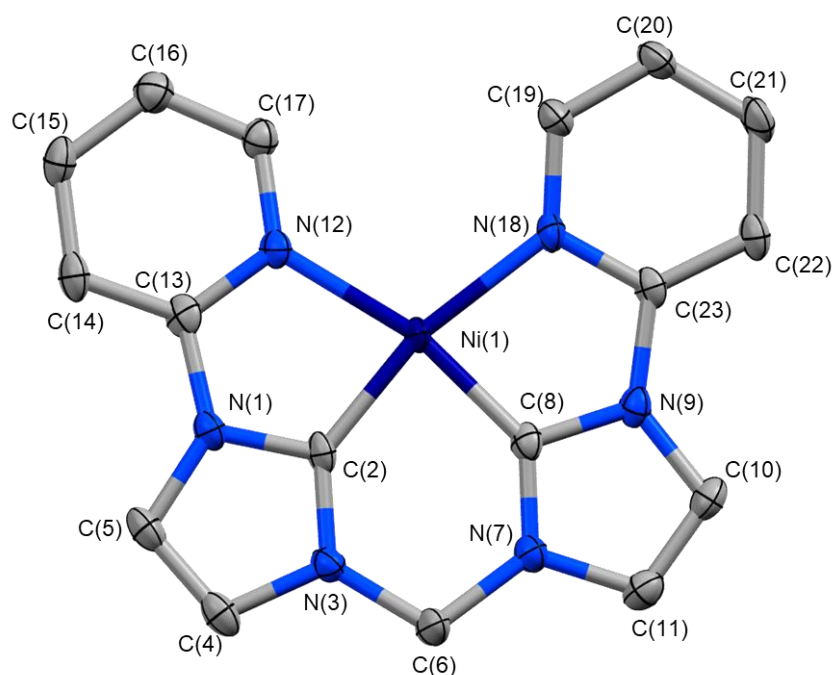
#### 4.2.3. Selectivity of flow vs batch

During our studies it was desirable to make a pure sample of **Ni11** for full characterisation, so that the outputs of flow reactions could be compared to it. To do this **L11** was electrolysed in batch with nickel electrodes by Megan Bradbury, a member of the Willans group. Analysis by <sup>1</sup>H NMR spectroscopy showed the presence of two sets of peaks, suggesting that two species had been produced (Figure 4.1). Of note were the doublets at 6.34 ppm and 6.20 ppm which correspond to a methylene that has been pushed out of the plane of the complex, thus making the two protons anisotropic and leading to two signals being seen in the spectrum. This would suggest that some of the expected **Ni11** has been synthesised, along with an unknown asymmetric nickel species.



**Figure 4.1:** Top: <sup>1</sup>H NMR spectrum of **Ni11** (400 MHz, CD<sub>3</sub>CN), prepared electrochemically in the flow reactor. Bottom: <sup>1</sup>H NMR spectrum of **Ni11** (500 MHz, CD<sub>3</sub>CN), prepared electrochemically in the bottle reactor and showing multiple sets of peaks.

Crystals suitable for single X-ray crystallography were grown by Megan Bradbury *via* vapour diffusion of diethyl ether into a concentrated solution of the reaction mixture in acetonitrile. Two types of visibly distinct crystals were found in the vial, orange needles and clear blocks. The crystal structure of the orange needles were solved to give **Ni11** (Figure 4.2) with a unique triclinic unit cell, in contrast to the previously reported monoclinic unit cell.<sup>198</sup> The nickel centre exhibits a distorted square planar geometry; **L11** remains within the plane but the bond angles differ from the 90° of a perfect square planar complex. The N(12)-Ni(1)-N(18) angle was 111°, while the other metal-ligand bond angles were between 82° and 85°. The bond angles and lengths are consistent with the previously reported structure.<sup>198</sup>

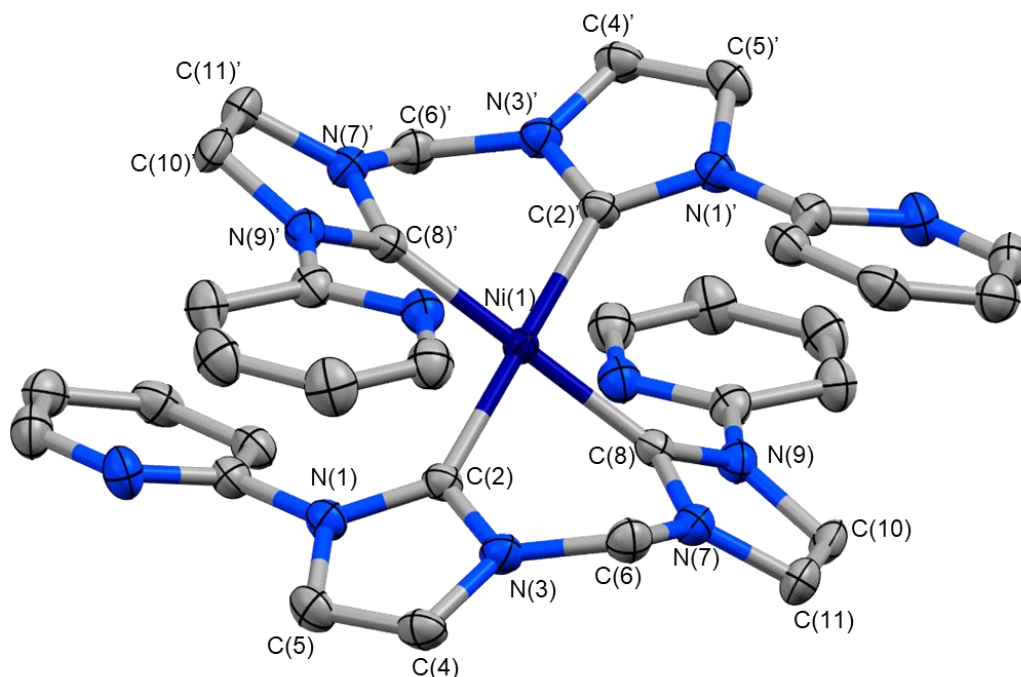


**Figure 4.2:** Molecular structure of **Ni11**. Ellipsoids are shown at 50% probability level. Hydrogen atoms and PF<sub>6</sub> counter ions are omitted for clarity.

Atoms	Bond lengths (Å) and angles (deg)
Ni(1)-C(2)	1.8068
Ni(1)-C(8)	1.8143
Ni(1)-N(12)	1.9891
Ni(1)-N(18)	1.9856
N(12)-Ni(1)-C(2)	82.44
C(2)-Ni(1)-C(8)	84.40
C(8)-Ni(1)-N(18)	82.20
N(18)-Ni(1)-N(12)	111.04
N(3)-C(6)-N(7)	109.62

**Table 4.1:** Selected bond lengths and angles for **Ni11**.

The colourless blocks were found to contain an asymmetric unit featuring **L11** bonded to a nickel centre through both NHCs. A centre of inversion lies at the nickel atom, giving **Ni(11)<sub>2</sub>** with two ligands bonded to the Ni(II) centre to give a tetrakis-NHC complex, with the pyridyl substituents remaining uncoordinated (Figure 4.3).



**Figure 4.3:** Molecular structure of **Ni(11)<sub>2</sub>**. Ellipsoids are shown at 50% probability level. Hydrogen atoms and PF<sub>6</sub> counter ions are omitted for clarity.

Atoms	Bond lengths (Å) and angles (deg)
Ni(1)-C(2)	1.9078
Ni(1)-C(8)	1.8872
C(2)-Ni(1)-C(8)	86.68
C(8)-Ni(1)-C(2')	93.32
N(3)-C(6)-N(7)	108.82

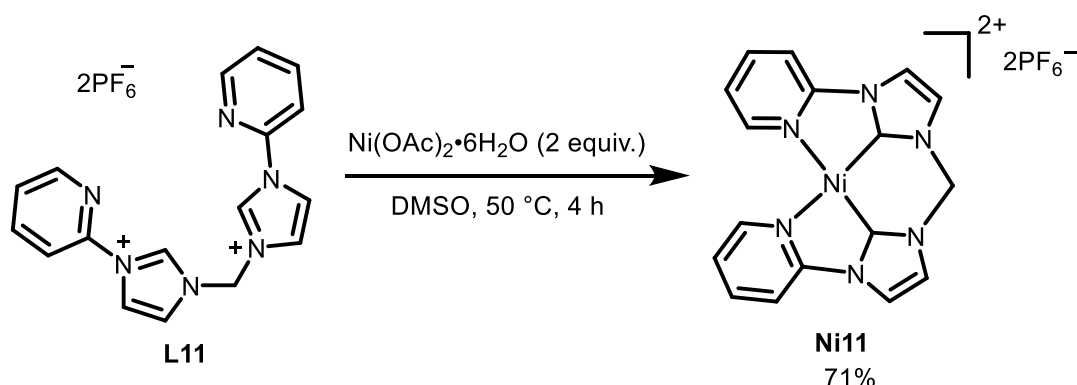
**Table 4.2:** Selected bond lengths and angles for **Ni(11)<sub>2</sub>**.

The lack of selectivity observed in the bottle reactor is likely due to poor mass transfer. During the reaction the stirrer bar could only turn slowly, because at fast revolutions it often stuck to the nickel electrodes. Consequently the mass transfer is likely to be poorer than when the reaction is conducted in flow and the electrodes are much closer together. This highlights the increased selectivity of conducting this reaction in flow, avoiding the inadvertent synthesis of **Ni(11)<sub>2</sub>**.

To circumvent the lack of selectivity observed in the bottler reactor, **Ni11** was chemically synthesised using a modified literature procedure.<sup>199</sup> **L11** and an excess of Ni(OAc)<sub>2</sub>·6H<sub>2</sub>O were dissolved in DMSO and heated to 50 °C (Scheme 4.8). After the solvent was removed under vacuum the solid was triturated with THF and recrystallised



with acetonitrile and diethyl ether to give **Ni11** as a pale yellow powder without any impurities.  $\text{Ni}(\text{OAc})_2 \cdot 6\text{H}_2\text{O}$  is readily soluble in THF and an excess was required to avoid unreacted **L11** in the product.



**Scheme 4.8:** Chemical synthesis of **Ni11**.

#### 4.2.4. Optimisation in flow

The synthesis of **Ni11** was used as model reaction due to the ease of synthesis of **L11** and the good charge balance that it displays. The solvent and current were initially identified as areas for the optimisation of this reaction.

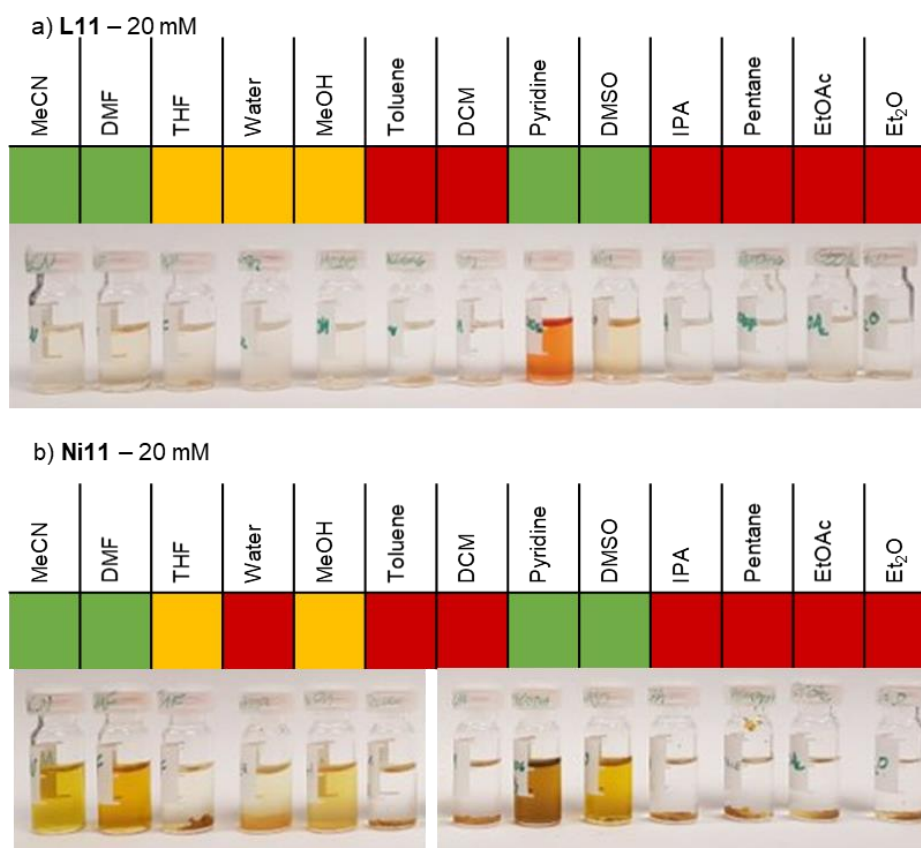
Acetonitrile is often used as a solvent for the electrochemical synthesis of metal complexes due to its broad electrochemical window.<sup>80</sup> Acetonitrile is also able to coordinate to metal centres, helping to stabilise metal ions and complexes in solution, something that the Willans group have found helpful in the synthesis of copper complexes.<sup>99,170,181,190,195</sup> Copper(I) centres are softer than nickel(II) and it was thought that a different solvent might help to stabilise nickel(II) more than the relatively soft acetonitrile.<sup>200,201</sup>

DMF, THF and methanol were chosen to test due to their relatively large electrochemical windows and their commercial availability in anhydrous forms.<sup>202</sup> DMF gave a comparable yield to acetonitrile (Table 4.3). No product was observed using THF or methanol, although precipitates were observed in the tubing suggesting that **Ni11** isn't soluble in these solvents.

Solvent	Yield
MeCN	19%
DMF	20%
THF	0% (ppt in tubing)
MeOH	0% (ppt in tubing)

**Table 4.3:** Solvent screen for the electrochemical synthesis of **Ni11**.

A series of solutions of **Ni11** and **L11** in different solvents were set up to test their solubility (Figure 4.4). This was partly for the development of a continuous synthetic methodology, but also for the development of catalytic protocols using these nickel complexes. 20 mM solutions were prepared, with complete dissolution of the ligand and the complex observed for acetonitrile, DMF, pyridine and DMSO and partial dissolution in THF and methanol. Interestingly, whilst solutions of **Ni11** were yellow in acetonitrile, DMF and DMSO the pyridine solution was slightly green. This perhaps suggests that there is some coordination of the pyridine, giving an octahedral geometry. The use of pyridine also exhibited a colour change when **L11** was dissolved, giving an orange colour, suggesting some form of interaction.



**Figure 4.4:** Solubility studies of **L11** (a) and **Ni11** (b) in a range of solvents. Green indicates complete dissolution, amber partial dissolution and red little or no dissolution.

For the electrochemical synthesis of nickel complexes the use of pyridine and DMSO was dismissed due to the difficulty in drying them and their narrow electrochemical windows. Acetonitrile was chosen in preference to DMF due to its broader electrochemical window and greener credentials.<sup>203</sup>

The effects of current and potential were investigated (Table 4.4). When conducting this reaction with a constant current of 1 mA the potential varied between 1.5 V and 2.5 V due to the presence of the Alternating Polarity Microcontroller (APM), giving a yield of 19%. A constant potential of 2.0 V was applied and this did not improve the production of **Ni11**. When under potentiostatic conditions the current will vary due to the APM, meaning that the amount of electrons delivered is unknown. To avoid this galvanostatic conditions were chosen.

As the reaction proceeds the starting material, which also acts as the electrolyte, is consumed. Although the product is also charged, the lack of mass balance may mean that the conductivity of the solution reduces as the solution flows through the reactor. To see if this has an effect  $\text{Bu}_4\text{NPF}_6$  was added to act as an electrolyte so that the conductivity remained constant, though the yield of **Ni11** remained the same. The APM was found to be essential for running the copper reaction for extended periods, but not necessary for short periods.<sup>170</sup> The synthesis of **Ni11** was carried out without the use of an APM and a significant drop in the yield was observed, suggesting that the APM is essential for this reaction.

Electrolyte	I or P	APM	Yield
No	0	0 Hz	0% (100% SM)
No	1 mA	1/60 Hz	19%
No	2.0 V	1/60 Hz	19%
Yes	1 mA	1/60 Hz	19%
Yes	1 mA	0 Hz	4%

**Table 4.4:** Effects of current and potential on the synthesis of **Ni11** in the presence and absence of electrolyte and alternating polarity.

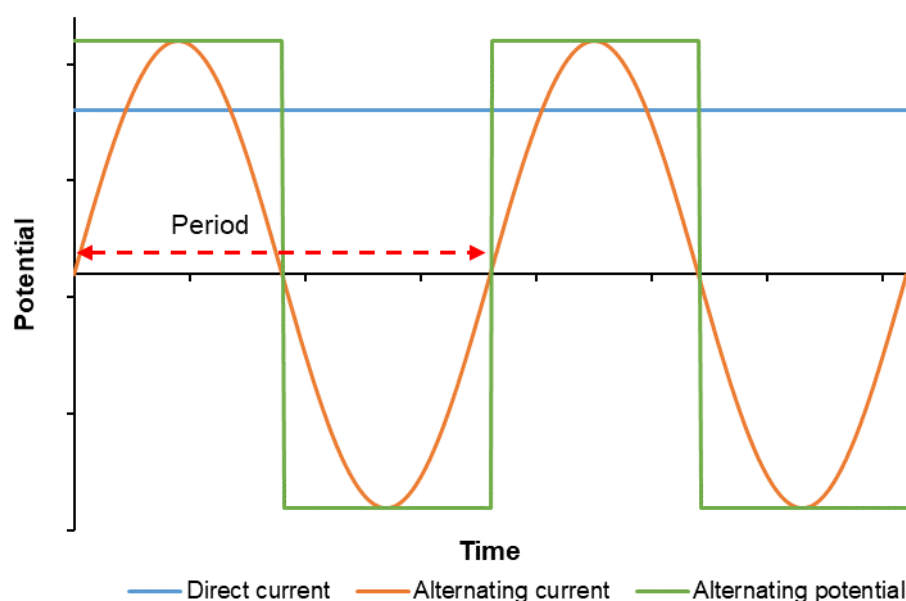
### 4.3. The mystery of the missing material – mechanistic studies

During the initial studies it was noted that the mass balance for the nickel reaction was very poor. The synthesis of **Ni11** and other bis-NHC complexes could be conducted with full conversion of the ligand precursor but very poor yield (<50% in all cases). No other

species were observed *via*  $^1\text{H}$  NMR spectroscopy and high resolution mass spectrometry (HRMS), meaning that a large amount of material was unaccounted for. To try and ascertain where this material was going, a series of mechanistic studies were conducted, looking at the effects of alternating polarity, examining the surface of the electrodes and using divided cells and colour analysis to investigate where the reaction is taking place.

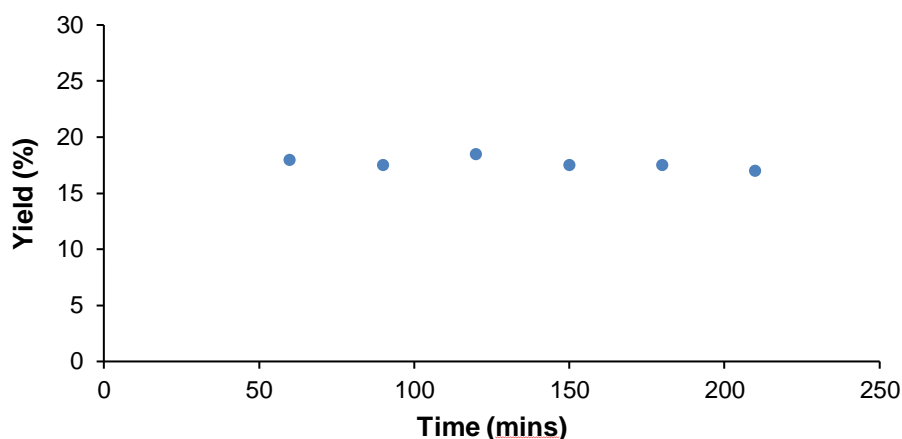
#### 4.3.1. Alternating polarity

During work on the copper reaction it was observed that when a direct current was applied the conversion was stable for a few hours, before dropping very quickly.<sup>170</sup> This was attributed to changes in the surface of the electrode, either from deposition or the formation of dendrites which could short circuit the cell. To circumvent this issue an APM was employed. This programmable Arduino circuit alternates the polarity of the electrodes, so that each electrode spends half of the time as an anode and half the time as a cathode. The current delivered by the APM is described as a square wave direct current (sometimes referred to as a reverse pulse); the potential (or current depending on whether galvanic or potentiostatic conditions are used) is constant (Figure 4.5). By contrast, alternating current, as delivered by the national grid, delivers potential that varies as a sinusoidal wave.



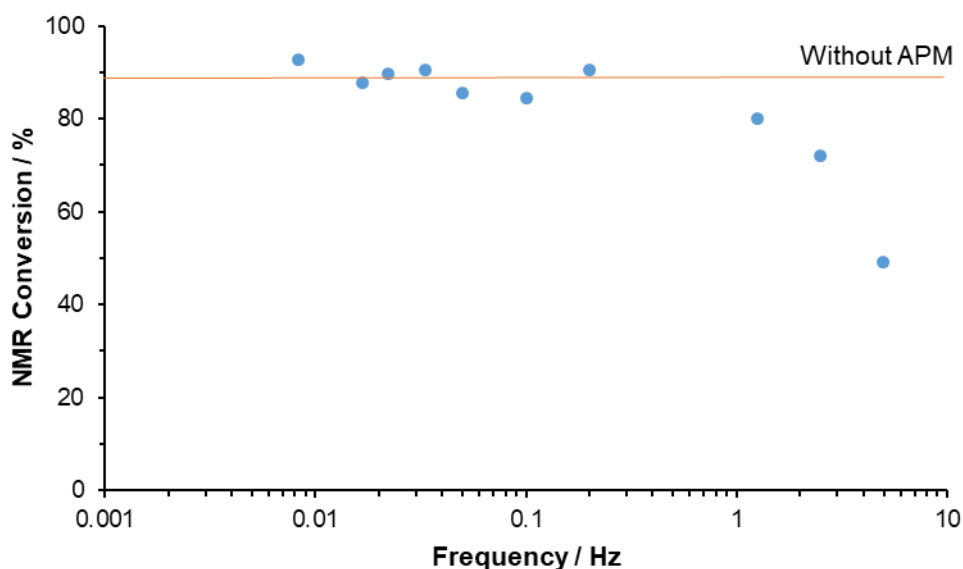
**Figure 4.5:** Descriptions of direct current (blue), alternating current (orange) and alternating potential (green). The period is indicated by a red arrow.

The use of alternating polarity was also found to aid the stability of the nickel reaction (Graph 4.1). The synthesis of **Ni11** could be conducted continuously for 3.5 hours with no loss in the yield, meaning that the reaction can be maintained at a steady state. This suggests that any fouling of the electrodes is held at a constant level by the APM.



**Graph 4.1:** Time monitoring of the electrochemical synthesis of **Ni11**. Samples of the outlet were taken at 30 minute intervals.

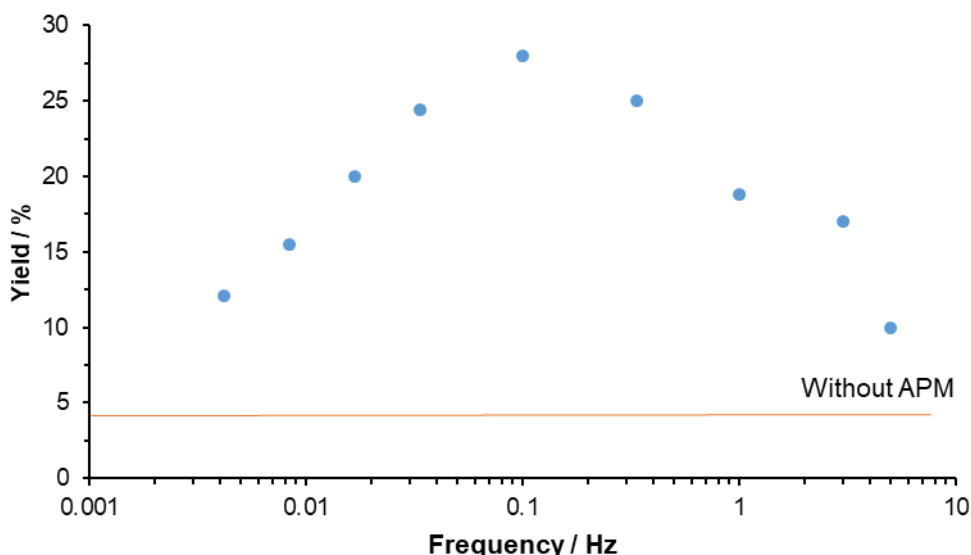
For the copper reaction it was found that alternating the polarity at a fast frequency led to a drop in the conversion (Graph 4.2).<sup>170</sup> It was hypothesised that that this was because the imidazolium was remaining 'stagnant' in the middle of the flow channel as the polarity of the electrode changes too quickly for it to move *via* migration to the cathode surface. Similarly Cu(I) ions generated at the anode might have insufficient time to diffuse away from the surface before the polarity is changed and they are reduced back to Cu(0).



**Graph 4.2:** Relationship between the conversion of **Cu1** and the frequency of the APM when 1.8V is applied. Conversion obtained without the APM (87%) is shown in orange.<sup>170</sup>

This phenomenon was also observed for the nickel reaction; as the frequency increases, from 1/10 to 10 Hz, the yield decreases. However, unlike the copper reaction, the yield is not constant at slower frequencies. Instead it decreases, leading to an inverted U

shape and an optimum frequency of 1/10 Hz (28% yield) (Graph 4.3). When the frequency is slow, species will spend longer near the surface of the electrode before the polarity is switched. This might suggest that there are undesirable reactions occurring which reduce the yield, possibly product degradation. Consequently there is a 'sweet spot' for the APM frequency; too fast and there is insufficient time for the reaction to take place, too slow and the product spends too long near one electrode and is degraded.



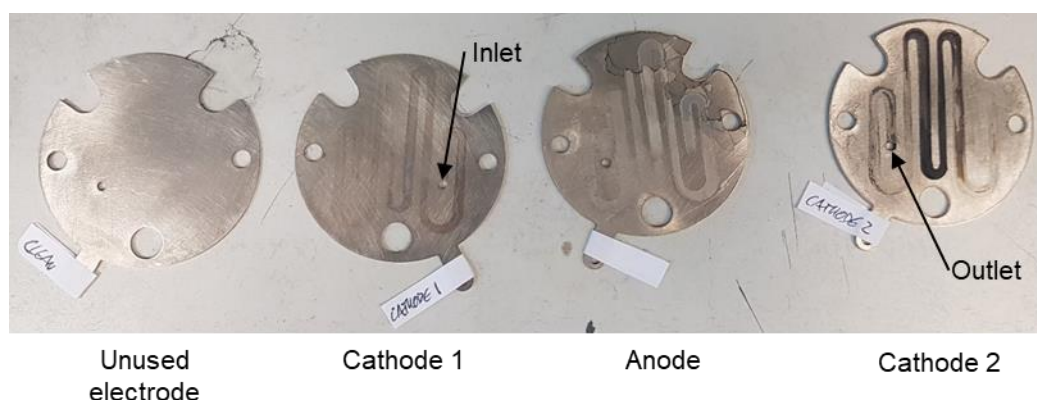
**Graph 4.3:** Relationship between the conversion of **Ni11** and the frequency of the APM when 1 mA is applied. Conversion obtained without the APM (4%) is shown in orange.

#### 4.3.2. Surface analysis

Throughout these studies black deposits have been observed visually on the surface of the electrode following a reaction. Consequently the electrodes were thoroughly cleaned in between uses by sandpapering the surface and then wiping it with hydrochloric acid (~3 M), water and finally acetone. To try and ascertain what these deposits might be, scanning electron microscopy (SEM) and energy dispersive X-ray spectroscopy (EDX) were used to examine the surfaces of electrodes which had been used in a reaction.

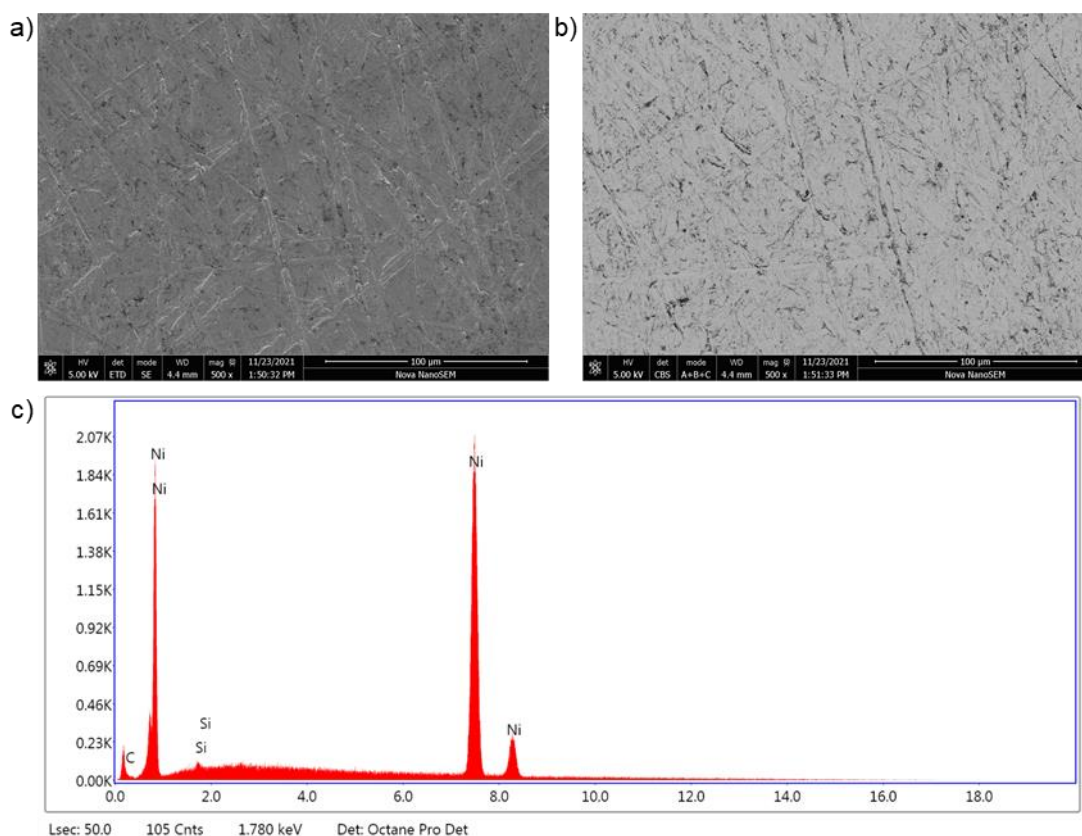
The synthesis of **Ni11** was performed without use of the APM so that the anode and cathodes could be examined separately. The reactor was disassembled and large quantities of black deposits could be seen on the cathode, by contrast the anode was relatively clean. SEM images were taken of the anode, the cathodes (two cathodes were used), and an electrode that had been cleaned, but not used (Figure 4.6). A combination of an Everhart-Thornley detector (ETD) and circular backscatter detector (CBS) were used. The ETD is able to collect secondary electrons, allowing topographical information to be obtained.<sup>204</sup> By contrast the CBS only collects backscattered electrons. This means

that the topology of a sample cannot be observed but it can be used to gain information about the composition of a sample. The heavier the element present, the higher energy the backscattered electrons have. Consequently bright areas on an image collected with a CBS typically contain heavy elements, such as metals, whilst darker area usually contain lighter elements, such as organic compounds.<sup>204</sup> EDX was used to specify which elements were present on the samples. During EDX, X-rays are used to remove an electron from an atom. An electron from a higher energy orbital then replaces the electron that has been lost, releasing an X-ray as it moves to a lower energy orbital. The energy of the emitted X-rays can be used to identify the element responsible.



**Figure 4.6:** Electrodes examined using SEM.

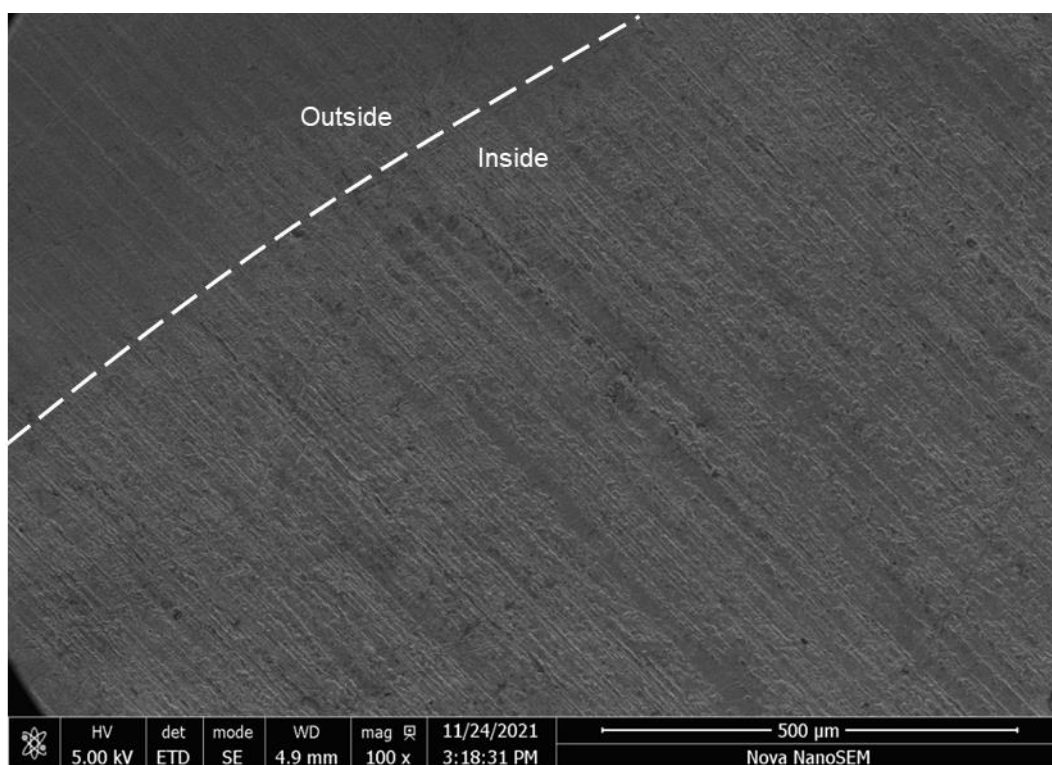
The unused electrode had scratches on the surface, consistent with the use of sandpaper (a, Figure 4.7). Use of the BSE, which displays metals in a light colour and organics in a dark colour, showed some dark patches in the corners of the scratches (b, Figure 4.7). These could be remnants of solvent from the cleaning procedure. EDX on the sample showed the presence of a very small amount of carbon, possibly from acetone, and a small amount of silicon (c, Figure 4.7). The silicon may be from the sandpaper.



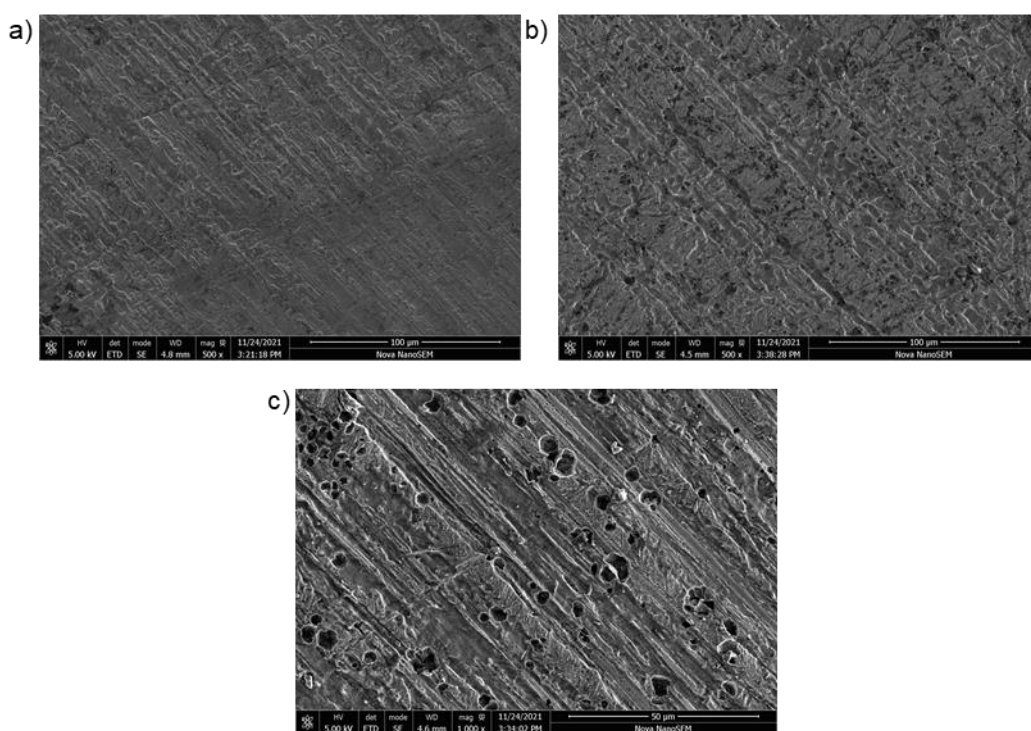
**Figure 4.7:** ETD (a) and CBS (b) images of an unused electrode, showing scratches from sandpaper and small amounts of organic material (500 x mag.). c) EDX spectrum showing small amounts of carbon and silicon.

The surface of the anode exhibited clear differences between the surface inside the flow channel, in contact with the solution, and the surface outside the flow channel that was in contact with the PTFE of the spacer (Figure 4.8). Outside the channel, scratches similar to the unused electrode can be seen, whilst inside the channel scarring and the presence of small craters, or pitting, can be observed. During analysis several parts of the anode were observed. Regions close to the inlet exhibited moderate scarring (a, Figure 4.9), with striations following along where you might have expected scratches to be before a current was applied. This might suggest that metal ions are produced preferentially at surface imperfections, such as scratches. Further along the flow channel pitting starts to occur. At first with relatively small craters (b, Figure 4.9), which increase in size closer to the outlet (c, Figure 4.9). This would suggest that metal ions are not produced at the same rate along the length of the channel.





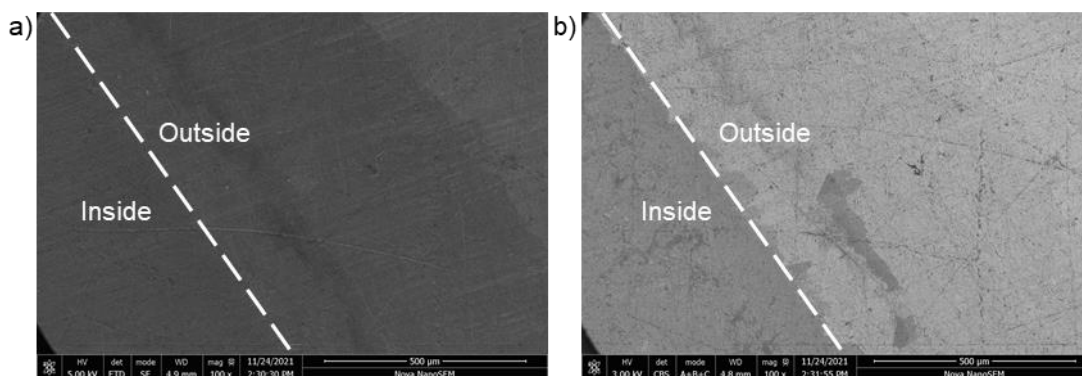
**Figure 4.8:** EDT image of the anode (100 x mag.). The top left of the image is outside of the flow channel, while the rest of the image was inside the flow channel, in contact with the reaction solution.



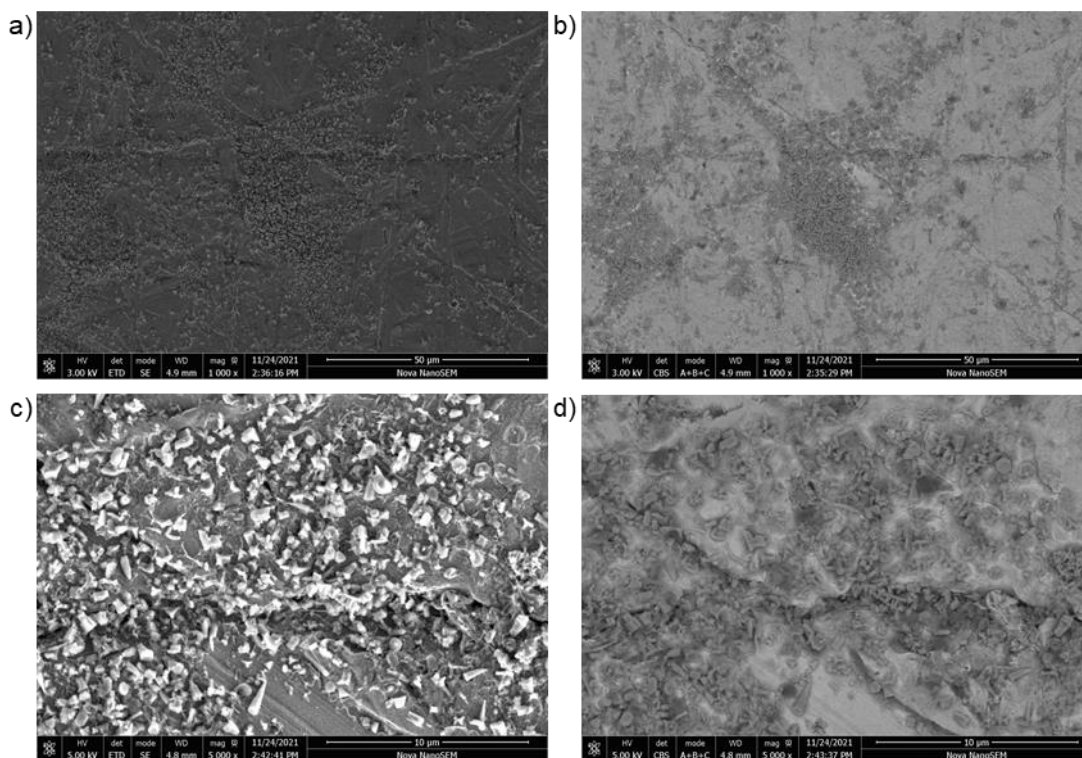
**Figure 4.9:** EDT images of the anode at different points along the flow channel. a) Striations close to the inlet (500 x mag.) b) Pitting starts to occur roughly halfway along the flow channel (500 x mag.). c) Large amounts of pitting was observed near the outlet (1000 x mag.).

This phenomenon, of a reaction proceeding unevenly along the length of a flow channel, was also observed on the cathodes. The surface close to the inlet showed relatively little

deposition (a, Figure 4.10). The portion inside the flow channel could be clearly identified using the backscattering detector, with a dark film of organics observed on the surface (b, Figure 4.10), however at low magnification few anomalous structures could be seen. On higher magnifications the deposition of organic and metallic species could be observed. Clusters of arborous organic deposits could be seen in some sections (a, b, Figure 4.11). In others, numerous conical structures were observed (c, d, Figure 4.11). The backscattering detector would suggest that these are a similar material to the electrode due to the low contrast between them. Other groups have reported nickel deposits from electrodeposition with similar morphologies, which would support these cones being nickel deposits.<sup>205,206</sup>

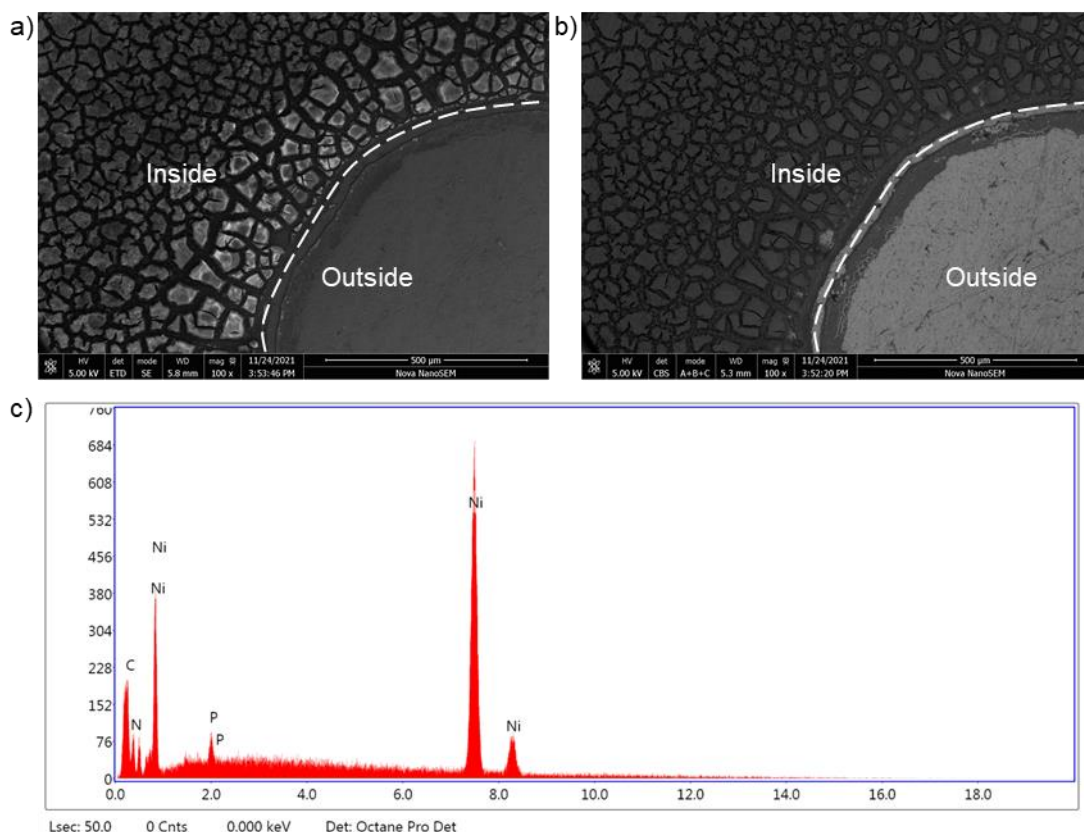


**Figure 4.10:** ETD (a) and CBS (b) images of the first cathode (100 x mag.).



**Figure 4.11:** ETD (a) and CBS (b) images of the first cathode showing organic deposits (1000 x mag.). ETD (c) and CBD (d) images of the first cathode showing conical nickel deposits (5000 x mag.).

The cathode close to the outlet looked markedly different. Even by eye, large amounts of deposition could be seen. Images taken by SEM show a clear difference between the surface inside the flow channel and that outside the flow channel, with large amounts of reticulated deposition inside the flow channel (a, Figure 4.12). Backscattering confirmed that this deposition was largely formed of organics (b, Figure 4.12). EDX of the cathode showed the presence of carbon, nitrogen and phosphorus (c, Figure 4.12). The phosphorus is presumably from the  $\text{PF}_6$  counter ion. It is not clear whether the carbon and nitrogen is from solvent, ligand, product degradation or a mixture of all three.



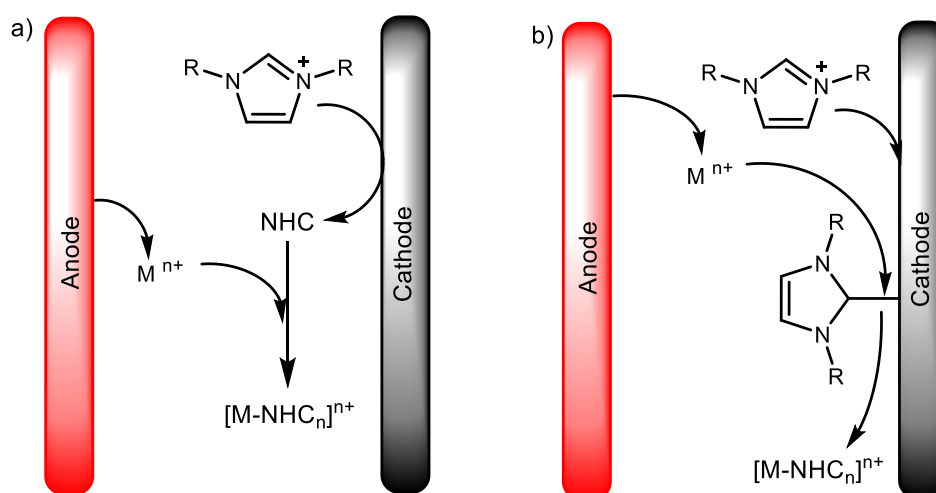
**Figure 4.12:** EDT (a) and CBS (b) images of the second cathode, showing large amounts of organic deposition (100 x mag.).

As previously noted, it is likely that the resistance changes along the course of the flow channel. This would result in different potentials and might explain why the amount of degradation increases closer towards the outlet. Similarly, more deposition in the second half of the reactor would be expected if product degradation is causing the fouling.

### 4.3.3. Divided cell experiments

The mechanism proposed for the synthesis of metal-NHC complexes involves the generation of metal ions at the cathode and the reduction of imidazolium to carbene at the cathode,<sup>170,189</sup> but it has not been directly studied. To try and understand why the synthesis of nickel-NHC complexes is more challenging than copper-NHC complexes a

series of divided cell experiments were designed to try and understand where different parts of the reaction are taking place. To the best of our knowledge, this is the first time that divided cells have been used to gather mechanistic information. For example, it is known that the imidazolium is reduced at the cathode, but not what happens afterwards. Once reduced there are two possibilities: the carbene could dissociate to become a free carbene in solution (a, Scheme 4.9) or it could remain coordinated to the electrode (b, Scheme 4.9). The Glorius group have demonstrated that carbenes can coordinate to gold surfaces<sup>207,208</sup> and the Crudden group have extended this to copper and platinum surfaces.<sup>209–211</sup> If this did occur then a metal ion would need to 'pick up' the carbene by inserting into this bond.

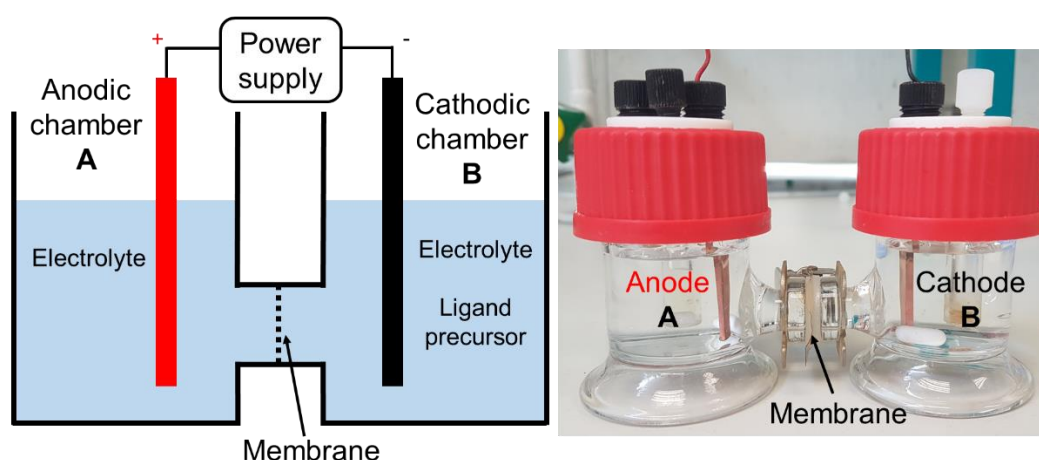


**Scheme 4.9:** Proposed mechanism for the formation of metal-NHC complexes where the carbene is free in solution (a) or remains coordinated to the cathode (b).

For single oxidations and reductions, such as the formation of copper(I)-NHCs, this is relatively simple. However when multiple reductions are involved, such as in the formation of nickel(II)- and iron(II)-NHCs, it could become more complicated. Are both carbenes of a bis-NHC ligand produced at the same time? Does the nickel go directly to Ni(II), or is it stepwise with ligand cooperation? Are there any differences in the mechanism and does this explain why the copper and nickel reaction appear to behave differently to one another?

A divided cell comprises of two chambers separated by an ion exchange membrane, allowing the transfer of charge. One chamber has the cathode and the other the anode. Typically these cells are used when the reaction at the counter electrode is deleterious for a process. The large distance between the electrodes and the presence of the membrane result in an increased cell resistance, consequently large concentrations of electrolyte are usually employed for divided electrochemical reactions.<sup>69,70</sup>

A divided cell was prepared using a Nafion-115 membrane, a proton exchange membrane which allows charge transfer through the movement of protons through it. The cathodic chamber **B** was charged with ligand precursor and electrolyte in anhydrous acetonitrile, and an anhydrous solution of electrolyte in acetonitrile was placed in the anodic chamber **A** (Figure 4.13). The solution was stirred on a low RPM to prevent the stirrer bars sticking to the electrodes and argon was bubbled through both chambers to aid mixing. When a current was applied it would be expected that metal ions would be produced in the anodic chamber and ligand precursor reduced to carbene (either in solution or on the electrode surface) in the cathodic chamber, but these species would be unable to pass through the membrane (a, Scheme 4.10). Consequently samples of each chamber would be expected to contain no product.

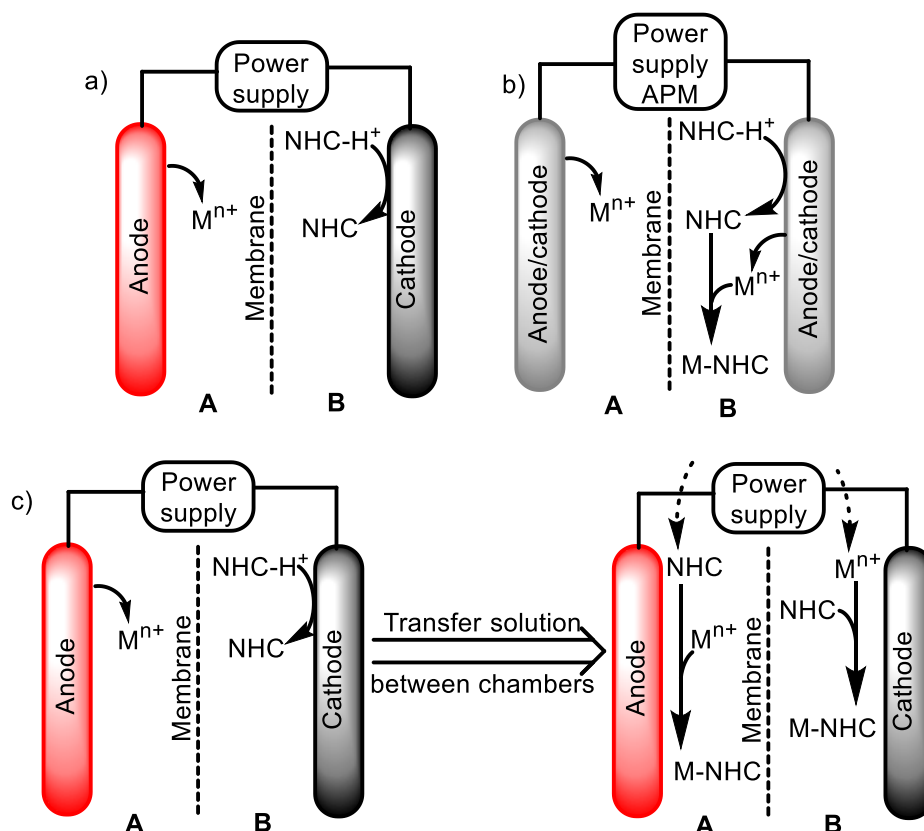


**Figure 4.13:** Divided cell experiments: the anodic chamber **A** contains electrolyte and the cathodic chamber **B** contains electrolyte and ligand precursor. Electrodes are either copper or nickel, depending upon the experiment.

If current was applied using an APM then you would expect to observe product in the 'cathodic' chamber **B** and no product in chamber **A** (b, Scheme 4.10). In this instance both electrodes are acting as anode and cathode. Chamber **A** only contains electrolyte, so metal ions will be produced in the anodic phases and then possibly reduced in the cathodic phase, either plating the electrode or forming aggregates. In chamber **B**, metal ions will be produced in the anodic phases and carbenes will be produced in the cathodic phases. These species can coordinate together to form the metal complex.

Both of these experiments are control experiments, the first should yield no product and tests whether species produced (other than protons) can pass through the membrane. The second acts as a positive control. The last experiment involves applying a current to the divided cell for a fixed amount of time, 1 F for example, and then halting the reaction. At this point half of the solution in each chamber is removed simultaneously and transferred to the opposite chamber (c, Scheme 4.10). If free carbenes are in solution

then product should be observed in the anodic chamber. If the carbenes remain stuck to the surface of the electrode then product will only be observed in the cathodic chamber.

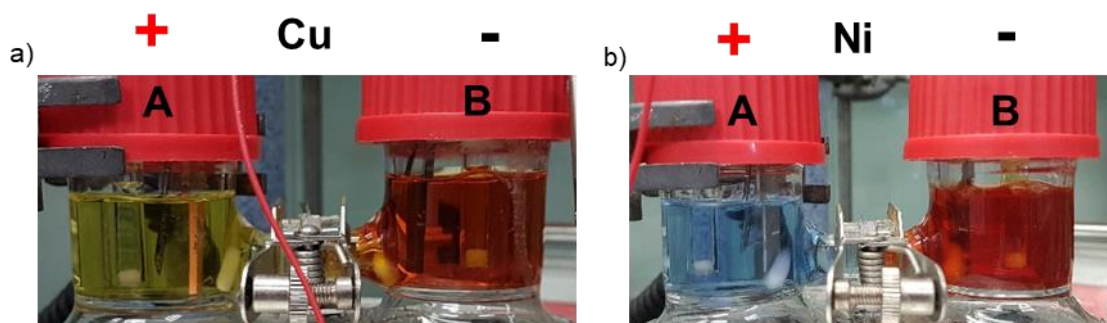


**Scheme 4.10:** Series of divided cell experiments and the expected results. a) Metal ions and carbenes are produced at opposite electrodes and unable to form the product. b) With an APM both electrodes act as anode and cathode. c) Transferring solution between the two chambers.

These reactions were performed using copper electrodes and **L10** as the ligand precursor, and using nickel electrodes with **L11** as the ligand precursor. When the first experiment, applying a current to the divided cell, was conducted with the copper electrodes, the anodic chamber turned a light green, which is interesting because  $[\text{Cu}(\text{MeCN})_4]^+$  is colourless (a, Figure 4.14).<sup>212</sup> This could suggest that some copper(II) ions are present. The cathodic chamber turned from colourless to red, a colour that corresponds to the presence of free carbene in solution.<sup>213</sup> Samples taken from each chamber and analysed with <sup>1</sup>H NMR spectroscopy and HRMS gave the expected results (Entry 1, Table 4.5); only electrolyte in the anodic chamber and electrolyte and **L10** in the cathodic chamber. Solvent was removed from the samples under reduced pressure and the residue was dissolved in hydrous deuterated acetonitrile. Consequently the free carbene would not be expected to be observed as protons from the water in the solvent would protonate the carbene, generating the starting material **L10**. It had been hoped that this technique could be used to produce quantitative conversions, however the electrolyte was in such large excess that product and starting material peaks could not



be fully resolved. Instead only qualitative analysis, i.e. the presence or absence of species, could be conducted.



**Figure 4.14:** Images of the first divided cell experiment at the end of the reaction. Chamber **A** contained electrolyte and chamber **B** contained electrolyte and ligand precursor. The reaction was carried out using copper electrode and **L10** (a) and using nickel electrodes and **L11** (b).

The use of nickel electrodes with **L11** gave the same results, no product was observed in either chamber (Entry 1, Table 4.5). The anodic chamber was blue suggesting the formation of Ni(II) ions, which when in acetonitrile would be expected to form the pale blue octahedral  $[\text{Ni}(\text{MeCN})_6]^{2+}$  (b, Figure 4.14).<sup>191</sup> Similar to the copper reaction, the solution in the cathodic chamber turned red indicating the presence of free carbene.

Copper and nickel reactions also gave the same result as each other for the second experiment, applying a current with the APM. In both cases no product was observed in the ‘anodic’ chamber **A** which contained no ligand precursor, and product (Cu- or Ni-NHC) was observed in the ‘cathodic’ chamber **B**, as would be expected (Entry 2, Table 4.5).

The final experiment, transferring solutions between the two chambers, saw the formation of **Cu10** and **Ni11** in both chambers when copper and nickel electrodes were used respectively (Entry 3, Table 4.5). This confirms the colour observations of the first experiment, that there is some free carbene in solution. Prior to the transfer of solutions the same colours as those observed in the first experiment were also seen. No partially reduced product, with one carbene and one imidazolium, were observed *via* HRMS. This is particularly interesting for the formation of **Ni11** which was found to be present in the anodic chamber, meaning that both imidazoliums in **L11** had been reduced to form the bis-carbene. This would suggest that the rate of electrochemical reduction of **L11** is fast as both imidazoliums are reduced before the ligand can diffuse away from the electrode. Although these experiments do not confirm the absence of ligand coordinated to the electrode, they do demonstrate that free carbenes and metal ions may be found in solution. Furthermore, they show that a similar mechanism is likely responsible for the formation of copper and nickel species.

Entry	Experiment	Copper reaction		Nickel reaction	
		Chamber A	Chamber B	Chamber A	Chamber B
1	50 mA	Bu <sub>4</sub> N <sup>+</sup>	Bu <sub>4</sub> N <sup>+</sup> <b>L10</b>	Bu <sub>4</sub> N <sup>+</sup>	Bu <sub>4</sub> N <sup>+</sup> <b>L11</b>
2	50 mA, 1/60 Hz	Bu <sub>4</sub> N <sup>+</sup>	Bu <sub>4</sub> N <sup>+</sup> <b>L10</b> <b>Cu10</b>	Bu <sub>4</sub> N <sup>+</sup>	Bu <sub>4</sub> N <sup>+</sup> <b>L11</b> <b>Ni11</b>
3	1) 50 mA 2) Remove half of the solution from each chamber and transfer it to the opposite chamber.	Bu <sub>4</sub> N <sup>+</sup> <b>L10</b> <b>Cu10</b>	Bu <sub>4</sub> N <sup>+</sup> <b>L10</b> <b>Cu10</b>	Bu <sub>4</sub> N <sup>+</sup> <b>L11</b> <b>Ni11</b>	Bu <sub>4</sub> N <sup>+</sup> <b>L11</b> <b>Ni11</b>

**Table 4.5:** Summary of the divided cell experiments and the species observed *via* <sup>1</sup>H NMR spectroscopy and HRMS. For the copper reactions the solution was electrolysed with copper electrodes for 1.2 F mol<sup>-1</sup>. For the nickel reactions the solution was electrolysed with nickel electrodes for 2.4 F mol<sup>-1</sup>.

#### 4.3.4. Colour analysis

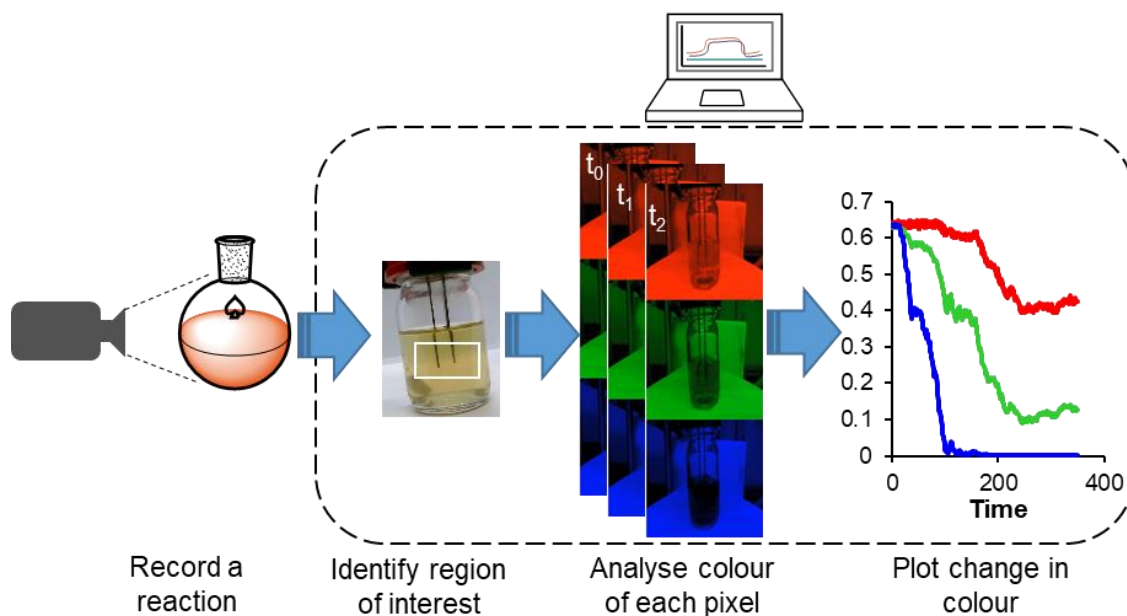
As demonstrated previously, the formation of nickel(II)-complexes exhibits a strong colour change from the pale yellow or colourless solutions of ligand precursors to the dark yellow and orange solutions characteristic of nickel(II)-square planar complexes. Colour changes are a useful observation for chemists to make and amongst the oldest analytical technique, along with taste and smell.<sup>214,215</sup> Whilst the modern chemist should be dissuaded from using their olfactory and gustatory senses, the colour of reactions remains a useful and often underutilised observation.

Typically the colour of a reaction is used qualitatively as a throw away remark in the experimental procedure whilst other techniques based upon similar principles, such as UV-vis spectroscopy, are used quantitatively. More recently there has been an increase in interest for using colour to analyse reaction progression.<sup>216,217</sup> Research by Dr Marc Reid (University of Strathclyde) has used the filming of reactions and subsequent computer processing to quantitatively analyse how the colour of a reaction changes as a reaction proceeds.<sup>218</sup>

First, a reaction is carried out and filmed (Figure 4.15). During the filming process it is important for the focus to remain constant (a camera with manual focus is recommended) and the lighting to remain even. To achieve this, reactions should be performed in a light box so that passing shadows do not affect the colour analysis. The footage is then uploaded to a computer and a region (or regions) of interest is selected. A script is run, analysing the hue of each pixel within the region of interest in each frame. How the hue

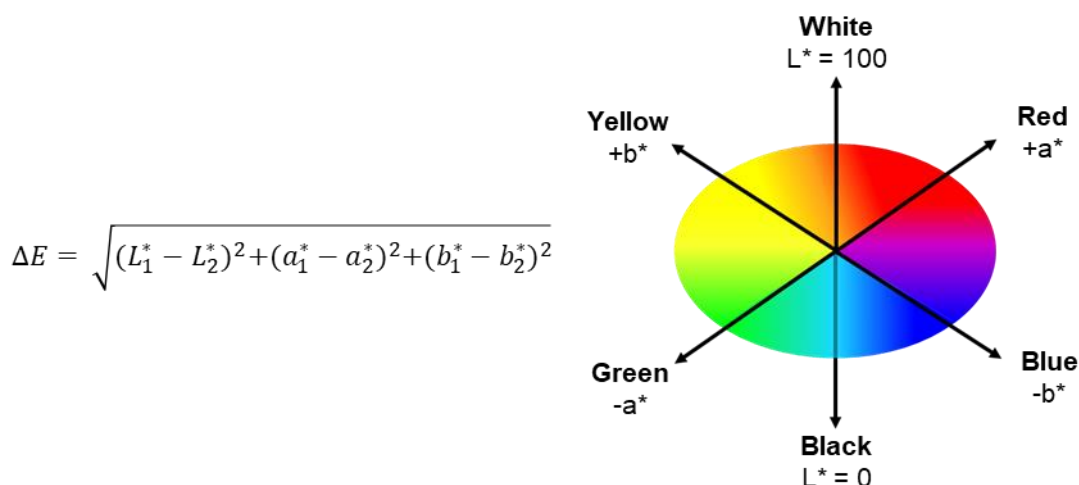


changes over time can be plotted as its red, green and blue components or as  $\Delta E$ , which combines all components and compares the hue, saturation and brightness at any given time point to the start of the reaction ( $t_0$ ). How fast a reaction changes colour can be used to gather kinetic information.



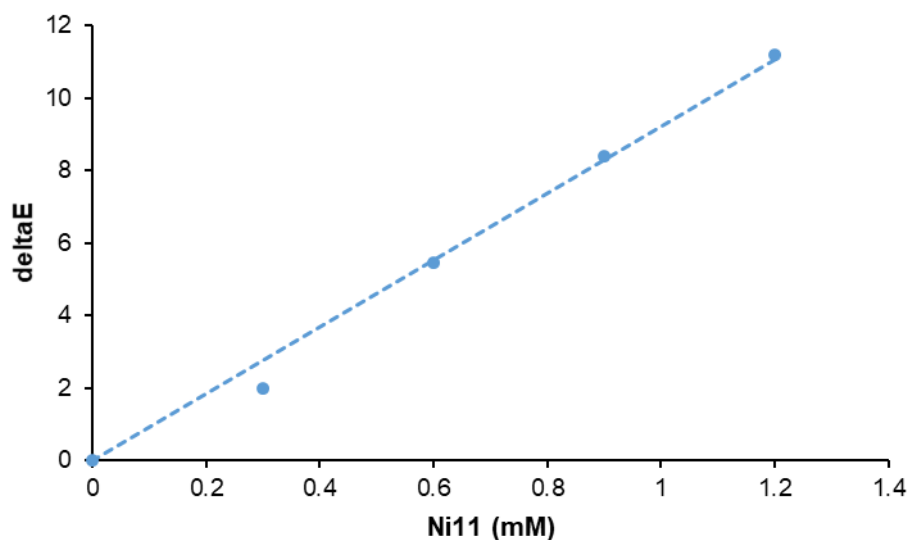
**Figure 4.15:** Workflow for the colour analysis of reactions.

More specifically,  $\Delta E$  is a colour independent measure of contrast. It is a measure of the distance between two colours in the CIEL<sup>\*</sup>A<sup>\*</sup>B<sup>\*</sup> colour space using the Euclidean distance formula (Equation 4.2). The CIEL<sup>\*</sup>A<sup>\*</sup>B<sup>\*</sup> colour space is defined by the International Commission on Illumination (CIE) as a three dimensional space with the axis  $a^*$ ,  $b^*$  and  $L^*$ . The  $L^*$  axis describes the lightness from white (100) to black (0), while the  $a^*$  and  $b^*$  axis describe the amount of red ( $+a^*$ ), green ( $-a^*$ ), yellow ( $+b^*$ ) and blue ( $-b^*$ ).<sup>219</sup>

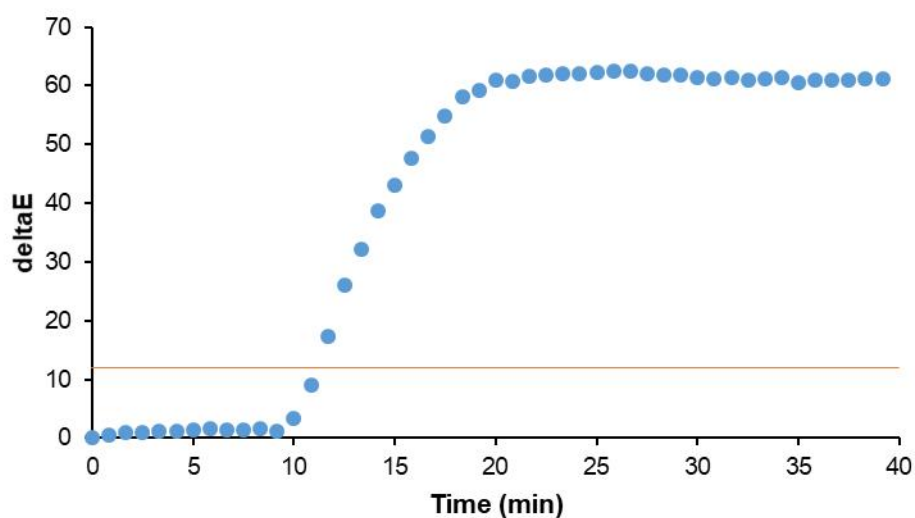


**Equation 4.2:** Calculating deltaE using the CIE L\*a\*b\* colour space.

UV-vis spectroscopy is frequently used as a form of inline analysis for flow reactions,<sup>46</sup> however it was thought to be impractical for this study due to the strongly absorbing nature of the nickel complexes. Instead it was anticipated that colour analysis of the outlet tubing could be used to monitor the reaction. The outlet of the electrochemical flow reactor was filmed by Helen Hoyle (a masters student in the Willans group) and analysed using colour analysis (by Dr Marc Reid – University of Strathclyde), with a sample also collected for analysis by  $^1\text{H}$  NMR spectroscopy. This was compared to a series of calibration films where solutions with a known concentration of **Ni11** and **L11** were placed in a piece of tubing and filmed for a short time (Graph 4.4). The electrochemical reaction eluent showed a stark contrast to the calibration solutions, with the eluent a much darker yellow (Graph 4.5). This would suggest that there might be species other than **Ni11** present in solution, giving it a much darker colour. Whilst these other species are unknown this technique will be of limited use for the inline analysis of this particular reaction.

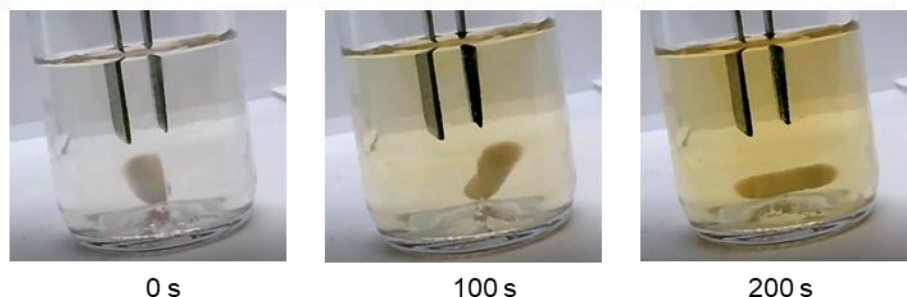
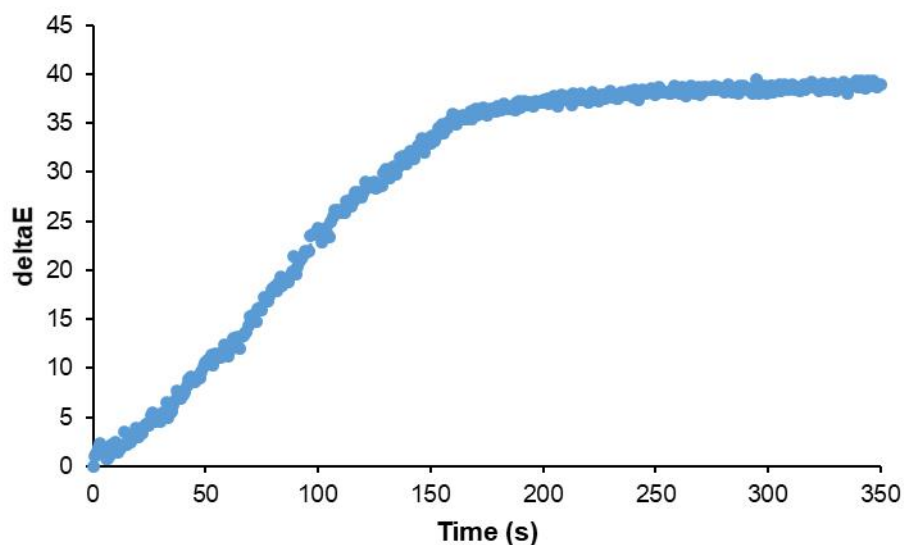


**Graph 4.4:** Top: Colour calibration for the flow reactions. A combined 6 mM solution of **Ni11** and **L11** were filmed. 1.2 mM of **Ni11** corresponds to 20% yield. Bottom: video stills of each concentration.



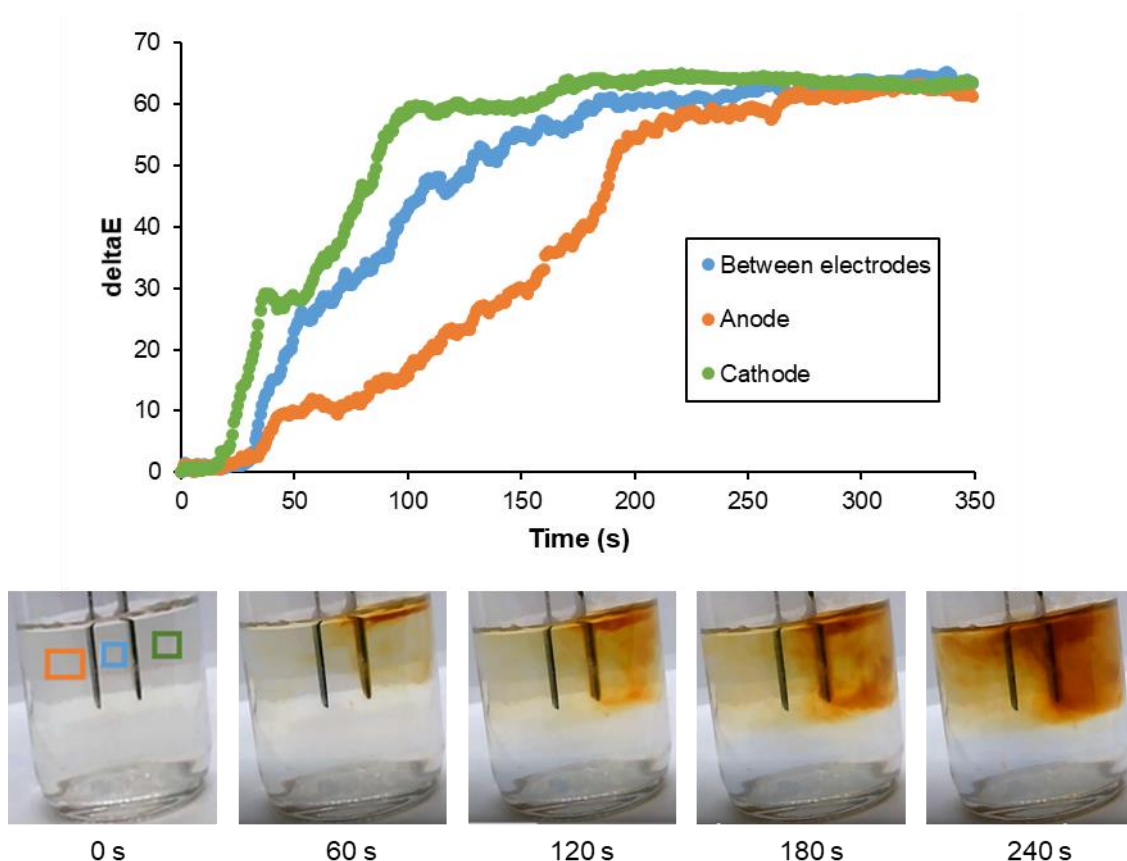
**Graph 4.5:** Colour analysis of the continuous electrochemical synthesis of **Ni11**: 6 mM, 1 mA, 1/60 Hz, 0.04 mL min<sup>-1</sup>. Orange line from calibration corresponds to 20% yield. <sup>1</sup>H NMR analysis showed a yield of 19%.

Colour analysis can be used to compare multiple regions of a reaction vessel, unlike other *in situ* techniques such as UV-vis or IR spectroscopy which look at a single point in the reaction. For heterogeneous reactions, such as electrochemistry, the ability to look at multiple regions of a reaction vessel might be of considerable use. Initial studies, by Helen Hoyle, on the preparation of **Ni11** in batch using the bottle reactor showed a typical kinetic curve when analysed by colour (Graph 4.6). These reactions were stirred, which even with imperfect stirring, would quickly render the reaction solution homogenous. Bubbles, likely hydrogen gas, could also be observed coming off the cathode.



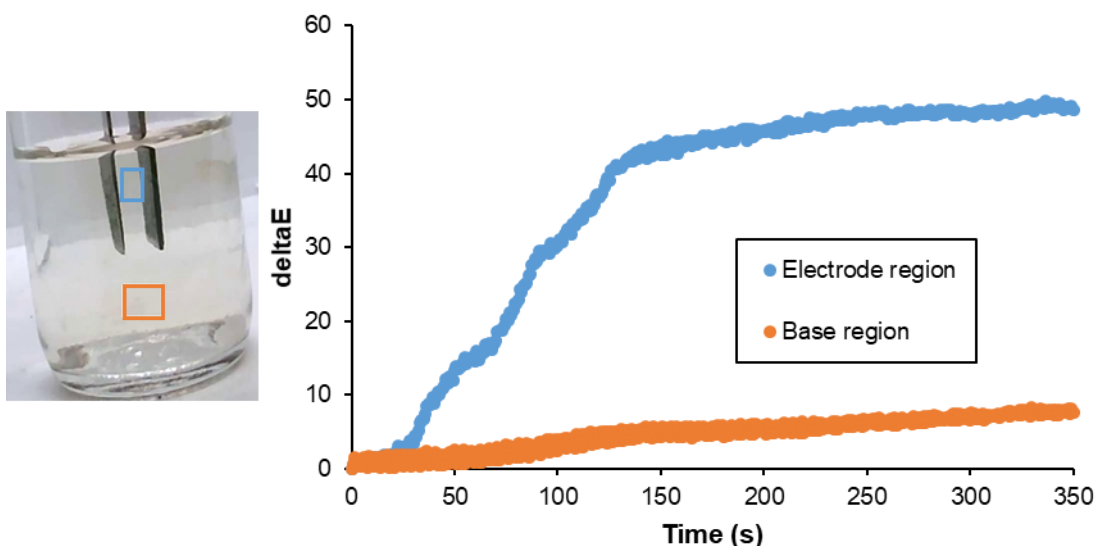
**Graph 4.6:** Colour analysis of the synthesis of **Ni11** in a stirred batch reactor.

To try and gain more insight into where the reaction takes place **Ni11** was prepared in batch, but without any stirring. Colour analysis clearly showed that the reaction did not occur evenly throughout the reactor, with streams of the product being observed coming off of the cathode (Graph 4.7). Any nickel ions produced at the anode are positively charged, meaning that they will be attracted to the negatively charged cathode, moving quickly *via* migration. By contrast, the neutral carbenes generated at the cathode will only be able to mix *via* diffusion which is significantly slower, resulting in the coordination of nickel ions to carbenes occurring close to the cathode.



**Graph 4.7:** Colour analysis of the synthesis of **Ni11** in an unstirred batch reactor, with regions of interest near the anode (orange), in between the electrodes (blue) and near the cathode (green).

When the reactor was divided in half, it was noted that the bottom half remained colourless, even when the solution around the anode became coloured (Graph 4.8). This would suggest that there is very poor mixing between the solution at the top of the reactor and the bottom of the reactor. The fact that this interface appears directly beneath the bottom of the electrodes might suggest that the electrochemistry bears some responsibility. Perhaps it is down to a difference in the conductivity or the presence of ions in solutions which allows this bilayer to appear. Alternatively the bubbles produced at the cathode may aid mixing in the top half of the reactor.



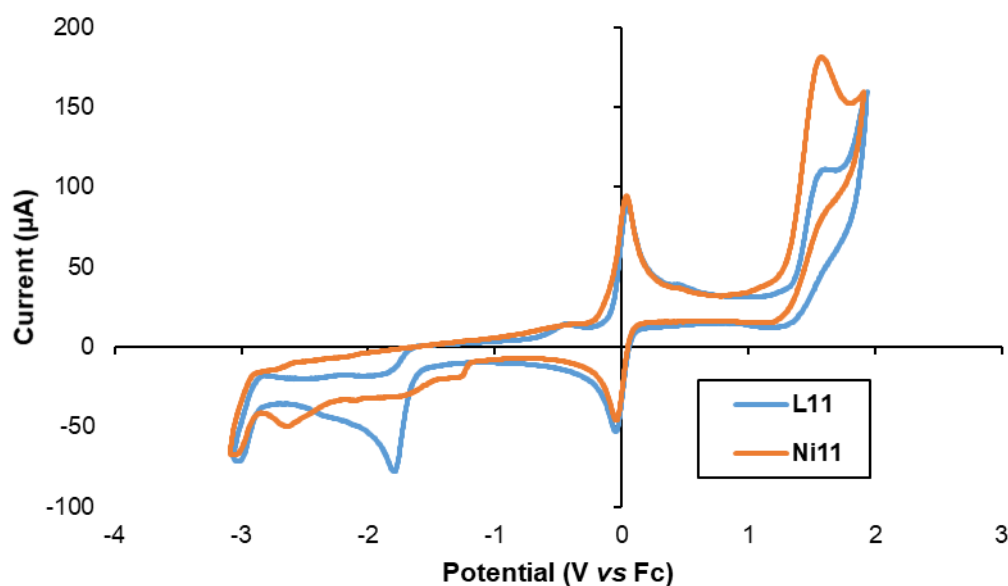
**Graph 4.8:** Colour analysis of the synthesis of **Ni11** in an unstirred batch reactor, with regions of interest near the electrodes (blue) and near the base (orange).

#### 4.4. Product degradation

As well as identifying where the nickel reaction might be taking place, the mechanistic studies suggested that some product degradation might be occurring; a drop in the yield was observed when a slow alternating polarity was used and organic deposits were observed on the cathode. Cyclic voltammetry and the electrolysis of **Ni11** were used to probe the likelihood of product degradation and identify conditions that might reduce the amount of degradation.

##### 4.4.1. Cyclic voltammetry

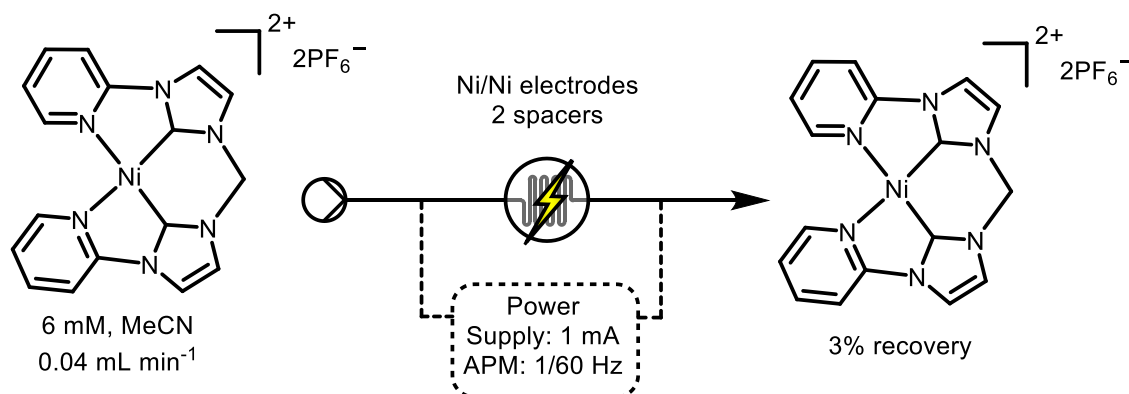
Cyclic voltammograms of **L11** and **Ni11** were obtained using the bottle reactor and a silver wire as a pseudo-reference electrode, with ferrocene as an internal standard (Figure 4.16). The ligand precursor has an irreversible reduction at -1.2 V. The nickel complex appears to have multiple irreversible reduction peaks at -1.25, -1.66, -2.01 and -2.63 V. The Chang group have reported cyclic voltammograms for the same complex in water, observing an irreversible reduction at -0.84 and a partially reversible peak at 1.69 V (vs SCE), they did not scan beyond 2.0 V.<sup>220</sup> Other groups have found that similar complexes exhibit a semi-reversible reduction around 0.9 V.<sup>221,222</sup> To see if this was the case for **Ni11** the scan rate was increased from 300 mV s<sup>-1</sup> to 500 and 800 mV s<sup>-1</sup>, however no reversible peaks were observed. The irreversible reductions observed for **Ni11** could suggest that the complex might be degraded under conditions that are required to produce carbenes.



**Figure 4.16:** Overlaid cyclic voltammograms of ligand precursors **L11** and **Ni11** (1 mM). A silver wire was used as pseudo-reference electrode with ferrocene (1 mM) as an internal standard. Experiments were performed with a scan rate of  $300 \text{ mV s}^{-1}$  in acetonitrile with  $\text{Bu}_4\text{NPF}_6$  (0.1 M) as a supporting electrolyte.

#### 4.4.2. Over-reaction of products

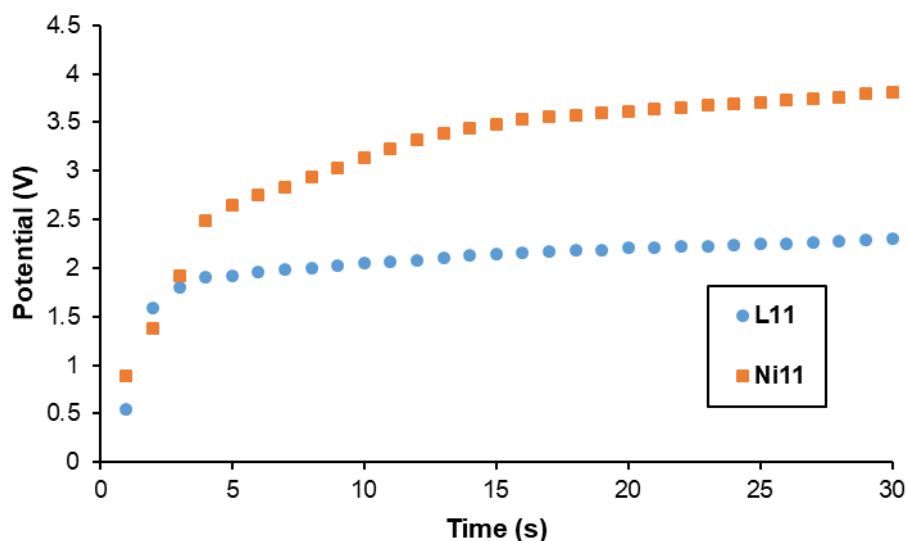
To ascertain whether **Ni11** is stable under reaction conditions a solution of **Ni11** was pumped through the reactor whilst a constant current of 1 mA was applied (Scheme 4.11). The potential was roughly twice that observed when a solution of the ligand precursor is electrolysed, suggesting that **Ni11** is less conductive than **L11**. Only 3% of **Ni11** was observed in the eluent, suggesting that **Ni11** is not stable under reaction conditions.



**Scheme 4.11:** **Ni11** was pumped through the reactor to test its stability under reaction conditions.

When using an APM under galvanostatic conditions the potential will vary, because charge will build up close to the surface of electrodes. When the polarity of the electrodes

swaps the Nernst layers are disrupted, resulting in a low potential that increases logarithmically. The potential was recorded when solutions of **L11** and **Ni11** were pumped through the reactor and a constant current (1 mA) was applied using the APM at 1/60 Hz (Graph 4.9). The potential remained between 1.5 V and 2.5 V for the solution of **L11** for most of the time. By contrast the solution of **Ni11** spent the majority of the time with a potential between 2.5 V and 3.8 V being applied. This would suggest that **Ni11** is less conductive than **L11**, resulting in a higher potential.



**Graph 4.9:** Average potential for half of a period at 1/60 Hz (30 s) when 1 mA is applied to a solution of **L11** or **Ni11**.

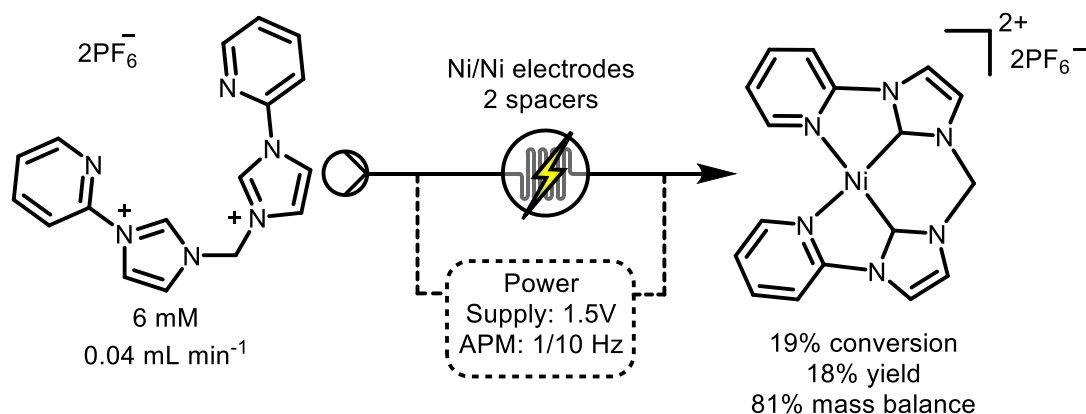
To try and reduce the amount of product degradation, potentiostatic conditions were adopted (Table 4.6). **Ni11** was flowed through the reactor while a constant potential of 2.0 V was applied. 13% of **Ni11** was observed in the eluent. The potential was further reduced to 1.5 V and the amount of **Ni11** observed increased to 19%. Further reductions in the potential were not attempted because the ligand is reduced at -1.40 V and a potential any lower would be insufficient for the formation of the carbene.

I or P	APM	Recovery
0	0 Hz	100%
1 mA	1/60 Hz	3%
2.0 V	1/60 Hz	13%
1.5 V	1/60 Hz	19%

**Table 4.6:** Testing the stability of **Ni11** under different reaction conditions.



The results of the alternating polarity experiments and the studies looking at the stability of **Ni11** were combined to produce new reaction conditions. **L11** was electrolysed using a constant potential of 1.5 V and using an APM with a frequency of 1/10 Hz (Scheme 4.12). This produced **Ni11** with a conversion of 19% and a yield of 18%. The mass balance (combination of **L11** and **Ni11**) was 81%, suggesting that product degradation has been reduced significantly.



**Scheme 4.12:** Reaction conditions for the synthesis of **Ni11** that reduce the amount of product degradation.

#### 4.5. Conclusions and future work

A range of nickel(II)-NHC complexes have been synthesised under continuous electrochemical conditions, with varying degrees of success. Given the ease at which the synthesis of copper(I)-NHCs proceeds, it was surprising that nickel complexes had proven to be considerably more challenging. Despite the difficulties, flow electrochemistry has been demonstrated to offer advantages with regards to the enhanced selectivity for the synthesis of **Ni11**, avoiding the production of **Ni(11)<sub>2</sub>** which is observed in batch.

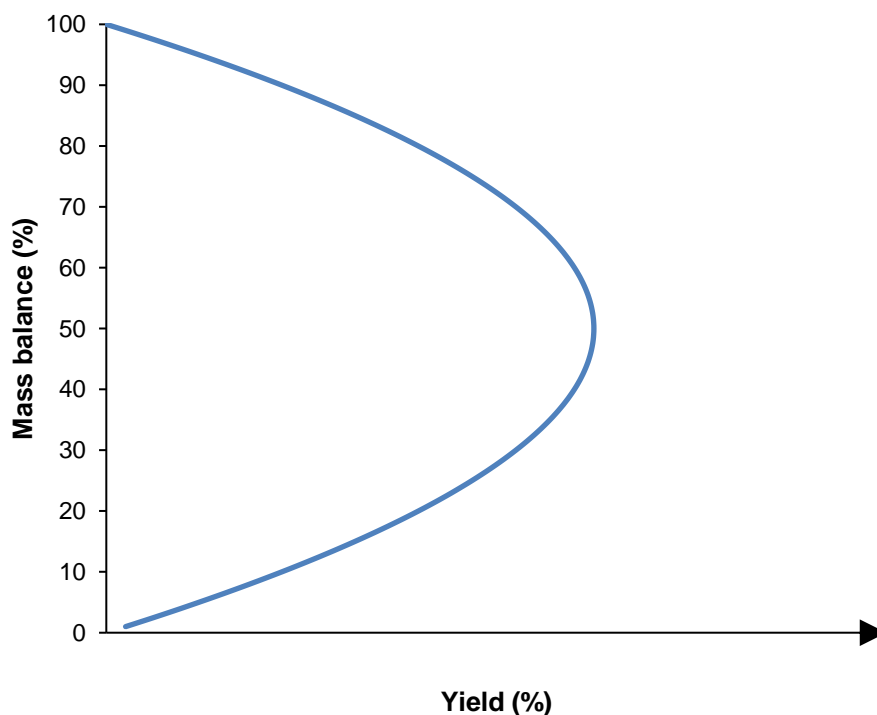
Initial studies identified that nickel-NHC complexes could be made but with a poor mass balance. Surface analysis using SEM and EDX showed large amounts of organic deposition on the cathode surface, particularly in the second half of the reactor. Cyclic voltammetry suggested that this could be as a result of product degradation, something confirmed by the electrolysis of the product under reaction conditions. The ligand screen, and the poor mass balance observed, suggests that product degradation is not limited to **Ni11**.

The frequency of the alternating polarity was found to have a significant effect on the yield, with fast and slow frequencies both leading to a reduction in the yield. This is thought to be because fast frequencies mean that species have insufficient time to diffuse or migrate to the electrode surface and undergo an electrochemical reaction, and

slow frequencies result in the product spending too long at the cathode, leading to product degradation.

Through monitoring a batch electrochemical reaction with colour analysis it was suggested that the majority of complex forms close to the cathode. This is because nickel(II) ions will migrate from the anode to the cathode faster than the neutral carbenes will diffuse from cathode to anode. The use of divided cells was also used to investigate the mechanism, confirming that free carbenes can be found in solution and that the copper and nickel reactions are likely to proceed *via* a similar mechanism. This further supports the idea that product degradation is responsible for the difference in mass balance between copper and nickel reactions, as opposed to a difference in the mechanism.

Using the knowledge obtained about how the potential and alternating polarity affects the reaction, reaction conditions were optimised to minimise the amount of product degradation by reducing the applied potential and using a moderate flicker frequency. Although this did not improve the yield of the reaction, it did increase the mass balance by fourfold. This is significant because if nickel complexes are to be produced on-demand to act as catalysts it is essential to know what species are being dispensed into a reaction, especially for the synthesis of pharmaceuticals. It is expected that there will be a trade-off between the yield and the mass balance, with more forcing conditions leading to more product but also more product degradation (Graph 4.10).



**Graph 4.10:** Hypothesised trade-off between yield and mass balance.

It is anticipated that the divided cell experiment could be used to investigate the mechanism of other reactions that involve successive oxidations and reductions, such as the domino oxidation-reduction reaction developed by the Waldvogel group.<sup>180</sup> The electrochemical synthesis literature is currently dominated by reactions involving a single oxidation or reduction with a counter reaction, typically involving the solvent, occurring at the opposite electrode. As electrochemistry matures it is expected that an increasing number of reactions will use both electrodes and a larger number of domino-type reactions will be developed. Consequently, techniques such as the divided cell experiments described here might be helpful in elucidating the mechanisms of such reactions.

## 4.6. Experimental

### 4.6.1. General considerations

NMR data was obtained on either a Bruker AVneo 500 (CH dual cryoprobe) or Bruker Ascend 400 spectrometer.  $^1\text{H}$  NMR and  $^{13}\text{C}\{^1\text{H}\}$  chemical shifts were referenced against residual solvent peaks. Mass spectra were collected on a Bruker Daltonics (micro TOF) instrument operating in the electrospray mode. Elemental Analyses were performed by Mr Stephen Boyer at London Metropolitan University.

Where stated, reactions were carried out under an inert atmosphere of dry nitrogen or argon, using standard Schlenk line or glovebox technique. Anhydrous solvents were dried by passing over activated alumina to remove water and copper catalyst to remove oxygen *via* the Dow-Grubbs solvent system. They were collected onto activated molecular sieves to remove any remaining water. Acetonitrile was degassed with argon. All reagents were used as supplied, without further purification.

All crystals were obtained by recrystallisation from MeCN/ Et<sub>2</sub>O. Data was collected at 120 K on crystals mounted on a Hampton Scientific cryoloop using a SuperNova, Dual, Cu at home/near, Atlas. The structures were solved by direct methods with SHELXT, refined using full-matrix least-squares routines against  $F^2$  with SHELXL, and visualized using OLEX2.<sup>151,152</sup> All non-hydrogen atoms were refined anisotropically. All hydrogen atoms were placed in calculated positions and refined using a riding model with fixed C–H distances of 0.95 Å ( $sp^2\text{CH}$ ), 1.00 Å (CH), 0.99 Å (CH<sub>2</sub>), 0.98 Å (CH<sub>3</sub>). The thermal parameters of all hydrogen atoms were estimated as  $U_{\text{iso}}(\text{H}) = 1.2U_{\text{eq}}(\text{C})$  except for CH<sub>3</sub> where  $U_{\text{iso}}(\text{H}) = 1.5U_{\text{eq}}(\text{C})$ .

Cyclic voltammetry of **L11** and **Ni11** were performed at room temperature in the bottle reactor using a Metrohm, DropSens,  $\mu\text{STAT}$  400 potentiostat and data acquired with DropView 8400 software. Experiments were performed in anhydrous, degassed acetonitrile (1 mM),  $n\text{Bu}_4\text{NPF}_6$  (0.1 M) supporting electrolyte (scan rate of 300 mV s<sup>-1</sup>), with an IKA glassy carbon disk (1 mm) working electrode, platinum wire counter electrode, and silver wire pseudo-reference electrode. Ferrocene (Fc) was added as an internal standard (1 mM,  $\text{Fc}^+/\text{Fc}$  at +0.380 V vs SCE) to reference experiments.

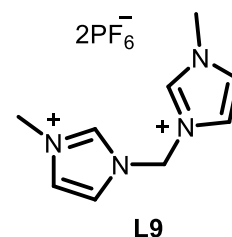
Scanning electron microscopy (SEM) and energy dispersive X-ray analysis (EDX) were conducted on an FEI NanoSEM Nova 450 by Dr Alexander Kulak (University of Leeds).

### 4.6.2. Ligand synthesis

**L12** was prepared by Dr Thomas Nicholls and was used without further purification.

#### 4.6.2.1. L9

N-methyl imidazole (4 mL, 50 mmol) was placed in an ampoule under nitrogen and dibromomethane (20 mL, 250 mmol) was added. The ampoule was sealed and heated to 100 °C for 25 hours to leave a yellow semi-solid mass. The remaining dibromomethane was removed under vacuum and the solid washed with diethyl ether (30 mL), acetone (30 mL) and diethyl ether (30 mL). The solid was redissolved in water (200 mL) with  $\text{NH}_4\text{PF}_6$  (10 g, 60 mmol) and stirred for 2 hours, forming a precipitate. The mixture was filtered and the solid washed with water and diethylether to leave **L9** as a white powder (5.77 g, 12.3 mmol, 25%).



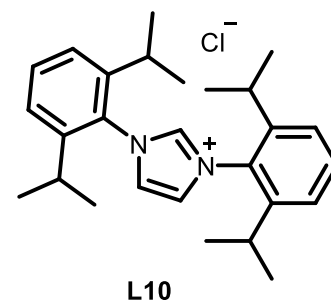
$^1\text{H}$  NMR (400 MHz,  $\text{CD}_3\text{CN}$ )  $\delta$  8.73 (s, 2H, NCHN), 7.59 (d,  $J = 1.8$  Hz, 2H, Imid<sub>backbone</sub>), 7.47 (d,  $J = 1.8$  Hz, 2H, imid<sub>backbone</sub>), 6.40 (s, 2H,  $\text{CH}_2$ ), 3.91 (s, 6H,  $\text{CH}_3$ ).

$^{13}\text{C}\{^1\text{H}\}$  NMR (101 MHz,  $\text{CD}_3\text{CN}$ )  $\delta$  137.92 (NCHN), 125.55 (CH), 122.60 (CH), 118.00 ( $\text{CH}_2$ ), 59.28 ( $\text{CH}_3$ ).

HRMS (ESI+):  $m/z$  89.0594 [ $\text{M}-2\text{PF}_6$ ] $^{2+}$ , calcd. 89.0607.

#### 4.6.2.2. L10

2,6-Diisopropyl aniline (50 mL, 400 mmol) was dissolved in methanol (200 mL). Acetic acid (3 mL) was added followed by the dropwise addition of glyoxal (30 mL, 160 mmol). The reaction was stirred for 6 hours, resulting in a bright yellow precipitate. The mixture was filtered and the precipitate washed with methanol before a portion (4.71 g, 12.5 mmol) was dissolved in ethyl acetate (100 mL). Paraformaldehyde (0.40 g, 13.1 mmol) was added and the solution was heated to 70 °C. A solution of TMSCl (1.7 mL, 13.1 mmol) in ethyl acetate (10 mL) was added dropwise and the solution was heated for a further 2 hours, resulting in the formation of a precipitate. The mixture was cooled, filtered under vacuum and washed with ethyl acetate (3x25 mL) to give **L10** as a white power (4.83 g, 11.3 mmol, 90%).



$^1\text{H}$  NMR (400 MHz,  $\text{CD}_3\text{CN}$ )  $\delta$  9.64 (s, 1H, NCHN), 7.87 (d,  $J = 1.6$  Hz, 2H, Imid<sub>backbone</sub>), 7.69 – 7.60 (t,  $J = 7.8$  Hz, 2H, ArH), 7.47 (d,  $J = 7.8$  Hz, 4H, ArH), 4.06, 2.42 (hept,  $J = 6.8$  Hz, 4H, CH), 1.30 – 1.16 (m, 24H,  $\text{CH}_3$ ).

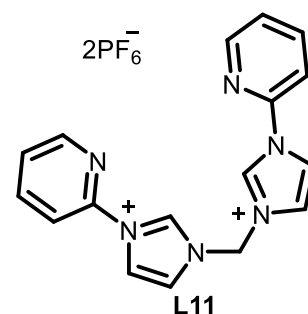
$^{13}\text{C}$  NMR (101 MHz,  $\text{CD}_3\text{CN}$ )  $\delta$  146.30 (NCHN), 138.62 ( $\text{CH}_{\text{imid}}$ ), 133.03 (ArH), 130.00 (ArH), 126.85 (ArH), 125.62 (ArH), 29.84 (CH), 24.53 ( $\text{CH}_3$ ), 23.71 ( $\text{CH}_3$ ).

HRMS (ESI+):  $m/z$  389.2749 [ $\text{M}-\text{Cl}$ ] $^+$ , calcd. 389.2951.

Consistent with data previously reported.<sup>223</sup>

#### 4.6.2.3. L11

Imidazole (9.19 g, 135 mmol) and potassium hydroxide (12.5 g, 250 mmol) were placed in an ampoule under nitrogen and 2-bromopyridine (4.3 mL, 45 mmol) was added. The ampoule was sealed and heated to 190°C for 21 hours. The resultant solid was dissolved in water and extracted with DCM (3x30 mL). The combined organic extracts were washed with aqueous solutions of sodium carbonate (5x50 mL) and water (50 mL), dried with magnesium sulphate and filtered before the solvent was removed to leave a yellow/orange oil. The oil was left to crystallise in the freezer over the course of 3 days. A portion of the solid (1.7 g, 11 mmol) was placed in an ampoule under nitrogen and dibromomethane (12 mL, 150 mmol) was added. The Ampoule was sealed and heated to 100°C for 21 hours, resulting in a solid yellow mass. This was suspended in ether (*via* sonication) and filtered. The solid was then dissolved in water and  $\text{NH}_4\text{PF}_6$  (7.0 g, 43 mmol) was added. The solution was stirred for 2 hours and the solid was filtered off and washed with water and diethyl ether to leave **L11** as an off-white powder (2.71g, 4.5 mmol, 41%).



$^1\text{H}$  NMR (400 MHz, DMSO)  $\delta$  10.38 (s, 2H, NCHN), 8.71 (d,  $J = 4.8$  Hz, 2H), 8.64 (dd,  $J = 2.6, 1.1$  Hz, 2H), 8.32 – 8.22 (m, 4H), 8.05 (d,  $J = 8.2$  Hz, 2H), 7.74 – 7.65 (m, 2H), 6.85 (s, 2H,  $\text{CH}_2$ ).

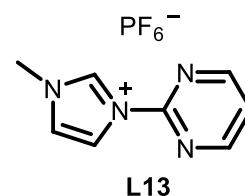
$^{13}\text{C}\{^1\text{H}\}$  NMR (101 MHz, DMSO)  $\delta$  149.93 (NCHN), 146.50 (ArH), 141.37 (ArH), 137.58 (ArH), 126.26 (ArH), 123.86 (CH), 120.22 (CH), 114.79 (ArH), 59.66 ( $\text{CH}_2$ ).

HRMS (ESI+):  $m/z$  152.0702 [ $\text{M}-2\text{PF}_6$ ] $^{2+}$ , calcd. 152.0713, 449.1089 [ $\text{M}-\text{PF}_6$ ] $^+$ , calcd. 449.1073.

Consistent with data previously reported.<sup>224</sup>

#### 4.6.2.4. L13

2-Chloropyrimidine (3 g, 26.4 mmol) was placed in an ampule and dissolved in *N*-methyl imidazole (2.1 mL, 26.2 mmol). The ampule was sealed and heated to 110 °C for 18 hours to give a brown solid. The solid was dissolved in methanol (5 mL) and THF was added (80 mL) to produce a pale yellow precipitate. The precipitate was filtered off and dissolved in water (20 mL) and ammonium hexafluorophosphate was added (4.2 g). The solution was stirred for 1.5 hours and the resultant pale yellow precipitate was filtered off, washed with diethyl ether and recrystallised in acetonitrile.



$^1\text{H}$  NMR (300 MHz,  $\text{CD}_3\text{CN}$ )  $\delta$  9.41 (s, 1H, NCHN), 8.88 (d,  $J$  = 4.9 Hz, 2H, ArH), 8.21 (d,  $J$  = 1.9 Hz, 1H,  $\text{CH}_{\text{imid}}$ ), 7.60 (t,  $J$  = 4.9 Hz, 1H, ArH), 7.53 (d,  $J$  = 1.9 Hz, 1H,  $\text{CH}_{\text{imid}}$ ), 3.97 (s, 3H,  $\text{CH}_3$ ).

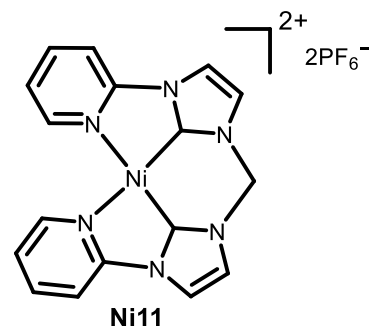
$^{13}\text{C}$  NMR (101 MHz,  $\text{CD}_3\text{CN}$ )  $\delta$  160.48 (NCHN), 152.89 (ArH), 136.01 (ArH), 125.54 (ArH), 123.03 ( $\text{CH}_{\text{imid}}$ ), 119.66 ( $\text{CH}_{\text{imid}}$ ), 37.27 ( $\text{CH}_3$ ).

HRMS (ESI+):  $m/z$  161.0824 [ $\text{M-PF}_6$ ] $^{2+}$ , calcd. 161.0822.

Consistent with data previously reported.<sup>225</sup>

#### 4.6.3. Chemical synthesis of Ni11

**L11** (0.50 g, 85 mmol) and  $\text{Ni}(\text{OAc})_2 \cdot 4\text{H}_2\text{O}$  (0.43 g, 170 mmol) were placed under argon and dissolved in DMSO. The green solution was heated at 50 °C for four hours to give a orange-brown solution. The solvent was removed under vacuum and the yellow solid washed with THF (3 x 30 mL) to give **Ni11** (0.41 g, 60 mmol, 71%).



$^1\text{H}$  NMR (400 MHz, DMSO)  $\delta$  8.83 (d,  $J$  = 4.9 Hz, 2H, ArH), 8.53 (s, 2H, Imid), 8.41 (t,  $J$  = 7.1 Hz, 2H, ArH), 8.21 (d,  $J$  = 7.6 Hz, 2H, ArH), 8.04 (s, 2H, Imid), 7.69 (t,  $J$  = 7.3 Hz, 2H, ArH), 6.59 (s, 2H,  $\text{CH}_2$ ).

$^{13}\text{C}$  NMR (101 MHz, DMSO)  $\delta$  159.60 (ArH), 150.07 (ArH), 149.51 (ArH), 143.62 (ArH), 124.63 ( $\text{CH}_{\text{imid}}$ ), 124.15 ( $\text{CH}_{\text{imid}}$ ), 118.97, 112.77 ( $\text{CH}_2$ ).

HRMS (ESI+):  $m/z$  180.0303 [ $\text{M-2PF}_6$ ] $^{2+}$ , calcd. 180.0311

Consistent with data previously reported.<sup>14</sup>

#### 4.6.4. Electrochemical batch reactions

##### 4.6.4.1. General procedure

A bottle reactor vial was charged with the ligand precursor (1 mmol), then the reactor was assembled and placed under an atmosphere of argon. MeCN (anhydrous, 15 mL) was added and nickel electrodes were used to apply a constant current of 50 mA for 80 minutes ( $2.4 \text{ F mol}^{-1}$ ) from a Tenma bench top power supply (72-10480 from Farnell). A sample of approximately 0.5 mL was taken at the end of the reaction and filtered through Celite after which the solvent was removed under reduced pressure. The resultant solid was redissolved in a suitable deuterated solvent and analysed using  $^1\text{H}$  NMR spectroscopy. Integrals for the complex and ligand were used to calculate the conversion.

#### 4.6.5. Electrochemical flow reactions

The third generation electrochemical flow reactor was machined out of stainless steel by the workshop in the School of Mechanical Engineering at the University of Leeds. Electrodes and spacers were designed on Corel Draw. Nickel foil (1.0 mm thick, 99.0%, NI000608) was purchased from Goodfellow Cambridge Limited and cut into electrodes by Laser Master (Redruth, TR16 6HY). Spacers were laser cut by Laser Web (Barnsley, S71 3HS) from PTFE sheets with a thickness of 1 mm.

##### 4.6.5.1. General procedure

6mM solutions of ligand precursor in anhydrous acetonitrile were prepared under argon. The solution was transferred to a syringe and pumped through the reactor (3 nickel electrodes, 2 'normal' spacers, 0.926 mL) using a syringe pump. A constant potential or current was applied using a Tenma bench top power supply (72-10480 from Farnell) with an alternating polarity microcontroller (Arduino MKZERO with Arduino MKR relay proto shield) in series.

Two residence times were allowed to elapse for the reactor to reach steady state, before the eluent was collected for one residence time in a round bottomed flask in air. A portion of eluent (1 mL) and TMB (6 mM, 0.33 mL) were combined. The solvent was removed under vacuum and the remaining solid dissolved in deuterated acetonitrile.  $^1\text{H}$  NMR spectroscopy was used to calculate the conversion from the integrals of the imidazolium salt and the nickel-NHC complexes and the yield from the integrals of the nickel-NHC and the TMB.

Where the potential was recorded (Graph 4.9), the power supply was recorded with a video camera and the potential noted manually for 2 periods (2 minutes). The potential was then averaged for each 30 s (each half period).

##### 4.6.5.2. Ni9

I or P	APM	Conversion	Yield
1.8 V	1/60 Hz	28%	-
2.3 V	1/60 Hz	55%	-
1 mA	1/60 Hz	100%	49%

**Table 4.7:** Results for the continuous electrochemical synthesis of Ni9.



## 4.6.5.3. Ni10

I or P	APM	Conversion	Yield
1 mA	1/60 Hz	40%	4%

**Table 4.8:** Results for the continuous electrochemical synthesis of **Ni10**.

## 4.6.5.4. Ni11

Solvent	Electrolyte	I or P	APM	Conversion	Yield
MeCN	No	0	0	0%	0%
MeCN	No	1 mA	1/60 Hz	100%	19%
DMF	No	1 mA	1/60 Hz	100%	19%
THF	No	1 mA	1/60 Hz	0%	0%
MeOH	No	1 mA	1/60 Hz	0%	0%
MeCN	No	2.0 V	1/60 Hz	100%	19%
MeCN	Yes	1 mA	1/60 Hz	100%	19%
MeCN	Yes	1 mA	0 Hz	100%	4%
MeCN	No	1 mA	5 Hz	100%	10%
MeCN	No	1 mA	3 Hz	100%	17%
MeCN	No	1 mA	1Hz	100%	19%
MeCN	No	1 mA	1/3 Hz	100%	25%
MeCN	No	1 mA	1/10 Hz	100%	28%
MeCN	No	1 mA	1/30 Hz	100%	24%
MeCN	No	1 mA	1/120 Hz	100%	16%
MeCN	No	1 mA	1/240 Hz	100%	12%
MeCN	No	1.5 V	1/10 Hz	19%	18%

**Table 4.9:** Results for the continuous electrochemical synthesis of **Ni11**.

#### 4.6.5.5. Ni12

I or P	APM	Conversion	Yield
1 mA	1/60 Hz	100%	24%

**Table 4.10:** Results for the continuous electrochemical synthesis of **Ni12**.

#### 4.6.5.6. Ni13

I or P	APM	Conversion	Yield
1 mA	1/60 Hz	0% (no <b>L13</b> )	0%

**Table 4.11:** Results for the continuous electrochemical synthesis of **Ni13**.

### 4.6.6. Divided cell experiments

The divided cell was assembled with Nafion-115 membrane and a metal anode and cathode. The cathodic chamber was charged with ligand precursor (1 mmol, **L10** with copper electrode and **L11** with nickel electrodes) and Bu<sub>4</sub>NBF<sub>4</sub> (4.0 g, 12.1 mmol) and the anodic chamber with Bu<sub>4</sub>NBF<sub>4</sub> (4.0 g, 12.1 mmol). Both chambers were placed under argon and anhydrous acetonitrile (20 mL) was added to both chambers and stirred until all material had dissolved. Both chambers were stirred and argon was bubbled through to aid mixing. A current was then applied for 2.5 F mol<sup>-1</sup>, after which a sample was removed and analysed using <sup>1</sup>H NMR and HRMS.

571.5734 was present in all samples analysed by HRMS, this is possibly from the membrane.

m/z	Species
242.2867	Bu <sub>4</sub> N <sup>+</sup>
389.2950	[ <b>L10</b> - H] <sup>+</sup>
492.2438	[ <b>Cu10</b> - Cl + MeCN] <sup>+</sup>
152.0702	[ <b>L11</b> - 2PF <sub>6</sub> ] <sup>2+</sup> ,
629.5337	[ <b>Ni11</b> - PF <sub>6</sub> + 3MeCN] <sup>+</sup>

**Table 4.12:** Species observed via HRMS during the divided cell experiments.

**Experiment 1:** 50 mA was applied for 2.5 F mol<sup>-1</sup>.

**Experiment 2:** 50 mA was applied for 2.5 F mol<sup>-1</sup> with an APM (1/60 Hz).

**Experiment 3:** 50 mA was applied for 2.5 F mol<sup>-1</sup>, half of the solution in each chamber was then removed and transferred to the opposite chamber.

Experiment		Copper reaction		Nickel reaction	
		Chamber A	Chamber B	Chamber A	Chamber B
1	50 mA	Bu <sub>4</sub> N <sup>+</sup>	Bu <sub>4</sub> N <sup>+</sup> <b>L10</b>	Bu <sub>4</sub> N <sup>+</sup>	Bu <sub>4</sub> N <sup>+</sup> <b>L11</b>
2	50 mA, 1/60 Hz	Bu <sub>4</sub> N <sup>+</sup>	Bu <sub>4</sub> N <sup>+</sup> <b>L10</b> <b>Cu10</b>	Bu <sub>4</sub> N <sup>+</sup>	Bu <sub>4</sub> N <sup>+</sup> <b>L11</b> <b>Ni11</b>
3	3) 50 mA 4) Remove half of the solution from each chamber and transfer it to the opposite chamber.	Bu <sub>4</sub> N <sup>+</sup> <b>L10</b> <b>Cu10</b>	Bu <sub>4</sub> N <sup>+</sup> <b>L10</b> <b>Cu10</b>	Bu <sub>4</sub> N <sup>+</sup> <b>L11</b> <b>Ni11</b>	Bu <sub>4</sub> N <sup>+</sup> <b>L11</b> <b>Ni11</b>

**Table 4.13:** Summary of the results from the divided cell experiments.

#### 4.6.7. Colour analysis

All video footage was collected using a RS Pro Webcam (part no. 201-3517). All footage was captured using the standard camera settings (30 frames per second, 1080x720 resolution). Due to a maximum video recording length of 10 mins, where reactions were recorded for longer, the collected 10-min video clips were combined into a single video file before analysis.

Video analysis was performed in collaboration with Dr Marc Reid (University of Strathclyde) using the developmental video analysis software Kineticolor. An early electrochemically-focused application of this software has been reported in the literature.<sup>218</sup> All video data in this report were analysed using the December 2021 version of the software.

All videos were analysed by breaking videos into their constituent frames, and each frame being analysed in turn. A user-selected region of interest was analysed, averaging all pixel values in the selected range. All background data outside the selected region was ignored in the analysis. Data were analysed according to a user-selected number of frames to be skipped. For example, most datasets were analysed at a sample rate of one datapoint per second. This was achieved by setting the software to analyse only every 30<sup>th</sup> frame. The analysed frames were curated in plots of various colour components versus time to enable semi-quantitative and comparative kinetic analysis between different video analysis datasets.

Extracted colour data was provided from across a common subset of colour models, namely: RGB, HSV, CIE-L\*a\*b\*, and CIE-XYZ. For the purposes of this report, analysis primarily focused on plots of Delta E versus time. Delta E is the colour-independent

measure of contrast, measured as the Euclidean distance between two colours in the CIE\_L\*a\*b\* colour space.<sup>216</sup>

## 5. Conclusion

Sustainable manufacturing is a key part of the UKRI's strategy to reach NET zero. Emerging technologies, such as electrochemistry, will be essential to reducing the environmental impact of large scale chemical processes. Electrochemistry is an atom efficient means of performing redox reactions, avoiding the use of stoichiometric reagents. Another key challenge is the replacement of second and third row metal catalysts, that are costly and scarce, with earth abundant base metals. Typically first row transition metal complexes are challenging to synthesise and store, making them unattractive catalysts for medicinal and process chemists that often have to design routes within a tight timeframe. This thesis has aimed to address these issues: the accessibility of electrochemical reactors, along with our understanding of electrochemical flow reactors, and the ability to produce first row metal complexes on demand *via* electrochemical methodologies.

Presently there is a lack of affordable reactors that researchers can use to develop electrochemical reactions. The bottle reactor was designed with versatility and cost in mind. It may be used with a wide array of electrodes with different dimensions, unlike many commercial counterparts, and it can be placed under an inert atmosphere with ease. Ports allow solutions to be added and removed during the reaction, or for analysis to be performed. The development and manufacture of the bottle reactor aims to increase the accessibility of electrochemistry to the synthetic chemist. The low cost and versatility of the bottle reactor will enable more research laboratories to experiment with electrochemistry.

Electrochemistry can be challenging to scale up in batch, instead most groups turn to flow chemistry, which typically has a higher throughput. In the course of developing an electrochemical flow reactor it was noted that hops, where the solution passes through an electrode, led to an increase in the amount of product observed. Computational studies and electrochemical analysis confirmed that the shape of the hops led to an increase in the effective mass transfer without changing the flow regime. This demonstrated that the increase in effective mass transfer came from the fact that during a hop the electrodes swap which side of the channel they are on, as opposed to the additional pumping power required, which is relatively modest. The increase in mass transfer without an appreciable pressure drop is likely to be of use for the scale up of electrochemical flow reactors, something that will be essential if electrochemistry is to become widely used for the manufacture of large quantities of product.

Flow electrochemistry may also be used to produce metal complexes and telescope them into reactions to act as catalysts. This is of particular interest as the chemistry community pivots towards the use of first row metals, which are challenging to synthesise using traditional methods and are particularly well suited to synthesis *via* electrochemical means. Such methodologies already exist for the synthesis of copper(I)-NHC complexes; this thesis aimed to extend it to nickel(II)-NHC complexes. This class of complexes is of particular interest due to its ability to act as catalysts for cross coupling reactions. During the course of synthesising nickel(II)-NHC complexes in flow it was noted that the reaction had a very poor mass balance and significant amounts of material was being destroyed. A raft of techniques were used to gain mechanistic understanding, demonstrating that the product was being degraded. These insights enabled reaction conditions to be modified to reduce the amount of product degradation and improved the mass balance. It is anticipated that such methodologies, which are generally simple to perform even for non-specialists, will increase the accessibility of first row complexes for the synthetic chemistry community.

## 6. References

- 1 P. de Frémont, N. Marion and S. P. Nolan, *Coord. Chem. Rev.*, 2009, **253**, 862–892.
- 2 M. N. Hopkinson, C. Richter, M. Schedler and F. Glorius, *Nature*, 2014, **510**, 485–496.
- 3 V. Charra, P. de Frémont and P. Braunstein, *Coord. Chem. Rev.*, 2017, **341**, 53–176.
- 4 S. Díez-González and S. P. Nolan, *Coord. Chem. Rev.*, 2007, **251**, 874–883.
- 5 H. - W Wanzlick and H. - J Schönherr, *Angew. Chem. Int. Ed.*, 1968, **7**, 141–142.
- 6 K. Ofele, *Angew. Chem.*, 1968, **7**, 950.
- 7 D. A. Dixon and A. J. Arduengo, *J. Phys. Chem.*, 1991, **95**, 4180–4182.
- 8 M. Scholl, S. Ding, C. W. Lee and R. H. Grubbs, *Org. Lett.*, 1999, **1**, 953–956.
- 9 S. Díez-González, N. Marion, S. P. Nolan and S. Díez-González, *Chem. Rev.*, 2009, **109**, 3612–3676.
- 10 K. Riener, S. Haslinger, A. Raba, M. P. Högerl, M. Cokoja, W. A. Herrmann and F. E. Kühn, *Chem. Rev.*, 2014, **114**, 5215–5272.
- 11 D. Bézier, J. B. Sortais and C. Darcel, *Adv. Synth. Catal.*, 2013, **355**, 19–33.
- 12 E. Charge and S. Energy, *Angew. Chem. Int. Ed.*, 1969, **8**, 889–930.
- 13 M. J. Ingleson and R. A. Layfield, *Chem. Commun.*, 2012, **48**, 3579–3589.
- 14 B. Liu, Y. Zhang, D. Xu and W. Chen, *Chem. Commun.*, 2011, **47**, 2883–2885.
- 15 L. Merics, G. Labat, A. Neels, A. Ehlers and M. Albrecht, *Organometallics*, 2006, **25**, 5648–5656.
- 16 I. Bauer and H.-J. Knölker, *Chem. Rev.*, 2015, **115**, 3170–3387.
- 17 J. Louie and R. H. Grubbs, *Chem. Commun.*, 2000, **1363**, 1479–1480.
- 18 R. B. Bedford, M. Betham, D. W. Bruce, A. a Danopoulos, R. M. Frost and M. Hird, *J. Org. Chem.*, 2006, **219**, 1104–1110.
- 19 F. Lazreg, F. Nahra and C. S. J. Cazin, *Coord. Chem. Rev.*, 2015, **293–294**, 48–79.
- 20 C. W. Tornøe, C. Christensen and M. Meldal, *J. Org. Chem.*, 2002, **67**, 3057–3064.
- 21 S. Díez-González, A. Correa, L. Cavallo and S. P. Nolan, *Chem. Eur. J.*, 2006, **12**, 7558–7564.
- 22 S. Díez-González, E. C. Escudero-Adán, J. Benet-Buchholz, E. D. Stevens, A. M. Z. Slawin and S. P. Nolan, *Dalt. Trans.*, 2010, **39**, 7595–7606.
- 23 S. Díez-gonzález and S. P. Nolan, *Acc. Chem. Res.*, 2008, **41**, 349–358.
- 24 C. Deutsch, N. Krause and B. H. Lipshutz, *Chem. Rev.*, 2008, **108**, 2916–2927.
- 25 S. Díez-González and S. P. Nolan, *Coord. Chem. Rev.*, 2007, **251**, 874–883.
- 26 S. Z. Tasker, E. A. Standley and T. F. Jamison, *Nature*, 2014, **509**, 299–309.
- 27 V. Ritleng, M. Henrion and M. J. Chetcuti, *ACS Catal.*, 2016, **6**, 890–906.
- 28 A. P. Prakasham and P. Ghosh, *Inorganica Chim. Acta*, 2015, **431**, 61–100.
- 29 F. S. Han, *Chem. Soc. Rev.*, 2013, **42**, 5270–5298.
- 30 S. Saito, M. Sakai and N. Miayura, *Tetrahedron Lett.*, 1996, **37**, 2993–2996.
- 31 T. Schaub, M. Backes and U. Radius, *J. Am. Chem. Soc.*, 2006, **128**, 15964–15965.
- 32 B. Gradel, E. Brenner, R. Schneider and Y. Fort, *Tetrahedron Lett.*, 2001, **42**, 5689–5692.
- 33 C. Desmarests, R. Schneider and Y. Fort, *J. Org. Chem.*, 2002, **67**, 3029–3036.
- 34 J. E. Dander, N. A. Weires and N. K. Garg, *Org. Lett.*, 2016, **18**, 3934–3936.
- 35 H. V. Huynh, Y. Han, R. Jothibasu and J. A. Yang, *Organometallics*, 2009, **28**, 5395–5404.
- 36 C. A. Citadelle, E. Le Nouy, F. Bisaro, A. M. Z. Slawin and C. S. J. Cazin, *Dalt. Trans.*, 2010, **39**, 4489–4491.
- 37 A. A. Danopoulos, N. Tsoureas, J. A. Wright and M. E. Light, *Organometallics*, 2004, **23**, 166–168.

- 38 I. Nieto, F. Cervantes-Lee and J. M. Smith, *Chem. Commun.*, 2005, 3811–3813.
- 39 C. D. Abernethy, R. J. Baker, M. L. Cole, A. J. Davies and C. Jones, *Transit. Met. Chem.*, 2003, **28**, 296–299.
- 40 B. Liu, B. Liu, Y. Zhou and W. Chen, *Organometallics*, 2010, **29**, 1457–1464.
- 41 B. Liu, Q. Xia and W. Chen, *Angew. Chem. Int. Ed.*, 2009, **48**, 5513–5516.
- 42 B. Liu, X. Liu, C. Chen, C. Chen and W. Chen, *Organometallics*, 2012, **31**, 282–288.
- 43 M. Atobe, *Curr. Opin. Electrochem.*, 2017, **2**, 1–6.
- 44 F. M. Cohan, J.-D. Graf, J. Wegner, S. Ceylan and A. Kirschning, *Chem. Commun.*, 2011, **47**, 4583–4592.
- 45 P. V. Danckwerts, *Chem. Eng. Sci.*, 1953, **1**, 1–13.
- 46 M. B. Plutschack, B. Pieber, K. Gilmore and P. H. Seeberger, *Chem. Rev.*, 2017, **117**, 11796–11893.
- 47 J. Wegner, S. Ceylan and A. Kirschning, *Chem. Commun.*, 2011, **47**, 4583–4592.
- 48 M. Guidi, P. H. Seeberger and K. Gilmore, *Chem. Soc. Rev.*, 2020, **49**, 8910–8932.
- 49 A. A. Folgueiras-Amador and T. Wirth, *J. Flow Chem.*, 2017, **7**, 1–2.
- 50 M. Movsisyan, E. I. P. Delbeke, J. K. E. T. Berton, C. Battilocchio, S. V. Ley and C. V. Stevens, *Chem. Soc. Rev.*, 2016, **45**, 4892–4928.
- 51 D. Cambié, C. Bottecchia, N. J. W. Straathof, V. Hessel and T. Noël, *Chem. Rev.*, 2016, **116**, 10276–10341.
- 52 R. L. Hartman, J. P. McMullen and K. F. Jensen, *Angew. Chem. Ed.*, 2011, **50**, 7502–7519.
- 53 A. S. Burange, S. M. Osman and R. Luque, *iScience*, 2022, **25**, 1–22.
- 54 F. E. Valera, M. Quaranta, A. Moran, J. Blacker, A. Armstrong, J. T. Cabral and D. G. Blackmond, *Angew. Chem. Ed.*, 2010, **49**, 2478–2485.
- 55 M. R. Chapman, M. H. T. Kwan, G. King, K. E. Jolley, M. Hussain, S. Hussain, I. E. Salama, C. González Nino, L. A. Thompson, M. E. Bayana, A. D. Clayton, B. N. Nguyen, N. J. Turner, N. Kapur and A. J. Blacker, *Org. Process Res. Dev.*, 2017, **21**, 1294–1301.
- 56 A. D. Clayton, J. Manson, C. J. Taylor, T. W. Chamberlain, B. Taylor, G. Clemens and R. Bourne, *React. Chem. Eng.*, 2019, **4**, 1545–1554.
- 57 C. J. Taylor, M. Booth, J. A. Manson, M. J. Willis, G. Clemens, B. A. Taylor, T. W. Chamberlain and R. A. Bourne, *Chem. Eng. J.*, 2021, **413**, 127017.
- 58 L. Degennaro, C. Carlucci, S. De Angelis and R. Luisi, *J. Flow Chem.*, 2016, **6**, 136–166.
- 59 J. Zhang, C. Gong, X. Zeng and J. Xie, *Coord. Chem. Rev.*, 2016, **324**, 39–53.
- 60 T. Brodmann, P. Koos, A. Metzger, P. Knochel and S. V. Ley, *Org. Process Res. Dev.*, 2012, **16**, 1102–1113.
- 61 M. E. Kopach, K. P. Cole, P. M. Pollock, M. D. Johnson, T. M. Braden, L. P. Webster, J. McClary Groh, A. D. McFarland, J. P. Schafer, J. J. Adler and M. Rosemeyer, *Org. Process Res. Dev.*, 2016, **20**, 1581–1592.
- 62 Q. Deng, R. Shen, R. Ding and L. Zhang, *Adv. Synth. Catal.*, 2014, **356**, 2931–2936.
- 63 M. Goldbach, E. Danieli, J. Perlo, B. Kaptein, V. M. Litvinov, B. Blümich, F. Casanova and A. L. L. Duchateau, *Tetrahedron Lett.*, 2016, **57**, 122–125.
- 64 S. M. Opalka, J. K. Park, A. R. Longstreet and D. T. McQuade, *Org. Lett.*, 2013, **15**, 996–999.
- 65 C. Lee, E. Pedrick and N. Leadbeater, *J. Flow Chem.*, 2012, **2**, 115–117.
- 66 A. Pagnoux-Ozherelyeva, D. Bolien, S. Gaillard, F. Peudru, J. F. Lohier, R. J. Whitby and J. L. Renaud, *J. Organomet. Chem.*, 2014, **774**, 35–42.
- 67 A. C. Gutierrez and T. F. Jamison, *J. Flow Chem.*, 2012, **1**, 24–27.
- 68 K. Watts, W. Gattrell and T. Wirth, *Beilstein J. Org. Chem.*, 2011, **7**, 1108–1114.
- 69 M. Yan, Y. Kawamata and P. S. Baran, *Chem. Rev.*, 2017, **117**, 13230–13319.
- 70 C. Schotten, T. P. Nicholls, R. A. Bourne, N. Kapur, B. N. Nguyen and C. E. Willans, *Green Chem.*, 2020, **22**, 3358–3375.
- 71 Y. Kumar, S. Rawal, B. Joshi and S. A. Hashmi, *J. Solid State Electrochem.*, 2019,



- 23**, 667–692.
- 72 L. Zhang and X. S. Zhao, *Chem. Soc. Rev.*, 2009, **38**, 2520–2531.
  - 73 C. Costentin and J. M. Savéant, *Proc. Natl. Acad. Sci. U. S. A.*, 2019, **166**, 11147–11152.
  - 74 J. E. Nutting, J. B. Gerken, A. G. Stamoulis, D. L. Bruns and S. S. Stahl, *J. Org. Chem.*, 2021, **86**, 15875–15885.
  - 75 N. Sbei, T. Hardwick and N. Ahmed, *ACS Sustain. Chem. Eng.*, 2021, **9**, 6148–6169.
  - 76 F. Battaglini, E. J. Calvo and F. Doctorovich, *J. Organomet. Chem.*, 1997, **547**, 1–21.
  - 77 A. M. Vecchio-Sadus, *J. Appl. Electrochem.*, 1993, **23**, 401–416.
  - 78 J. Grobe, *Comments Inorg. Chem.*, 1990, **9**, 149–179.
  - 79 M. C. Chakravorti, *Proc. Indian Acad. Sci. Chem. Sci.*, 1996, **108**, 175–180.
  - 80 A. D. Garnovskii, L. M. Blanco, B. I. Kharisov, D. A. Garnovskii and A. S. Burlov, *J. Coord. Chem.*, 1999, **48**, 219–263.
  - 81 D. G. Tuck, *Pure Appl. Chem.*, 1979, **51**, 2005–2018.
  - 82 A. Rodríguez and J. A. García-Vázquez, *Coord. Chem. Rev.*, 2015, **303**, 42–85.
  - 83 J. J. Habeeb, D. G. Tuck and F. H. Walters, *J. Coord. Chem.*, 1978, **8**, 27–33.
  - 84 J. J. Habeeb, L. Neilson and D. G. Tuck, *Inorg. Chem.*, 1978, **17**, 306–310.
  - 85 C. Geloso, R. Kumar, J. R. Lopez-Grado and D. G. Tuck, *Can. J. Chem.*, 1987, **65**, 928–932.
  - 86 J. L. Hencher, M. Khan, F. F. Said, R. Sieler and D. G. Tuck, *Inorg. Chem.*, 1982, **21**, 2787–2791.
  - 87 H. Lehmkuhl and W. Eisenbach, *Justus Liebigs Ann. Chem.*, 1975, 672–691.
  - 88 J. J. Habeeb and D. G. Tuck, *J. Chem. Soc. Chem. Commun.*, 1975, 808–809.
  - 89 J. J. Habeeb, F. Said and D. G. Tuck, *Inorg. Nucl. Chem. Lett.*, 1978, **15**, 113–116.
  - 90 N. Kumar and D. G. Tuck, *Can. J. Chem.*, 1982, **60**, 2579–2582.
  - 91 J. J. Habeeb, A. Osman and D. G. Tuck, *J. Chem. Soc. Chem. Commun.*, 1976, 379–380.
  - 92 S. R. Long and J. J. Lagowski, *Synth. React. Inorganic, Met. Nano-Metal Chem.*, 2007, **37**, 813–815.
  - 93 N. Kumar, D. G. Tuck and K. D. Watson, *Can. J. Chem.*, 1987, **65**, 740–743.
  - 94 T. A. Annan, R. Kumar and D. G. Tuck, *J. Chem. Soc. Dalt. Trans.*, 1991, 11–18.
  - 95 J. H. Green, R. Kumar, N. Seudeal and D. G. Tuck, *Inorg. Chem.*, 1989, **28**, 123–127.
  - 96 R. Kumar and D. G. Tuck, *Inorganica Chim. Acta*, 1989, **157**, 51–56.
  - 97 T. A. Annan, J. Kickham and D. G. Tuck, *Can. J. Chem.*, 1991, 0–5.
  - 98 M. R. Chapman, S. E. Henkelis, N. Kapur, B. N. Nguyen and C. E. Willans, *ChemistryOpen*, 2016, **5**, 351–356.
  - 99 B. R. M. Lake, E. K. Bullough, T. J. Williams, A. C. Whitwood, M. A. Little and C. E. Willans, *Chem. Commun.*, 2012, **48**, 4887–4889.
  - 100 B. R. M. Lake, E. K. Bullough, T. J. Williams, A. C. Whitwood, M. A. Little and C. E. Willans, *Chem. Commun.*, 2012, **48**, 4887–4889.
  - 101 L. Bustos, J. H. Green, J. L. Hencher, M. A. Khan and D. G. Tuck, *Can. J. Chem.*, 1983, **61**, 2141–2146.
  - 102 M. R. Bermejo, A. M. González, M. Fondo, A. García-Deibe, M. Maneiro, J. Sanmartín, O. L. Hoyos and M. Watkinson, *New J. Chem.*, 2000, **24**, 235–241.
  - 103 M. R. Bermejo, R. Pedrido, A. M. González-Noya, M. J. Romero, M. Vázquez and L. Sorace, *New J. Chem.*, 2003, **27**, 1753–1759.
  - 104 R. Weast, *Handbook of Chemistry and Physics*, CRC press, Boca Raton, Florida, 1st edn., 1987.
  - 105 G. Laudadio, & Wouter De Smet, L. Struik, Y. Cao and T. Noël, 1981, 157–165.
  - 106 C. Gütz, A. Stenglein and S. R. Waldvogel, *Org. Process Res. Dev.*, 2017, **21**, 771–778.
  - 107 A. A. Folgueziras-Amador, K. Philipps, S. Guilbaud, J. Poelakker and T. Wirth, *Angew. Chem. Int. Ed.*, 2017, **56**, 15446–15450.

- 108 T. Noël, Y. Cao and G. Laudadio, *Acc. Chem. Res.*, 2019, **52**, 2858–2869.
- 109 M. A. Cataldo-Hernández, A. Bonakdarpour, J. T. English, M. Mohseni and D. P. Wilkinson, *React. Chem. Eng.*, 2019, **4**, 1116–1125.
- 110 R. A. Green, R. C. D. Brown, D. Pletcher and B. Harji, *Org. Process Res. Dev.*, 2015, **19**, 1424–1427.
- 111 G. Laudadio, N. J. W. Straathof, M. D. Lanting, B. Knoops, V. Hessel and T. Noël, *Green Chem.*, 2017, **19**, 4061–4066.
- 112 M. R. Chapman, Y. M. Shafi, N. Kapur, B. N. Nguyen and C. E. Willans, *Chem. Commun.*, 2015, **51**, 1282–1284.
- 113 D. Horii, T. Fuchigami and M. Atobe, *J. Am. Chem. Soc.*, 2007, **129**, 11692–11693.
- 114 B. K. Peters, K. X. Rodriguez, S. H. Reisberg, S. B. Beil, D. P. Hickey, Y. Kawamata, M. Collins, J. Starr, L. Chen, S. Udyavara, K. Klunder, T. J. Gorey, S. L. Anderson, M. Neurock, S. D. Minter and P. S. Baran, *Science*, 2019, **363**, 838–845.
- 115 M. Elsherbini, B. Winterson, H. Alharbi, A. A. Folguez-Amador, C. Génot and T. Wirth, *Angew. Chem. Int. Ed.*, 2019, **58**, 9811–9815.
- 116 A. Wiebe, T. Gieshoff, S. Möhle, E. Rodrigo, M. Zirbes and S. R. Waldvogel, *Angew. Chem. Int. Ed.*, 2018, **57**, 5594–5619.
- 117 S. Möhle, M. Zirbes, E. Rodrigo, T. Gieshoff, A. Wiebe and S. R. Waldvogel, *Angew. Chem. Int. Ed.*, 2018, **57**, 6018–6041.
- 118 Jun-ichi Yoshida, Kazuhide Kataoka, Roberto Horcajada and Aiichiro Nagaki, *Chem. Rev.*, 2008, **108**, 2265–2299.
- 119 M. D. Kärkäs, *Chem. Soc. Rev.*, 2018, **47**, 5786–5865.
- 120 S. R. Waldvogel, S. Lips, M. Selt, B. Riehl and C. J. Kampf, *Chem. Rev.*, 2018, **118**, 6706–6765.
- 121 S. R. Waldvogel and B. Janza, *Angew. Chem. Int. Ed.*, 2014, **53**, 7122–7123.
- 122 J. Grobe, *Comments Inorg. Chem.*, 1990, **9**, 149–179.
- 123 M. Yan, Y. Kawamata and P. S. Baran, *Angew. Chem. Int. Ed.*, 2018, **57**, 4149–4155.
- 124 E. J. Horn, B. R. Rosen, Y. Chen, J. Tang, K. Chen, M. D. Eastgate and P. S. Baran, *Nature*, 2016, **533**, 77–81.
- 125 A. G. O'Brien, A. Maruyama, Y. Inokuma, M. Fujita, P. S. Baran and D. G. Blackmond, *Angew. Chem. Int. Ed.*, 2014, **53**, 11868–11871.
- 126 Y. Kawamata, M. Yan, Z. Liu, D. H. Bao, J. Chen, J. T. Starr and P. S. Baran, *J. Am. Chem. Soc.*, 2017, **139**, 7448–7451.
- 127 I. M. Malkowsky, U. Griesbach, H. Pütter and S. R. Waldvogel, *European J. Org. Chem.*, 2006, 4569–4572.
- 128 G. Laudadio, E. Bampoutsis, C. Schotten, L. Struik, S. Govaerts, D. L. Browne and T. Noël, *J. Am. Chem. Soc.*, 2019, **141**, 5664–5668.
- 129 X. Luo, X. Ma, F. Lebreux, I. E. Markó and K. Lam, *Chem. Commun.*, 2018, **54**, 9969–9972.
- 130 P. Baran, E. Horn, S. Waldmann, 2018, US Patent No. 2018/0217096.
- 131 P. J. Rae and D. M. Dattelbaum, *Polymer*, 2004, **45**, 7615–7625.
- 132 C. A. Sperati and H. W. Starkweather, 1961, **5**, 465–495.
- 133 E. Altiok, M. R. Alvis, Y. P. Arramon, D. Baykal, B. Berg-Johansen, M. Brady, A. Briscoe, C. L. Brockett, N. M. Cordaro, J. Day, D. Eglin, T. Fintan Moriarty, M. Garcia-Leiner, R. Geoff Richards, O. Ghita, J. Graham, S. Green, N. J. Hickok, D. Hovda, K. Ishihara, D. J. Jaekel, M. Jarman-Smith, S. M. Kurtz, M. Kyomoto, S. Lal, T. Lanman, S. Lovald, M. K. C. Lui, R. McKay, T. Moro, J. Nevelos, K. Ong, E. Ouellette, K. M. Pasko, J. Peck, M. Plaza-Castro, A. H. C. Poulsson, M. Reitman, C. M. Rimnac, P. Robotti, E. T. J. Rochford, R. K. Roeder, N. Sereno, B. Siewert, R. Siskey, M. C. Sobieraj, A. A. Stratton-Powell, J. L. Tipper, J. M. Toth, R. J. Underwood, W. R. Walsh and G. Zappini, *PEEK Biomaterials Handbook*, William Andrew Publishing, Second ed., 2019.
- 134 L. Lozada-Rodríguez, J. B. Pelayo-Vázquez, I. I. Rangel-Salas, J. G. Alvarado-Rodríguez, A. A. Peregrina-Lucano, A. Pérez-Centeno, F. A. López-Dellamary-

- Toral and S. A. Cortes-Llamas, *Dalt. Trans.*, 2017, **46**, 3809–3811.
- 135 S. T. Lin, M. F. Ding, C. W. Chang and S. S. Lue, *Tetrahedron*, 2004, **60**, 9441–9446.
- 136 C. E. Housecroft and A. G. Sharpe, *Inorganic Chemistry*, Pearson Education Limited, Harlow, 4th edition, 2012.
- 137 N. Elgrishi, K. J. Rountree, B. D. McCarthy, E. S. Rountree, T. T. Eisenhart and J. L. Dempsey, *J. Chem. Educ.*, 2018, **95**, 197–206.
- 138 K. J. Rountree, B. D. McCarthy, E. S. Rountree, T. T. Eisenhart and J. L. Dempsey, *J. Chem. Educ.*, 2018, **95**, 197–206.
- 139 L. R. Faulkner, *J. Chem. Educ.*, 1983, **60**, 262–264.
- 140 D. G. Gusev, *Organometallics*, 2009, **28**, 6458–6461.
- 141 H. G. Roth, N. A. Romero and D. A. Nicewicz, *Synlett*, 2016, **27**, 714–723.
- 142 H.-Y. Gao, G. Wang, M. Knor, S. Amirjalayer, N. L. Doltsinis, A. Rühling, H. Fuchs, A. Timmer, J. B. Ernst, C. Richter, H.-J. Gao and F. Glorius, *Nat. Chem.*, 2016, **9**, 152–156.
- 143 S. Díez-González, E. C. Escudero-Adán, J. Benet-Buchholz, E. D. Stevens, A. M. Z. Slawin and S. P. Nolan, *Dalt. Trans.*, 2010, **39**, 7595–7606.
- 144 F. V. Singh and T. Wirth, *Synth.*, 2013, **45**, 2499–2511.
- 145 M. Brown, R. Kumar, J. Rehbein and T. Wirth, *Chem. Eur. J.*, 2016, **22**, 4030–4035.
- 146 V. V. Zhdankin and P. J. Stang, *Chem. Rev.*, 2002, **102**, 2523–2584.
- 147 E. A. Merritt and B. Olofsson, *Angew. Chem. Int. Ed.*, 2009, **48**, 9052–9070.
- 148 M. Elsherbini and T. Wirth, *Chem. Eur. J.*, 2018, **24**, 13399–13407.
- 149 R. Francke, T. Broese and A. F. Roesel, *PATAI'S Chem. Funct. Groups*, 2018, 1–22.
- 150 G. De Robillard, C. H. Devillers, D. Kunz, H. Cattey, E. Digard and J. Andrieu, *Org. Lett.*, 2013, **15**, 4410–4413.
- 151 G. M. Sheldrick, *Acta Crystallogr. Sect. C Struct. Chem.*, 2015, **71**, 3–8.
- 152 O. V. Dolomanov, L. J. Bourhis, R. J. Gildea, J. A. K. Howard and H. Puschmann, *J. Appl. Crystallogr.*, 2009, **42**, 339–341.
- 153 D. Degner, *Top. Curr. Chem.*, 1988, **148**, 1–95.
- 154 S. A. May, *J. Flow Chem.*, 2017, **7**, 137–145.
- 155 M. D. Kärkäs, *Chem. Soc. Rev.*, 2018, **47**, 5786–5865.
- 156 Y. Yu, P. Guo, J. S. Zhong, Y. Yuan and K. Y. Ye, *Org. Chem. Front.*, 2019, **7**, 131–135.
- 157 T. P. Nicholls, C. Schotten and C. E. Willans, *Curr. Opin. Green Sustain. Chem.*, 2020, 100355.
- 158 D. Pletcher, R. A. Green and R. C. D. Brown, *Chem. Rev.*, 2018, **118**, 4573–4591.
- 159 R. A. Green, R. C. D. Brown, D. Pletcher and B. Harji, *Org. Process Res. Dev.*, 2015, **19**, 1424–1427.
- 160 J. Kuleshova, J. T. Hill-Cousins, P. R. Birkin, R. C. D. Brown, D. Pletcher and T. J. Underwood, *Electrochim. Acta*, 2011, **56**, 4322–4326.
- 161 W. Jud, C. O. Kappe and D. Cantillo, *Chemistry-Methods*, 2021, **1**, 36–41.
- 162 A. Folgueiras-Amador, 2017, PhD Thesis, Cardiff University, Cardiff.
- 163 Y. Cao and T. Noël, *Org. Process Res. Dev.*, 2019, **23**, 403–408.
- 164 A. N. Colli, R. Toelzer, M. E. H. Bergmann and J. M. Bisang, *Electrochim. Acta*, 2013, **100**, 78–84.
- 165 A. Storck and F. Coeuret, *Electrochim. Acta*, 1977, **22**, 1155–1160.
- 166 A. Storck and D. Hutin, *Electrochim. Acta*, 1981, **26**, 127–137.
- 167 L. Carlsson, B. Sandegren, D. Simonsson and M. Rihovsky, *J. Electrochem. Soc.*, 1983, **83-6**, 8–16.
- 168 C. F. Oduoza, A. A. Wragg and M. A. Patrick, *Chem. Eng. J.*, 1997, **68**, 145–155.
- 169 J. Kuleshova, J. T. Hill-Cousins, P. R. Birkin, R. C. D. Brown, D. Pletcher and T. J. Underwood, *Electrochim. Acta*, 2012, **69**, 197–202.
- 170 C. Schotten, C. J. Taylor, R. A. Bourne, T. W. Chamberlain, B. N. Nguyen, N. Kapur and C. E. Willans, *React. Chem. Eng.*, 2021, **6**, 147–151.
- 171 A. N. Colli and J. M. Bisang, *J. Electrochem. Soc.*, 2018, **165**, E81–E88.

- 172 F. Incropera, D. Dewitt, T. Bergman and A. Lavine, *Fundamentals of Heat and Mass Transfer*, John Wiley and Sons, Sixth., 2007.
- 173 J. Douglas, J. Gasoriek, J. Swaffield and L. Jack, *Fluid Mechanics*, Pearson Education Limited, Fifth., 2005.
- 174 H. K. Moffatt, *J. Fluid Mech.*, 1964, **18**, 1–18.
- 175 E. N. Kimuli, I. I. Onyemelukwe, B. Benyahia and C. D. Rielly, *Characterisation of axial dispersion in a Meso-scale Oscillatory Baffled Crystalliser using a Numerical Approach*, Elsevier Masson SAS, 2017, vol. 40.
- 176 D. Rossi, L. Gargiulo, G. Valitov, A. Gavrilidis and L. Mazzei, *Chem. Eng. Res. Des.*, 2017, **120**, 159–170.
- 177 P. Coñizares, J. García-Gómez, I. Fernández de Marcos, M. A. Rodrigo and J. Lobato, *J. Chem. Educ.*, 2006, **83**, 1204–1207.
- 178 S. Petrovic, *Chem. Educ.*, 2000, **5**, 231–235.
- 179 F. Amemiya, J. E. Soc, F. Amemiya, D. Horii, T. Fuchigami and M. Atobe, *J. Electrochem. Soc.*, 2008, **155**, E162.
- 180 M. F. Hartmer and S. R. Waldvogel, *Chem. Commun.*, 2015, **51**, 16346–16348.
- 181 H. R. Stephen, C. Schotten, T. P. Nicholls, M. Woodward, R. A. Bourne, N. Kapur and C. E. Willans, *Org. Process Res. Dev.*, 2020, **24**, 1084–1089.
- 182 O. C. Zienkiewicz, R. L. Taylor and P. Nithiarasu, *The Finite Element Method for Fluid Dynamics*, Elsevier Butterworth Heinemann, Amsterdam, The Netherlands, 6th edn., 2005.
- 183 S. Z. Tasker, E. A. Standley and T. F. Jamison, *Nature*, 2014, **509**, 299–309.
- 184 K. S. Egorova and V. P. Ananikov, *Organometallics*, 2017, **36**, 4071–4090.
- 185 K. S. Egorova and V. P. Ananikov, *Angew. Chem. Int. Ed.*, 2016, **55**, 12150–12162.
- 186 J. D. Hayler, D. K. Leahy and E. M. Simmons, *Organometallics*, 2019, **38**, 36–46.
- 187 International Conference on Harmonisation (ICH), ICH guideline Q3D (R1): Guideline for Elemental Impurities.
- 188 National Toxicology Program, *15th Report on Carcinogens: Nickel Compounds and Metallic Nickel*, 2021.
- 189 B. Liu, Y. Zhang, D. Xu and W. Chen, *Chem. Commun.*, 2011, **47**, 2883–2885.
- 190 T. P. Nicholls, R. A. Bourne, B. N. Nguyen, N. Kapur and C. E. Willans, *Inorg. Chem.*, 2021, **60**, 6976–6980.
- 191 G. Cotton, F. A.; Wilkinson, *Advanced Inorganic Chemistry*, John Wiley and Sons, Third Edit., 1980.
- 192 M. Schultz, P. N. Plessow, F. Rominger and L. Weigel, *Acta Crystallogr. Sect. C Cryst. Struct. Commun.*, 2013, **69**, 1437–1447.
- 193 R. G. Hayter and F. S. Humiec, *Inorg. Chem.*, 1965, **4**, 1701–1706.
- 194 H. R. Stephen, S. Boyall, C. Schotten, R. A. Bourne, N. Kapur and C. E. Willans, *React. Chem. Eng.*, 2022, **7**, 264–268.
- 195 M. R. Chapman, Y. M. Shafi, N. Kapur, B. N. Nguyen and C. E. Willans, *Chem. Commun.*, 2015, **51**, 1282–1284.
- 196 S. Maljuric, W. Jud, C. O. Kappe and D. Cantillo, *J. Flow Chem.*, 2020, **10**, 181–190.
- 197 R. Green, R. Brown and D. Pletcher, *J. Flow Chem.*, 2015, **5**, 31–36.
- 198 Z. Xi, X. Zhang, W. Chen, S. Fu and D. Wang, *Organometallics*, 2007, **26**, 6636–6642.
- 199 H. M. Shahadat, H. A. Younus, N. Ahmad, M. A. Rahaman, Z. A. K. Khattak, S. Zhuikyov and F. Verpoort, *Catal. Sci. Technol.*, 2019, **9**, 5651–5659.
- 200 R. G. Pearson, *J. Chem. Educ.*, 1968, **45**, 581–587.
- 201 R. G. Pearson, *J. Chem. Educ.*, 1968, **45**, 643–648.
- 202 C. Zoski, *Handbook of Electrochemistry*, Elsevier B.V, Amsterdam, First edit., 2007.
- 203 F. P. Byrne, S. Jin, G. Paggiola, T. H. M. Petchey, J. H. Clark, T. J. Farmer, A. J. Hunt, C. Robert McElroy and J. Sherwood, *Sustain. Chem. Process.*, 2016, **4**, 1–24.
- 204 W. Zhou and Z. L. Wang, *Scanning Microscopy for Nanotechnology: Techniques*

- and Applications*, Springer Science + Business Media, LLC, New York, First edit., 2007.
- 205 T. Hang, M. Li, Q. Fei and D. Mao, *Nanotechnology*, 2008, **19**, 035201.
  - 206 J. M. Lee, K. K. Jung and J. S. Ko, *J. Mater. Sci.*, 2016, **51**, 3036–3044.
  - 207 A. Bakker, A. Timmer, E. Kolodzeiski, M. Freitag, H. Y. Gao, H. Mönig, S. Amirjalayer, F. Glorius and H. Fuchs, *J. Am. Chem. Soc.*, 2018, **140**, 11889–11892.
  - 208 G. Wang, A. Rühling, S. Amirjalayer, M. Knor, J. B. Ernst, C. Richter, H. J. Gao, A. Timmer, H. Y. Gao, N. L. Doltsinis, F. Glorius and H. Fuchs, *Nat. Chem.*, 2017, **9**, 152–156.
  - 209 Y. Zeng, T. Zhang, M. R. Narouz, C. M. Crudden and P. H. McBreen, *Chem. Commun.*, 2018, **54**, 12527–12530.
  - 210 C. R. Larrea, C. J. Baddeley, M. R. Narouz, N. J. Mosey, J. H. Horton and C. M. Crudden, *ChemPhysChem*, 2017, **18**, 3536–3539.
  - 211 E. Angove, F. Grillo, H. A. Früchtl, A. J. Veinot, I. Singh, J. H. Horton, C. M. Crudden and C. J. Baddeley, *J. Phys. Chem. Lett.*, 2022, **13**, 2051–2056.
  - 212 R. Angelici, *Inorganic syntheses: Reagents for transition metal complex and organometallic syntheses, Volume 28*, John Wiley and Sons, New York, First edit., 1990.
  - 213 J. P. Morgan, 2002, PhD Thesis, California Institute of Technology, Pasadena.
  - 214 W. B. Jensen, *Educ. Quim.*, 2017, **28**, 217–224.
  - 215 F. Szabadvary, *History of Analytical Chemistry*, Pergamon Press Ltd, Oxford, First Edit., 1966.
  - 216 L. F. Capitán-Vallvey, N. López-Ruiz, A. Martínez-Olmos, M. M. Erenas and A. J. Palma, *Anal. Chim. Acta*, 2015, **899**, 23–56.
  - 217 M. S. Woolf, L. M. Dignan, A. T. Scott and J. P. Landers, *Nat. Protoc.*, 2021, **16**, 218–238.
  - 218 A. G. Wills, D. L. Poole, C. M. Alder and M. Reid, *ChemElectroChem*, 2020, **7**, 2771–2776.
  - 219 R. Belasco, T. Edwards, A. J. Munoz, V. Rayo and M. J. Buono, *Front. Nutr.*, 2020, **7**, 1–9.
  - 220 V. S. Thoi and C. J. Chang, *Chem. Commun.*, 2011, **47**, 6578–6580.
  - 221 I. Klawitter, S. Meyer, S. Demeshko and F. Meyer, *Zeitschrift für Naturforsch. - Sect. B J. Chem. Sci.*, 2013, **68**, 458–466.
  - 222 V. S. Thoi, N. Kornienko, C. G. Margarit, P. Yang and C. J. Chang, *J. Am. Chem. Soc.*, 2013, **135**, 14413–14424.
  - 223 T. Fujimoto and T. Ritter, *Org. Lett.*, 2015, **17**, 544–547.
  - 224 T. Wagner, A. Pöthig, H. M. S. Augenstein, T. D. Schmidt, M. Kaposi, E. Herdtweck, W. Brütting, W. A. Herrmann and F. E. Kühn, *Organometallics*, 2015, **34**, 1522–1529.
  - 225 Z. Xi, B. Lui, C. Lu and W. Chen, *Dalt. Trans.*, 2009, 6903–6914.

